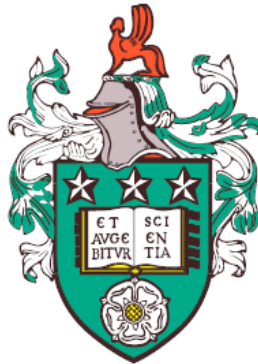


Novel Phase Behaviour in Bent-Core Nematic Liquid Crystals and their Mixtures



Shajeth Srigengan

School of Physics and Astronomy

University of Leeds

Submitted in accordance with the requirements for the degree of

Doctor of Philosophy

March 2019

The candidate confirms that the work submitted is his own, except where work which has formed part of jointly authored publications has been included. The contribution of the candidate and other authors to this work has been explicitly indicated below. The candidate confirms that appropriate credit has been given within the thesis where reference has been made to the work of others.

Chapter 4 and 5 includes material which has been published in the paper by Shajeth Srigengan, Mamatha Nagaraj, Alberta Ferrarini, Richard Mandle, Stephen J. Cowling, Mikhail A. Osipov, Grzegorz Pająk, John W. Goodby and Helen F. Gleeson in the journal *Journal of Materials Chemistry C* in 2018 (volume 6, issue (5) and pages 980-988). The experimental work and the majority of the writing of this paper was performed by myself. A. Ferrarini carried out the computational calculations. M. A. Osipov and G. Pająk carried out the theoretical calculations. R. Mandle, S. J. Cowling and J. W. Goodby were involved in the synthesis of the pure materials. M. Nagaraj and H. F. Gleeson provided edits and comments to drafts of this paper.

Chapter 5 includes material which is in a paper currently in review in the journal *Journal of Materials Chemistry C*. The authors of the paper are Shajeth Srigengan, Harry Liu, Mikhail A. Osipov, Richard Mandle, Stephen J. Cowling and Helen F. Gleeson. The majority of the experimental work and writing of this paper was performed by myself. H. Liu carried out measurements of the elastic constants on mixture 9 in this thesis (mixture 6 in the paper). M. A. Osipov carried out the theoretical calculations. R. Mandle and S. J. Cowling were involved in the synthesis of the pure materials. H. F. Gleeson provided edits and comments to drafts of this paper.

This copy has been supplied on the understanding that it is copyright material and that no quotation from the thesis may be published without proper acknowledgement.

© 2018 The University of Leeds and Shajeth Srigengan

The right of Shajeth Srigengan to be identified as Author of this work has been asserted by him in accordance with the Copyright, Designs and Patents Act 1988.

To Mum and Dad,
for all the sacrifices you both made to get me to where I am today.

Acknowledgements

First of all I'd like to thank my supervisors Prof. Helen Gleeson and Dr. Mamatha Nagaraj for giving me the opportunity to study and learn under guidance. I've learnt an incredible amount throughout this PhD and a lot of that couldn't have happened without the help from both of you. I'd like to thank my industrial supervisors Dr. Rachel Tuffin and Joe Sargent at Merck Chemicals for your help and interesting discussions through the years. I'd also like to thank EPSRC and Merck Chemicals Ltd. for funding my project.

Thank you to everyone in the SMP family, both past and present, for all the support, motivation and distraction. Thanks to other PhD students; Sophie, Edgar, Ethan, Yunhao, Pete, Rowan, James, Nikita, Adam, Zach, Nina, Mariam, Tom, Peter, Harry, Bart, Ben, Devesh, Steve, Outi, Helen, Matt, Guangui, Wafa, and Winke. You lot made my time at Leeds all that more enjoyable, and those still around kept me sane enough at the height of thesis-writing. Thanks to the academics and postdocs, namely Prof. Cliff Jones, Drs. Sarabjot Kaur, James Bailey, Dan Baker, Maryam Nikkou, Markus Wahle, Antariksh Saxena, and Mr Dan Paterson, for the help and useful discussions throughout my PhD. Special thanks to Glenys for all the help you've given all of us over the years.

Finally I'd like to thank my family for all the support, not only whilst I've been at Leeds but since the very beginning. Thanks to my brother Braj and sister-in-law Aimée for all the trips to see the cats and dogs whenever I was back in Belfast; it was always nice to start those visits on a high note. Most of all I'd like to thank my parents. You were both always there for me, whether I needed it or not, and always made

sure I lived up to my potential. Without you pushing me forward I don't think I'd ever be where I am here today. Also thanks for the free food whenever I visited home!

Abstract

Studies of bent-core liquid crystals have provided a fascinating insight into these systems, not only for their potential use in applications but also for fundamental research. It is known that the elastic behaviour in bent-core liquid crystals is different than in calamitic liquid crystals; the splay elastic constant $K_{11} < K_{33}$ (bend elastic constant) in bent-cores, compared to $K_{33} < K_{11}$ in calamitics. This thesis will investigate the elastic behaviour in oxadiazole based bent-core liquid crystals and in their mixtures, aiming to gain an insight into the phase behaviour that is exhibited in these systems.

An oxadiazole based bent-core liquid crystal was found to exhibit anomalously low twist (K_{22}) and bend elastic constants. Computational and theoretical calculations were carried out on this material; the elastic behaviour was explained by considering the contributions of spontaneous chirality and polarity. Fluctuations of the chiral conformers of the molecule cause a negative correction to K_{22} which was found to be large in this material. In a similar fashion, fluctuations in the local polar order cause a negative correction to K_{33} which was also found to be large in this material.

Binary mixtures of two bent-core liquid crystals were created and the elastic constants measured. It was found that the values measured for the mixtures lie in between those measured for the two pure materials, as expected when considering simple mixing rules. Mixtures of calamitic liquid crystals doped with 10% of bent-core mesogens were also investigated. In all of these mixtures the splay constant was unaffected by the bent-core dopant, with the bend constant reducing by 10-20% and the twist constant reducing by up to 40%. The splay

results are explained by considering that the bent-core dopants have no scope to exhibit any wedge-shaped conformers, thus having no significant impact on K_{11} . The bend results are in line with simple mixing rules and existing literature. The twist results suggest that the fluctuations in chiral conformers of the bent-core molecules enhance fluctuations of chirality in the conformers in the calamitic host, thus providing a large negative correction to K_{22} .

Investigating the phase behaviour of the binary mixtures of two bent-core liquid crystals showed that two different underlying phases were exhibited, dependent on the concentrations of the bent-core materials. It was found that the elastic behaviour in the nematic phases of the mixtures had no discernible influence on the formation of the underlying phases, and thus the elastic constants are not the sole driving factor in the formation of the underlying phases. In mixtures of calamitic liquid crystals doped with bent-core mesogens, it was found that some of the mixtures exhibited self-assembling filament structures that grow in phases below the isotropic phase. Results showed that the filament growth is dependent on the director, and exhibited time-dependent behaviour that is analogous to that observed in certain lyotropic systems.

This thesis forms part of a project funded by the EPSRC CASE award with Merck Chemicals Ltd., aiming to investigate the potential of bent-core liquid crystals for both display and non-display applications. The results described here aid in understanding the novel elastic and phase behaviour in bent-core liquid crystals and their mixtures.

Abbreviations

AFM	Atomic force microscopy
BP	Blue phase
C18	Trichloro(octadecyl)
Cr	Crystal phase
DC	Dark conglomerate phase
DFT	Density functional theory
DSC	Differential scanning calorimetry
FWHM	Full width half maximum
IPS	In-plane switching
Iso	Isotropic phase
I+F	Isotropic phase with filaments
MC	Monte Carlo
N	Nematic phase
N*	Chiral nematic phase
N_{TB}	Twist-bend nematic phase
N+F	Nematic phase with filaments
POM	Polarising optical microscopy
RIS	Rotational isomeric state
SAXS	Small angle x-ray scattering
SEM	Scanning electron microscopy
SI	Surface interaction
SmA	Smectic A phase
SmA+F	Smectic A phase with filaments
SmC	Smectic C phase
SmC*	Chiral smectic C phase
SmX	Smectic phase of unknown type
TN	Twisted nematic
ULP	Underlying phase

Nomenclature

ε	Dielectric permittivity
ε_{\perp}	Perpendicular component of ε
ε_{\parallel}	Parallel component of ε
d	Device thickness
d_s	Lattice spacing in X-ray scattering
$\Delta\varepsilon$	Dielectric anisotropy
ΔF	Frank elastic free energy
K_{11}	Splay elastic constant
K_{22}	Twist elastic constant
K_{33}	Bend elastic constant
K_{24}	Saddle-splay elastic constant
L	Molecular length
n_o	Ordinary refractive index
n_e	Extra-ordinary refractive index
Δn	Birefringence
T_{N-DC}	Nematic to dark conglomerate phase transition temperature
T_{NI}	Nematic to isotropic phase transition temperature
T_{N-SmX}	Nematic to smectic X phase transition temperature
θ_t	Tilt angle
V_{th}	Threshold voltage

Contents

List of Figures	xv
List of Tables	xxv
1 Introduction	1
1.1 Introduction to Liquid Crystals	1
1.2 Elasticity in Liquid Crystals	4
1.3 The Dark Conglomerate Phase	5
1.4 Roadmap of Thesis	7
1.5 Motivation	8
2 Elastic Theory of Liquid Crystals	9
2.1 Introduction	9
2.2 Elastic Constant Theory	9
2.3 Types of Order	16
2.3.1 Polar order	16
2.3.2 Chiral order	19
2.4 Spontaneous Polarity and Chirality	20
2.4.1 Polar and chiral order considerations	20
2.4.2 Twist-bend nematic phase	23
2.5 Fluctuations in Polarity and Chirality	26
2.6 Summary	27
3 Experimental Methodology	28
3.1 Introduction	28
3.2 Materials and Devices	28
3.2.1 Materials	28

3.2.2	Devices	34
3.3	Polarising Optical Microscopy	36
3.4	Differential Scanning Calorimetry	37
3.5	Measuring Dielectric Anisotropy	38
3.6	Measuring Elastic Constants	42
3.6.1	Optical measurements of the splay and bend elastic constants	42
3.6.2	Dielectric measurements of the splay and bend elastic constants	47
3.6.3	Optical measurements of the twist elastic constant	49
3.7	X-Ray Scattering	49
3.8	Measuring Birefringence	53
3.9	High Resolution Microscopy	54
3.9.1	Atomic Force Microscopy	54
3.9.2	Scanning Electron Microscopy	56
3.10	Summary	56
4	Elastic Behaviour in DT12: Experimental and Theoretical Results	58
4.1	Introduction	58
4.2	Experimental Methodology	60
4.2.1	Materials and devices	60
4.2.2	Measurements of dielectric anisotropy and elastic constants	61
4.2.3	Calculations of the elastic constants	62
4.3	Results	65
4.4	Discussion	67
4.5	Molecular Mean Theory	71
4.6	Conclusions	75
5	Elastic Behaviour in Bent-Core Liquid Crystal Mixtures	77
5.1	Introduction	77
5.2	Mixtures of DT12 and VBG93	80
5.2.1	Experimental methodology	80
5.2.2	Results of mixtures of DT12 and VBG93	82

5.2.3	Discussion of mixtures of DT12 and VBG93	85
5.3	Bent-Core and Calamitic Liquid Crystal Mixtures	86
5.3.1	Experimental methodology	86
5.3.2	Results of mixtures of calamitic and bent-core mesogens	90
5.3.2.1	5CB mixtures; mixtures 6 and 10	90
5.3.2.2	8CB mixtures; mixtures 7 and 11	93
5.3.2.3	ZLI 1132 mixtures; mixtures 9 and 12	96
5.3.3	Discussion of mixtures of calamitic and bent-core mesogens	98
5.3.4	Theoretical Insight	99
5.4	Conclusions	106
6	Phase Behaviour in Bent-Core Liquid Crystal Mixtures	109
6.1	Introduction	109
6.2	Experimental Methodology	110
6.2.1	Materials	110
6.2.2	X-ray scattering	112
6.3	X-Ray Scattering in Bent-Core Mixtures	115
6.3.1	Optically isotropic phases; mixtures 1 and 2	115
6.3.2	Smectic phases; mixtures 3-5	119
6.4	Discussion	122
6.4.1	Characterisation of the optically isotropic phases	124
6.4.2	Spacing in the smectic phases	124
6.4.3	FWHM in the smectic phases	124
6.4.4	Tilt angle in the smectic phases	125
6.4.5	POM images of the smectic phases	125
6.4.6	Elastic behaviour in DC phase mixtures	126
6.4.7	Elastic behaviour in smectic phase mixtures	129
6.5	Summary	131
7	Phase Behaviour in Calamitic and Bent-Core Liquid Crystal Mixtures	134
7.1	Introduction	134
7.2	Experimental Methodology	136

CONTENTS

7.2.1	Materials	136
7.2.2	High Resolution Microscopy	140
7.2.3	Measurments of birefringence	140
7.3	High Resolution Microscopy Measurements	140
7.3.1	5CB mixture; mixture 6	142
7.3.2	8CB mixture; mixture 7	145
7.3.3	TM 1001 mixture; mixture 16	147
7.3.4	Discussion	150
7.4	Director Field Behaviour in Filament Mixtures	150
7.4.1	Initial observations in the photo-chromic mixture	150
7.4.2	Observations in the SmA mixture	151
7.4.3	Investigations using a waveplate	152
7.4.4	Proposed structure within the filaments	154
7.4.5	Investigations under illumination of 405 nm light	156
7.5	Birefringence Behaviour in Filament Mixtures	158
7.5.1	Temperature dependent studies	158
7.5.2	Time dependent studies	160
7.6	Summary	164
8	Conclusion and Future Work	167
8.1	Conclusion	167
8.2	Future Work	172
A	Error Analysis	174
	References	177

List of Figures

1.1	Simple representation of the three known types of thermotropic liquid crystals; calamitic (left), bent-core (middle), and discotic (right).	2
1.2	Representation of director orientation in a nematic phase.	3
1.3	Representation of the director orientation (\mathbf{n}) in a smectic A phase (left) and a smectic C phase (right). The layer normal is denoted as \mathbf{L} and θ_C is the angle of the director from the layer normal in the smectic C phase.	3
1.4	Simple representation of the three elastic distortions; splay (left), twist (middle), and bend (right).	5
2.1	Representation of Fréedericksz transition in a liquid crystal device. The left hand image is when the electric field is off and the right hand image is when the electric field is on and above the threshold field. The axes show the coordinate system that is used for the derivations in this section.	10
2.2	Example of the interlocking finger pattern used for the electrodes (shown in orange) in an IPS device, with the nematic director direction shown by the arrow. Figure not to scale.	15
2.3	Phases of bent-core liquid crystals where the left-hand diagram is (a) a uniaxial nematic with director $\hat{\mathbf{n}}$ and the right-hand diagram is (b) a nematic with uniform $\hat{\mathbf{n}}$ and polarity \mathbf{P}_\perp	17
2.4	Phase of bent-core liquid crystals with polar order \mathbf{P}_\perp and bend in the nematic director $\hat{\mathbf{n}}$	17
2.5	Phase of bent-core liquid crystals with polar order \mathbf{P}_\parallel and splay in the nematic director $\hat{\mathbf{n}}$	18

LIST OF FIGURES

2.6	Representation of chiral dimers of bent-core liquid crystals taken from a paper by Longa et al.[45]	19
2.7	Representation of the twist bend nematic phase in bent-core liquid crystals, taken from a paper by Dozov.[49]	24
2.8	Molecular structure of CB7CB which forms the twist-bend nematic phase.	25
3.1	Molecular structures and phase transition temperatures for the pure bent-core liquid crystals described in this thesis. Temperatures are recorded in °C where Iso = isotropic phase, N = nematic phase, DC = dark conglomerate phase, Cr = crystalline phase, and SmX = smectic phase of unknown type.	30
3.2	Molecular structures and phase transition temperatures for the pure calamitic liquid crystals described in this thesis. Temperatures are recorded in °C where Iso = isotropic phase, N = nematic phase, Cr = crystalline phase, and SmA = smectic A phase.	31
3.3	Representation of how the molecular shape of BAAB2 changes as it undergoes trans-cis (top) and cis-trans isomerisation (bottom) respectively.	32
3.4	Examples of how the liquid crystal nematic director lies in both a planar (left) and homeotropic (right) device. \hat{n} represents the nematic director direction in each device. Figure not to scale. . .	35
3.5	Molecular structure of trichloro(octadecyl)silane (C18).	35
3.6	Example of the interlocking finger pattern used for the ITO layer (shown in orange) in an IPS device. The rubbing direction can be either parallel (left) or perpendicular (right) to the electrodes. Figure not to scale.	36
3.7	Example of a schlieren texture observed in the nematic phase of 5CB.	37
3.8	DSC trace obtained for DT12 at a rate of 5 °C/min.	38
3.9	Capacitance as a function of frequency for 5CB at 1 V_{RMS} at room temperature.	39

LIST OF FIGURES

3.10 Dielectric permittivity ϵ as a function of V_{RMS} for mixture 6 at a reduced temperature $T-T_{NI} = -5$ K. The blue crosses represent the experimental data with the red line showing a fit to the data. ϵ was measured to an accuracy of 5%, which are not included in this plot to provide more clarity of the fit on the raw data.	41
3.11 Transmitted light intensity as a function of V_{RMS} for DT12 at $T-T_{NI} = -2.5$ K.	45
3.12 Transmitted light intensity as a function of V_{RMS} for mixture 1 at $T-T_{NI} = -42.5$ K.	46
3.13 $\sin(\delta/2)$ as a function of V_{RMS} for mixture 1 at $T-T_{NI} = -42.5$ K.	46
3.14 $\sin(\delta/2)$ as a function of V_{RMS} for mixture 1 at $T-T_{NI} = -42.5$ K, including the regions of manipulation to calculate $\delta/2$	47
3.15 δ as a function of V_{RMS} for mixture 1 at $T-T_{NI} = -42.5$ K.	48
3.16 Example plots of intensity as a function of d_x for VBG93. For both bent-core liquid crystals and the mixtures, the red plots represent the isotropic phase, the blue plots represent the nematic phase, the green plots represent the underlying phase, and the black plots represent the crystal phase. In the case of DT12 and mixtures 3-5 the underlying phase is a SmX phase, and for VBG93 it is a DC phase. For mixtures 1 and 2 the underlying phase is an optically isotropic phase.	51
3.17 X-ray scattering intensity as a function of periodicity d_x for VBG93 5 °C into the DC phase. The blue data points represent the experimental data and the red line represents the Gaussian fit applied to the data.	52
3.18 Schematic of the components of an AFM with the laser (a), photodiode (b), cantilever (c), piezoelectric (d), tip (e), sample (f), and stage (g). Diagram not scale.	55
4.1 Molecular structure of DT12 with its phase transitions temperatures on cooling. Temperatures were recorded in °C where Iso = isotropic phase, N = nematic phase, SmX = smectic phase of unknown type and Cr = crystal phase.	60

LIST OF FIGURES

4.2	Molecular structure of DT12 without hydrogen atoms. The labels show which bonds (χ_i) are allowed to rotate in the Monte Carlo conformation sampling. The molecular frame (x, y, z) has the z axis passing through the carbon atoms of the oxadiazole ring and y perpendicular to the plane of the ring. Figure taken from the paper by Srigengan et al.[57]	63
4.3	Torsional potential, V_{tors} , as a function of the C–C–C=O dihedral angle, calculated for phenyl benzoate with different substituents in the ortho position of the benzoate ring: H (green solid line with stars), CH ₃ (red dotted line with circles), OCH ₃ (blue dashed line with diamonds). The chemical structures on the bottom show the conformation of the benzoate group in correspondence of the minima of the torsional potential. The yellow sphere is in the position of the lateral substituent. Figure taken from the paper by Srigengan et al.[57]	64
4.4	Dielectric anisotropy as a function of T–T _{NI} for DT12.	65
4.5	The splay, K_{11} (crosses), twist, K_{22} (circles) and bend, K_{33} (squares) elastic constants as a function of T–T _{NI} for DT12. The experimental data are represented by the blue data points and the calculated data by the red data points. Note the break in the y-axis and the change in scale to make visible the very low twist and bend elastic constants.	66
4.6	Elastic constants calculated for the nematic phase of DT12 as a function of the orientational order parameter S_{zz} , which quantifies the alignment of the z molecular axis (see figure 4.2) to the nematic director. Here K_{11} is represented by the blue line, K_{22} by the red, and K_{33} by the green. Figure taken from the paper by Srigengan et al.[57]	69

LIST OF FIGURES

4.7	Elastic constants calculated for the nematic phases of VBG93 (left, taken from a paper by Kaur et al.[63]) and DT12 (right, taken from the paper by Srigengan et al.[57]) as a function of the order parameter S_{zz} . For the VBG93 plot K_{11} is represented by the solid line, K_{22} by the dash-dotted line, and K_{33} by the dashed line. For the DT12 plot K_{11} is represented by the blue line, K_{22} by the red line, and K_{33} by the green line.	70
4.8	Theoretical profiles of the splay K_{11}^{eff} , twist K_{22}^{eff} and bend K_{33}^{eff} elastic constants in DT12, calculated as functions of the reduced temperature. The results shown in this figure take into account the effect of chiral fluctuations and polar interactions of the bent-core molecules. Figure taken from the paper by Srigengan et al.[57] . . .	74
5.1	Molecular structures and phase transition temperatures for the liquid crystals used in this chapter. Temperatures are recorded in °C.	78
5.2	The phase diagram of mixtures of DT12 and VBG93. The blue points mark the isotropic to nematic transition, the red points represent the transition from the nematic to an unknown smectic phase, the black points represent the transition from a nematic to an optically isotropic phase, and the orange data points represent the transition from the mesophase to crystal phase. In the case of VBG93, the optically isotropic phase is the DC phase.	81
5.3	Dielectric anisotropy, $\Delta\epsilon$ as a function of $T-T_{NI}$ for DT12, VBG93, and mixtures 1-5. As mentioned earlier in the chapter, the mixtures were constrained to temperatures below 180 °C which explains why some datasets begin at lower temperatures.	83
5.4	The splay, K_{11} (a), twist, K_{22} (b) and bend, K_{33} (c) elastic constants as a function of $T-T_{NI}$ for DT12, VBG93, and mixtures 1-5. . . .	84
5.5	Molecular structures and phase transitions temperatures for the liquid crystals used in this chapter. Temperatures are recorded in °C.	87

5.6	Histogram showing the phase transitions with the transition temperatures on cooling for the mixtures discussed in this chapter. Everything above the bars indicates the isotropic phase, with the dark blue bars representing the nematic phase, the light blue bar representing the nematic phase with filaments, the orange bars representing the smectic A phase and the light orange bar representing the smectic A phase with filaments.	88
5.7	Dielectric anisotropy, $\Delta\varepsilon$ as a function of $T-T_{NI}$ for 5CB, mixture 6 and 10.	91
5.8	The splay, K_{11} (a), twist, K_{22} (b) and bend, K_{33} (c) elastic constants as a function of $T-T_{NI}$ for DT12, VBG93, 5CB, and mixtures 6 and 10.	92
5.9	Dielectric anisotropy, $\Delta\varepsilon$ as a function of $T-T_{NI}$ for 8CB, and mixtures 7 and 11.	93
5.10	The splay, K_{11} (a), twist, K_{22} (b) and bend, K_{33} (c) elastic constants as a function of $T-T_{NI}$ for DT12, VBG93, 8CB, and mixtures 7 and 11.	95
5.11	The splay, K_{11} (a), twist, K_{22} (b) and bend, K_{33} (c) elastic constants as a function of $T-T_{NI}$ for DT12, VBG93, ZLI 1132, and mixtures 9 and 12.[109]	97
6.1	Molecular structures and phase transitions temperatures for the liquid crystals used in this chapter. Temperatures are recorded in °C.	110
6.2	The phase diagram of mixtures of DT12 and VBG93. The blue points mark the isotropic to nematic transition, the red points represent the transition from the nematic to an unknown smectic phase, the black points represent the transition from a nematic to an optically isotropic phase, and the orange data points represent the transition from the mesophase to crystal phase. In the case of VBG93, the optically isotropic phase is the DC phase.	111

LIST OF FIGURES

6.3	Example plots of intensity as a function of d_x for VBG93. For both bent-core liquid crystals and the mixtures, the red plots represent the isotropic phase, the blue plots represent the nematic phase, the green plots represent the underlying phase, and the black plots represent the crystal phase. In the case of DT12 and mixtures 3-5 the underlying phase is a SmX phase, and for VBG93 it is a DC phase. For mixtures 1 and 2 the underlying phase is an optically isotropic phase.	113
6.4	X-ray scattering intensity as a function of spacing d_x for VBG93 5 °C into the DC phase. The blue data points represent the experimental data and the red line represents the Gaussian fit applied to the data.	114
6.5	Spacing (a) and FWHM (b) as a function of $T-T_{N-OI}$ in the optically isotropic phases for VBG93, and mixtures 1 and 2. . . .	116
6.6	The raw X-ray data for the DC phases observed in VBG93 (a), mixture 1 (b) and 2 (c) respectively, just below the transition into the DC phases. The DC phase can be characterised by the bright yellow diffuse ring in the middle of the images.	118
6.7	Spacing (a) and FWHM (b) as a function of $T-T_{N-SmX}$ in the smectic phases for DT12, and mixtures 3-5.	120
6.8	The raw X-ray data for the smectic phases observed in DT12 (a), mixture 5 (b), 4 (c) and 3 (d) respectively, just below the transition into the smectic phases.	121
6.9	The tilt angle measured as a function of $T-T_{N-SmX}$ in the smectic phases for DT12, and mixtures 3-5	123
6.10	POM images taken for the underlying phases exhibited by (a) DT12, (b) mixture 5, (c) mixture 4, and (d) mixture 3 respectively. The width of the images are 0.6 mm.	127
6.11	The splay, K_{11} (a), twist, K_{22} (b), and bend, K_{33} (c) elastic constants as a function of $T-T_{NI}$ for VBG93 and mixtures 1 and 2.	128
6.12	The splay, K_{11} (a), twist, K_{22} (b), and bend, K_{33} (c) elastic constants as a function of $T-T_{NI}$ for DT12 and mixtures 3-5.	130

LIST OF FIGURES

7.1	Molecular structures and phase transitions temperatures for the liquid crystals used in this chapter. Temperatures are recorded in °C.	137
7.2	Molecular structures and phase transitions temperatures for the liquid crystals used in this chapter. Temperatures are recorded in °C.	137
7.3	Histogram showing the phase transitions with the transition temperatures on cooling for the mixtures discussed in this chapter. Everything above the bars indicates the isotropic phase, with the dark blue bars representing the nematic phase, the light blue bars representing the nematic phase with filaments, the light orange bars representing the smectic A phase with filaments, the dark green bar representing the chiral nematic phase, the light green bar representing the chiral nematic phase with filaments, the gold bar representing the blue phase 1 phase, and the light gold bar representing the blue phase 2 phase.	139
7.4	SEM images of mixture 6 (10% VBG93 in 5CB) taken at 10kx (a), 50kx (b), 100kx (c), and 150kx (d) magnifications.	142
7.5	AFM images of mixture 6 (10% VBG93 in 5CB). The left hand images show the 2D images and the right hand images show the corresponding 3D images taken. The magnification increases from top to bottom.	144
7.6	SEM images of mixture 7 (10% VBG93 in 8CB) taken at 10kx (a), 50kx (b), 100kx (c), and 150kx (d) magnifications.	145
7.7	AFM images of mixture 7 (10% VBG93 in 8CB). The left hand images show the 2D images and the right hand images show the corresponding 3D images taken. The magnification increases from top to bottom.	146
7.8	SEM images of mixture 16 (8% VBG93 in TM 1001) taken at 10kx (a), 50kx (b), 100kx (c), and 150kx (d) magnifications.	148
7.9	AFM images of mixture 16 (8% VBG93 in TM 1001). The left hand images show the 2D images and the right hand images show the corresponding 3D images taken. The magnification increases from top to bottom.	149

LIST OF FIGURES

7.10 Growth of the filaments as the system is cooled through the nematic phase. The orange arrow shows the direction of the nematic director, with the red arrows showing the orientations of the polariser and analyser.	151
7.11 Mixture 7 heated to the isotropic phase with filaments. Filaments were grown in the SmA phase. The red arrows represent the polariser orientations and the orange arrow represents the director orientation.	152
7.12 Sample in the isotropic phase with filaments, (a) without the waveplate, and (b) with the waveplate.	152
7.13 Mixture 15 in an un-rubbed planar aligned device with a waveplate in the optical set-up, (a) when the sample was cooled into the nematic phase at 42 °C from the isotropic phase, and (b) when the sample was heated to isotropic phase with filaments still present at 50 °C. The white arrows in (b) denote the direction of the nematic director in the two different regions, one blue in colour with the other orange in colour.	153
7.14 Proposed structure of the filaments in a bulk calamitic host, (a) in the nematic phase with filaments, and (b) in the isotropic phase with filaments. The right hand images show how the filaments are usually viewed using POM, with the left hand images showing the formation of the bent-core and calamitic liquid crystal molecules within the filaments.	155
7.15 Growth of the filaments though mixture 15 whilst under the illumination of a 405 nm blue laser, whilst the sample was held at 30 °C.	157
7.16 The birefringence Δn as a function of $T-T_{NI}$ for VBG93,[63] 5CB, and mixtures 6, 8, 13 and 14. It should be noted that the lower temperature results for VBG93 have not been included for better clarity of the data taken for the mixtures.	159
7.17 The birefringence Δn as a function of $T-T_{NI}$ for mixture 6 (black squares). The red circle highlights the "plateau" in the trend. . .	160

LIST OF FIGURES

7.18	POM images of mixture 6 held at $T-T_{NI} = -15$ K whilst filaments grow through the sample. The times at which the images were taken were (a) 0 mins, (b) 1 min, (c) 2 mins, (d) 3 mins, (e) 4 mins, (f) 5 mins, (g) 6 mins, and (h) 60 mins.	161
7.19	The birefringence Δn as a function of time for mixtures 6, 13 and 14.	162
7.20	The birefringence Δn as a function of time for mixture 6 (black squares) fitted with the $e^{-t^{1/2}}$ function (red line).	164
A.1	δ as a function of V_{RMS} for DT12 at $T-T_{NI} = -2.5$ K.	174
A.2	δ as a function of V_{RMS} for DT12 at $T-T_{NI} = -2.5$ K, denoting where V_{th} is obtained.	175
A.3	δ as a function of V_{RMS} for DT12 at $T-T_{NI} = -2.5$ K, denoting where V_{th-3} and V_{th-4} are obtained.	176

List of Tables

3.1	Compositions of mixtures used in this thesis with the corresponding phase transitions and transition temperatures, where Iso = isotropic phase, I+F = isotropic phase with filaments, N = nematic phase, N+F = nematic phase with filaments, N* = chiral nematic phase, N*+F = chiral nematic phase with filaments, OI = optically isotropic phase, BPI = blue phase 1, BPI+F = blue phase 1 with filaments, BPII = blue phase 2, BPII+F = blue phase 2 with filaments, SmX = smectic phase of unknown type, SmA = smectic A phase, SmA+F = smectic A phase with filaments and Cr = crystalline phase.	33
3.2	Transition temperatures on cooling for DT12.	38
5.1	Compositions of the bent-core mixtures used in this chapter with the corresponding phase transitions and transition temperatures determined on cooling. The elastic constants of the pure materials and the mixtures are all given in the results section.	80
5.2	Compositions of mixtures used in this chapter with the corresponding phase transitions and transition temperatures determined on cooling. The elastic constants of the pure materials and the mixtures are all given in the results section.	87
6.1	Compositions of the bent-core mixtures used in this chapter with the corresponding phase transitions and transition temperatures determined on cooling, where OI = optically isotropic phase. . . .	111

7.1 Compositions of mixtures used in this chapter with the corresponding phase transitions and transition temperatures determined on cooling, where N^* = chiral nematic phase, N^*+F = chiral nematic phase with filaments, BPI = blue phase 1, BPI+F = blue phase 1 with filaments, BPII = blue phase 2, and BPII+F = blue phase 2 with filaments. 138

Chapter 1

Introduction

The aim of this thesis is to provide an understanding of novel phase behaviour exhibited by bent-core liquid crystals; more specifically how the elastic behaviour in the nematic phase can give an insight into the formation of underlying phases, as well as show the potential of bent-core liquid crystals in applications.

This chapter will go into the detail on the physical properties of liquid crystals before delving into bent-core liquid crystals and the phase behaviour that have been investigated so far in literature. The chapter will conclude with an explanation of the thesis plan, including a brief overview of the content of each of the following chapters, as well discussing the motivation for the research presented in this thesis.

1.1 Introduction to Liquid Crystals

Liquid crystals are materials which are anisotropic that exhibit phases with a partially ordered structure whilst maintaining a level of fluidity. The first liquid crystal compounds were discovered by Friedrich Reinitzer in 1888 when he observed one particular compound (a cholesteric derivative) exhibit two melting points.[1] It was later found by Otto Lehmann that certain phases from these compounds affected polarised light and thus the term "liquid crystals" was given these phases. Since then a considerable number of liquid crystalline phases have been discovered with various different structures.[2]

The most common liquid crystalline materials can be categorised into two groups; thermotropics and lyotropics.[3, 4] Thermotropic liquid crystals are meso-

1.1 Introduction to Liquid Crystals

gens that exhibit phases that be controlled via temperature. Lyotropic liquid crystals on the other hand exhibit phases that can be controlled by the concentration of the mesogen in a solvent. This thesis will only consider thermotropic liquid crystals. Thermotropics can be further categorised based on the molecular shape; calamitics, bent-cores and discotics.[2] The general shape of these types of thermotropics are shown in figure 1.1. Calamitic liquid crystals will be used as the main example in the rest of this chapter to help explain the basics of liquid crystals.

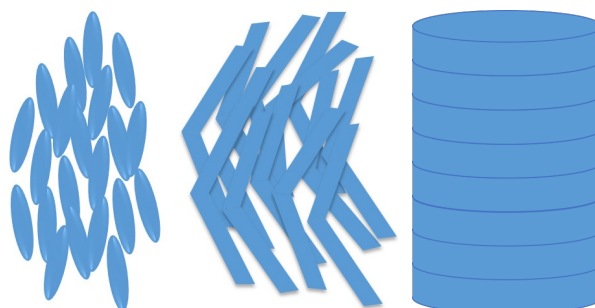


Figure 1.1: Simple representation of the three known types of thermotropic liquid crystals; calamitic (left), bent-core (middle), and discotic (right).

The most common and widely-used liquid crystal phase is the nematic phase, shown in figure 1.2. In this phase the liquid crystal molecules align with the molecular long axes oriented on average in a specific direction defined by a unit vector known as the director[5] and denoted as \mathbf{n} . The nematic phase exhibits long range orientational order with no positional order. It is generally the phase exhibited at temperatures just below that of the isotropic phase (where the material exhibits no ordering of any sort). As the material is cooled, other liquid crystal phases can be formed. One collection of underlying phases are known as smectic phases, with two examples of smectic phases shown in figure 1.3. Here the liquid crystal molecules exhibit positional ordering by forming layers. The most common smectic phases are the smectic A and C phases, where the director is parallel to the layer normal or at an angle respectively.

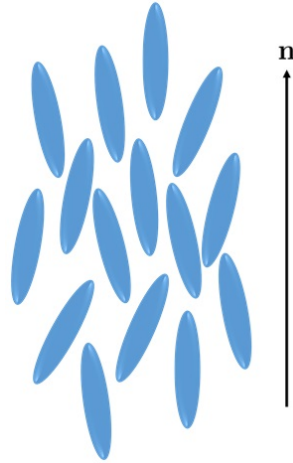


Figure 1.2: Representation of director orientation in a nematic phase.

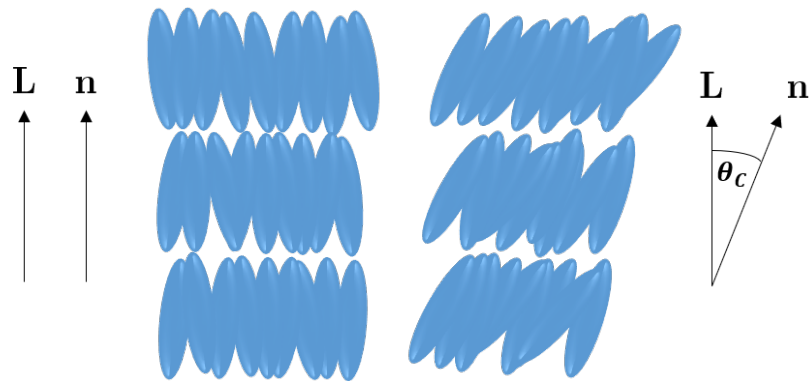


Figure 1.3: Representation of the director orientation (\mathbf{n}) in a smectic A phase (left) and a smectic C phase (right). The layer normal is denoted as \mathbf{L} and θ_C is the angle of the director from the layer normal in the smectic C phase.

As liquid crystal phases are ordered, it necessary to define an order parameter S . In the bulk nematic cylindrical symmetry is assumed with the liquid crystal being uniaxial, so S is defined by the following equation, derived from the second term of a set of Legendre polynomials;[\[4\]](#)

$$S = \left\langle \frac{3}{2} \cos^2 \theta_d - \frac{1}{2} \right\rangle, \quad (1.1)$$

where θ_d is the angle between the long axis of the liquid crystal molecule and the director. The angle brackets denote that a statistical average is taken over the ensemble. S is 0 for a fully isotropic system and 1 for a perfectly ordered system.

1.2 Elasticity in Liquid Crystals

Deformations to the nematic director cause an elastic restorative force to be induced within the liquid crystal to bring the director back to its equilibrium orientation. The elastic constant of a liquid crystal can be modelled mathematically as a tensor (see section [2.2](#) for more details). The three elastic constants that are relevant to the bulk nematic phase are the splay, twist, and bend elastic constants denoted as K_{11} , K_{22} , and K_{33} [\[6, 7\]](#). Figure [1.4](#) shows a simple representation of how the director is distorted in each case respectively. There is a fourth elastic constant known as the saddle splay constant, denoted as K_{24} . Whilst initially thought to be important for the formation of defects[\[8–10\]](#) and distortions[\[11, 12\]](#) within the director field in certain geometries, more recently K_{24} has been suggested to be important for the formation of the dark conglomerate (DC) phase, which will be looked at in more detail later on in section [1.3](#). The elastic constants K_{11} , K_{22} and K_{33} can be measured by investigating the Fréedericksz transition in devices, which will be discussed in more detail in section [2.2](#) in chapter [2](#).

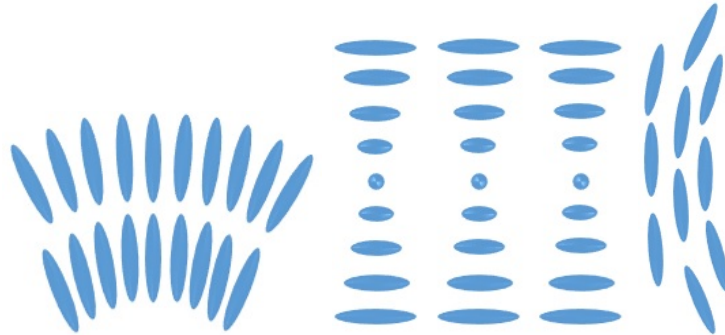


Figure 1.4: Simple representation of the three elastic distortions; splay (left), twist (middle), and bend (right).

1.3 The Dark Conglomerate Phase

This chapter has so far introduced concepts that apply to all types of thermotropic liquid crystals, but has used calamitic liquid crystals as the main example for the explanations. There are a number of interesting phases exhibited in bent-core liquid crystals, including the B phases, the twist-bend nematic (N_{TB}) phase, and the helical nano-filament (HNF) phase. More information about these phases can be found in review articles by Jáklí et al.,[13] and by Takezoe and Takanishi.[14] This section will instead focus on the dark conglomerate (DC) phase which is exhibited by a bent-core liquid crystal investigated in this thesis, denoted as VBG93.

The DC phase is an optically isotropic phase that is typically exhibited directly below the isotropic phase,[15–20], however in VBG93 the DC phase is exhibited below the nematic phase. The phase has an optically isotropic structure under crossed polarisers as the correlation length of the structure (polar smectic layers) is less than the wavelength of visible light (~ 100 nm).[21] Some optical activity can be observed such as chiral domains of opposite handedness when the phase is viewed under slightly uncrossed polarisers.

The behaviour of the dark conglomerate phase has been studied in detail by several groups.[15, 18, 22–24] It was found that under the application of an electric field the optical isotropy turns into optical anisotropy, i.e. birefringent. The birefringent texture remains even after the field is removed, with the optically

1.3 The Dark Conglomerate Phase

isotropic texture only returning only once the sample is heated to the isotropic phase before being cooling back into the DC phase.

The structure of the dark conglomerate phase has been studied by several groups using X-ray diffraction and freeze-fracture transmission electron microscopy (FFTEM).[21, 24-28] These studies revealed the presence of 20-100 nm size domains with saddle-splay type layer structures, similar to the sponge phase of lyotropic systems.[29] The saddle-splay structure is thought to arise due to the mismatch of the in-plane area of the tails and cores of the bent-core molecules, that can be relieved by a tilt of the molecules.[21] This in-layer frustration of the tilting produces a strong tendency for the negative Gaussian curvature of the layers, which occurs via the coupling of the polar order and the tilt. The saddle-splay curvature of the layers is believed to contribute to the large optical activity of the phase, which cannot be explained by the layer chirality of the tilted polar phase alone.[17, 21]

In the context of the bent-core materials investigated in this thesis, one material (denoted as VBG93) exhibits a DC phase. Unlike the DC phases described earlier in this section, the DC phase in VBG93 is exhibited below the nematic phase, with the transition into the DC phase occurring at ~ 170 °C. The DC phase does not exhibit chiral domains of opposite handedness in the ground state. Instead the chiral domains appear under application of an electric field, above a certain threshold field (~ 12 V/ μ m) and only under slightly uncrossed polarisers. As the electric field increases beyond this threshold the chiral domains grow to from larger domains until at another threshold (~ 15 V/ μ m) the chiral domains disappear, leaving a uniform achiral texture.[30, 31] The emergence of the chiral domains and their subsequent disappearance coincides with an interesting decrease in the average refractive index of the DC phase, varying from ~ 1.66 - 1.61 .[31, 32] The unusual behaviour exhibited by the DC phase in VBG93 provided a basis to investigate the phase behaviour of bent-core liquid crystals. One aim of this thesis is to understand the driving factors into the formation of bent-core phases, including this DC phase, by investigating the elastic behaviour in the nematic phases of bent-core materials. This work will be discussed in chapter 5. Another aim is to find out if this DC phase can be formed at lower temperatures using

binary liquid crystal mixtures of VBG93 with another bent-core liquid crystal denoted as DT12 in this thesis. This work will be discussed in chapter 6.

1.4 Roadmap of Thesis

This section will provide brief information on what each of the following chapters on this thesis will entail.

Chapter 2 will detail the elastic theory of liquid crystals, more specifically the origins of the equations used to measure the elastic constants. The chapter will also discuss the concept of spontaneous chirality and polarity and how they arise in bent-core liquid crystals, using the twist-bend nematic phase as one of the key examples of chiral symmetry breaking occurring in liquid crystals.

Chapter 3 will provide details on the materials and devices used to obtain the results discussed in this thesis, along with the methods in which the experiments were carried out.

Chapter 4 will go into detail on the elastic properties of an oxadiazole-based bent-core liquid crystal we denote as DT12. More specifically the chapter will show the anomalously low twist and bend elastic constants measured in this liquid crystal along with the computational and theoretical calculations that back up the experimental data as well as changes to the molecular mean theory on spontaneous chirality and polarity that involve corrections to the equations that calculate the twist and bend constants respectively.

Chapter 7 will provide details on the elastic behaviour in mixtures of bent-core liquid crystals; showing that the low twist and bend constants measured in DT12 persist in mixtures of DT12 and VBG93, as well how the elastic constants can be affected in calamitic systems when they are doped with bent-core liquid crystals. This chapter will introduce the concept of filaments seen in the bent-core/calamitic mixtures, but the phase behaviour of the filament structures will be discussed further in chapter 7.

Chapter 6 will discuss the optically isotropic and smectic phases observed in the mixtures of DT12 and VBG93 (introduced in chapter 5). This chapter discusses results of X-ray scattering carried out on the mixtures to understand the phase behaviour and uses the elastic behaviour discussed in chapter 5 to learn

more about the driving factors in the formation of the underlying phases in the bent-core mixtures.

Chapter 7 will discuss the filament phases introduced in chapter 5, looking into the phase behaviour. More specifically this chapter will present data about the birefringence and director field measurements that were carried out to understand the mechanism of the filament growth, as well images taken using atomic force microscopy (AFM) and scanning electron microscopy (SEM) that were carried out to gain information of the microscale structure of the filaments.

Chapter 8 will conclude the results presented in this thesis whilst also providing a look at some of the future work and potential that can come from this work on bent-core liquid crystals.

1.5 Motivation

The motivation for the research presented in this thesis comes from earlier work on an oxadiazole-based bent-core liquid crystal that exhibits a DC phase. It was found that the DC phase in this particular material could exhibit a change in the average refractive index upon application of an electric field.^[32] The change in refractive index occurs whilst the phase remains optically isotropic, a phenomenon which has rarely been seen previously in literature. The electro-optical properties of the DC phase provide potential for non-display applications such as liquid crystal lenses, waveguides and diffraction gratings. However the draw-back to the material is that the phenomenon occurs at ~ 170 °C, which is much higher than what would be preferred for any real-life applications. One method in reducing the transition temperature into the DC phase is by mixing this material with other liquid crystals. This thesis showcases the results and work carried out with this aim in mind.

Chapter 2

Elastic Theory of Liquid Crystals

2.1 Introduction

This chapter will go into detail on the theory of liquid crystals, initially showing the derivation of the equations which allow one to measure the splay, twist and bend elastic constants. The chapter will then introduce the concept of polar and chiral order in nematic liquid crystals before detailing how spontaneous polarity and chirality arises in bent-core liquid crystals. Lastly, using the twist-bend nematic phase as an example, the chapter will show how spontaneous polarity and chirality can explain the behaviour of elastic constants in bent-core liquid crystals and how they are a driving factor in the formation of more exotic phases.

2.2 Elastic Constant Theory

The derivations detailed in this section are based on the assumption that we have a planar rubbed (nematic director parallel to substrates) device (of thickness d) filled with a positively dielectric liquid crystal, i.e. when a sufficiently strong electric field (above the threshold) is applied across the device, the nematic director will tend to a state that is more parallel to the electric field (see figure [2.1](#)).

2.2 Elastic Constant Theory

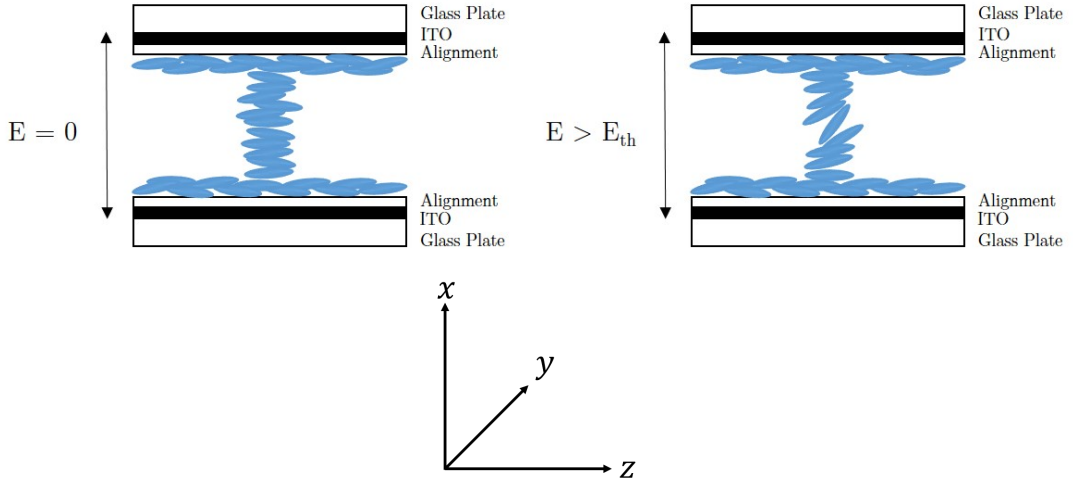


Figure 2.1: Representation of Fréedericksz transition in a liquid crystal device. The left hand image is when the electric field is off and the right hand image is when the electric field is on and above the threshold field. The axes show the coordinate system that is used for the derivations in this section.

As mentioned briefly in section 1.2, electric fields can interact with nematic liquid crystals to produce deformations in the nematic director. The electric field vector \mathbf{E} normally can not be considered parallel to the electric displacement vector \mathbf{D} . This results in a non-uniform electric field in the sample.[33] In a volume V , the electric distortional energy due to the electric field $G_{electric}$ is given by the relationship;

$$G_{electric} = \frac{1}{2} \int_V \mathbf{D} \cdot \mathbf{E} d\tau. \quad (2.1)$$

When considering a deformation in the sample, the condition $\nabla \times \mathbf{E} = 0$ requires that $E_y = E_z = 0$, because $\phi(x)$ (where ϕ is the angle of the nematic director from the electric field direction) is a deformation depending only on the x -direction. The additional condition $\nabla \cdot \mathbf{D} = 0$ gives the following relationship between the electric field and the deformation;

$$E_z(x) = \frac{V}{\left(1 + \left(\frac{\Delta\varepsilon}{\varepsilon_\perp}\right) \sin^2\phi\right) \int_{\langle d \rangle} \left(1 + \left(\frac{\Delta\varepsilon}{\varepsilon_\perp}\right) \sin^2\phi\right)^{-1} dx}, \quad (2.2)$$

where the dielectric anisotropy $\Delta\varepsilon = \varepsilon_{\parallel} - \varepsilon_{\perp}$, ε_{\parallel} and ε_{\perp} are the dielectric permittivities measured parallel and perpendicular to the director, V is the voltage applied to the device, and $\langle d \rangle$ is the statistical average over the thickness of the device. The electric field clearly depends on the location in the device. From equation 2.2 and using $\nabla \cdot \mathbf{D} = 0$, one can obtain;

$$D_x = \frac{V\varepsilon_0\varepsilon_\perp}{\int_{\langle d \rangle} \left(1 + \left(\frac{\Delta\varepsilon}{\varepsilon_\perp}\right) \sin^2\phi\right)^{-1} dx}. \quad (2.3)$$

D_x is uniform throughout the sample. Substituting equations 2.3 and 2.2 into equation 2.1 one obtains;

$$\begin{aligned} G_{electric} &= \frac{1}{2}V^2\varepsilon_0\varepsilon_\perp \frac{1}{\int_{\langle d \rangle} \left(1 + \left(\frac{\Delta\varepsilon}{\varepsilon_\perp}\right) \sin^2\phi\right)^{-1} dx} \\ &= \frac{1}{2} \frac{V^2\varepsilon_0^2\varepsilon_\perp^2}{\varepsilon_0\varepsilon_\perp} \frac{\int_{\langle d \rangle} \left(1 + \left(\frac{\Delta\varepsilon}{\varepsilon_\perp}\right) \sin^2\phi\right)^{-1} dx}{\left(\int_{\langle d \rangle} \left(1 + \left(\frac{\Delta\varepsilon}{\varepsilon_\perp}\right) \sin^2\phi\right)^{-1} dx\right)^2} \\ &= \frac{1}{2} \frac{D_x^2}{\varepsilon_0\varepsilon_\perp} \int_{\langle d \rangle} \left(1 + \left(\frac{\Delta\varepsilon}{\varepsilon_\perp}\right) \sin^2\phi\right)^{-1} dx \\ &= \frac{1}{2} \frac{D_x^2}{\varepsilon_0\varepsilon_\perp} \int_{\langle d \rangle} \frac{dx}{\left(1 + \left(\frac{\Delta\varepsilon}{\varepsilon_\perp}\right) \sin^2\phi\right)}. \end{aligned} \quad (2.4)$$

Equation 2.4 expresses the total electric energy per unit area in terms of the deformation angle $\phi(x)$. By considering that the total energy of the system is

2.2 Elastic Constant Theory

conserved, the resulting Euler-Lagrange differential equation becomes;[\[34\]](#)

$$\frac{d}{dx} \left(\left(\frac{d\phi}{dx} \right)^2 (K_{11} \cos^2 \phi + K_{33} \sin^2 \phi) - \frac{D_x^2}{\varepsilon_0 \varepsilon_{\perp}} \left(1 + \frac{\Delta \varepsilon}{\varepsilon_{\perp}} \sin^2 \phi \right)^{-1} \right) = 0, \quad (2.5)$$

where K_{11} and K_{33} are the splay and bend elastic constants respectively. Accounting for strong anchoring ($\phi(0) = \phi(d) = 0$) equation 2.5 can be solved to provide the director distribution throughout the nematic layer giving;[\[35\]](#)

$$\begin{aligned} \frac{x}{d} &= \frac{\int_0^{\phi} \left(\frac{(1+\eta \sin^2 \phi)(1+\frac{\Delta \varepsilon}{\varepsilon_{\perp}} \sin^2 \phi)}{\sin^2(\phi_M) - \sin^2 \phi} \right) d\phi}{\int_0^{\phi_M} \left(\frac{(1+\eta \sin^2 \phi)(1+\frac{\Delta \varepsilon}{\varepsilon_{\perp}} \sin^2 \phi)}{\sin^2(\phi_M) - \sin^2 \phi} \right)^{1/2} d\phi} \\ &= \frac{1}{\pi} \sin^{-1} \left(\frac{\phi}{\phi_M} \right) - \phi (\phi_M^2 - \phi^2)^{1/2} \frac{1+3\left(\eta+\left(\frac{\Delta \varepsilon}{\varepsilon_{\perp}}\right)\right)+\dots}{12\pi\left(1+\frac{1}{4}\left(\eta+\left(\frac{\Delta \varepsilon}{\varepsilon_{\perp}}\right)+1\right)\phi_M^2+\dots\right)}, \end{aligned} \quad (2.6)$$

$$\begin{aligned} \frac{V}{V_0} &= \frac{2}{\pi} \left(1 + \frac{\Delta \varepsilon}{\varepsilon_{\perp}} \sin^2(\phi_M) \right)^{1/2} \int_0^{\phi_M} \left(\frac{1+\eta \sin^2 \phi}{(1+\frac{\Delta \varepsilon}{\varepsilon_{\perp}} \sin^2 \phi)(\sin^2(\phi_M) - \sin^2 \phi)} \right)^{1/2} d\phi \\ &= 1 + \frac{1}{4} \left(\eta + \frac{\Delta \varepsilon}{\varepsilon_{\perp}} + 1 \right) \phi_M^2 + o(\phi_M^4), \end{aligned} \quad (2.7)$$

At the threshold voltage, $V = V_0$, and $\phi = \phi_M = 0$ which gives the following equation, using equations 2.6 and 2.7;

$$V_0^{K_{11}} = \pi \left(\frac{K_{11}}{\varepsilon_0 \Delta \varepsilon} \right)^{1/2}, \quad (2.8)$$

where V_0 is the threshold voltage, ϕ_M is the maximum deformation angle, and $\eta = (K_{33} - K_{11}/K_{11})$.

Equation 2.8 allows one to directly calculate the splay elastic constant from measuring the threshold voltage of a liquid crystal device. This is crucial to begin to fully understand the elastic behaviour of any liquid crystal material. Equation 2.7 shows that the deformation above the threshold voltage depends on

2.2 Elastic Constant Theory

the additional parameter $\Delta\varepsilon/\varepsilon_{\perp}$, and thus K_{33} can be calculated from measuring the change in dielectric permittivity of the liquid crystal device as the voltage applied is increased. By knowing the behaviour of K_{11} from equation 2.8 one can use equation 2.7 to determine the behaviour of K_{33} analytically. Next I provide how one can determine K_{33} by considering that the deformation of the liquid crystal under an applied electric field is related to the retardance of the liquid crystal device.

To determine the equation defining the bend constant K_{33} , one can remember that the deformation can be measured from a change in birefringence, which occurs due to the voltage applied to the sample. Nematic liquid crystals are uniaxial thus a normally incident polarised monochromatic light beam splits inside the liquid crystal into an ordinary beam and extraordinary beam. The electric field vector of the ordinary beam is always perpendicular to the optical axis, and therefore propagates with a velocity determined by the ordinary refractive index n_o . The extraordinary ray is polarised perpendicular to this direction and its average velocity is determined by an effective refractive index given by;

$$n_{eff} = \frac{1}{d} \int_0^d \frac{n_e n_o}{\sqrt{n_e^2 \sin^2 \phi + n_o^2 \cos^2 \phi}} dx, \quad (2.9)$$

where n_e is the extraordinary index of refraction. It is clear from equation 2.9 that n_{eff} depends on the deformation angle ϕ throughout the sample. The phase difference $\delta(V)$ existing between the two beams on the other side of the sample is given by;

$$\delta(V) = \frac{2\pi d}{\lambda} (n_{eff} - n_o). \quad (2.10)$$

The maximum value of $\delta(V)$ occurs at $V = 0$. Saupe[36] defined a phase difference δ where $\delta = \delta(0) - \delta(V)$, which can be related to the normalised voltage, V/V_0 (where V_0 is the threshold voltage) by;

$$\begin{aligned} \delta &= \frac{2\pi dn_e}{\lambda} \left(1 - \frac{2V}{\pi V_0} \int_0^{\phi_M} \frac{(1 + \eta \sin^2 \phi)^{1/2}}{(1 + \eta \sin^2 \phi)^{1/2} (\sin^2(\phi_M) - \sin^2 \phi)^{1/2}} d\phi \right) \\ &= \frac{2\pi dn_e \nu}{\lambda} \left(\frac{V-V_0}{V_0} \frac{1}{\eta+1} - \left(\frac{V-V_0}{V_0} \right)^2 \left(\frac{1}{\eta+1} \right)^2 \left(3 + \frac{9}{4}\nu - \frac{5}{4}(\eta+1) \right) + \dots \right), \end{aligned} \quad (2.11)$$

where $\nu = (n_e^2 - n_o^2)/n_o^2$. Considering small angles of ϕ which occur close to the threshold, the first term dominates. Equation 2.11 thus simplifies to;

$$\delta = \frac{2\pi dn_e \nu}{\lambda(\eta+1)} \left(\frac{V}{V_0} - 1 \right). \quad (2.12)$$

It is clear that measurements of δ at various fields can give K_{33} , provided that one already knows K_{11} from the threshold voltage from equation 2.8. Equations 2.8 and 2.12 can also apply to a homeotropic device in which case n_e and n_o , K_{11} and K_{33} , and ε_{\perp} and ε_{\parallel} have to be interchanged in the respective derivations.

To summarise, the splay elastic constant K_{11} , can be calculated directly from the threshold voltage of the liquid crystal device. The bend elastic constant K_{33} can be calculated by measuring the extend of the director deformation. Equation 2.7 allows the director deformation to be measured by considering the change in the dielectric permittivity in the liquid crystal device. The dielectric permittivity can be calculated from measurements of the capacitance; the methodology is described in full in section 3.6.2 of chapter 3. The other method to measure K_{33} is by using equation 2.12 which considers the change in retardance when a voltage is applied to the liquid crystal device. The methodology for measuring K_{33} optically is described in full in section 3.6.1 in chapter 3. Next I provide how one can determine the equation and conditions to measure the twist elastic constant K_{22} .

In order to derive the equation for K_{22} , one can consider the Fréedericksz transition in the in-plane switching (IPS) mode. For a nematic liquid crystal with a positive dielectric anisotropy, the nematic director should be parallel to the electrodes in order for switching to occur. A representation of the electrode design in an IPS device is shown in figure 2.2.

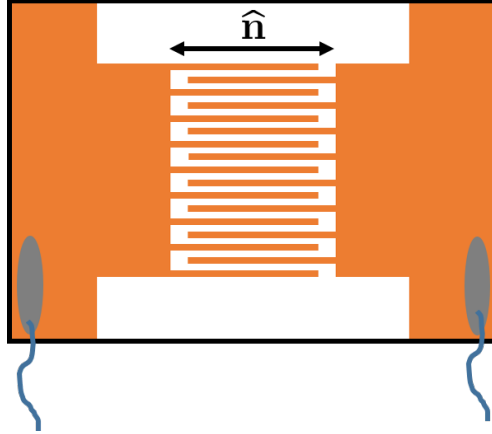


Figure 2.2: Example of the interlocking finger pattern used for the electrodes (shown in orange) in an IPS device, with the nematic director direction shown by the arrow. Figure not to scale.

By using the continuum elastic theory[37] and assuming strong anchoring on the surface of the substrates, the free energy F_{twist} of the twist deformation can be written as;

$$F_{twist} = \frac{1}{2} \int_0^d \left(K_{22} \left(\frac{d\phi}{dx} \right)^2 - \varepsilon_0 \Delta \varepsilon E^2 \sin^2 \phi \right) dx, \quad (2.13)$$

where K_{22} is the twist elastic constant and E is the magnitude of the electric field. Using the Euler-Lagrange equation, one can obtain;

$$K_{22} \frac{d^2 \phi}{dx^2} + \varepsilon_0 \Delta \varepsilon E^2 \sin \phi \cos \phi = 0. \quad (2.14)$$

With the assumption that the twist angle is small and the boundary condition $\phi(0) = \phi(d) = 0$, it has been shown that $\sqrt{\varepsilon_0 \Delta \varepsilon / K_{22}} E d = \pi$. [38] This equation corresponds to the point at which the twist angle ϕ just begins to change. Thus the threshold field, E_0 and subsequent threshold voltage, V_0 is;

$$E_0^{K_{22}} = \frac{\pi}{d} \sqrt{\frac{K_{22}}{\varepsilon_0 \Delta \varepsilon}},$$

$$V_0^{K_{22}} = E_0^{K_{22}} l = \frac{\pi l}{d} \sqrt{\frac{K_{22}}{\varepsilon_0 \Delta \varepsilon}},$$
(2.15)

where l denotes the electrode spacing.

To summarise, the equations to determine the splay, twist and bend elastic constants from the behaviour of the director in an electric field have been derived in this section. The elastic constants can be measured either optically or dielectrically; the methodology required to carry out both sets of experiments will be discussed in more detail in the next chapter. The next sections of this chapter will introduce the concept of polarity and chirality, and how spontaneous polarity and chirality arises in bent-core liquid crystals, and can be used to explain the elastic behaviour in these systems.

2.3 Types of Order

2.3.1 Polar order

In general in the nematic phase of calamitic liquid crystals, the polarity of the molecules is in the direction of the nematic director $\hat{\mathbf{n}}$. However, in the nematic phase of bent-core liquid crystals, the long axes of the molecules are aligned along the local director $\hat{\mathbf{n}}$, with the polarity of the molecules aligned randomly in the plane perpendicular to $\hat{\mathbf{n}}$ (figure 2.3a). A bent-core nematic phase with polar order would have a polarity defined by a vector \mathbf{P}_\perp , which is perpendicular to $\hat{\mathbf{n}}$ (figure 2.3b).

The concept of polar order in a nematic phase of bent-core molecules was first investigated by Meyer^[39] when he proposed that the polar order \mathbf{P}_\perp coupled with the bend in nematic director $\hat{\mathbf{n}}$. This coupling arises through a mechanism called the bend flexoelectric effect (figure 2.4). This bend creates an anisotropic environment in the plane perpendicular to $\hat{\mathbf{n}}$, in one particular direction, with \mathbf{P}_\perp aligning in that direction.

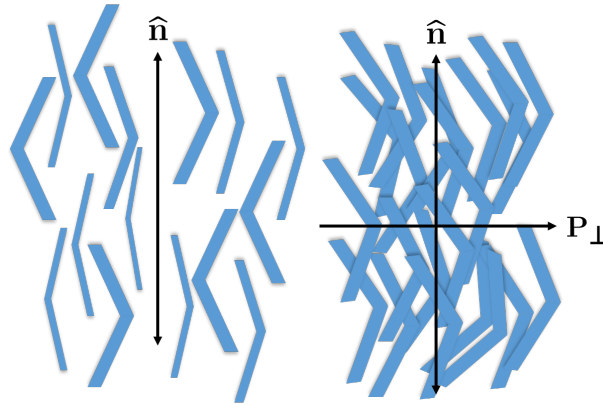


Figure 2.3: Phases of bent-core liquid crystals where the left-hand diagram is (a) a uniaxial nematic with director $\hat{\mathbf{n}}$ and the right-hand diagram is (b) a nematic with uniform $\hat{\mathbf{n}}$ and polarity \mathbf{P}_\perp .

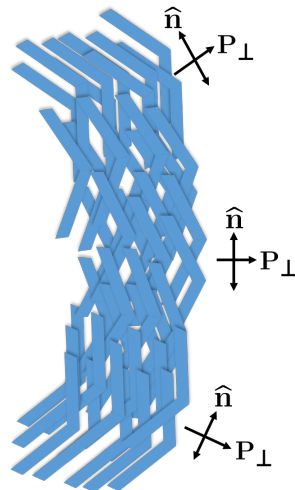


Figure 2.4: Phase of bent-core liquid crystals with polar order \mathbf{P}_\perp and bend in the nematic director $\hat{\mathbf{n}}$.

In addition to polar order perpendicular to $\hat{\mathbf{n}}$, Meyer also investigated polar order parallel to $\hat{\mathbf{n}}$.^[39] Polar order \mathbf{P}_{\parallel} is coupled with splay in $\hat{\mathbf{n}}$ through a mechanism called the splay flexoelectric effect. If the nematic liquid crystal has a splay in $\hat{\mathbf{n}}$, this splay creates an asymmetry between the two directions upward and downward along $\hat{\mathbf{n}}$, and \mathbf{P}_{\parallel} tends to align in the direction with lower free energy. As a consequence, the nematic director $\hat{\mathbf{n}}$ is not uniform but instead has a specific splay (figure 2.5).

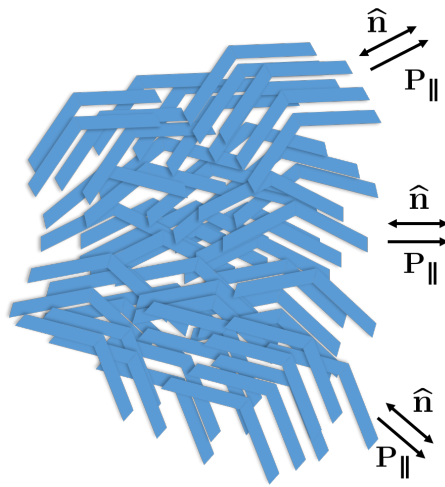


Figure 2.5: Phase of bent-core liquid crystals with polar order \mathbf{P}_{\parallel} and splay in the nematic director $\hat{\mathbf{n}}$.

\mathbf{P}_{\perp} and \mathbf{P}_{\parallel} are electrostatic polarisation vectors that characterise the statistical order of the molecular orientations perpendicular and parallel to $\hat{\mathbf{n}}$, respectively. The total electrostatic polarisation arising from the combination of splay and bend effects becomes;^[40, 41]

$$\mathbf{P} = e_1 \hat{\mathbf{n}}(\nabla \cdot \hat{\mathbf{n}}) - e_3(\hat{\mathbf{n}} \times \nabla \times \hat{\mathbf{n}}), \quad (2.16)$$

where e_1 and e_3 are the splay and bend flexoelectric coefficients, respectively. Over the years, numerous theoretical studies have calculated e_1 and e_3 in specific model systems, beginning with the early work of Helfrich,^[42] and Derzhanski and Petrov.^[43] Recently Kaur et al. measured the flexoelectric coefficients (both experimentally and computationally) for an oxadiazole based bent-core

nematic liquid crystal.[40] They found that the value exhibited were a factor of 2-3 times higher than those reported in most calamitic liquid crystals, but were comparable to those reported in other bent-core materials using similar experimental methodologies.

2.3.2 Chiral order

One particular property in bent-core liquid crystals is chiral symmetry breaking. Even if the individual bent-core molecules are not chiral (this is the case for the bent-core liquid crystals that are described in this thesis), the arrangement of the molecules can become spontaneously chiral. The chirality can be either left- or right-handed, or the system can form domains of left- and right-handed chirality. Mathematically, the spontaneous chirality can be understood through the theory of Lubensky and Radzihovsky[44] as a combination of quadrupolar and octupolar order parameters. Physically, it can be described as seen in figure 2.6 taken from a paper by Longa et al.[45] In this structure, pairs of bent-core molecules come together, with an oblique angle between the molecular planes to form a chiral dimer. In particular, dimers that are mirror images of each other cannot be superimposed on each other through any proper rotations or translations.

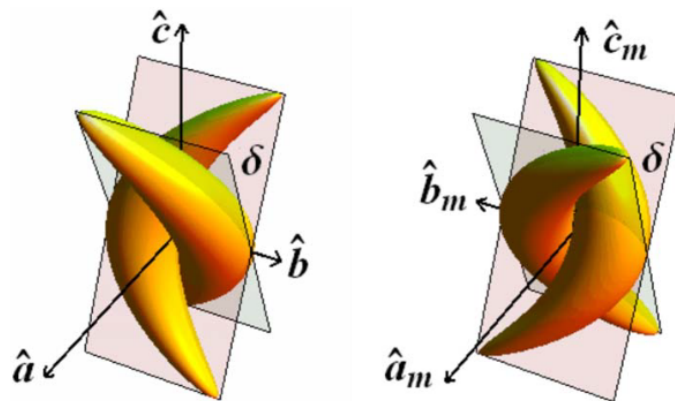


Figure 2.6: Representation of chiral dimers of bent-core liquid crystals taken from a paper by Longa et al.[45]

2.4 Spontaneous Polarity and Chirality

2.4.1 Polar and chiral order considerations

In this section, a detailed discussion is presented of how polarity and chirality can induce a transition from a uniform liquid crystal phase to a non-uniform phase. This is particularly important in the theory of bent-core liquid crystals, because it predicts the formation of the twist-bend nematic phase.

The initial ground work was carried out by Robert Meyer[39] when he proposed the possibility of spontaneous polar order leading to spontaneous splay or bend. First consider the Frank free energy density for elastic distortions in the director field $\hat{\mathbf{n}}(\mathbf{r})$. For a nonchiral, nonpolar nematic phase, this free energy density can be written as:[7]

$$F_{Frank} = \frac{1}{2}K_{11}(\nabla \cdot \hat{\mathbf{n}})^2 + \frac{1}{2}K_{22}(\hat{\mathbf{n}} \cdot \nabla \times \hat{\mathbf{n}})^2 + \frac{1}{2}K_{33}(\hat{\mathbf{n}} \times \nabla \times \hat{\mathbf{n}})^2. \quad (2.17)$$

The third term can be expressed in terms of the bend vector $\mathbf{b} = \hat{\mathbf{n}} \times \nabla \times \hat{\mathbf{n}}$, which shows the magnitude and direction of the bend in the plane perpendicular to $\hat{\mathbf{n}}$. Likewise, the second term can be written in terms of the twist pseudoscalar $t = \hat{\mathbf{n}} \cdot \nabla \times \hat{\mathbf{n}}$, which represents the magnitude and sign of the twist. One might be tempted to characterise the first term in equation 2.17 by the scalar $\nabla \cdot \hat{\mathbf{n}}$. However, this quantity is not uniquely defined, because the nematic director $\hat{\mathbf{n}}$ is equivalent to $-\hat{\mathbf{n}}$. Hence, the splay vector can be defined instead as $\mathbf{s} = \hat{\mathbf{n}}(\nabla \cdot \hat{\mathbf{n}})$, which is parallel to $\hat{\mathbf{n}}$ and thus is uniquely defined. The free energy for a nonchiral, nonpolar nematic phase can then be written as;

$$F_{Frank} = \frac{1}{2}K_{11}\mathbf{s}^2 + \frac{1}{2}K_{22}t^2 + \frac{1}{2}K_{33}\mathbf{b}^2. \quad (2.18)$$

Minimising F_{Frank} corresponds to a uniform nematic phase with no splay, twist nor bend. Next consider the liquid crystal to be composed of chiral molecules, which favours twist. In this case, the chirality of the molecules is characterised

2.4 Spontaneous Polarity and Chirality

by some pseudoscalar t_0 , which couples with the twist t . The free energy is now defined as;

$$F_{Frank} = \frac{1}{2}K_{11}\mathbf{s}^2 + \frac{1}{2}K_{22}(t - t_0)^2 + \frac{1}{2}K_{33}\mathbf{b}^2, \quad (2.19)$$

where the minimum corresponds to a cholesteric phase. It exhibits no splay nor bend, but a non-zero twist t_0 . If one considers a liquid crystal which favours splay or bend instead of twist, the free energy can be defined as;

$$F_{Frank} = \frac{1}{2}K_{11}(\mathbf{s} - \mathbf{s}_0)^2 + \frac{1}{2}K_{22}t^2 + \frac{1}{2}K_{33}(\mathbf{b} - \mathbf{b}_0)^2, \quad (2.20)$$

which is analogous to equation 2.19.

Because \mathbf{s} is a vector parallel to $\hat{\mathbf{n}}$, the only way for \mathbf{s} and \mathbf{s}_0 to couple is if \mathbf{s}_0 is also a vector parallel to $\hat{\mathbf{n}}$, i.e. \mathbf{s} and \mathbf{s}_0 are parallel to each other. Likewise, because \mathbf{b} is a vector perpendicular to $\hat{\mathbf{n}}$, the only way for \mathbf{b} and \mathbf{b}_0 to couple is if \mathbf{b}_0 is also a vector perpendicular to $\hat{\mathbf{n}}$, i.e. \mathbf{b} and \mathbf{b}_0 lie on the same plane. Hence, one can write them as the parallel and perpendicular components of the vector \mathbf{P} , with $\mathbf{s}_0 = (x_{\parallel}/K_{11})\mathbf{P}_{\parallel}$ and $\mathbf{b}_0 = (x_{\perp}/K_{33})\mathbf{P}_{\perp}$. With these coefficients, the Frank free energy becomes defined as;

$$F_{Frank} = \frac{1}{2}K_{11}\left(\mathbf{s} - \frac{x_{\parallel}}{K_{11}}\mathbf{P}_{\parallel}\right)^2 + \frac{1}{2}K_{22}t^2 + \frac{1}{2}K_{33}\left(\mathbf{b} - \frac{x_{\perp}}{K_{33}}\mathbf{P}_{\perp}\right)^2, \quad (2.21)$$

where x_{\parallel} and x_{\perp} are arbitrary constants assigned to \mathbf{P}_{\parallel} and \mathbf{P}_{\perp} respectively. It is important to note that \mathbf{P}_{\parallel} and \mathbf{P}_{\perp} are vectors with polarity and thus, are not equivalent to their negatives, in contrast to $\hat{\mathbf{n}}$ which is equal to $-\hat{\mathbf{n}}$.

In addition to the Frank free energy, the system must have additional contributions to represent the free energy cost or benefit for developing polar order. These additional contributions can be written as a Ginzburg-Landau expansion[46, 47] in powers of \mathbf{P}_{\parallel} and \mathbf{P}_{\perp} . Based on these theoretical considerations, one can begin to understand the coupling between the director and polar/chiral order.

2.4 Spontaneous Polarity and Chirality

Considering polar order, one can impose a splay \mathbf{s} or bend \mathbf{b} and then measure the resulting polar order of the system. By minimising the free energy from equation 2.21 over \mathbf{P} , and assuming \mathbf{P} is small and uniform, one can obtain the expression;

$$\mathbf{P} = \frac{x_{\parallel}}{y_{\parallel}}\mathbf{s} + \frac{x_{\perp}}{y_{\perp}}\mathbf{b} = \frac{x_{\parallel}}{y_{\parallel}}(\hat{\mathbf{n}}(\nabla \cdot \hat{\mathbf{n}})) + \frac{x_{\perp}}{y_{\perp}}(\hat{\mathbf{n}} \cdot \nabla \times \hat{\mathbf{n}}), \quad (2.22)$$

where y_{\parallel} and y_{\perp} are arbitrary constants similar to x_{\parallel} and x_{\perp} . It can be seen that equation 2.22 is analogous to the expression for the flexoelectric effect in equation 2.16, where $e_1 = x_{\parallel}/y_{\parallel}$ and $e_3 = x_{\perp}/y_{\perp}$.

Considering chiral order, one can impose a twist t and measure the resulting pseudoscalar order parameter. This type of consideration was carried out in recent work by Basu et al.[48] which found that macroscopic twist induces conformational deracemisation (the difference in concentration between right- and left-handed conformations), just as macroscopic splay and bend induce polar order. In considering chiral order, the population difference between the left- and right-handed conformers provides a favoured twist t_0 . When considering polar order, one needs to apply an electric field which couples to the polar order through the free energy $F_{total} = F_{Frank} - \mathbf{E} \cdot \mathbf{P}$. Minimising the free energy over polar order, bend and splay gives;

$$\begin{aligned} \mathbf{P}_{\parallel} &= \frac{K_{11}}{y_{\parallel}K_{11} - x_{\parallel}^2}\mathbf{E}_{\parallel}, & \mathbf{s} &= \frac{x_{\parallel}}{y_{\parallel}K_{11} - x_{\parallel}^2}\mathbf{E}_{\parallel}, \\ \mathbf{P}_{\perp} &= \frac{K_{33}}{y_{\perp}K_{33} - x_{\perp}^2}\mathbf{E}_{\perp}, & \mathbf{b} &= \frac{x_{\perp}}{y_{\perp}K_{33} - x_{\perp}^2}\mathbf{E}_{\perp}. \end{aligned} \quad (2.23)$$

An applied electric field parallel to the director induces a splay, whilst an applied electric field perpendicular to the director induces a bend. The ratios $x_{\parallel}/(y_{\parallel}K_{11} - x_{\parallel}^2)$ and $x_{\perp}/(y_{\perp}K_{33} - x_{\perp}^2)$ are the susceptibilities of splay and bend to the applied field. One should notice that each of these susceptibilities involves a characteristic denominator, and thus it can be deduced that the susceptibilities diverge when the denominator approaches zero. If the denominator becomes zero, one must then consider spontaneous polar or chiral order.

2.4.2 Twist-bend nematic phase

A good example of chiral symmetry breaking with spontaneous polarity and chirality is the twist-bend nematic phase. Whilst none of the bent-core materials investigated in this thesis exhibit the N_{TB} phase, they do exhibit interesting elastic behaviour in the nematic phase which can be explained by considering spontaneous polarity and chirality (see chapter 4). This subsection will go into detail on how the polarisation theory can be used to explain the formation of the N_{TB} phase, as well as the reduction in K_{33} that has been observed in bent-core liquid crystals previously. Thus this section is only included for completeness in understanding the effect of spontaneous polarity and chirality.

In the context of polarity, spontaneous polar order is disfavoured by entropy and electrostatic interactions. However, it might be favoured by steric packing considerations, which can occur in bent-core molecules when the polar order is perpendicular to the director (figure 2.4). When this happens, one can induce spontaneous bend. In the context of chirality, spontaneous symmetry breaking has been studied in many liquid crystals and related systems. Calculations have shown that a domain of left-handed chirality will have one sign of twist, whilst a domain of right-handed chirality will have the opposite sign of twist. In some cases, a material can show alternating stripes of left- and right-handed chirality, which are accompanied by alternating twist in the director field.

Splay and bend are different from twist in an important way; a cholesteric liquid crystal can have pure uniform twist everywhere, but a liquid crystal cannot have pure uniform splay or bend everywhere. Hence, a liquid crystal with spontaneous splay or bend is not able to form the ideal structure because of geometric constraints. Instead, it must make some compromise between different terms in the free energy.

When considering spontaneous bend, which is more relevant to bent-core liquid crystals, one finds that the liquid crystal cannot fill space with uniform bend everywhere. However, it can fill space with a combination of bend and twist by forming the twist-bend nematic (N_{TB}) phase (figure 2.7, taken from a paper by Dozov[49]).

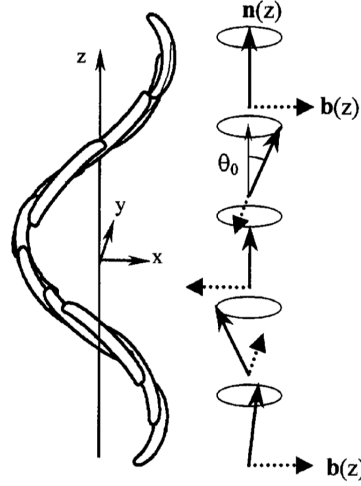


Figure 2.7: Representation of the twist bend nematic phase in bent-core liquid crystals, taken from a paper by Dozov.[49]

The theoretical work of Dozov on what is now known as the N_{TB} phase, was motivated by considering the bend elastic constant K_{33} of bent-core liquid crystals.[49] Initially, without considering polar order, Dozov proposed that bent-core liquid crystals can have an anomalously small value of K_{33} , compared with other nematic liquid crystals. In the case where K_{33} becomes negative, the free energy would need to include higher-order terms of the director field in order to be stable. The competition between the negative K_{33} term and the positive higher-order terms would favour a certain spontaneous bend. Because it is impossible to have pure bend everywhere, the liquid crystal could form either a twist-bend phase (with a heliconical structure) or a splay-bend phase (with alternating domains).

Quantitatively, Dozov's theory predicts that the nematic phase becomes unstable when forming the twist-bend phase at the critical point when $K_{33} = 0$. If one considers K_{33} to be a temperature-dependent coefficient, where $K_{33}(T) = K'_{33}(T - T_C)$, then the transition occurs at the critical temperature T_C . At this transition, the system enters the twist-bend phase if $K_{11} > 2K_{22}$.

The theory of Dozov was especially influential because it suggested that the formation of the twist-bend phase is related to molecular shape of the liquid crystal. Thus it seemed intuitive that highly bent liquid crystals would be more likely to form the N_{TB} phase. As a result, a number of liquid crystal dimers were

2.4 Spontaneous Polarity and Chirality

synthesised, for example CB7CB (figure 2.8).^[50–53]

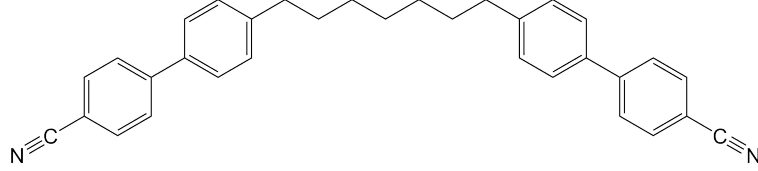


Figure 2.8: Molecular structure of CB7CB which forms the twist-bend nematic phase.

One can apply the polarisation theory (introduced earlier in this section) to the twist-bend phase by minimising over \mathbf{P}_{\parallel} and \mathbf{P}_{\perp} . Assuming \mathbf{P}_{\parallel} and \mathbf{P}_{\perp} are small and slowly varying, one obtains the effective free energy;

$$F_{eff} = \frac{1}{2} \left(K_{11} - \frac{x_{\parallel}^2}{y_{\parallel}} \right) |S|^2 + \frac{1}{2} K_{22} t^2 + \frac{1}{2} \left(K_{33} - \frac{x_{\perp}^2}{y_{\perp}} \right) |B|^2 + \dots \quad (2.24)$$

This free energy is the Frank free energy seen in equations 2.21 and 2.22, but with effective, renormalised Frank constants;

$$K_{11}^R = K_{11} - \frac{x_{\parallel}^2}{y_{\parallel}}, \quad K_{33}^R = K_{33} - \frac{x_{\perp}^2}{y_{\perp}}. \quad (2.25)$$

There is an important difference between K_{33} and the renormalised constant K_{33}^R ; K_{33} gives the energy cost of a bend if one constrains $\mathbf{P}_{\perp} = 0$ during the bend, whilst K_{33}^R gives the energy cost of a bend if \mathbf{P}_{\perp} relaxes to its optimum value during the bend. The same is true for K_{11} and \mathbf{P}_{\parallel} . Usually when one measures elastic constants, no constraints are imposed on the polar or chiral order. Instead, the experiment normally allows the elastic constants to relax. Hence, K_{11}^R and K_{33}^R are usually the relevant elastic constants when one does not consider polar order.

In bent-core liquid crystals, it is reasonable to suppose that x_{\perp} is particularly large, and y_{\perp} is anomalously small. If this is the case, then the polarisation theory provides an explanation as to why the effective bend constant K_{33}^R can become

anomalously small. Indeed, if x_{\perp} becomes large enough and y_{\perp} becomes small enough, the polarisation theory can explain why K_{33}^R might become negative.

2.5 Fluctuations in Polarity and Chirality

The twist-bend nematic phase is a good example of how spontaneous polarity and chirality arises in achiral molecules,[54–56] and how it can affect the behaviour of the elastic constants as the nematic to twist-bend nematic phase transition is approached.

It is important to note that in the bent-core molecules discussed in this thesis, the pure materials exhibit fluctuations in both polarity and chirality throughout the nematic phase, which provide a negative correction leading to a reduction in the bend and twist elastic constants respectively.[57] Corrections to the bend elastic constant can be explained using the theory already discussed in this chapter and have shown to be a factor in the formation of the twist-bend nematic phase.[56] However the nature of the negative correction in the twist elastic constant has yet to be explained. Earl et al. showed that chiral conformations of bent-core molecules induced some deracemisation, contributing to a higher helical twisting power in the cholesteric doped with bent-core molecules.[58] It can be shown that the same chiral conformers can also reduce the twist constant and thus affect the pitch directly through the equation;

$$\frac{2\pi}{p} = \frac{\lambda}{K_{22}}, \quad (2.26)$$

where p is the pitch of the cholesteric, K_{22} is the twist elastic constant, and λ is a constant related to the helical twisting power. From equation 2.26 that both a higher helical twisting power and a lower K_{22} would reduce the pitch, thus explaining the results Earl et al. measured. The derivations of the corrections in both the twist and bend elastic constants will be discussed in chapter 4 to explain the elastic behaviour in an oxadiazole based bent-core liquid crystal.

2.6 Summary

To summarise, this chapter introduces the elastic constant theory and spontaneous polarity and chirality in liquid crystals, in particular how spontaneous polarity and chirality arises in bent-core liquid crystals. This chapter also details how phenomena such as the reduction in the bend elastic constant can give rise to the formation of more exotic phases such as the twist-bend nematic phase.

The theory of elastic constants is important in understanding how one can measure the level of distortion that occurs when an external field is applied to a liquid crystal device. In this thesis only electric fields are considered and thus the derivations in this chapter cover how the application of electric fields can allow one to calculate the elastic constants from experiments. Equations 2.7, 2.8, 2.12, and 2.15 will be used throughout this thesis and are adapted for bent-core liquid crystals.

Understanding polarity and chirality in liquid crystals is essential to understanding the phase behaviour in bent-core liquid crystals. This chapter shows the manner in which spontaneous polarity and chirality arises in bent-core mesogens due to the particular shape of the molecules, and how more exotic phases can form using the twist-bend nematic phase an example.

The next chapter, chapter 3, will detail the experimental methodology described in this thesis, as well as introduce the materials and mixtures that were investigated.

Chapter 3

Experimental Methodology

3.1 Introduction

In this chapter I will discuss the experimental methods used in this thesis. The chapter begins by detailing the materials and devices used and then discussing the methodology carried out as part of the project. Throughout this chapter I will provide context to the methods by referencing which results chapters contain the appropriate methodology used to obtain the corresponding results.

3.2 Materials and Devices

3.2.1 Materials

Five pure liquid crystal compounds were used as part of this project; two bent-core mesogens and three calamitic mesogens. The molecular structures, with the corresponding phase transition temperatures, of the bent-core liquid crystals are shown in figure 3.1, and for the calamitic liquid crystals in figure 3.2. The transition temperatures were measured using differential scanning calorimetry (DSC) and confirmed using polarising optical microscopy (POM). The transition temperatures reported in both figures are from POM. The two bent-core liquid crystals were synthesised by the Goodby group at the University of York. 5CB and 8CB were synthesised by Merck, with BAAB2 obtained from a collaboration with S. V. Serak and V. A. Grozhik, funded through INTAS-BELARUS N97-0635

(2001). Two other materials were also used; one was a nematic mixture, referred to as ZLI 1132, synthesised by Merck, and the other was a mixture, referred to as TM 1001, synthesised by Merck which exhibited chiral nematic and blue phases. ZLI 1132 is nematic at room temperature, with a nematic to isotropic transition temperature of $T_{NI} = 71.2$ °C. TM 1001 has the following phase transitions on cooling (determined using DSC); isotropic-blue phase 1 at 43.5 °C, blue phase 1-blue phase 2 at 43.4 °C, blue phase 2-chiral nematic at 43.3 °C and chiral nematic-smectic A at 24.3 °C.

As mentioned at the end of chapter 1, VBG93 was used as the main basis of the research for this project. DT12 was used as it has a much lower nematic to isotropic phase transition temperature T_{NI} compared with VBG93, making it a suitable material to create mixtures that exhibit lower temperature DC phases. 5CB was used to mix with VBG93 to create filament structures (see chapter 7 for more information). 8CB was used as another host calamitic material to create filaments in the SmA phase. BAAB2 was used as a photochromic material to induce lower temperature nematic to isotropic transitions in the filament mixtures. ZLI 1132 was used as a higher temperature calamitic host to check if filaments could still form. TM 1001 was used to check if filaments could form in other phases such as the chiral nematic phase, or blue phase.

VBG93 has been investigated thoroughly and has shown to exhibit unusual properties, for example in the phase behaviour[30–32, 59–61] and in the elastic properties.[62, 63] DT12 had not been characterised before this work; it was investigated at the point of synthesis. Chapter 4 will go into more detail on the elastic properties of DT12, both experimentally and theoretically. 5CB and 8CB are common nematic mesogens and have also been thoroughly investigated since they were first synthesised in the 1970s.[64, 65] BAAB2 is an azo-benzene based photochromic material; it undergoes a trans-cis isomerisation under the illumination of light of wavelength ~ 350 nm, and a cis-trans isomerisation at a wavelength of ~ 432 nm (see figure 3.3).[66, 67] The relaxation from the cis state to trans state can also occur thermally. The transition temperatures taken for BAAB2 were taken in the dark to avoid any isomerisation.

Mixtures were created from these pure materials in varying concentrations in order to understand the effect of the elastic behaviour and any interrelationship

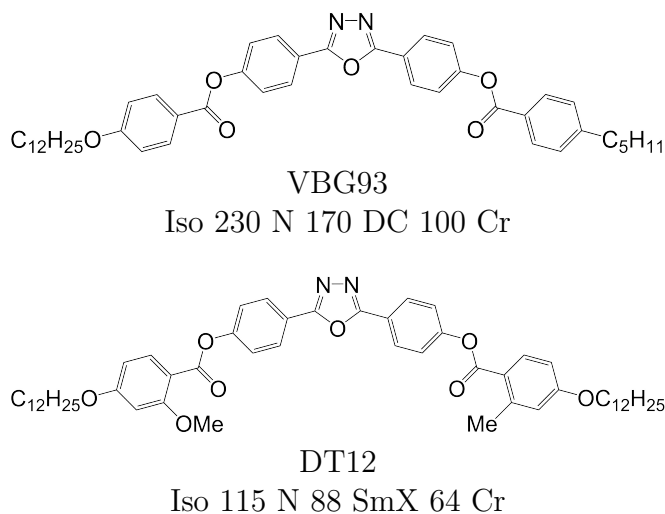
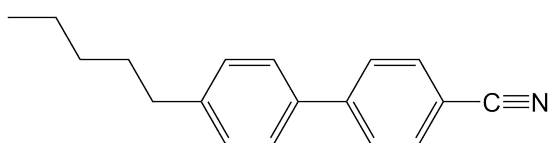
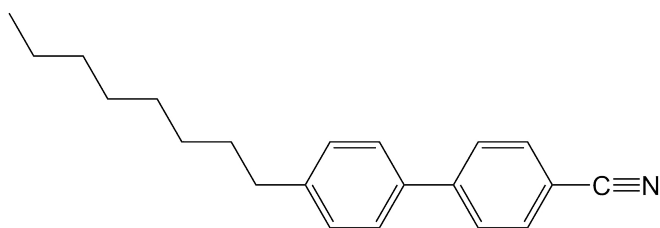


Figure 3.1: Molecular structures and phase transition temperatures for the pure bent-core liquid crystals described in this thesis. Temperatures are recorded in °C where Iso = isotropic phase, N = nematic phase, DC = dark conglomerate phase, Cr = crystalline phase, and SmX = smectic phase of unknown type.

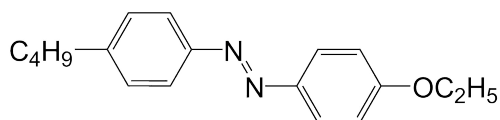
between that and the phase behaviour of the mixtures. The mixtures used are shown with their respective compositions and phase transition temperatures in table 3.1. All results detailed in this thesis were taken on cooling. Mixtures 6-9 and 13-16 exhibit filaments and data is provided on both heating and cooling phase transitions to highlight the thermal hysteresis observed in these mixtures. The behaviour of the filaments and investigations into their elastic behaviour and structure will be discussed in further detail in chapters 5 and 7.



5CB
Iso 35 N 18 Cr



8CB
Iso 40 N 33.5 SmA 21.5 Cr



BAAB2
Iso 83 N 33 Cr

Figure 3.2: Molecular structures and phase transition temperatures for the pure calamitic liquid crystals described in this thesis. Temperatures are recorded in °C where Iso = isotropic phase, N = nematic phase, Cr = crystalline phase, and SmA = smectic A phase.

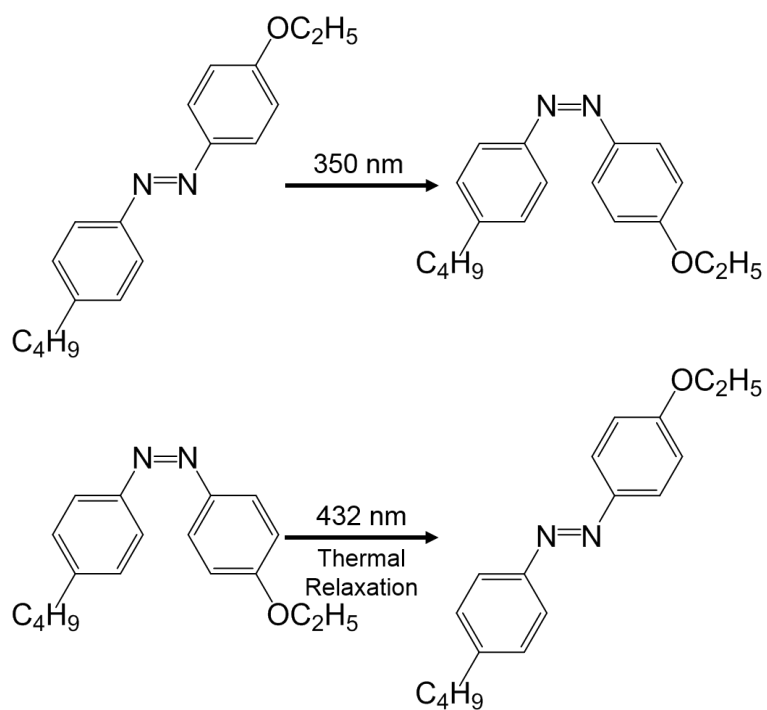


Figure 3.3: Representation of how the molecular shape of BAAB2 changes as it undergoes trans-cis (top) and cis-trans isomerisation (bottom) respectively.

3.2 Materials and Devices

Mixture Number	Composition	Phase Transitions T/°C
Mixture 1	10:90 DT12:VBG93	Iso 224 N 164 OI 94 Cr
Mixture 2	25:75 DT12:VBG93	Iso 200 N 144 OI 95 Cr
Mixture 3	50:50 DT12:VBG93	Iso 190 N 140 SmX 90 Cr
Mixture 4	70:30 DT12:VBG93	Iso 170 N 117 SmX 80 Cr
Mixture 5	90:10 DT12:VBG93	Iso 140 N 100 SmX 70 Cr
Mixture 6	10:90 VBG93:5CB	N+F 40.5 I+F 51.8 Iso
		Iso 49.0 N 26.1 N+F
Mixture 7	10:90 VBG93:8CB	SmA+F 36.0 N+F 45.6 I+F 60.1 Iso
		Iso 52.0 N 40.0 N+F 38.4 SmA+F
Mixture 8	5:95 VBG93:5CB	N+F 39.7 I+F 49.1 Iso
		Iso 41.9 N 28.0 N+F
Mixture 9	10:90 VBG93:ZLI 1132	N 80.7 Iso
		Iso 84.9 N
Mixture 10	10:90 DT12:5CB	Iso 42.0 N
Mixture 11	10:90 DT12:8CB	Iso 46.3 N 29.8 SmA
Mixture 12	10:90 DT12:ZLI 1132	Iso 72.5 N
Mixture 13	10.4:1.2:88.4 VBG93:DT12:5CB	N+F 42.7 I+F 53.7 Iso
		Iso 51.6 N 28.4 N+F
Mixture 14	9.9:3.3:86.8 VBG93:DT12:5CB	N+F 44.5 I+F 55.1 Iso
		Iso 54.3 N 30.6 N+F
Mixture 15	10:10:80 VBG93:BAAB2:5CB	N+F 48.8 I+F 58.4 Iso
		Iso 56.2 N 30.6 N+F
Mixture 16	8:92 VBG93:TM 1001	SmA+F 24.6 N*+F 32.0 BP11+F 42.6 BP1+F 45.5 I+F 68.1 Iso
		Iso 52.6 BP1 49.3 BP11 45.5 N* 35.4 N*+F 26.4 SmA+F

Table 3.1: Compositions of mixtures used in this thesis with the corresponding phase transitions and transition temperatures, where Iso = isotropic phase, I+F = isotropic phase with filaments, N = nematic phase, N+F = nematic phase with filaments, N* = chiral nematic phase, N*+F = chiral nematic phase with filaments, OI = optically isotropic phase, BP1 = blue phase 1, BP1+F = blue phase 1 with filaments, BP11 = blue phase 2, BP11+F = blue phase 2 with filaments, SmX = smectic phase of unknown type, SmA = smectic A phase, SmA+F = smectic A phase with filaments and Cr = crystalline phase.

3.2.2 Devices

Devices were constructed using two parallel glass substrates separated by spacer beads. Whilst spacer beads can range in size from $2\ \mu\text{m}$ to upwards of $50\ \mu\text{m}$, the size used to obtain the results discussed in this thesis were all $5\ \mu\text{m}$ in size. UV curable glue was used to create a seal to ensure uniform thickness.

Ordinarily both glass substrates are coated on one side with a transparent layer of indium tin oxide (ITO) of thickness $\sim 0.02\ \mu\text{m}$; another type of device was used which had the ITO layer on only one of the glass substrates, known as an in-plane switching device which will be discussed later. The ITO side faced in towards the centre of the device, ie. adjacent to with the liquid crystal layer. By soldering wires onto the ITO coated substrate, an electric field can be applied across the device (perpendicular to the glass substrates). The ITO layer is usually etched (using dilute hydrochloric acid) to obtain a specifically desired electrode area. It is important that the glue seal is not included in the electrode area as that will influence the capacitance measurements due a voltage drop across the glue (see sections 3.5 and 3.6). This is carried out for more accurate dielectric measurements of the capacitance of the device.

An alignment layer is added on top of the ITO layer on the glass substrate. This allows a preferential direction of the liquid crystal nematic director to be obtained. Alignment layers tend to be composed of a polymer (or mixture of polymers). The polymers interact with the liquid crystal molecules and anchor the molecules to the alignment layer. There are two types of alignment; planar and homeotropic. With planar alignment the director lies parallel to the glass substrates, whereas with homeotropic alignment the director lies perpendicular to the glass substrates. Usually when planar alignment is applied, the substrate is rubbed in a particular direction. This causes the director to lie in one preferred direction. When an electric field is applied to the device the director reorientates in one particular manner. Figure 3.4 shows a schematic of how the director lies in planar and homeotropic devices.

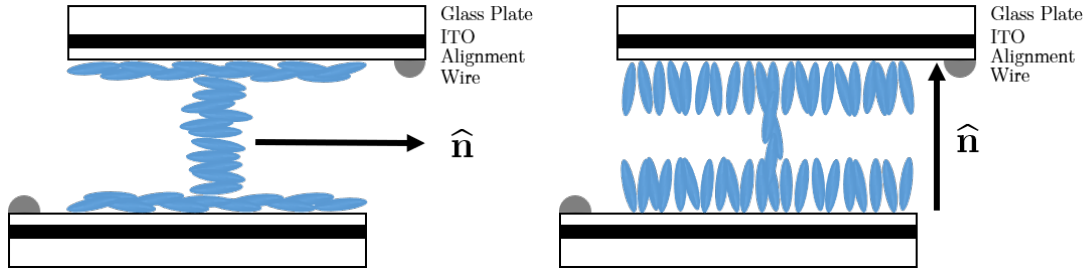


Figure 3.4: Examples of how the liquid crystal nematic director lies in both a planar (left) and homeotropic (right) device. $\hat{\mathbf{n}}$ represents the nematic director direction in each device. Figure not to scale.

For the devices described in this thesis, the planar devices achieved alignment using a rubbed high-temperature (SE130) polyimide layer. Homeotropic alignment was achieved using trichloro(octadecyl)silane (C18), the structure of the silane is shown in figure 3.5. Homeotropic alignment of bent-core liquid crystals is a particular challenge and thus measurements were taken only when the alignment was deemed good enough by viewing the alignment using polarising optical microscopy (and through comparison with known data in literature) and the experimental uncertainties take account of this.

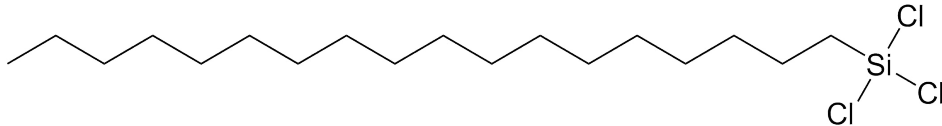


Figure 3.5: Molecular structure of trichloro(octadecyl)silane (C18).

Planar aligned devices allow switching of liquid crystals with positive dielectric anisotropy, whilst homoetropically aligned devices allow switching of liquid crystals with negatively dielectric anisotropy. A third type of device was used as part of this thesis, known as an in-plane switching (IPS) device. In this device, the alignment is planar rubbed however only one of the glass substrates has a layer of ITO on it. The ITO is etched in a specific interlocking finger pattern (shown in figure 3.6). This allows a Fréedericksz transition to occur that induces only a twist deformation in the nematic director at the threshold. It is important to note the direction of rubbing in order to achieve a Fréedericksz transition to occur. For a material with positive dielectric anisotropy the rubbing needs to be perpendicular

to the electric field, whereas for a material with negative dielectric anisotropy the rubbing needs to be parallel to the electric field.

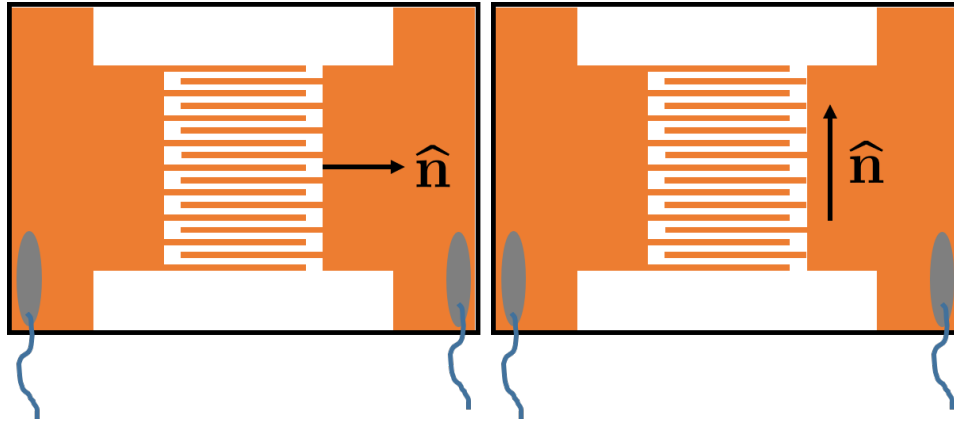


Figure 3.6: Example of the interlocking finger pattern used for the ITO layer (shown in orange) in an IPS device. The rubbing direction can be either parallel (left) or perpendicular (right) to the electrodes. Figure not to scale.

In this thesis the homoetropic devices were created in house by myself whilst the planar aligned and IPS devices were commercially made.

3.3 Polarising Optical Microscopy

Polarizing optical microscopy (POM) is one of the fundamental tools used to understand liquid crystal properties by observing liquid crystal textures and inferring the structure.[2, 68–70] The most important aspect of POM is having crossed polarisers, ie. two linear polarisers (the second is usually denoted the analyser) that are aligned perpendicular to each other. When placed between the two polarisers, liquid crystals will retard the light such that the polarised light passes through the analyser. The retardance that the light experiences is related to both the birefringence of the liquid crystal and the thickness of the liquid crystal device. The retardance can be measured using a Berek compensator, which will be discussed later on in this chapter in section 3.8. Using a white light source, the birefringence of the liquid crystal allows only certain wavelengths to pass through the system. This gives liquid crystal textures their characteristic colourful images. More information on liquid crystal textures and how they can

3.4 Differential Scanning Calorimetry

be imaged can be found in references [2] and [122]. An example of a liquid crystal texture is shown in figure 3.7.

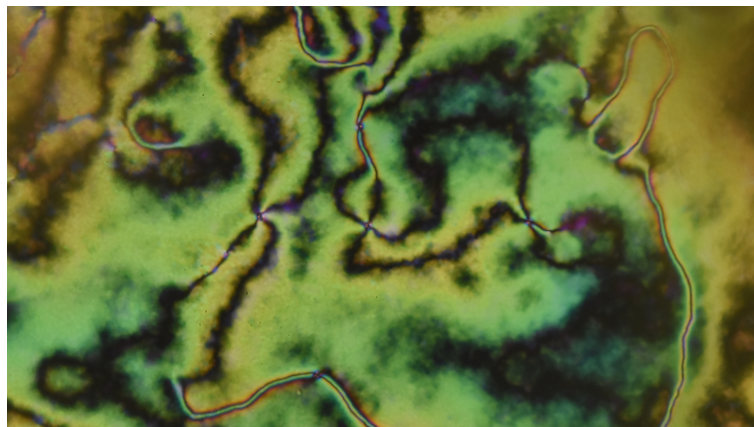


Figure 3.7: Example of a schlieren texture observed in the nematic phase of 5CB.

By coupling a hot stage and temperature controller to the microscope one can change the temperature of a liquid crystal device and observe any changes in the liquid crystal texture. This is important for identifying when specific phase transitions occur. By using a function generator and multimeter one can also apply electric fields across their devices and a change in the birefringence/director orientation is readily visible through POM. The change in director orientation can be used to measure the elastic constants of the liquid crystal, through a change in the retardance of the liquid crystal device. More details on the measuring elastic constants will be discussed later on in this chapter in section 3.6

3.4 Differential Scanning Calorimetry

Another method to measure transition temperatures of liquid crystals is to use differential scanning calorimetry, more commonly referred to as DSC. Using DSC, the heat flow through the liquid crystal is measured as a function of temperature, both on heating and on cooling. The phase transitions that occur, in the materials mentioned in section 3.2, can be characterised by peaks/troughs in the DSC traces. An example of a DSC trace is shown in figure 3.8, taken for DT12.

3.5 Measuring Dielectric Anisotropy

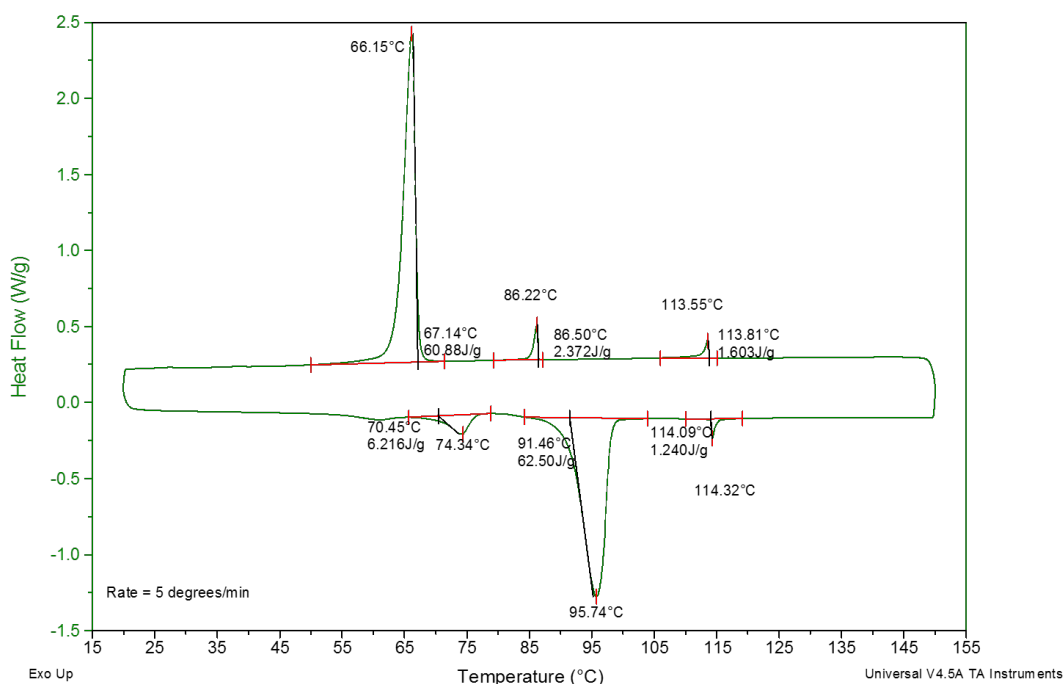


Figure 3.8: DSC trace obtained for DT12 at a rate of 5 °C/min.

The transition temperatures were taken to be the onset temperatures from the DSC traces; in the plot from figure 3.8, the transition temperatures on cooling are:

Cooling	Iso \rightarrow N	N \rightarrow SmX	SmX \rightarrow Cr
5 °C/min	113.8 °C/min	86.5 °C/min	67.1 °C/min

Table 3.2: Transition temperatures on cooling for DT12.

3.5 Measuring Dielectric Anisotropy

The dielectric anisotropy ($\Delta\epsilon$) of the liquid crystals was measured using an Agilent Precision LCR Meter E4980A, with the temperature controlled by a Linkam LTS 350 hot stage connected to a TMS 94 temperature controller. The hot stage and temperature controller allowed the temperature to be determined to an accuracy of ± 0.1 °C. The Precision Meter measured the capacitance of a liquid crystal device as a function of frequency at a specific voltage and temperature. A value for

3.5 Measuring Dielectric Anisotropy

the capacitance at a specific frequency was then chosen to avoid any relaxations. For the results discussed in this thesis, the frequency chosen was 10 kHz to avoid any relaxations. An example of a frequency scan using the LCR Meter is shown in figure 3.9, taken for 5CB at 1 V_{RMS} at room temperature.

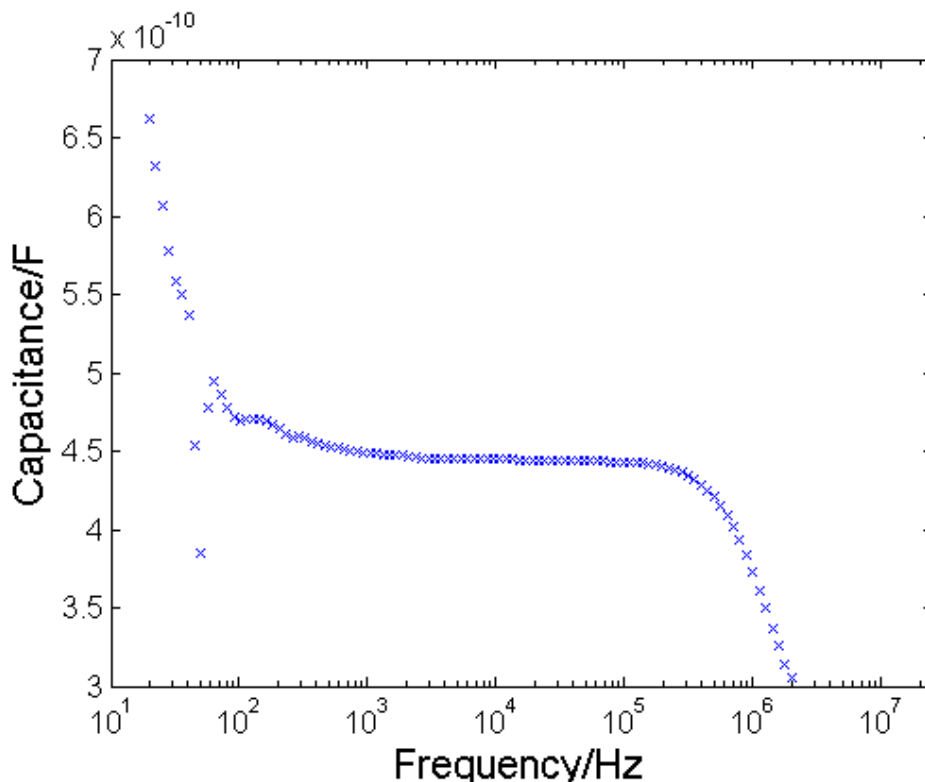


Figure 3.9: Capacitance as a function of frequency for 5CB at 1 V_{RMS} at room temperature.

The capacitance was measured for both an empty device and a filled device. This allows one to calculate the dielectric permittivity of the liquid crystal, denoted as ϵ in equation 3.2. Equation 3.2 comes from considering the capacitances of the empty device and the filled device, which both account for stray capacitance C_s ;

$$C_o = \frac{\epsilon_o A}{d} + C_s, \quad C_{LC} = \frac{\epsilon \epsilon_o A}{d} + C_s, \quad (3.1)$$

where d is the device thickness, A is the electrode area, C_{LC} is the capacitance mea-

3.5 Measuring Dielectric Anisotropy

sured for the filled device, and C_o is the capacitance measured for the empty device. It should be noted that C_s takes into account any contribution to the capacitance due to the alignment layers or the wires. Subtracting the two capacitances allows one to arrive at equation 3.2;

$$C_{LC} - C_o = \frac{\epsilon_o A}{d} (\epsilon - 1),$$
$$\epsilon = \frac{d}{\epsilon_o A} (C_{LC} - C_o) + 1, \quad (3.2)$$

which accounts for stray capacitance. Here The dielectric anisotropy was then calculated by finding the difference between the perpendicular (ϵ_{\perp}) and parallel (ϵ_{\parallel}) components of ϵ as shown in equation 3.3;

$$\Delta\epsilon = \epsilon_{\parallel} - \epsilon_{\perp}. \quad (3.3)$$

This thesis provides two methods to calculate $\Delta\epsilon$; one was used for DT12, VBG93, and mixtures 1-5, all of which exhibited high temperature nematic phases (> 100 °C), and thus was carried out to avoid applying voltages across these samples for long periods of time; the samples were found to degrade when held in the nematic phases for too long. The other method was used for the other materials (5CB, 8CB, and mixtures 6, 7, and 9-12) that exhibited close to room temperature nematic phases, which were stable under the effect of electric fields for long periods of time.

Using the first method a probe voltage of $0.1 V_{RMS}$ was applied to the liquid crystal device to measure ϵ for both a planar and homeotropic device. A probed planar device will give ϵ_{\perp} whilst a probed homeotropic device will give ϵ_{\parallel} . Thus $\Delta\epsilon$ can be calculated easily using equation 3.3 for one specific temperature. This method was then carried out for a number of temperatures to determine how $\Delta\epsilon$ varies with temperature. This method was carried out for VBG93, DT12 (results shown in chapter 4), and mixtures 1-5 (results shown in chapter 5).

3.5 Measuring Dielectric Anisotropy

Using the second method a planar device was used and voltages up to $20 V_{RMS}$ were applied. This method was used for mixtures that exhibited positive $\Delta\epsilon$, and so a planar device was used to allow switching of the liquid crystal to occur. Voltage steps of $0.05 V_{RMS}$ were used between $0.1-2 V_{RMS}$ and steps of $0.5 V_{RMS}$ were used between $2.5-20 V_{RMS}$. This allowed a larger number of data points around the threshold voltage V_{th} to be obtained. An example showing the how ϵ varies with V_{RMS} is shown in figure 3.10.

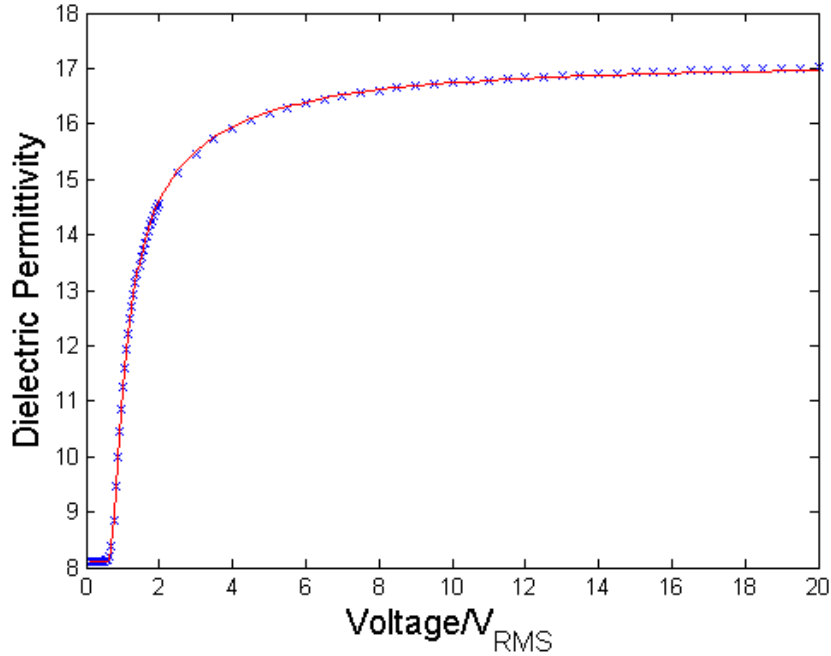


Figure 3.10: Dielectric permittivity ϵ as a function of V_{RMS} for mixture 6 at a reduced temperature $T-T_{NI} = -5$ K. The blue crosses represent the experimental data with the red line showing a fit to the data. ϵ was measured to an accuracy of 5%, which are not included in this plot to provide more clarity of the fit on the raw data.

From the data ϵ_{\perp} was measured at voltages below V_{th} whereas ϵ_{\parallel} was measured at voltages much larger than V_{th} . $\Delta\epsilon$ was then calculated as before using equation 3.3. These measurements were repeated for a range of temperatures to determine how $\Delta\epsilon$ varies with temperature. As part of this method, a fit to the $\epsilon-V_{RMS}$ curve was applied to accurately calculate values of ϵ_{\perp} and ϵ_{\parallel} . Section 3.6.2 goes into

more detail of how this fit is calculated and used. This method was carried out for 5CB, 8CB, and mixtures 6, 7, and 9-12, the results of which are shown in chapter 5. It should be noted that if this method is used on a negative $\Delta\varepsilon$ liquid crystal then a homeotropic device would need to be used, which would allow ε_{\parallel} to be observed at voltages below V_{th} and ε_{\perp} at voltages much larger than V_{th} .

Both methods discussed in this section allow the dielectric anisotropy to be measured to an accuracy of $\sim 10\%$ or 0.5 (whichever is larger). This value takes into account the stray capacitance associated with measuring the capacitance (using the LCR Meter), and the thickness and electrode area of the liquid crystal device.

3.6 Measuring Elastic Constants

It was mentioned in section 3.5 that two methods were used to measure $\Delta\varepsilon$. Similarly, two methods were used to measure the elastic constants. One method was carried out optically whereas the other method was carried out dielectrically. Both methods were used for measuring the splay (K_{11}) and bend (K_{33}) elastic constants, however the twist constants of all samples were only measured using the optical method. This section references equations that have been derived in section 2.2 in chapter 2.

3.6.1 Optical measurements of the splay and bend elastic constants

The optical method for measuring K_{11} and K_{33} was used for VBG93, DT12, and mixtures 1-5 and these results are discussed in chapters 4 and 5. The optical method allowed for the homeotropic alignment to be checked to ensure that reliable measurements of the optical Fréedericksz transition can be obtained. VBG93, DT12, and mixtures 1-5 exhibit a negative $\Delta\varepsilon$ in their nematic phases, thus a homeotropic device was used to analyse the electric-field induced Fréedericksz transition. A monochromatic laser of wavelength 675 nm was used as the light source for the optical measurements. The laser light was transmitted through the liquid crystal device and the transmitted light intensity was measured using

3.6 Measuring Elastic Constants

a photodiode mounted on a polarising microscope with crossed polarisers. The device was oriented in the microscope such that director was at 45° to both polarisers which allowed the maximum light intensity to be transmitted through the device. In order to measure K_{11} and K_{33} the intensity I transmitted as a function of voltage for the homeotropic device was converted into a retardance, δ using the equation;

$$I = I_o \sin^2(\delta/2), \quad (3.4)$$

where I_o is the maximum transmitted intensity. K_{33} is directly related to the threshold voltage of the homeotropic device;

$$V_{th}^{K_{33}} = \pi \sqrt{\frac{K_{33}}{\varepsilon_0 |\Delta\varepsilon|}}. \quad (3.5)$$

Equation 3.5 is analogous to equation 2.8 in chapter 2, however equation 3.5 applies to a liquid crystal with a negative dielectric anisotropy in a homeotropic device, whilst equation 2.8 applies to a liquid crystal with positive dielectric anisotropy in a planar device. Equation 3.5 allows K_{33} to be measured with an accuracy of $\sim 10\%$ or 0.2 pN (whichever is larger). See appendix A on how this error was assigned. The splay and bend elastic constants influence the steepness of the retardance above threshold and thus the splay constant can be deduced using equation 3.6 (adapted from equation 2.12 in section 2.2);[71, 72]

$$\delta = \frac{2\pi d n_o \nu}{\lambda(\eta + 1)} \left(\frac{V}{V_{th}^{K_{33}}} - 1 \right), \quad (3.6)$$

where $\nu = (n_e^2 - n_o^2)/n_e^2$ and $\eta = (K_{11} - K_{33})/K_{33}$. n_o and n_e are the ordinary and extra-ordinary refractive indices, λ is the wavelength of monochromatic light and V is the applied voltage. By considering the steep section of the retardance just above the threshold, the splay elastic constant can be deduced by substituting the gradient (m) of the steep section into equation 3.6;

3.6 Measuring Elastic Constants

$$m = \frac{2\pi dn_o\nu}{\lambda(\eta + 1)V_{th}^{K_{33}}}. \quad (3.7)$$

Rearranging for $\eta + 1$ gives;

$$\eta + 1 = \frac{2\pi dn_o\nu}{\lambda m V_{th}^{K_{33}}}. \quad (3.8)$$

Substituting in $(K_{11}/K_{33}) - 1$ for η gives;

$$\frac{K_{11}}{K_{33}} = \frac{2\pi dn_o\nu}{\lambda m V_{th}^{K_{33}}}. \quad (3.9)$$

Rearranging for K_{11} gives us the equation to determine K_{11} using the gradient of the steep section of the graph;

$$K_{11} = \frac{2\pi dn_o\nu K_{33}}{\lambda m V_{th}^{K_{33}}}. \quad (3.10)$$

Equation 3.6 allows K_{11} to be measured with an accuracy of $\sim 15\%$ or 2 pN (whichever is larger). See appendix A on how this error was assigned.

The assumption with equation 3.10 is that the transmitted light intensity increases as a function of V_{RMS} from a minimum light intensity to a maximum light intensity, analogous to the plot in figure 3.10. An example of this is seen in figure 3.11. The plot in figure 3.11 was taken close to T_{NI} when the birefringence is low. The retardance δ can be easily calculated from the light intensity using equation 3.4.

However as the temperature decreases the birefringence of the nematic phase in a liquid crystal device increases such that the retardance becomes degenerate and the liquid crystal device exhibits multiple full-wave plate and half-wave plate conditions. An example of how the transmitted light intensity varies as a function of V_{RMS} in this case is shown in figure 3.12;

The degeneracy in δ can be removed by including sign information when square-rooting the \sin^2 , and including phase information when taking the inverse

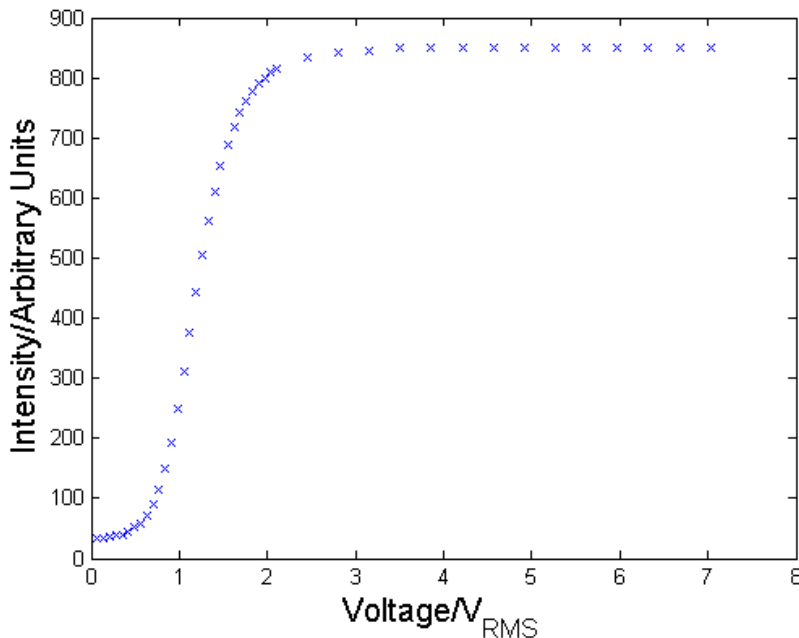


Figure 3.11: Transmitted light intensity as a function of V_{RMS} for DT12 at $T - T_{NI} = -2.5$ K.

sine to obtain $\delta/2$. When considering sign information it is important to remember that calculations only return positive roots. To account for this every second peak was inverted to provide the correct sinusoidal variation of $\delta/2$, as seen in figure 3.13.

When considering phase information, it is important to remember that the sin function is not only repetitive, but that calculations typically return values between $-\pi/2$ and $\pi/2$. Thus the $\delta/2$ data must be added to or subtracted from multiples of π . The choice of addition or subtraction depends on the region of the data point in the plot shown in figure 3.13. Figure 3.14 shows these regions using the same plot shown in figure 3.13.

When both the sign and the phase are accounted for, the resulting plot of δ as a function of V_{RMS} is as shown in figure 3.15. It can be seen that figure shows a similar trend to figure 3.11, from which the gradient of the step section of the plot can be obtained, and thus a value for K_{11} . It can be seen from figure 3.15 that the threshold is not as sharp as the threshold seen in figure 3.11. This

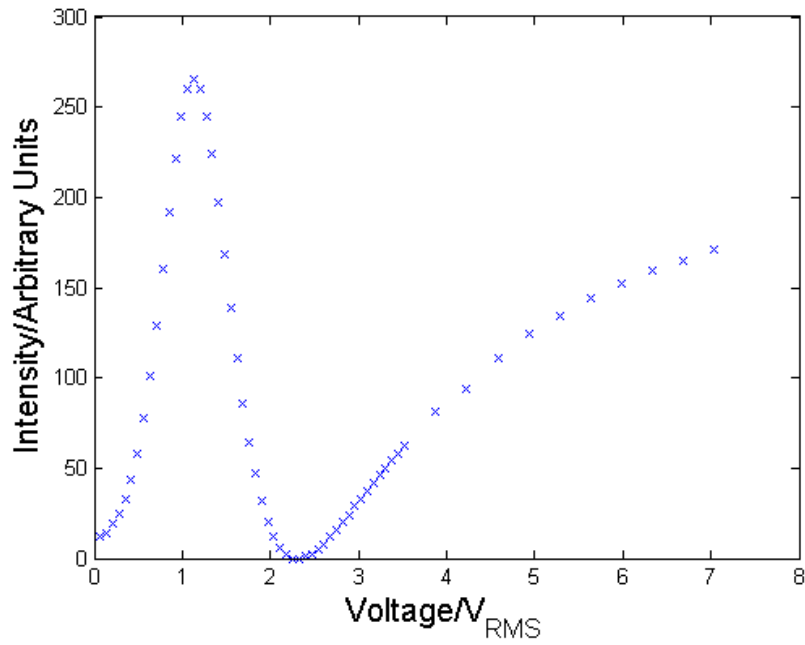


Figure 3.12: Transmitted light intensity as a function of V_{RMS} for mixture 1 at $T-T_{NI} = -42.5$ K.

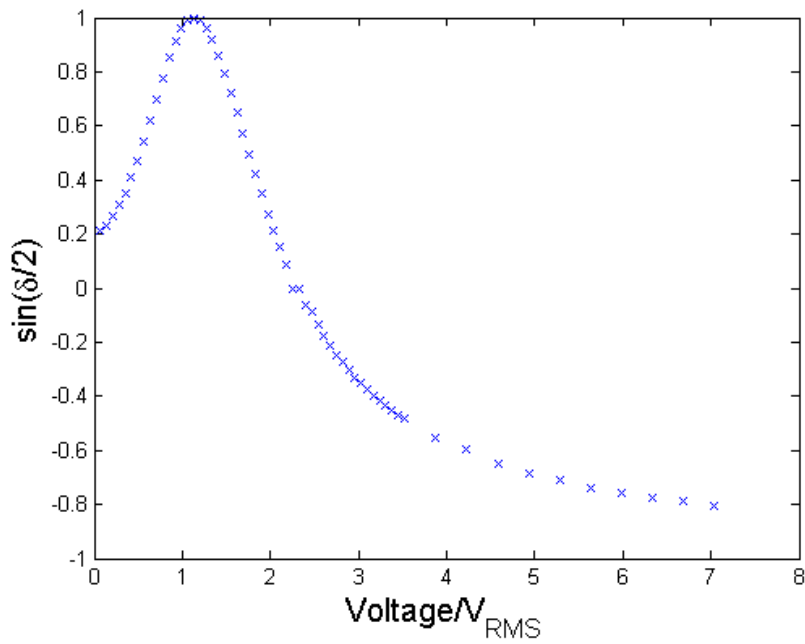


Figure 3.13: $\sin(\delta/2)$ as a function of V_{RMS} for mixture 1 at $T-T_{NI} = -42.5$ K.

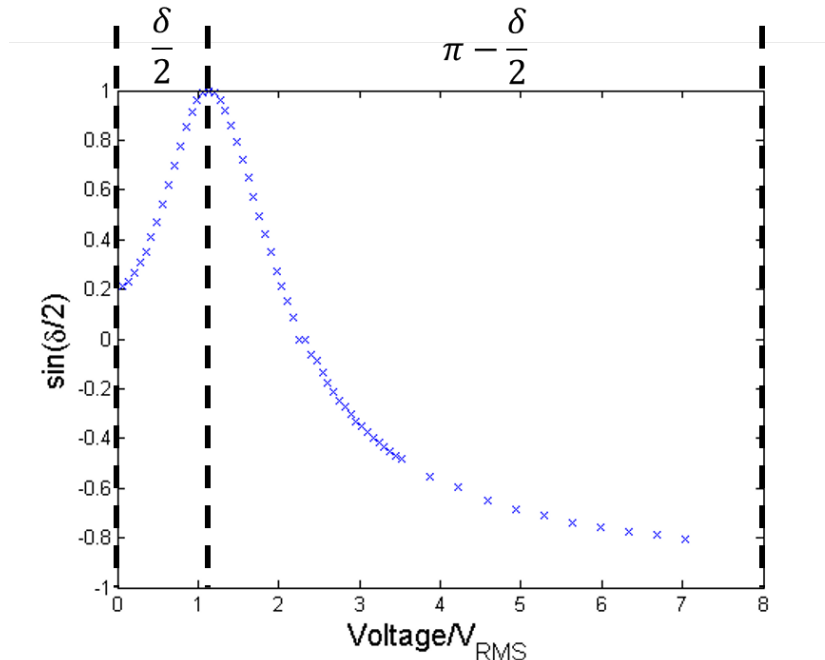


Figure 3.14: $\sin(\delta/2)$ as a function of V_{RMS} for mixture 1 at $T-T_{NI} = -42.5$ K, including the regions of manipulation to calculate $\delta/2$.

would obviously affect how the threshold is measured, which would affect the measurement of K_{33} and thus the measurement of K_{11} . The assignment of the uncertainties on K_{11} and K_{33} takes this into account, and appendix A goes into more detail as to how the assignment is carried out.

Although the optical method described in this section does not take account of any contributions from flexoelectric effects, it has been determined that in VBG93, the flexoelectric coefficients are only a factor of 2 greater than in calamitic liquid crystals[40], so this omission is justified. It should be noted that the errors assigned to both K_{11} and K_{33} using this method refer to the absolute accuracy of the measurement, with the relative accuracy being much better within data sets.

3.6.2 Dielectric measurements of the splay and bend elastic constants

This method was used for 5CB, 8CB, and mixtures 6, 7, and 9-12 and these results are discussed in chapter 5. These samples all have a positive $\Delta\epsilon$ and

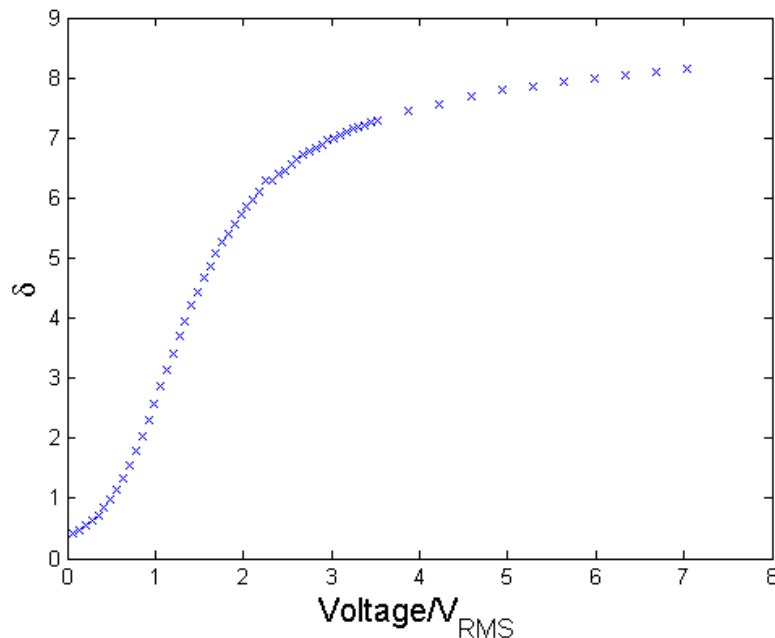


Figure 3.15: δ as a function of V_{RMS} for mixture 1 at $T - T_{NI} = -42.5$ K.

so a planar device was used to analyse the electric-field induced Fréedericksz transition. The capacitance across the liquid crystal device was measured using the Agilent Precision LCR Meter E4980A, which was then converted into the dielectric permittivity using equation 3.2. The splay and bend elastic constants were deduced by using a computer fitting program (see figure 3.10 for an example of the fit to the data), which employs the following equation (adapted from equation 2.7 in section 2.2),

$$\frac{V}{V_{th}} = \frac{2}{\pi} (1 + \gamma \sin^2 \phi_M)^{1/2} \int_0^{\pi/2} \left(\frac{F_k}{F_\zeta F_\gamma} \right)^{1/2} d\phi, \quad (3.11)$$

where $F_k(\phi) = 1 + k \sin^2(\phi_M)$, $F_\zeta(\phi) = 1 - \sin^2(\phi_M)$, $F_\gamma(\phi) = 1 + \gamma \sin^2(\phi_M)$, $k = (K_{11}/K_{33}) - 1$, $\gamma = (\varepsilon_\perp/\varepsilon_\parallel) - 1$, and ϕ_M is the director angle in the centre of the liquid crystal layer.[35] K_{11} is calculated from the threshold voltage $V_{th}^{K_{11}}$ (see equation 2.8, repeated here for clarity), whilst K_{33} is calculated from the steepness of the curve above the threshold. This is analogous to measuring

K_{11} and K_{33} optically. This methodology allowed K_{11} and K_{33} to be deduced with an accuracy of $\sim 5\%$. Again, as with the optical measurements, flexoelectric contributions were not taken into account, as the coefficients are only a factor of 2 greater than in calamitic liquid crystals.[40]

$$V_{th}^{K_{11}} = \pi \sqrt{\frac{K_{11}}{\varepsilon_0 \Delta \varepsilon}}. \quad (\text{equation 2.8})$$

3.6.3 Optical measurements of the twist elastic constant

An IPS device was used to measure K_{22} . For this measurement, the IPS device was oriented such that the director was parallel to one of the polarisers. This meant that with no voltage applied to the device, no light would be transmitted through it. However due to the twist deformation induced by the applied voltage, the light intensity measured using the photodiode increased as the voltage increased. This allowed the threshold voltage to be measured. K_{22} is directly related to the threshold voltage:[38]

$$V_{th}^{K_{22}} = \frac{\pi l}{d} \sqrt{\frac{K_{22}}{\varepsilon_0 |\Delta \varepsilon|}}. \quad (3.12)$$

where d is the device thickness and l is the electrode separation in the in-plane device; for the devices discussed in this thesis, the separation was $20 \mu\text{m}$. This method allows K_{22} to be determined with a relative accuracy of $\sim 20\%$ for each data set measured in this way, though the absolute accuracy of this method is no better than $\sim 33\%$ because of the non-uniform electric fields in the geometry.[63, 73]

3.7 X-Ray Scattering

For the materials used in this thesis, small angle X-ray scattering (SAXS) was used to determine the lattice spacing in the various liquid crystal phases investigated. SAXS was carried out using a Bruker D8 Discover which was equipped with a temperature controlled, bored graphite rod furnace, custom built at the University of York which allowed the temperature to be measured to an accuracy of $0.1 \text{ }^\circ\text{C}$.

3.7 X-Ray Scattering

The radiation used was a copper $K\alpha$ (wavelength of 0.154 nm) source. Samples were filled into 1 mm diameter capillary tubes and the system was used in transmission. The detector was placed 127 mm from the sample, which allowed spacings between 4-100 nm to be determined with an accuracy of 0.1 Å. The liquid crystal was heated to the isotropic phase and readings were taken as the sample was cooled. All the measurements were carried out under an applied magnetic field of ~ 0.7 T.

This methodology allowed the intensity of the X-ray scattering to be measured as a function of d_x , which allows one to understand how the periodicity and FWHM of the samples varied as a function of temperature. Here d_x refers to the lattice spacing of the sample. With the detector placed 127 mm away from the sample, the maximum lattice spacing that could be measured was 100 Å. An example of the plot of intensity against d_x for VBG93 is shown in figure [3.16](#).

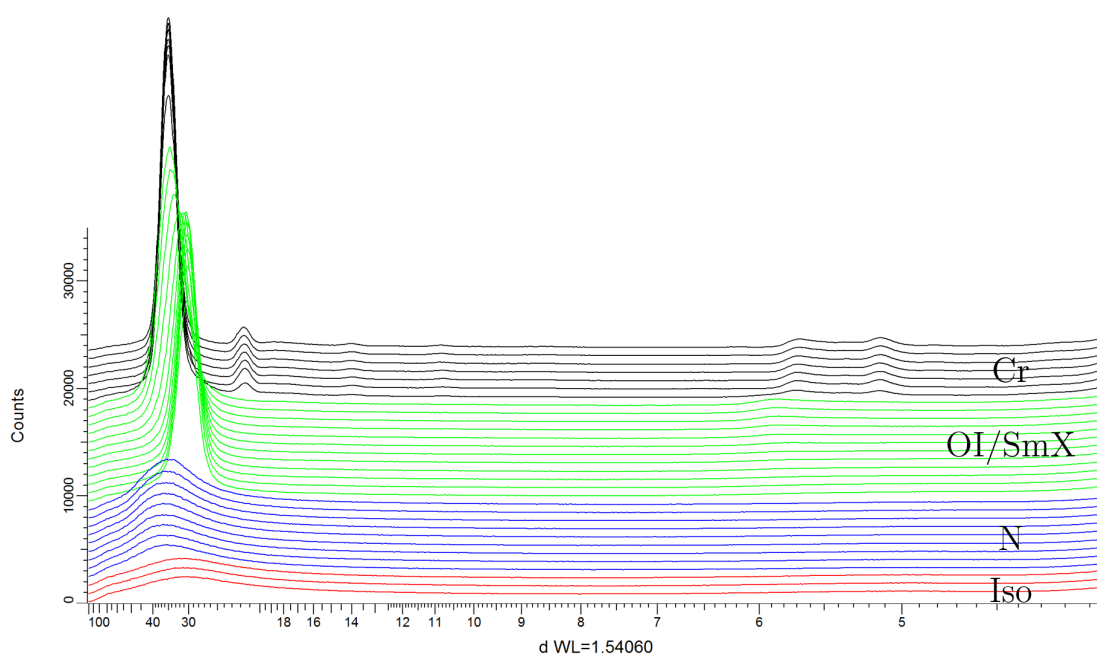


Figure 3.16: Example plots of intensity as a function of d_x for VBG93. For both bent-core liquid crystals and the mixtures, the red plots represent the isotropic phase, the blue plots represent the nematic phase, the green plots represent the underlying phase, and the black plots represent the crystal phase. In the case of DT12 and mixtures 3-5 the underlying phase is a SmX phase, and for VBG93 it is a DC phase. For mixtures 1 and 2 the underlying phase is an optically isotropic phase.

3.7 X-Ray Scattering

The plots of intensity against d_x were obtained by integrating an average over the whole detector i.e. integrating in rings. Using the Bragg equation $2d_x \sin\theta = n\lambda$, the spacings that are of interest can be determined. For the measurements on the bent-core mixtures described in this chapter, the spacings that were of interest were ~ 30 Å. The chosen peaks around 30 Å were fitted using MATLAB in order to obtain the peak position and the full width at half maximum (FWHM) of the peak. The fit chosen was a Gaussian fit. Figure 3.17 shows an example of this fit applied to an X-ray spectrum taken for VBG93. The Gaussian fit allowed the spacing to be measured to an accuracy of 0.1 Å and the FWHM to 0.2 Å, however the instrument limited the resolution to 3 Å. X-ray scattering was carried out on VBG93, DT12 and mixtures 1-5 with the results discussed in chapter 6.

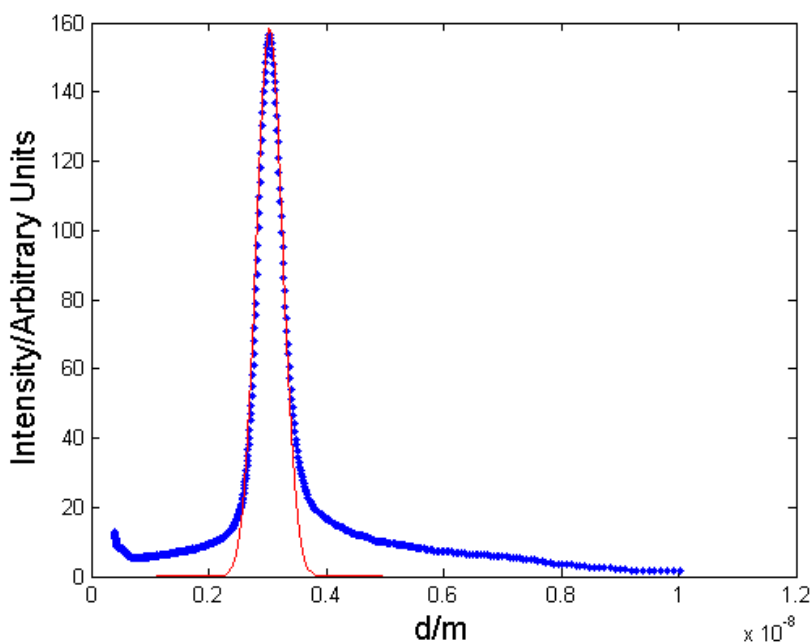


Figure 3.17: X-ray scattering intensity as a function of periodicity d_x for VBG93 5 °C into the DC phase. The blue data points represent the experimental data and the red line represents the Gaussian fit applied to the data.

3.8 Measuring Birefringence

The birefringence Δn of the nematic phase was measured using a Berek compensator. Ordinarily an Abbe refractometer is used to measure the ordinary and extraordinary refractive indices of the liquid crystal; however the mixtures that were investigated using this technique (mixtures 6, 8, 13, and 14) exhibited self-assembling filaments below T_{NI} . It was believed that the filaments would not allow one to measure n_o and n_e accurately and hence the Berek compensator was used instead. A Berek compensator composes of a birefringent material that can tilt, thus changing the retardance that any light passing through it experiences. In this thesis, the compensator was used to match the retardance of the liquid crystal device, and thus the birefringence of the liquid crystal could be obtained.

The compensator was inserted into the polarising optical microscope at 45° to the crossed polarisers. The liquid crystal device was then orientated such that the director of the liquid crystal was perpendicular to the fast axis of the compensator. The tilt α of the compensator was adjusted such that its retardance $\Delta\Gamma$ matched the retardance due to the liquid crystal device, thus cancelling each other out. The tilt is related to the retardance;[74]

$$\Delta\Gamma = n_o d_{Ber} \left(\sqrt{1 - \frac{\sin^2\alpha}{n_o^2}} - \sqrt{1 - \frac{\sin^2\alpha}{n_e^2}} \right), \quad (3.13)$$

where d_{Ber} is the thickness of the compensator, and n_o and n_e are the ordinary and extraordinary refractive indices of the compensator. n_o and n_e are related to the wavelength of light λ ;[75]

$$n_i = \sqrt{A_i + \frac{B_i}{\lambda^2 - C_i}}, \quad (3.14)$$

where $i = o$ or e referring to the ordinary or extraordinary refractive index respectively. In this case $A_o = 5.913$, $B_o = 2.441 \times 10^7$, $C_o = 0.803 \times 10^7$, $A_e = 7.917$, $B_e = 3.322 \times 10^7$, and $C_e = 0.843 \times 10^7$ with λ in nm. The birefringence of the liquid crystal device is related to the retardance;

$$\Delta n = \frac{\Delta\Gamma}{d_{LC}}, \quad (3.15)$$

where d_{LC} is the thickness of the liquid crystal in the device. These measurements allowed the birefringence to be determined with an accuracy of $\sim 5\%$ or 0.01 (whichever is larger). All values of the birefringence are quoted for monochromatic light of wavelength 589 nm. Birefringence measurements were carried out on 5CB, and mixtures 6, 8, 13, and 14. These results are discussed further in chapter 7.

3.9 High Resolution Microscopy

As mentioned earlier in this chapter, polarising optical microscopy is one of the fundamental tools used in liquid crystals research to observe textures of liquid crystal phases. However it can be limited by the resolution achieved using standard objective lenses such as 10x and 20x lenses. This section introduces two higher resolution techniques that were used to image the liquid crystals used in this thesis; atomic force microscopy (AFM) and scanning electron microscopy (SEM). The results obtained using these two techniques are discussed further in chapter 7. This work was carried out at the Merck Chemicals Ltd. Chilworth site with the help of James Allen (AFM) and Vicki Poole (SEM).

3.9.1 Atomic Force Microscopy

Atomic force microscopy (AFM) is a type of probing microscopy that allows imaging of samples down to a resolution of a nanometre. The main components of an AFM consist of a tip attached to a cantilever, with a laser which illuminates the end of the cantilever, and a piezoelectric element connected to the other end of the cantilever. A simple schematic is shown in figure 3.18.

The laser allows the user to determine the position of the tip which typically rests close to or on top of the surface that is being imaged. The topography of the sample is determined by analysing the forces between the tip and the surface of the sample based on the corresponding deflections of the cantilever. There are typically three types of imaging modes; contact mode, non-contact mode and

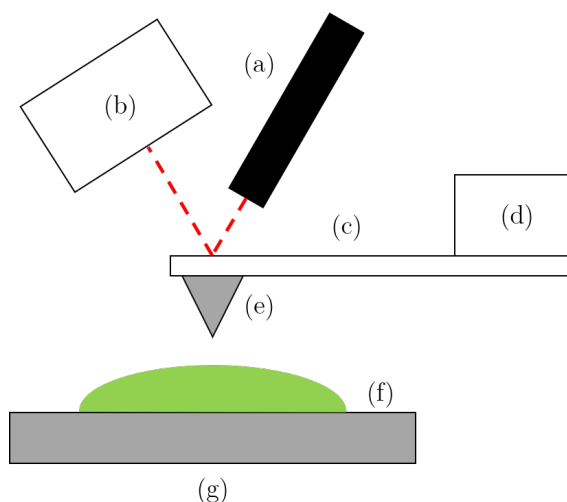


Figure 3.18: Schematic of the components of an AFM with the laser (a), photodiode (b), cantilever (c), piezoelectric (d), tip (e), sample (f), and stage (g). Diagram not scale.

tapping mode. The measurements presented in this chapter were taken using the tapping mode.

In tapping mode, the cantilever is driven to oscillate at its resonance frequency using the piezoelectric element. The oscillation frequency and amplitude are calibrated before any interaction between the tip and the sample occurs. When the tip approaches the surface of the sample a number of forces cause the oscillation amplitude of the cantilever to change from its initial value. These forces include Van der Waals forces and dipole-dipole interactions. The change in the oscillations varies based on the topography of the sample and thus an image of the surface of the sample can be created.

Tapping mode is generally used to avoid continuous contact between the tip and the sample, and is appropriate for imaging soft solids such as the filaments described in this thesis. To obtain the images presented in this chapter the filaments were grown in planar aligned homogeneous devices. The devices were then split apart to provide two substrates with filaments on each of them. AFM was carried out on mixtures 6, 7, and 16.

3.9.2 Scanning Electron Microscopy

Scanning electron microscopy is a type of electron microscopy that allows imaging of samples down to a resolution of a nanometre. The sample is scanned by a focused beam of electrons which interact with the surface of the sample. The resulting signal from the sample is detected which is then used to produce an image. We only want the electron beam to be interacting with the sample, and so the experiment is carried out under a high vacuum to avoid interactions between the electron beam and any particles in the air. For imaging the filaments, the sample preparation was similar to that used for using the AFM; the filaments were grown in planar aligned homogeneous devices. The devices were then split apart to provide two substrates with filaments on each of them. For use in the SEM set up, the samples were then sputter-coated with platinum to avoid any build-up of charge on the sample when scanning with the electron beam. SEM was carried out on mixtures 6, 7, and 16.

3.10 Summary

This chapter provides an overview of the experimental methods used within this thesis. POM was necessary in order to observe the phase behaviour in the bent-core liquid crystals and their mixtures, and when coupled with specialist equipment it was possible to obtain information on the elastic behaviour of these samples (see chapters 4 and 5 for more detail). The X-ray scattering set-up allowed us to understand the structure that the mixtures exhibited in their various phases, most importantly showing that the optically isotropic phases in the bent-core mixtures were indeed DC phases similar to the the DC phase seen in VBG93 (see chapter 6 for more detail). The Berek compensator allowed the birefringence of the devices to be measured, which allowed us to obtain information on the order of the filament mixtures. This in turn provided us with data that showed a time dependency of the birefringence, which will be discussed further in chapter 7. The high resolution microscopy of AFM and SEM gave two different methods of detailed imaging of the filaments which in turn gave vital information into the mechanism in which the filaments form.

3.10 Summary

The next chapter will be the first of the results chapters, which will delve into the elastic behaviour observed and measured in DT12, and how calculations and theoretical models agree with the experimental results.

Chapter 4

Elastic Behaviour in DT12: Experimental and Theoretical Results

4.1 Introduction

This chapter will go into detail on the elastic behaviour measured in DT12, an oxadiazole-based bent-core liquid crystal, discussing how computational and theoretical calculations agree with the experimental results. The experimental measurements were carried out by myself, whilst the computational work was carried out by Alberta Ferrarini, and the theoretical calculations by Mikhail Osipov and Grzegorz Pająk. This chapter reproduces the publication by Srigengan et al.[57] in *J. Mater. Chem. C*, **6**, 980, 2018, and largely follows the format and content of that paper.

As mentioned in chapter 1, nematic liquid crystals are fluids generally characterised by long range uniaxial, orientational order that manifests as anisotropy in their optical, electrical and elastic properties. These anisotropic properties and their responsiveness together make liquid crystals useful in display devices. The nematic phase that is most commonly used for devices is formed from calamitic molecules, but markedly different behaviour is observed in the nematic phase formed from bent-core mesogens. The differences include increased flexoelectricity,[40, 76] and the potential to exhibit exotic phases such as the

twist-bend nematic (N_{TB}) phase[49, 51, 56, 77, 78] and the dark conglomerate (DC) phase.[21, 28, 30–32, 79] The remarkable spontaneous segregation of chiral domains of opposite handedness has also been reported in the nematic phase formed from bent-core molecules.[60, 61]

The elastic properties of nematic liquid crystals are critical parameters, influencing their behaviour in devices as they define both the threshold voltage and steepness of the electro-optic response. The three elastic constants that will be looked at in this chapter are the splay, twist and bend constants denoted as K_{11} , K_{22} and K_{33} respectively. It is now well established that there is a distinct difference in the behaviour of the elastic constants in calamitic and bent-core liquid crystals. Generally for calamitic systems $K_{11} < K_{33}$, whereas bent-core systems exhibit the opposite, ie. $K_{11} > K_{33}$,[80–86] a difference which is naturally explained by the bend angle that arises in bent-core liquid crystals.[73, 80, 87] Furthermore, it has been shown that for a family of oxadiazole-based bent-core liquid crystals, all of the elastic constant values are smaller than those measured in calamitic liquid crystals[63] with VBG93 (see figure 3.1) exhibiting especially low elastic constant values.[62, 63]

This chapter discusses the elastic constants exhibited by DT12 (see figure 4.1). DT12 was initially chosen as interesting material due to its wide, low temperature nematic phase, in comparison to other similar oxadiazole-based bent-core nematics.[63] It was originally believed that the lower transition temperatures in DT12 would help reduce the temperature at which the DC phase forms in VBG93; which is justified using simple mixing rules. Knowing that the DC phase is influenced by the elastic behaviour of the bent-core mesogen,[88, 89] investigating the elastic behaviour in mixtures of DT12 and VBG93 should lead to a better understanding into the formation of the DC phase observed in VBG93. As mentioned earlier the elastic behaviour of VBG93 has already been investigated thoroughly,[62, 63] however the elastic behaviour in DT12 has yet to be measured. This chapter aims to introduce the elastic behaviour in DT12 using experimental results carried out by myself and backed up by computational calculations carried out by Alberta Ferrarini. A theoretical model using molecular mean-field theory also confirms the experimental results, which was carried out by Mikhail Osipov

and Grzegorz Pająk. As mentioned at the beginning of this chapter, all these results have been published by Srigenan et al.[57]

4.2 Experimental Methodology

4.2.1 Materials and devices

The molecular structure of DT12 along with its phase transition temperatures on cooling are shown in figure 4.1. The transition temperatures were determined by differential scanning calorimetry (DSC) and confirmed using polarising optical microscopy (POM). The transition temperatures reported in figure 4.1 are from POM. All electrical and electro-optic measurements were carried out using 5 μm thick devices with wires attached to the electrodes using high-temperature conducting glue (H21D, Epoxy Technology). The planar devices used a high temperature (SE130) polyimide for the alignment whilst the homeotropic devices used C18 silane in hexane.

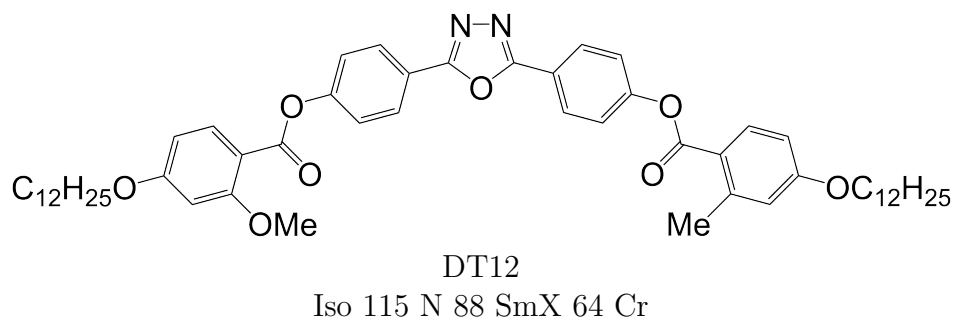


Figure 4.1: Molecular structure of DT12 with its phase transitions temperatures on cooling. Temperatures were recorded in $^{\circ}\text{C}$ where Iso = isotropic phase, N = nematic phase, SmX = smectic phase of unknown type and Cr = crystal phase.

4.2.2 Measurements of dielectric anisotropy and elastic constants

Measurements of the dielectric anisotropy $\Delta\varepsilon$ were taken using the probe voltage method, as described in section 3.5. Using a probe voltage of $0.1 V_{RMS}$, the perpendicular component of the dielectric permittivity ε_{\perp} was measured using a planar device whilst the parallel component ε_{\parallel} was measured using a homeotropic device. The dielectric anisotropy was then calculated using equation 3.3 (repeated below for clarity) for a number of different temperatures in the nematic phase. $\Delta\varepsilon$ was then used to calculate the elastic constants K_{11} , K_{22} and K_{33} , which were measured using the optical methods described in sections 3.6.1 and 3.6.3. The transmitted light intensity through a homeotropic device filled with DT12 was measured using a photodiode, with the wavelength of light being 675 nm. The light intensity was then converted into a retardance δ using the equation $I = I_o \sin^2(\delta/2)$. This equation allowed δ to be determined as a function of V_{RMS} . K_{33} was calculated from the resulting graph by finding the threshold voltage $V_{th}^{K_{33}}$, whilst K_{11} was calculated by measuring the gradient m of the steep section of the graph. The equations used to measure K_{33} and K_{11} respectively are equations 3.5 and 3.10 (repeated below for clarity). K_{22} was calculated from measuring the threshold voltage $V_{th}^{K_{22}}$ via an optical Fréedericksz transition in an IPS device. K_{22} was calculated using equation 3.12 (repeated below for clarity);

$$\Delta\varepsilon = \varepsilon_{\parallel} - \varepsilon_{\perp}, \quad (\text{equation 3.3})$$

$$V_{th}^{K_{33}} = \pi \sqrt{\frac{K_{33}}{\varepsilon_0 |\Delta\varepsilon|}}, \quad (\text{equation 3.5})$$

$$K_{11} = \frac{2\pi d n_o \nu K_{33}}{\lambda m V_{th}^{K_{33}}}, \quad (\text{equation 3.10})$$

$$V_{th}^{K_{22}} = \frac{\pi l}{d} \sqrt{\frac{K_{22}}{\varepsilon_0 |\Delta\varepsilon|}}. \quad (\text{equation 3.12})$$

where d is the thickness of the liquid crystal device, $\nu = (n_e^2 - n_o^2)/n_e^2$, with n_o and n_e being the ordinary and extraordinary refractive indices respectively, λ is the

wavelength of light (675 nm), and l is the electrode spacing.

These measurements allow the dielectric anisotropy to be measured with an accuracy of $\sim 10\%$ or 0.5 (whichever is larger), K_{11} to $\sim 15\%$ or 2 pN (whichever is larger), K_{22} to $\sim 20\%$, and K_{33} to $\sim 10\%$ or 0.2 pN (whichever is larger). More information on how the errors were assigned can be found in appendix A.

4.2.3 Calculations of the elastic constants

The elastic constants of DT12 were calculated (by Alberta Ferrarini) using a computational methodology based on a molecular field approach with atomistic modelling. This consisted of three steps;

- (i) geometry parameters and torsional potentials were obtained from quantum chemical calculations for selected conformers of DT12 and for respective molecular fragments,
- (ii) Metropolis Monte Carlo (MC)[90] sampling of the conformational space was performed, using the energy and geometry parameters determined in the previous step,
- (iii) orientational order parameters and elastic constants, calculated according to the Surface Interaction (SI) model,[91] were obtained as averages over conformers.

The whole procedure is described in detail by Greco et al.[92]

Density functional theory (DFT) was used to optimise the molecular geometries and in the calculation of the torsional potential. The B3LYP functional and 6-31G** basis set was used for this calculation. The conformers of DT12 were generated according to the Rotational Isomeric State (RIS) approximation.[93] Figure 4.2[57] shows the molecular structure with the bonds that were allowed to rotate (denoted as χ_i), which were 27 in number.

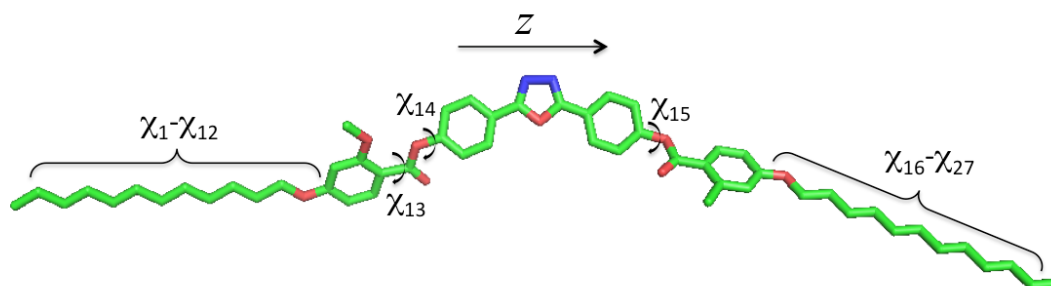


Figure 4.2: Molecular structure of DT12 without hydrogen atoms. The labels show which bonds (χ_i) are allowed to rotate in the Monte Carlo conformation sampling. The molecular frame (x, y, z) has the z axis passing through the carbon atoms of the oxadiazole ring and y perpendicular to the plane of the ring. Figure taken from the paper by Srigengan et al.[57]

DT12 is similar to other compounds investigated by Addis et al.[76] and Kaur et al.[63], therefore most of the geometry and energy parameters used in step ii of the computational procedure were the same as those reported in the previous studies. The only important difference is the presence of the methyl and methoxy lateral substituents on the benzoate rings of DT12. The effect of these substituents on the torsional potentials around the C-C-C=O dihedral angle of the substituted benzoate group was investigated using DFT calculations. The results obtained by relaxed scans at the B3LYP/6-31G** level of the theory[94] are shown in figure 4.3.[57]

It can be seen from figure 4.3[57] that the methyl and methoxy groups do not modify the general shape of the torsional potential, which exhibits two minima for the planar configurations of the benzoate group, separated by potential barriers related to the perpendicular geometries of the benzoate group. The methyl and methoxy groups do affect the height of the barriers, which decrease with increasing size of the substituents, from the H atom, to the CH₃ group and finally the OCH₃ group. However the heights remain sufficiently high to let one assume that non-planar geometries must give a relatively low contribution to conformational averages. For this reason, in the sampling of conformers of DT12, planar benzoate groups were assumed; for the methoxy benzoate the C-C bond was allowed to shift between two equivalent configurations, with the methoxy group on either side of the benzoate with respect to the carbonyl group. In the case of the methyl

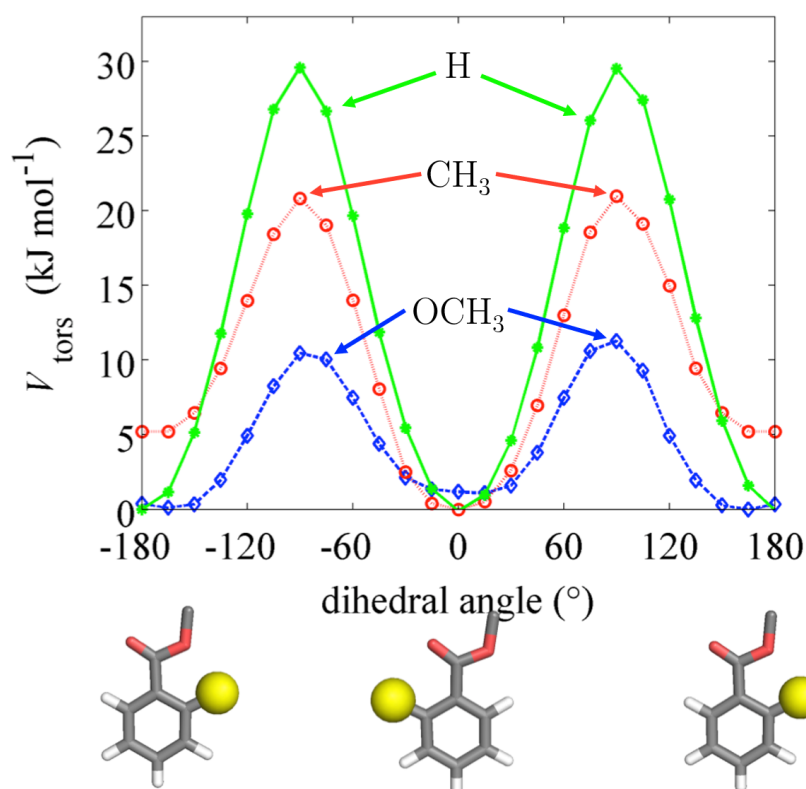


Figure 4.3: Torsional potential, V_{tors} , as a function of the C–C–C=O dihedral angle, calculated for phenyl benzoate with different substituents in the ortho position of the benzoate ring: H (green solid line with stars), CH_3 (red dotted line with circles), OCH_3 (blue dashed line with diamonds). The chemical structures on the bottom show the conformation of the benzoate group in correspondence of the minima of the torsional potential. The yellow sphere is in the position of the lateral substituent. Figure taken from the paper by Srigenan et al. [57]

benzoate, due the energy difference between the two minima of the torsional potential, a single planar conformer was assumed, with the methyl group on the same side of benzoate with respect to the ester group.

4.3 Results

The magnitude of the dielectric anisotropy in DT12 was found to increase as the temperature was reduced in the nematic phase regime as seen in figure 4.4. Such behaviour is similar to that observed in other oxadiazole based bent-core liquid crystals.[63] The values of $\Delta\varepsilon$ from figure 4.4 were used in equation 3.5, 3.10 and 3.12 in deducing the elastic constants from measurements of the optical Fréedericksz transition. Figure 4.5 presents the experimentally determined values of K_{11} , K_{22} and K_{33} together with values calculated computationally (by Alberta Ferrarini) as a function of the reduced temperature, $T-T_{NI}$.

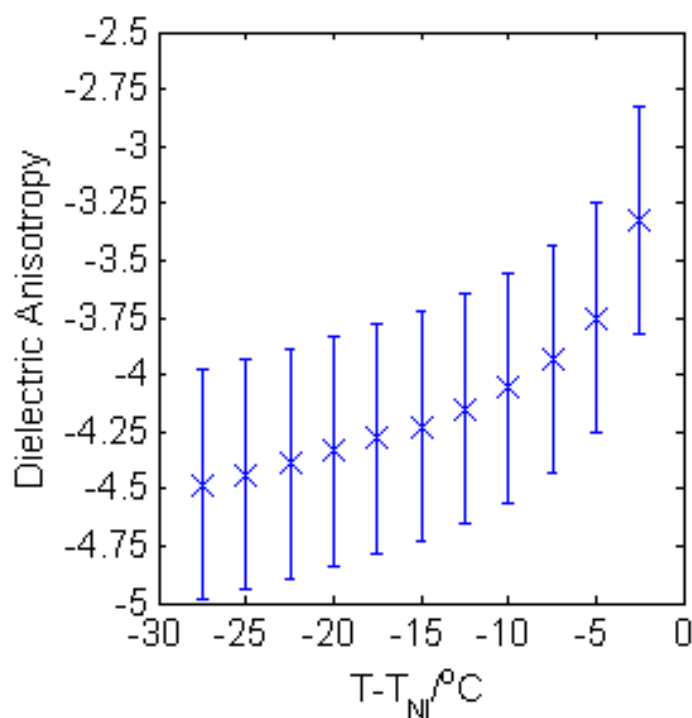


Figure 4.4: Dielectric anisotropy as a function of $T-T_{NI}$ for DT12.

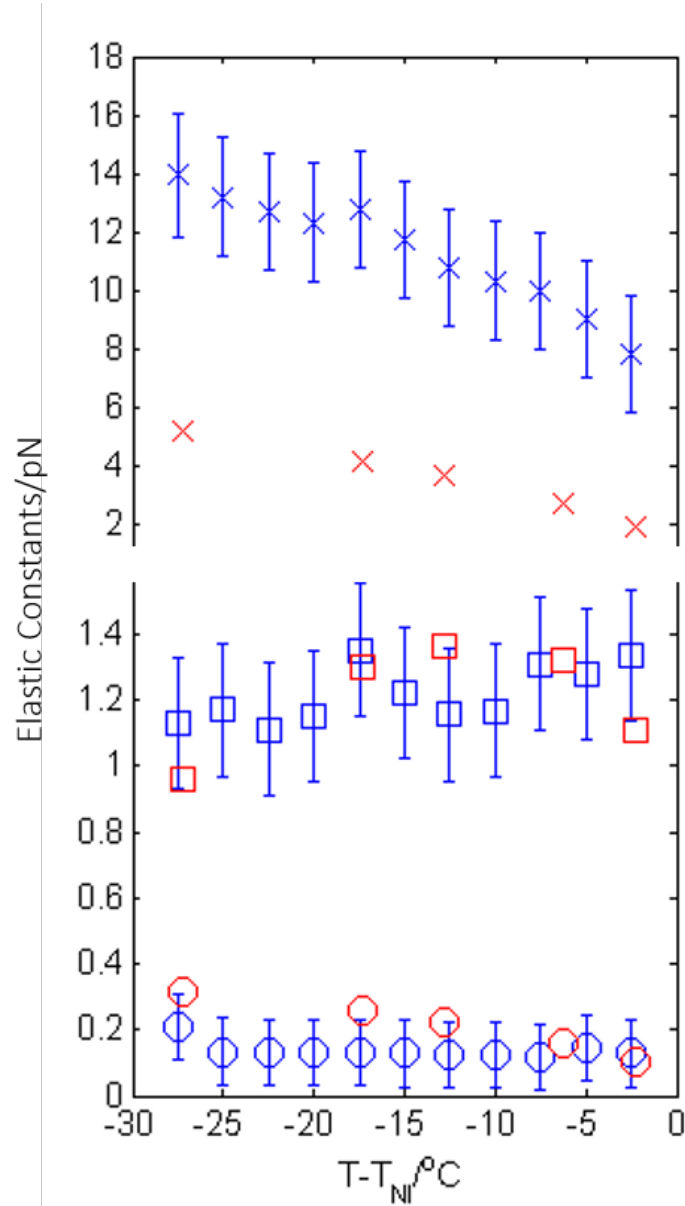


Figure 4.5: The splay, K_{11} (crosses), twist, K_{22} (circles) and bend, K_{33} (squares) elastic constants as a function of $T-T_{NI}$ for DT12. The experimental data are represented by the blue data points and the calculated data by the red data points. Note the break in the y-axis and the change in scale to make visible the very low twist and bend elastic constants.

The experimental data show that K_{11} takes values between ~ 8 – 14 pN and increases in magnitude as the temperature decreases. This is common behaviour and has been observed in many calamitic and bent-core liquid crystals, though the values for DT12 are higher than those for other oxadiazole based bent-core liquid crystals which typically exhibit values between ~ 3 – 9 pN.[63] However, both K_{22} and K_{33} take extremely small values and are practically temperature independent, which is very unusual. The absolute values measured for K_{22} and K_{33} in DT12 (~ 0.15 pN and ~ 1.2 pN respectively) are significantly lower than the lowest values reported for other oxadiazole based bent-core liquid crystals, which exhibit values between ~ 0.4 – 1.3 pN for K_{22} and ~ 2 – 5 pN for K_{33} .

The calculated elastic constants for DT12, also shown in figure 4.5, were determined on the basis of the molecular shape within the SI approach.[91] There is good agreement with the experimental data; the temperature dependence of the splay elastic constant K_{11} is reproduced, though the calculated values are smaller, closer to those exhibited by other oxadiazoles.[63] The calculated values of K_{22} and K_{33} are in excellent quantitative and qualitative agreement with the experimental values.

4.4 Discussion

Figure 4.5 show that DT12 exhibits low values for K_{22} and K_{33} , with both elastic constants being practically temperature independent. The only other reports of lower values of K_{33} are very close to T_{NI} in resorcinol-based bent core materials. Majumdar et al.[81] found $K_{33} \sim 0.9$ pN at $T - T_{NI} = -2$ K in a chloro-substituted material while Tadapatri et al.[82] reported strong temperature dependence of K_{33} with a value of ~ 1 pN very close to T_{NI} , increasing to ~ 5 pN deeper in the nematic phase in a cyanosubstituted material. Majumdar et al.[81] also found $K_{22} \sim 0.3$ pN at $T - T_{NI} = -2$ K in their resorcinol based material, which is larger by a factor of 2 than the K_{22} values exhibited by DT12. The complete set of values measured for DT12 show very low K_{22} and K_{33} values across the whole nematic phase range, at temperatures as low as $T - T_{NI} = -27.5$ K, together with clearly temperature independent behaviour. Although temperature independent behaviour, and small bend and twist elastic constants are also seen in

VBG93 ($K_{22} \sim 0.4$ pN and $K_{33} \sim 2.5$ pN), other oxadiazole based bent-core liquid crystals (compounds 1–3 in ref. [63]) exhibit a significant variation in elastic constants across even a relatively narrow nematic range (K_{11} increases from ~ 3 –8 pN, K_{22} increases from ~ 0.4 –1.3 pN and K_{33} increases from ~ 2 –5 pN for these compounds).

With regards to the computational calculations, the SI approach was able to provide an explanation for the low bend elastic constant of bent mesogens, on the basis of the molecular shape. Thus, in comparing DT12 with analogous bent-core mesogens with unsubstituted benzoates,[63] the changes in molecular shape induced by the methyl and methoxy substituents have to be considered. However, the presence of the lateral substituents do not seem to have a direct effect on the elastic constants of DT12. In fact according to the DFT calculations, these substituents do not largely change the conformational preferences of the benzoate groups, as discussed in section 4.2.3. Likewise, geometry optimizations do not suggest any significant effects of the substituents on the geometry of the oxadiazole core. On the other hand, the presence of the two lateral substituents causes a considerable decrease of the nematic–isotropic transition temperature, and this could have an indirect influence on the elastic constants through a change in the conformer distribution.

Figure 4.6[57] shows the elastic constants calculated for DT12 as a function of the orientational order parameter S_{zz} , which quantifies the alignment of the z molecular axis (see figure 4.2) to the nematic director. Compared with other bent-core mesogens investigated in previous studies,[63, 90] the results shown in the figure were obtained by averaging over 1.5 million conformers; a large conformational space had to be sampled due to the length of the terminal alkyl chains in DT12. Averaging over a large number of conformers showed a magnification of the fluctuations of conformer shapes, which is particularly important for the bend elastic constant K_{33} , as there are conformers which are extended and approximately rod-like. These, more rod-like conformers, give high positive contributions to K_{33} , whilst more bent conformers give strong negative contributions to K_{33} . The results for DT12 suggest that more bent conformers exist in the system, which would reduce the measured K_{33} shown in figure 4.5. In general, the calculations

of conformations indicate that extensive sampling is needed to obtain reliable averages for K_{22} and K_{33} .

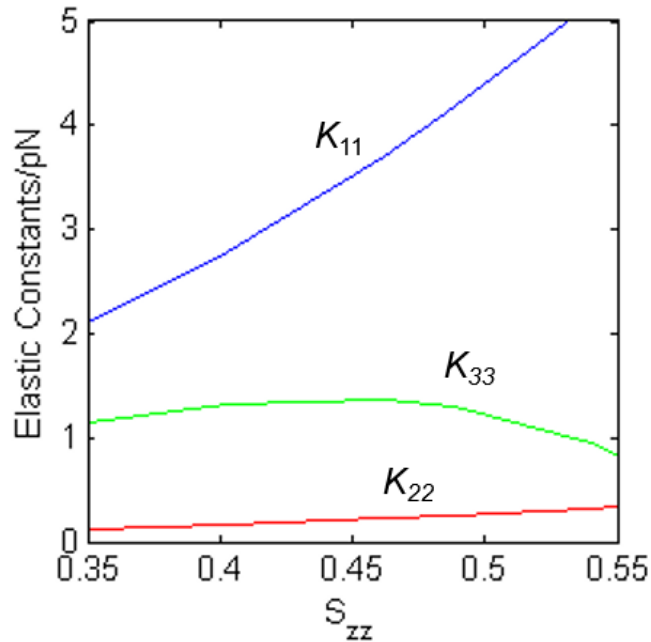


Figure 4.6: Elastic constants calculated for the nematic phase of DT12 as a function of the orientational order parameter S_{zz} , which quantifies the alignment of the z molecular axis (see figure 4.2) to the nematic director. Here K_{11} is represented by the blue line, K_{22} by the red, and K_{33} by the green. Figure taken from the paper by Srigengan et al.[57]

In summary both the calculations and the experimental measurements reveal values of both the twist and bend elastic constants that are unusually low and virtually temperature independent. Low values of K_{33} have been found in bent-core liquid crystals above the transition into the twist-bend phase[51, 77, 78, 95, 96] but such low values of both K_{22} and K_{33} over the full nematic phase regime have never been observed in any other liquid crystal material. The current molecular theory indicates that all three elastic constants should generally increase with decreasing temperature as some power of the nematic order parameter, S , [36, 97–100] and are roughly of the same order of magnitude. The results for DT12 shown in this chapter contradict this general theory. Indeed if one looks at the elastic behaviour of VBG93 as a function of order parameter S_{zz} (figure 4.7 contains plots for

VBG93 and DT12), it can easily be shown that only K_{11} for DT12 behaves as one would expect, with both K_{22} and K_{33} for DT12 being found to be very small and practically independent of S_{zz} .

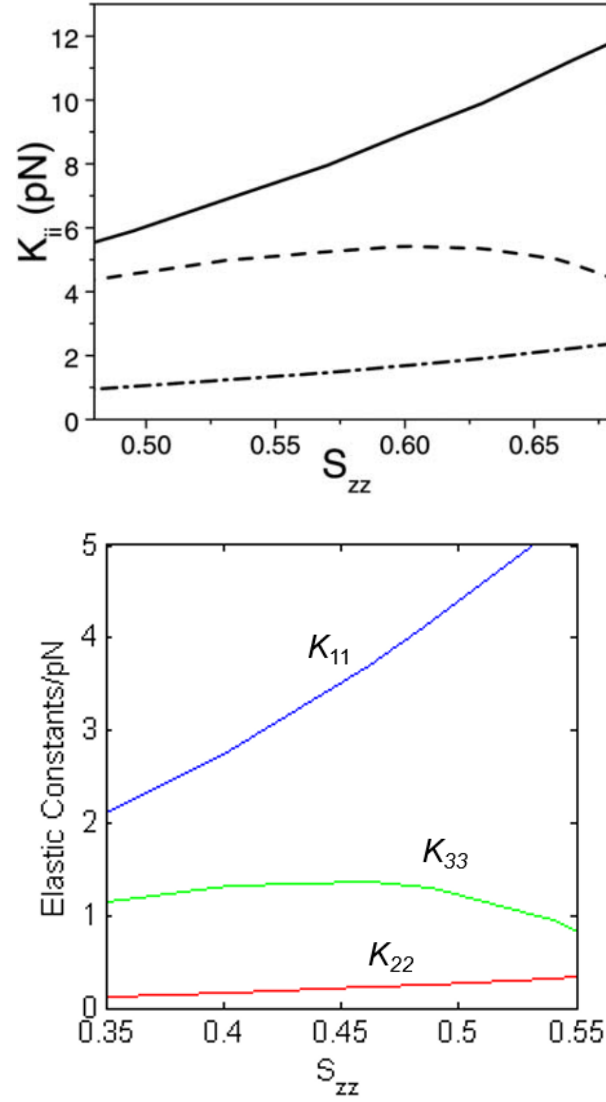


Figure 4.7: Elastic constants calculated for the nematic phases of VBG93 (left, taken from a paper by Kaur et al.[63]) and DT12 (right, taken from the paper by Srigengan et al.[57]) as a function of the order parameter S_{zz} . For the VBG93 plot K_{11} is represented by the solid line, K_{22} by the dash-dotted line, and K_{33} by the dashed line. For the DT12 plot K_{11} is represented by the blue line, K_{22} by the red line, and K_{33} by the green line.

This unusual behaviour can be accounted for using an extension to the molecular field theory that was carried out by Mikhail Osipov and Grzegorz Pająk, and this extension is presented in the next section.

4.5 Molecular Mean Theory

In the context of the molecular mean field theory, the difference between K_{11} and K_{33} is determined by the 4th order orientational order parameter $\langle P_4 \rangle$ [101, 102] which is typically relatively small. Thus K_{11} is expected to be less than K_{33} with the difference not being very large. This is indeed the case for most calamitic liquid crystals. Recently the strong reduction of K_{33} observed in bent-core liquid crystals, just above the transition into the twist–bend nematic phase, has been explained by the effect of polar intermolecular interactions between bent shaped molecules. [56] Shamid et al. [47] showed that a coupling between local polarisation and the bend deformation in bent-core liquid crystals can lead to a negative correction to K_{33} . This correction is defined as $-e_b^2/2\gamma$ where e_b is the bend flexocoefficient and γ is the mean-field susceptibility. This correction can only be significant if the flexocoefficient e_b is sufficiently large or if γ is sufficiently small.

The theory that Shamid et al. [47] put forward has been tested by Osipov and Pająk. [56] This was carried out using a molecular theory which allows one to calculate all the elastic constants and flexocoefficients using the same model interaction potential between bent-core molecules. It has been shown that the effective K_{33} is significantly reduced using a broad range of model parameters. A characteristic K_{33} profile was calculated numerically using equations 57–59 from ref. [56], repeated here for clarity;

$$\chi_{\parallel} = \chi_0 \left(1 - \frac{1}{3}(4\pi\chi_0 - 2(1 + 2S)A_0\sin^2\alpha) \right)^{-1}, \quad (\text{equation 57})$$

$$\chi_{\perp} = \chi_0 \left(1 - \frac{1}{3}(4\pi\chi_0 - (2 + S)A_0\sin^2\alpha) \right)^{-1}, \quad (\text{equation 58})$$

$$\bar{K}_{11} = K_{11} - \frac{1}{2}\chi_{\parallel}e_{11}^2, \quad \bar{K}_{33} = K_{33} - \frac{1}{2}\chi_{\perp}e_{33}^2, \quad (\text{equation 59})$$

where χ_{\parallel} and χ_{\perp} are the parallel and perpendicular components of the dielectric susceptibility, S is the nematic order parameter, e_{11} and e_{33} are the splay and bend flexocoefficients respectively, χ_0 , A_0 , and α are tuneable parameters, and \bar{K}_{11} and \bar{K}_{33} are the effective splay and bend elastic constants.

The results based on the above equations are presented in figure 4.8,[57] where reduced temperature is given by $\tau = (t - t_{NI})/t_{NI}$. It can be seen that, similar to the experimental data shown in figure 4.5, the effective K_{33} is very weakly temperature dependent and is a few factors smaller than the effective K_{11} . Recently it has been shown that this reduction mechanism is more general and is not restricted to flexoelectricity or to strongly polar molecules.[101, 103] In fact, it is the polar molecular shape that is more important as it leads to some polar interactions and polar corrections to the orientational distribution function which determine some negative correction to K_{33} . The absolute value of this correction, however, is very sensitive to the molecular parameters which are different for different compounds. This explains why a dramatic reduction of K_{33} compared to K_{11} is observed only in some nematic materials. Whilst the reduction in K_{33} with respect to K_{11} is well-established for bent-core liquid crystals, all other reports show only a factor of two or three difference in the values whereas the reduction in K_{33} is larger in DT12, as shown in figures 4.5 and 4.8.[57]

In contrast to K_{33} , the reduction in the twist elastic constant K_{22} has not been considered in the literature before. Computational calculations based on atomistic modelling presented in figures 4.5 and 4.6 indicate that the anomalously low values of K_{22} may be related to enhanced flexibility of the oxadiazole compounds. In general, bent-core molecules are known to be flexible and most of the conformational states are strongly chiral.[58] This observation leads to the suggestion that one should consider a simple model where the bent-core nematic can locally exist in two states of opposite chirality. These states can be rotamers, conformers or chiral molecular ensembles. In the ground state of the nematic phase, the system is non-chiral with equal probabilities of either states of chirality

possible. At the same time there are chiral fluctuations in time and space which may renormalise the twist elastic constant K_{22} . This is analogous to polar fluctuations in a non-polar nematic renormalising the bend elastic constant K_{33} . When there are chiral fluctuations, the free energy of the corresponding liquid crystal can be expressed as:

$$\begin{aligned} \Delta F = kT\rho_o x_L \ln x_L + kT\rho_o x_R \ln x_R + \frac{1}{2}\rho_o^2 U_{LL} x_L^2 + \frac{1}{2}\rho_o^2 U_{RR} x_R^2 + \\ \rho_o^2 U_{LR} x_R x_L + \mu(x_R - x_L)(\hat{\mathbf{n}} \cdot \nabla \times \hat{\mathbf{n}}) + \frac{1}{2}K_{22}(\hat{\mathbf{n}} \cdot \nabla \times \hat{\mathbf{n}})^2, \end{aligned} \quad (4.1)$$

where ρ_o is the average number density of bent-core molecules, x_R and x_L are the molar fractions of the left and right local chiral states respectively, $(\hat{\mathbf{n}} \cdot \nabla \times \hat{\mathbf{n}})$ is the twist deformation of the nematic director $\hat{\mathbf{n}}$, and μ is the helical twisting power. Here, $U_{LL} = U_{RR} = U$, U_{LR} is the effective coupling constant between local states of equal and opposite handedness respectively, and $\Delta U = U_{LR} - U$ is the chiral discrimination energy. The first two terms in equation 4.1 describe the mixing entropy of the two chiral states and the sixth term describes the linear coupling between the two scalar quantities; the twist deformation $(\hat{\mathbf{n}} \cdot \nabla \times \hat{\mathbf{n}})$ and the difference in molar fractions between the right and left chiral states, defined as $\Delta x = x_R - x_L$. Minimizing the free energy with respect to Δx and assuming $\Delta x \ll 1$, one obtains;

$$\Delta x \cong \frac{2\mu(\hat{\mathbf{n}} \cdot \nabla \times \hat{\mathbf{n}})}{kT\rho_o - \rho_o^2 \Delta U/2}. \quad (4.2)$$

Substituting equation 4.2 back into equation 4.1 one obtains the following expression for the renormalised twist elastic constant;

$$K_{22}^{eff} = K_{22} - \frac{\mu^2}{kT\rho_o - \rho_o^2 \Delta U/2} \equiv K_{22} - \frac{A}{t - t_c}, \quad (4.3)$$

where $A = \mu^2/kT_{NI}\rho_o$ and $t_c = \frac{\rho_o \Delta U}{2kT_{NI}}$ is a critical temperature. The effective twist constant K_{22}^{eff} will become small as long as the second term in equation 4.3 is large. As already mentioned,[58] some conformational states of bent-core molecules are strongly chiral and chiral molecular ensembles may possess even

stronger chirality.[60, 61] This may lead to large values of μ and ΔU , which could be amplified in DT12 by the long terminal alkyl chains. In DT12, the nematic phase occurs ~ 100 °C lower in temperature than VBG93 (see figure 3.1) and other similar oxadiazole-based bent-core liquid crystals,[63] which means that kT is smaller and the difference $kT\rho_o - \rho_o^2\Delta U/2$ in equation 4.3 is further reduced. In this case the negative correction to K_{22} is expected to be strongly temperature dependent, which can lead to an overall weak temperature dependence of K_{22}^{eff} . A characteristic profile of K_{22}^{eff} is presented in figure 4.8 using the profile of the unrenormalised constant K_{22} from reference [56] and assuming for simplicity that $A = A_oS$. It can be shown that K_{22} is very low and practically temperature independent, in agreement with the experimental measurements using these assumptions. The ‘unrenormalised K_{22} ’ is analogous to the ‘bare K_{33} ’ in ref. [56]. It is unlikely that either of these phenomena (larger μ or lower temperature) alone can account for anomalously low K_{22} , but are instead coupled to reduce K_{22} overall.

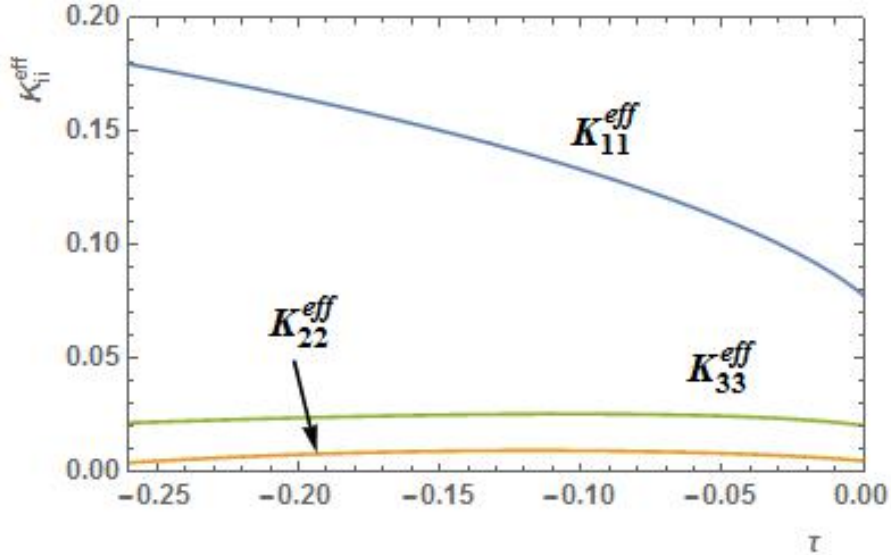


Figure 4.8: Theoretical profiles of the splay K_{11}^{eff} , twist K_{22}^{eff} and bend K_{33}^{eff} elastic constants in DT12, calculated as functions of the reduced temperature. The results shown in this figure take into account the effect of chiral fluctuations and polar interactions of the bent-core molecules. Figure taken from the paper by Srigengan et al.[57]

4.6 Conclusions

To conclude, the splay, twist and bend elastic constants of DT12 have been reported in this chapter. K_{11} was found to be rather high and to exhibit an expected temperature dependence (see figure 4.7), with K_{22} and K_{33} being anomalously small and almost temperature independent throughout the whole nematic phase range. Such unusual, simultaneous behaviour of both the bend and twist constants has not been observed in other bent-core liquid crystals or in other types of thermotropic liquid crystals. The behaviour of the elastic constants has been investigated further using two theoretical approaches: a molecular theory based on atomistic simulations of the real molecular structure of DT12 including its conformations (carried out by Alberta Ferrarini), and an analytical mean-field theory which explicitly takes into account polar intermolecular interactions and chiral fluctuations between bent shaped molecules (carried out by Mikhail Osipov and Grzegorz Pająk).

Atomistic modelling was carried out to calculate the elastic constants of DT12, showing excellent agreement with the experimental data for both K_{22} and K_{33} . Whilst the absolute values of the calculated and experimental results differ for K_{11} , both sets of data exhibit similar temperature dependence. In the context of the qualitative mean-field theory the reduction of K_{33} is related to the existence of the local polar order of bent-core molecules which is linearly coupled to the bend deformation vector. This coupling reduces the free energy and results in a negative correction to the bend constant, which may be sufficiently large for bent-core liquid crystals. The reduction in K_{33} is common in bent-core liquid crystals. However, the results additionally show that in a similar way, the free energy is reduced when the fluctuations in the population of the two local states of the opposite chirality is linearly coupled to the fluctuating twist. This yields a negative correction to K_{22} which may be large if the bent-core nematic possesses strongly chiral local states. The results of the theory have been used to calculate the profiles of the elastic constants, which agree qualitatively with the experimental data shown in figure 4.5.

This new theoretical approach also gives insight into the low values of K_{22} that have been reported for other oxadiazole systems.[63] In that paper by Kaur et al.,

K_{22} took values of ~ 1.2 pN and the temperature dependence was rather weak; a variation from ~ 0.4 - 1.0 pN in VBG93 and from ~ 0.4 - 1.2 pN in the other three considered. This is a weaker temperature dependence than seen for K_{11} which varied by a factor of 4 or 5 across the temperature range for each of the materials. Although the magnitude of the negative correction to K_{22} will depend on the material, the correction always leads to a weaker temperature variation of K_{22} than that of K_{11} in relative terms.

Understanding the mechanisms for the dramatic reduction in the twist elastic constant K_{22} is important. It is widely accepted that a reduction and vanishing of the bend elastic constant K_{33} may induce a transition into the twist-bend phase, which is locally polar. In a similar way vanishing of the twist constant may induce a spontaneous chiral symmetry-breaking when the system is split into macroscopic chiral domains of the opposite handedness, as observed in VBG93 and other oxadiazole based nematic liquid crystals at low temperatures.[31, 61] This may provide a long-awaited explanation of why many similar non-chiral bent-core materials exhibit chiral SmC*-like phases or the dark conglomerate phase, which are also composed of chiral domains.

After coming closer to understanding the interesting elastic behaviour in both pure DT12 and VBG93, it seems logical to investigate whether these low twist and bend elastic constants are still exhibited in liquid crystal mixtures of these two bent-core materials. One can then use the elastic behaviour of the bent-core mixtures to understand the phase behaviour in the mixtures, which will be discussed in chapter 6. Another point of interest is the effect of these low elastic constants in DT12 and VBG93 on the phase behaviour of calamitic liquid crystals; bent-core/calamitic liquid crystal mixtures have been of particular interest for a number of groups,[104–108] but the elastic behaviour of calamitic liquid crystals doped with DT12 or VBG93 have yet to be investigated. The observations and results obtained for these bent-core/calamitic mixtures will be discussed in chapter 7.

The next chapter will provide the elastic constant results measured experimentally for both bent-core mixtures and bent-core/calamitic mixtures, and will discuss the implications of these results on the resulting phase behaviour.

Chapter 5

Elastic Behaviour in Bent-Core Liquid Crystal Mixtures

5.1 Introduction

This chapter will go into detail describing the elastic behaviour in mixtures that include bent-core liquid crystals. This will be detailed in two parts; the first will introduce how the anomalous elastic constants measured in DT12 (given in chapter 4) are affected when DT12 is mixed in various concentrations with VBG93. The second part will show how the elastic constants of calamitic liquid crystals are affected when they are doped with bent-core liquid crystals. This chapter reproduces results in two papers; one that has been published in the Journal of Materials Chemistry C,^[57] and the other that is currently in review. As a result, this chapter largely follows the format and content of these papers. The results for mixtures of DT12 and VBG93 are reproduced from the paper by Srigengan et al., *J. Mater. Chem. C*, **6**, 980, 2018,^[57] whilst the results for the bent-core/calamitic mixtures are reproduced from a paper by Srigengan et al. that is in review.^[109] In both papers the experimental work was carried out mainly by myself, with the elastic behaviour for pure ZLI 1132 and mixture 9 (ZLI 1132 doped with 10% VBG93) being carried out by Harry Liu.^[110] The theoretical work presented at the end of this chapter was carried out by Mikhail Osipov which has been reproduced from the paper that is review.^[109]

With regards to the mixtures of DT12 and VBG93, the main structural differences between DT12 and VBG93 lie in their lateral substitution and terminal chains; the former has asymmetric methoxy- and methyl-substitutions with symmetrical terminal alkyl chains, while the latter has no lateral substituents but asymmetric terminal chains (see figure 5.1). The lateral substitution serves to reduce the temperature at which the nematic phase is exhibited,[59] an important factor if any practical applications of bent-core mesogens are to be realised. As mentioned in chapter 4, mixtures of DT12 and VBG93 were created to find a lower temperature DC phase, and to investigate whether the low twist and bend constants exhibited by DT12 affect the formation of the DC phase. Section 5.2 of this chapter examines the elastic behaviour of the nematic phases in these mixtures of DT12 and VBG93, whilst the underlying phases and resulting phase behaviour will be discussed further in chapter 6. DT12 was found to degrade at temperatures above 180 °C, which is not important for measurements of the pure material as all the mesophase behaviour is below that. For mixtures 1-5, however, all the measurements were constrained to temperatures below 180 °C.

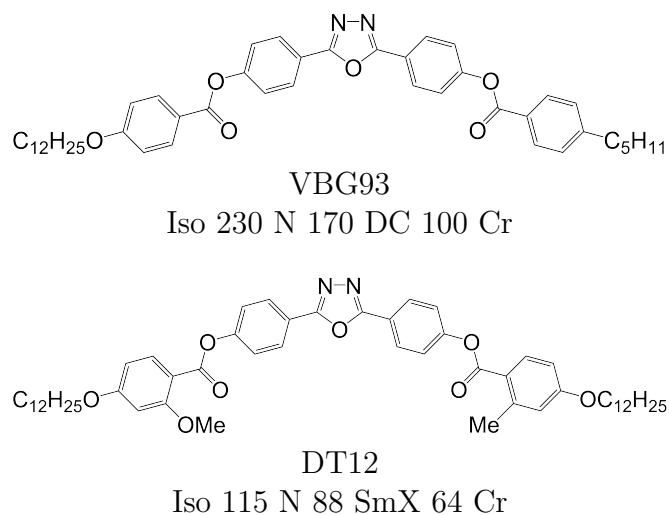


Figure 5.1: Molecular structures and phase transition temperatures for the liquid crystals used in this chapter. Temperatures are recorded in °C.

With regards to the bent-core/calamitic mixtures, two of the calamitic liquid crystals chosen are 5CB and 8CB; both have very well-known elastic behaviour and 8CB exhibits pretransitional divergence of the twist and bend elastic constants close to the smectic A phase. Section 5.3 considers the elastic behaviour in the nematic phases of these bent-core doped liquid crystal mixtures. Section 5.3 also discusses mixtures of the bent-core materials with a broad temperature-range nematic mixture known as ZLI 1132 synthesised by Merck. The underlying phases and resulting phase behaviour exhibited by bent-core doped calamitic mixtures will be discussed further in chapter 7.

It has been shown that the elastic constants are a driving factor in forming more exotic phases, such as the N_{TB} phase[49, 51, 77, 78], the dark conglomerate (DC) phase,[88, 89] and more recently the splay nematic phase, discovered by Mertelj et al., which exhibits low splay and twist values (K_{11} and $K_{33} \sim 2$ pN).[111] Indeed, two of the mixtures described in this chapter (mixtures 6 and 7 in table 5.1) also exhibit unusual behaviour in the nematic phase; filaments form through self-assembly at temperatures below the isotropic-nematic transition. Mixture 6 has already been described by Gleeson et al.[112] to demonstrate interesting rheological and structural properties when the filaments form. The X-ray scattering data in ref. [112] suggests that the filaments form a rectangular columnar structure, similar to that observed in the N_{TB} phase described by Chen et al.,[52] which then evolves into a hexagonal columnar structure. By understanding the behaviour of the elastic constants in the nematic phase of the mixtures, one can also draw conclusions regarding whether the formation of this filament phase is analogous to any of the nematic variant phases. This filament formation will also be discussed in chapter 7.

The next section will introduce the various mixtures of DT12 and VBG93 investigated and will detail the elastic behaviour measured in the nematic phases of these mixtures.

5.2 Mixtures of DT12 and VBG93

5.2.1 Experimental methodology

The molecular structures and phase transition temperatures of the pure bent-core materials used in this chapter are shown in figure 5.1. Transition temperatures of the pure materials and the mixtures were determined by differential scanning calorimetry (DSC) and polarising optical microscopy (POM); the temperatures in table 5.1 were taken from the DSC measurements. Mixtures were made by melting the two pure materials in the same vial, giving time for the samples to mix before cooling back into the crystal phase. The phase diagram of the mixed system is shown in figure 5.2, determined on cooling at a rate of 5 °C/min. The phase diagram shows an approximately linear dependence of all of the phase transitions on concentration. An optically isotropic phase occurs at higher concentrations of VBG93, while a smectic phase is observed at lower concentrations. The phase behaviour of the bent-core mixtures will be discussed in further detail in chapter 6.

Mixture Number	Composition	Phase Transitions T/°C
Mixture 1	10:90 DT12:VBG93	Iso 224 N 164 OI 94 Cr
Mixture 2	25:75 DT12:VBG93	Iso 200 N 144 OI 95 Cr
Mixture 3	50:50 DT12:VBG93	Iso 190 N 140 SmX 90 Cr
Mixture 4	70:30 DT12:VBG93	Iso 170 N 117 SmX 80 Cr
Mixture 5	90:10 DT12:VBG93	Iso 140 N 100 SmX 70 Cr

Table 5.1: Compositions of the bent-core mixtures used in this chapter with the corresponding phase transitions and transition temperatures determined on cooling. The elastic constants of the pure materials and the mixtures are all given in the results section.

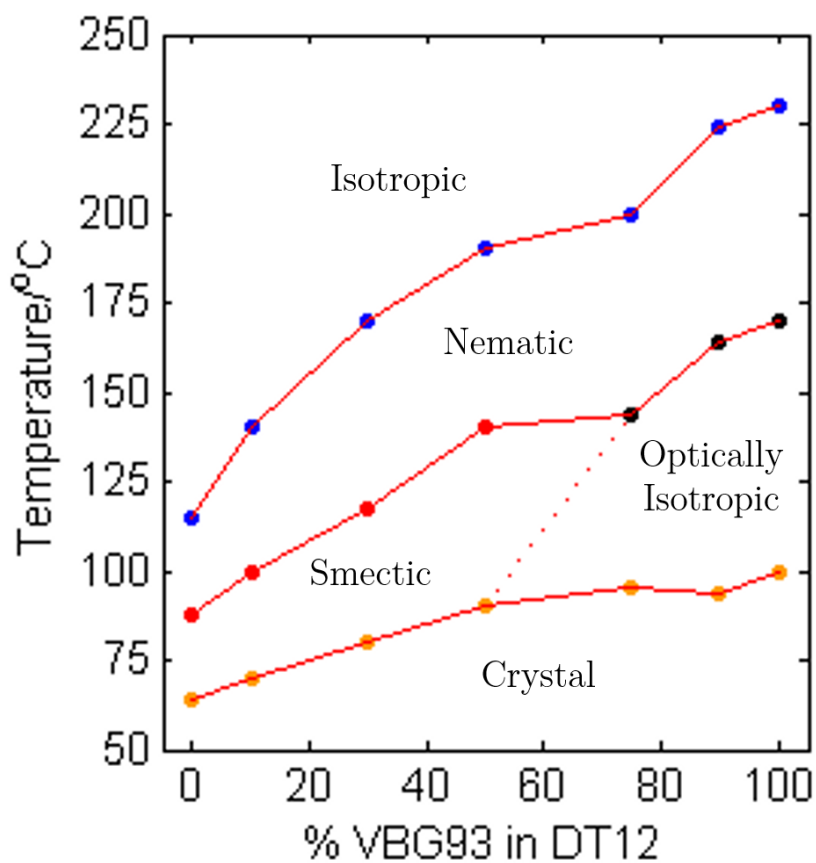


Figure 5.2: The phase diagram of mixtures of DT12 and VBG93. The blue points mark the isotropic to nematic transition, the red points represent the transition from the nematic to an unknown smectic phase, the black points represent the transition from a nematic to an optically isotropic phase, and the orange data points represent the transition from the mesophase to crystal phase. In the case of VBG93, the optically isotropic phase is the DC phase.

The electrical and electro-optic measurements for mixtures 1-5 were carried out using the same types of devices and same methodology that were used for pure DT12, described in section 4.2 in chapter 4. Mixtures 1-5 exhibited a negative dielectric anisotropy and thus homeotropic aligned devices were used to measure K_{11} and K_{33} , whilst IPS devices (with rubbing parallel to the electric field) were used to measure K_{22} . All devices were 5 μm thick. The equations used to measure the elastic constants are repeated below for clarity;

$$V_{th}^{K_{33}} = \pi \sqrt{\frac{K_{33}}{\varepsilon_0 |\Delta\varepsilon|}}, \quad (\text{equation 3.5})$$

$$K_{11} = \frac{2\pi dn_o \nu K_{33}}{\lambda m V_{th}^{K_{33}}}, \quad (\text{equation 3.10})$$

$$V_{th}^{K_{22}} = \frac{\pi l}{d} \sqrt{\frac{K_{22}}{\varepsilon_0 |\Delta\varepsilon|}}. \quad (\text{equation 3.12})$$

where $\nu = (n_e^2 - n_o^2)/n_e^2$.

5.2.2 Results of mixtures of DT12 and VBG93

Figure 5.3 shows the dielectric anisotropy as a function of $T-T_{NI}$ for the mixtures together with values for the pure compounds as a reference, assuming an uncertainty of ± 0.5 in $\Delta\varepsilon$. It can be seen that $\Delta\varepsilon$ for the mixtures is always relatively small and negative and generally lies in between the values measured for the two pure compounds, as might be expected. The elastic constant values are shown in figure 5.4 and are shown separately to provide a clear view of the relationship with $T-T_{NI}$.

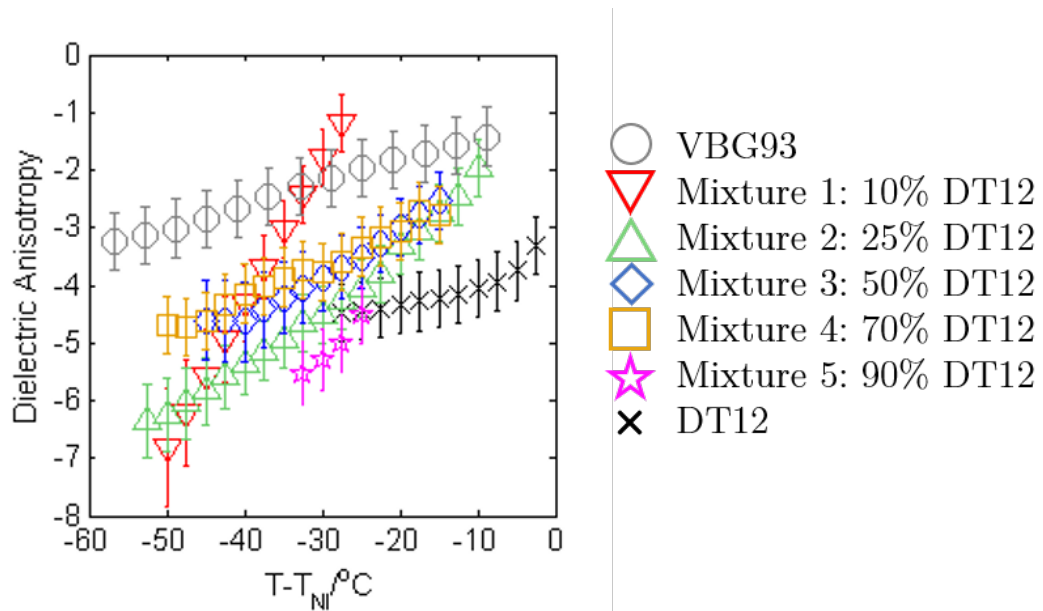


Figure 5.3: Dielectric anisotropy, $\Delta\epsilon$ as a function of $T - T_{NI}$ for DT12, VBG93, and mixtures 1-5. As mentioned earlier in the chapter, the mixtures were constrained to temperatures below 180 °C which explains why some datasets begin at lower temperatures.

5.2 Mixtures of DT12 and VBG93

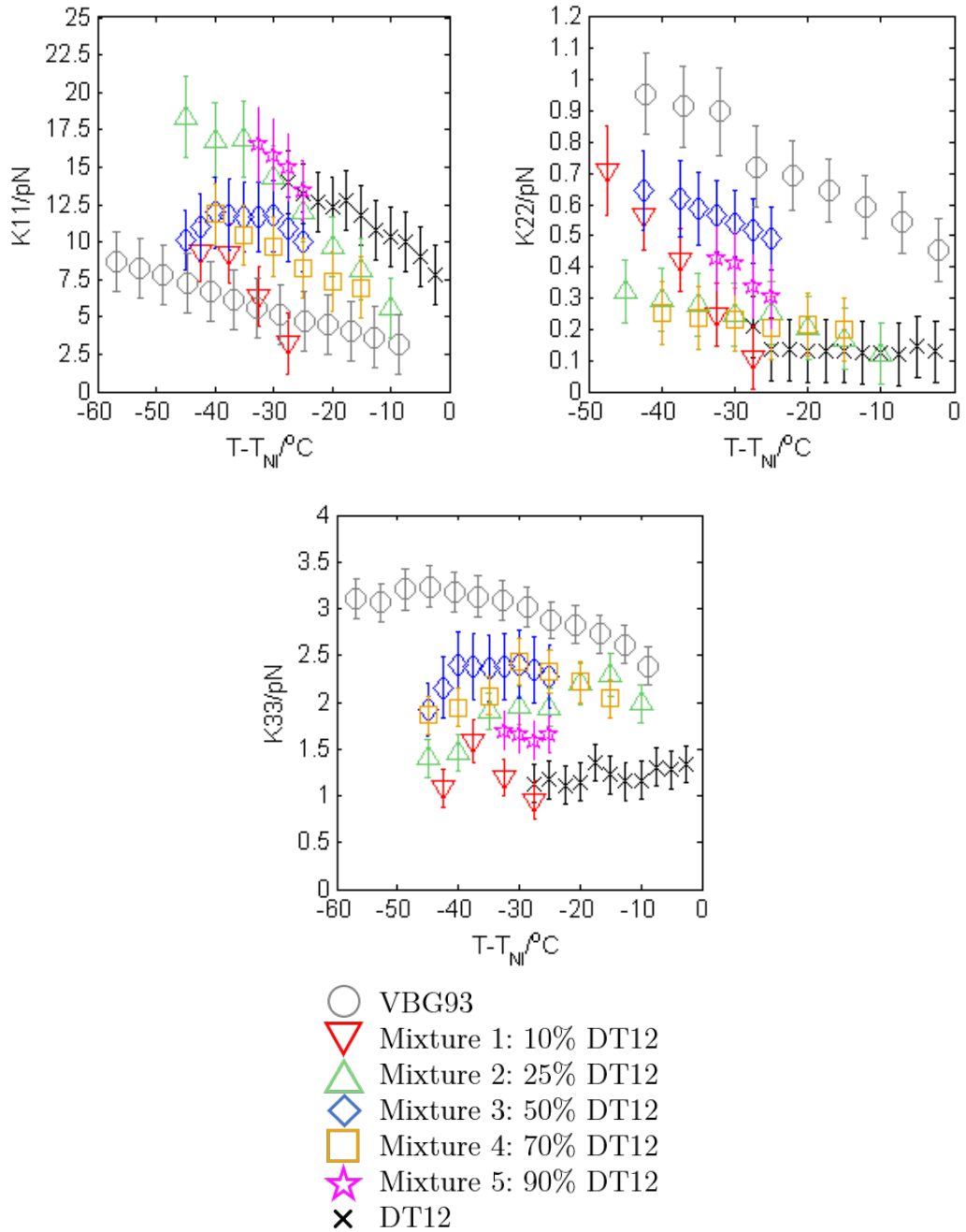


Figure 5.4: The splay, K_{11} (a), twist, K_{22} (b) and bend, K_{33} (c) elastic constants as a function of $T - T_{NI}$ for DT12, VBG93, and mixtures 1-5.

As one would expect, all of the measurements of physical properties of the mixtures (dielectric anisotropy and elastic constants) lie between the values measured for pure DT12 and VBG93. However, the differences in absolute values across the mixture set are relatively small and this fact, together with the relatively large uncertainties in the measurements means that there isn't an experimentally significant difference between each data set. Nonetheless, it can be said that the splay elastic constant, K_{11} , of the mixtures follow a similar temperature dependence to that of the pure materials; the magnitude increases as the temperature increases (see figure 5.4). For the twist elastic constant K_{22} , where the temperature dependence is practically non-existent in DT12, we see more of a temperature dependence of K_{22} as more VBG93 is added to the mixture. For the bend elastic constant K_{33} , where the values for the pure compounds were deemed to be effectively temperature independent, the values measured for the mixtures show a similar temperature independence.

The results show that the very small and temperature-independent values of the bend and twist elastic constants measured for DT12 are reproduced in mixtures with a high proportion of DT12.

5.2.3 Discussion of mixtures of DT12 and VBG93

The results shown in figure 5.4 indicate that if the two bent-core materials are mixed, the values of the elastic constants lie in between the respective values of the pure bent-core liquid crystals. There does not seem to be any distinct behaviour in the elastic constants in the nematic phases of the mixtures which indicate whether the underlying phase is smectic or OI. The standard theoretical elastic approach predicts that the saddle-splay elastic constant $K_{24} \leq 2K_{11} + K_{22}$, or $K_{24} < K_{22}$, whichever is smaller.[113–115] The results from figure 5.4 suggest that only the second inequality applies, as K_{22} is small in the pure bent-core liquid crystals and for all the mixtures. The lower K_{22} values are exhibited by DT12 and mixtures with a larger percentage of this mesogen in the mixtures. However these samples do not exhibit a DC/OI phase, whilst VBG93 and mixtures 1 and 2 do. Interestingly, mixture 2 and 3 exhibit similar behaviour (within error) for all three elastic constants in the nematic phase, yet mixture 2 exhibits an underlying

5.3 Bent-Core and Calamitic Liquid Crystal Mixtures

OI phase and mixture 3 exhibits an underlying smectic phase. Clearly some other mechanism for driving the formation of the DC/OI phase is at play, and this will be discussed further in chapter 6 using small angle X-ray scattering data to determine the nature of the underlying OI and smectic phases in the mixtures.

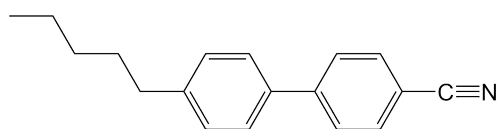
Next, I will introduce mixtures of calamitic liquid crystals doped with 10% of DT12 or VBG93. The next section will detail the elastic behaviour measured in these mixtures, carried out by myself and Harry Liu, along with a theoretical explanation to the corresponding results, carried out by Mikhail Osipov. The following work has been reproduced from the publication by Srigengan et al.[109]

5.3 Bent-Core and Calamitic Liquid Crystal Mixtures

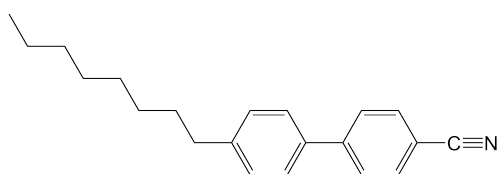
5.3.1 Experimental methodology

The calamitic liquid crystals used in this section are 5CB and 8CB; their molecular structures and phase transition temperatures are shown in figure 5.5. The bent-core liquid crystals used to dope calamitic liquid crystals were DT12 and VBG93; their molecular structures and phase transition temperatures can be found in figure 5.1 earlier in this chapter. In addition to the pure materials, a nematic mixture, ZLI 1132 was also used. ZLI 1132 is a Merck mixture that is nematic at room temperature, with a nematic to isotropic transition temperature of $T_{NI} = 71.2$ °C. The transition temperatures of the pure materials and the mixtures were determined by differential scanning calorimetry (DSC) and confirmed using polarising optical microscopy (POM); the temperatures of the mixtures in table 5.2 were taken from the DSC measurements. Mixtures were made by dissolving the pure compounds in a vial using dichloromethane (DCM) before allowing the DCM to evaporate completely at a temperature of 50 °C. Figure 5.6 shows a graphical representation of the transition temperatures for all mixtures from table 5.2.

5.3 Bent-Core and Calamitic Liquid Crystal Mixtures



5CB
Iso 35 N 18 Cr



8CB
Iso 40 N 33.5 SmA 21.5 Cr

Figure 5.5: Molecular structures and phase transitions temperatures for the liquid crystals used in this chapter. Temperatures are recorded in °C.

Mixture Number	Composition	Phase Transitions T/°C
Mixture 6	10:90 VBG93:5CB	N+F 40.5 I+F 51.8 Iso
		Iso 49.0 N 26.1 N+F
Mixture 7	10:90 VBG93:8CB	SmA+F 36.0 N+F
		45.6 I+F 60.1 Iso
		Iso 52.0 N 40.0 N+F 38.4 SmA+F
Mixture 9	10:90 VBG93:ZLI 1132	N 80.7 Iso
		Iso 84.9 N
Mixture 10	10:90 DT12:5CB	Iso 42.0 N
Mixture 11	10:90 DT12:8CB	Iso 46.3 N 29.8 SmA
Mixture 12	10:90 DT12:ZLI 1132	Iso 72.5 N

Table 5.2: Compositions of mixtures used in this chapter with the corresponding phase transitions and transition temperatures determined on cooling. The elastic constants of the pure materials and the mixtures are all given in the results section.

5.3 Bent-Core and Calamitic Liquid Crystal Mixtures

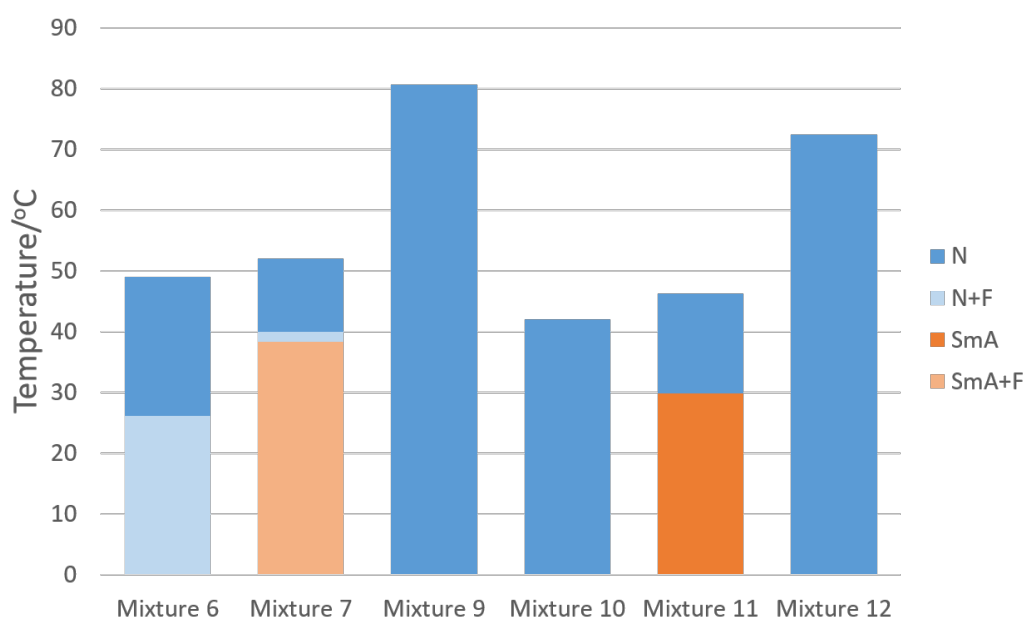


Figure 5.6: Histogram showing the phase transitions with the transition temperatures on cooling for the mixtures discussed in this chapter. Everything above the bars indicates the isotropic phase, with the dark blue bars representing the nematic phase, the light blue bar representing the nematic phase with filaments, the orange bars representing the smectic A phase and the light orange bar representing the smectic A phase with filaments.

5.3 Bent-Core and Calamitic Liquid Crystal Mixtures

As mentioned earlier in this chapter, mixtures 6 and 7 (5CB and 8CB respectively doped with 10% VBG93) exhibited the formation of filaments at temperatures below T_{NI} . Gleeson et al.[112] reported that the filaments caused the system to become very viscous; the complex viscosity was measured to be $\sim 3.12 \times 10^7$ mPas at 25 °C in mixture 6, compared to pure 5CB which normally exhibits a complex viscosity of ~ 100 mPas at the same temperature. To avoid this regime of high viscosity, the measurements were taken in the nematic phases of the mixtures with the experiment completed before the filaments were observed to grow. The mechanism of this filament formation and the resulting phase behaviour will be looked at in further detail in chapter 7.

This mixtures discussed in this section all exhibited a positive dielectric anisotropy, and thus measurements of the dielectric anisotropy $\Delta\varepsilon$ were carried out using the voltage run method, as described in section 3.5 in chapter 3. The perpendicular component of the dielectric permittivity ε_{\perp} was measured at voltages well below the threshold voltage V_{th} , whilst the parallel component ε_{\parallel} was measured at voltages well above V_{th} . The dielectric anisotropy was then calculated using equation 3.3 (repeated below for clarity). The elastic constants K_{11} and K_{33} were measured using the dielectric method described in section 3.6.2 in chapter 3. A fit was applied to the ε - V_{RMS} curve using equation 3.11 from which the threshold voltage $V_{th}^{K_{11}}$ and the gradient of the step section of the graph were calculated. Using these two parameters K_{11} and K_{33} were measured, analogous to the optical method described in section 3.6.1 in chapter 3. K_{22} for the mixtures was measured optically by measuring the optical Fréedericksz transition in an IPS device, and obtaining the threshold voltage $V_{th}^{K_{22}}$. K_{11} , K_{22} and K_{33} were calculated using equations 2.8, 3.11, 3.12 (repeated here for clarity);

$$\Delta\varepsilon = \varepsilon_{\parallel} - \varepsilon_{\perp}, \quad (\text{equation 3.3})$$

$$V_{th}^{K_{11}} = \pi \sqrt{\frac{K_{11}}{\varepsilon_0 |\Delta\varepsilon|}}, \quad (\text{equation 2.8})$$

$$\frac{V}{V_{th}^{K_{11}}} = 2\pi^{-1} (1 + \gamma \sin^2 \phi_m)^{1/2} \int_0^{\pi/2} \left(\frac{F_k}{F_{\zeta} F_{\gamma}} \right)^{1/2} d\phi, \quad (\text{equation 3.11})$$

5.3 Bent-Core and Calamitic Liquid Crystal Mixtures

$$V_{th}^{K_{22}} = \frac{\pi l}{d} \sqrt{\frac{K_{22}}{\varepsilon_0 |\Delta\varepsilon|}}. \quad (\text{equation 3.12})$$

where $F_k(\phi) = 1 + k \sin^2(\phi_M)$, $F_\zeta(\phi) = 1 - \sin^2(\phi_M)$, $F_\gamma(\phi) = 1 + \gamma \sin^2(\phi_M)$, $k = (K_{11}/K_{33}) - 1$, $\gamma = (\varepsilon_\perp/\varepsilon_\parallel) - 1$, ϕ_M is the director angle in the centre of the liquid crystal layer,[35] d is the thickness of the device, and l is the electrode spacing of the IPS device. This methodology allowed K_{11} and K_{33} to be deduced with an accuracy of $\sim 5\%$, and K_{22} with an accuracy of $\sim 20\%$. Flexoelectric contributions were not taken into account for these measurements.

5.3.2 Results of mixtures of calamitic and bent-core mesogens

Due to the three different host calamitic liquid crystals used to make the mixtures, it is appropriate to compare mixtures with the same host liquid crystal. Thus, the following results section will be discussed in three parts; the first will compare the mixtures of 5CB, whilst the second and third will do so for mixtures of 8CB and ZLI 1132 respectively.

5.3.2.1 5CB mixtures; mixtures 6 and 10

The dielectric anisotropy, $\Delta\varepsilon$ of mixtures 6 and 10 increased as the temperature decreased, as seen in figure 5.7. The mixtures exhibited reduced $\Delta\varepsilon$ values ($\sim 10\%$) with respect to 5CB,[116, 117] due to the negative dielectric anisotropy of the bent-core mesogens,[57, 62, 63] varying between ~ 6 -12 in mixtures 6 and 10 compared to ~ 8.5 -12.5 in 5CB. Figure 5.7 shows that the datasets for each bent-core dopant can be considered to be within error of each other. Figure 5.8a, b, and c respectively show the values of the splay, twist and bend elastic constants measured for DT12,[57] VBG93[62, 63] and mixtures 6 and 10.

5.3 Bent-Core and Calamitic Liquid Crystal Mixtures

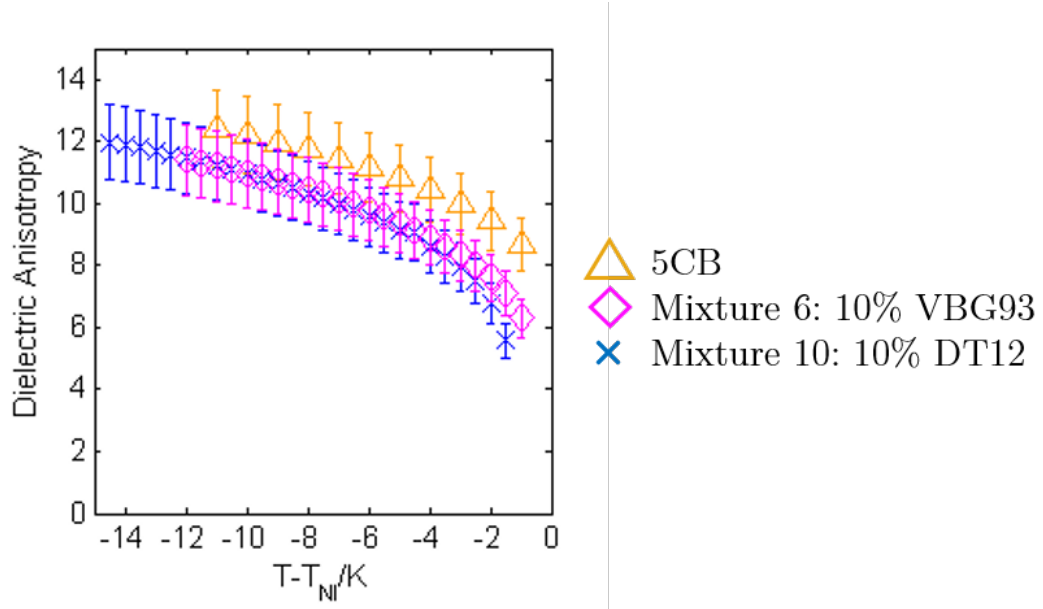


Figure 5.7: Dielectric anisotropy, $\Delta\epsilon$ as a function of $T-T_{NI}$ for 5CB, mixture 6 and 10.

All three plots in figure 5.8 show that the temperature dependence of the elastic constants is retained when 5CB is doped with the bent-core mesogens. Interestingly, figure 5.8a shows that the mixtures exhibit no difference in their values of the splay constant with respect to 5CB; K_{11} varies from ~ 1.5 - 6.5 pN. This set of results is surprising given that DT12 exhibits much higher K_{11} values (~ 8 - 12 pN) compared to VBG93 (~ 3 - 4 pN), yet there is no difference in the values of K_{11} that mixtures 6 and 10 exhibit. In contrast to figure 5.8a, figure 5.8b and c show that the mixtures exhibit a decrease in values of the twist and bend constants with respect to 5CB. The values measured vary between ~ 2 - 4 pN and ~ 4 - 10 pN for K_{22} and K_{33} in 5CB, to ~ 1 - 3.5 pN and ~ 2 - 9 pN for K_{22} and K_{33} in mixtures 6 and 10. It can also be seen that the K_{33} values for mixtures 6 and 10 are practically identical across the temperature range measured. However there is insufficient evidence to suggest that mixture 6 and 10 exhibit different values for K_{22} due to the errors assigned to the data points. Thus it can be stated that mixtures 6 and 10 exhibit K_{22} values that are similar within error.

5.3 Bent-Core and Calamitic Liquid Crystal Mixtures

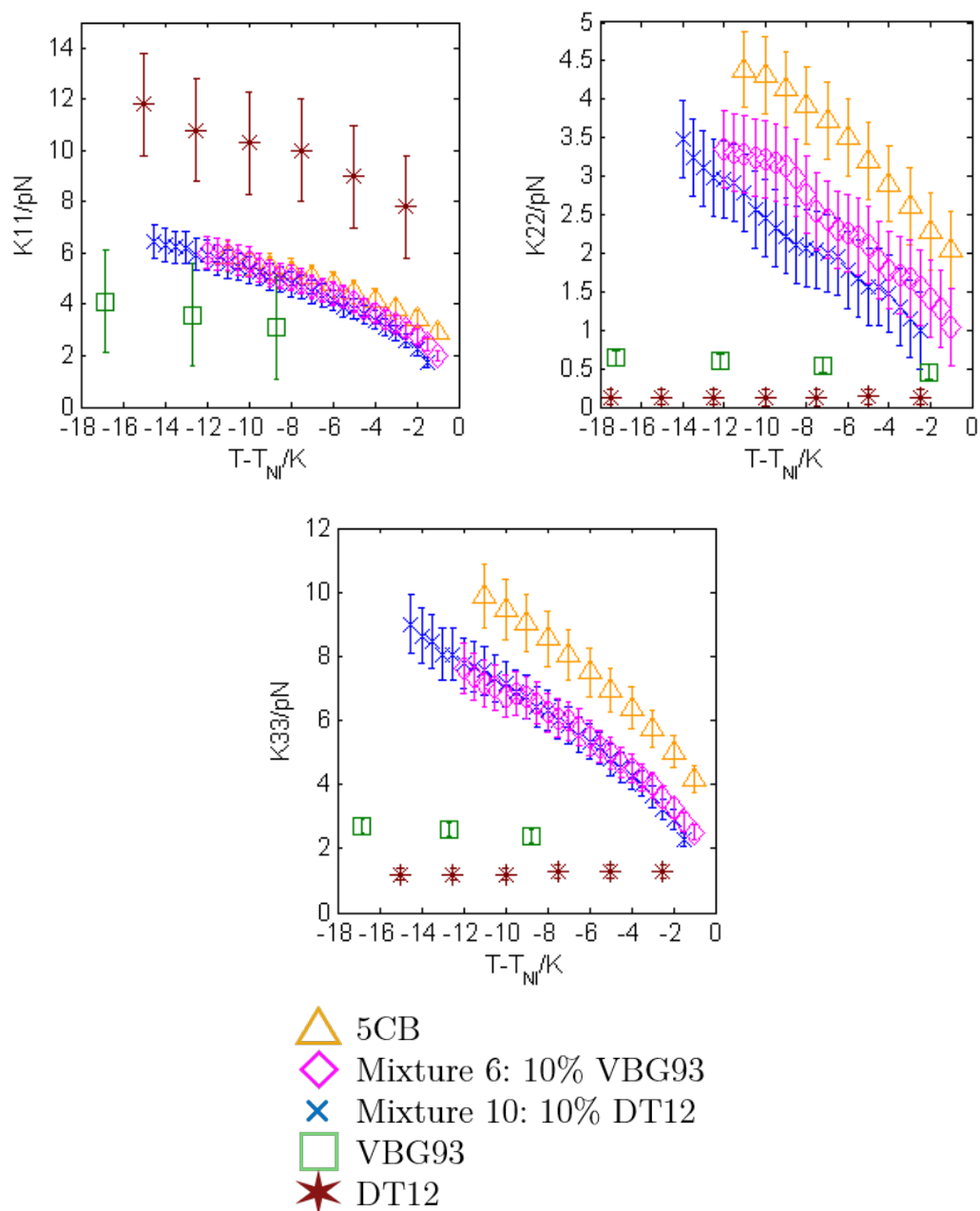


Figure 5.8: The splay, K_{11} (a), twist, K_{22} (b) and bend, K_{33} (c) elastic constants as a function of $T - T_{NI}$ for DT12, VBG93, 5CB, and mixtures 6 and 10.

5.3 Bent-Core and Calamitic Liquid Crystal Mixtures

In summary, it can be seen that when 5CB is doped with 10% of DT12 or VBG93 only the K_{22} and K_{33} values are reduced with respect to 5CB by $\sim 30\%$ and $\sim 20\%$ respectively. There is no change in the temperature dependence of all three elastic constants, and both mixtures 6 and 10 exhibit elastic constant values that are practically indistinguishable from each other.

The next section will present the elastic behaviour exhibited by mixtures of 8CB.

5.3.2.2 8CB mixtures; mixtures 7 and 11

The values measured for $\Delta\varepsilon$ for mixtures 7 and 11 (shown in figure 5.9) are lower than those measured for pure 8CB, the latter of which exhibits $\Delta\varepsilon$ values varying between ~ 6 and 8.5. However, while mixture 6 and 10 were indistinguishable in their values of $\Delta\varepsilon$, here mixture 7 exhibits an apparently lower dielectric anisotropy with respect to mixture 11, varying between ~ 4 -7 in mixture 7 and ~ 6 -8.5 in mixture 11 across the temperature range measured. However, as with figure 5.7, the datasets can be considered to be within error of each other.

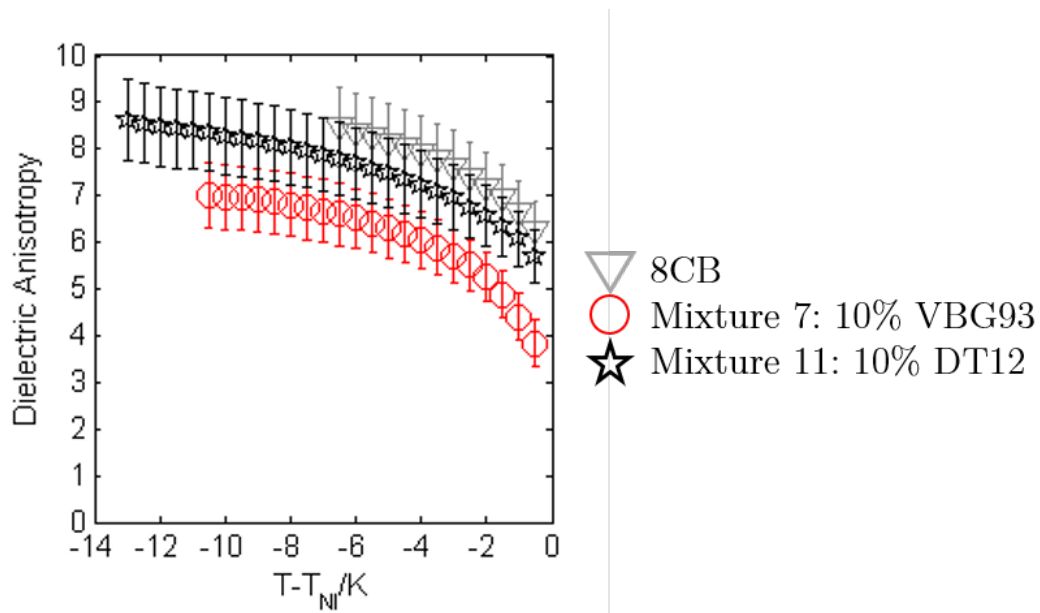


Figure 5.9: Dielectric anisotropy, $\Delta\varepsilon$ as a function of $T - T_{NI}$ for 8CB, and mixtures 7 and 11.

5.3 Bent-Core and Calamitic Liquid Crystal Mixtures

The values of K_{11} , K_{22} and K_{33} as a function of $T-T_{NI}$ are shown in figure 5.10a, b and c respectively for 8CB, DT12, VBG93, and mixtures 7 and 11. It can be seen from all three plots in figure 5.10 that mixtures 7 and 11 not only exhibit elastic constant values lower than pure 8CB, but they also don't quite follow the same temperature dependence as 8CB. In 8CB one would expect to observe a divergence of the twist and bend elastic constants as the smectic A (SmA) transition is approached. This is clearly seen in the K_{33} measurements for 8CB in figure 5.10c but is less obvious for K_{22} (figure 5.10b). The divergence of K_{33} is retained in mixture 11 but occurs at a lower reduced temperature as the nematic phase has been broadened in the mixture and the SmA phase occurs at a lower temperature. It may seem as if the divergence is lost in mixture 7, however filament growth occurs in this system at lower temperatures which prevents the measurement of elastic constants at lower reduced temperatures where the critical divergence would be expected.

In all three plots in figure 5.10, mixture 7 exhibits similar elastic constants (within error) with respect to mixture 11. With respect to 8CB, figure 5.10a shows that K_{11} for mixtures 7 and 11 are both effectively unchanged with respect to 8CB, figure 5.10b shows $\sim 40\%$ reduction in K_{22} , and figure 5.10c shows $\sim 15\%$ reduction in K_{33} . K_{33} in mixture 7 increases up to ~ 20 pN as the SmA transition is approached, reflecting the critical divergence phenomenon. The large change in K_{22} ($\sim 40\%$) when 8CB is doped with the bent-core mesogens is especially dramatic when compared to the behaviour in mixtures 6 and 10. Such a dramatic reduction in K_{22} in bent-core/calamitic mixtures has not been previously reported and is discussed further later.

5.3 Bent-Core and Calamitic Liquid Crystal Mixtures

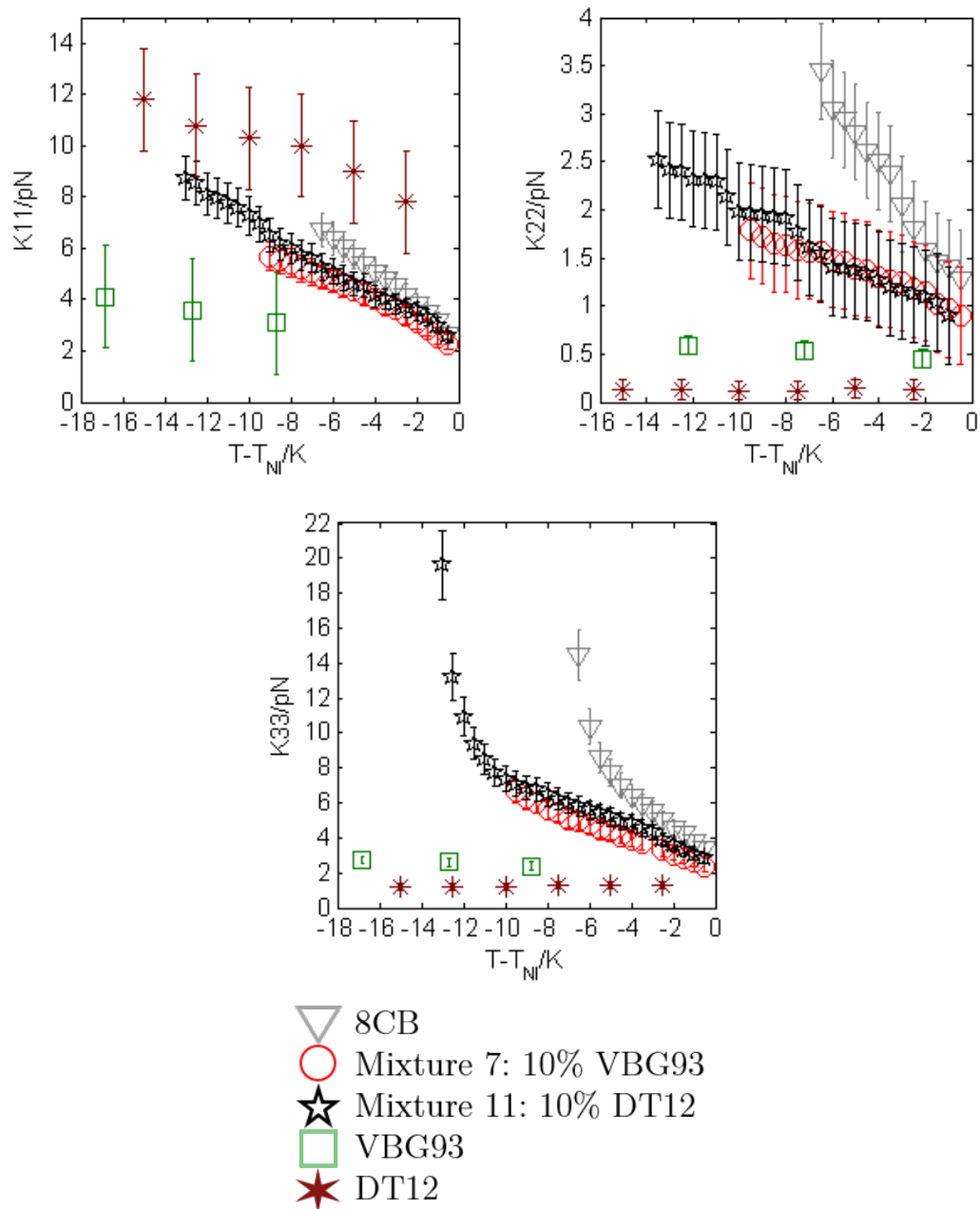


Figure 5.10: The splay, K_{11} (a), twist, K_{22} (b) and bend, K_{33} (c) elastic constants as a function of $T - T_{NI}$ for DT12, VBG93, 8CB, and mixtures 7 and 11.

5.3 Bent-Core and Calamitic Liquid Crystal Mixtures

In summary, when 8CB is doped with 10% of DT12 and VBG93 a different temperature dependence is observed for all elastic constants with respect to that of 8CB. Whilst the divergence of K_{33} at lower temperatures (approaching the SmA phase) was maintained in mixture 11, it was not measured in mixture 7 due to filament growth. The absolute values of the elastic constants are lower in the mixtures with respect to 8CB, with K_{22} being reduced the most, by $\sim 40\%$ compared to 8CB.

Next I present the elastic behaviour exhibited by mixtures of the bent-core compounds with the Merck mixture ZLI 1132. As mentioned at the beginning of this chapter, the elastic behaviour for pure ZLI 1132 and mixture 9 was investigated by Harry Liu,[109, 110] whilst the elastic behaviour for DT12, VBG93, and mixture 14 was investigated by myself.

5.3.2.3 ZLI 1132 mixtures; mixtures 9 and 12

The values of K_{11} , K_{22} and K_{33} as a function of $T-T_{NI}$ are shown in figure 5.11a, b and c respectively for ZLI 1132, VBG93, DT12 and mixtures 9 and 12. It can be seen from all three plots in figure 5.11[109] that mixtures 9 and 12 exhibit lower K_{22} and K_{33} values with respect to ZLI 1132. The K_{11} values exhibited by ZLI 1132, and mixtures 9 and 12 can be considered to be similar within error. The temperature dependence for all three elastic constants can be considered to have been maintained in the mixture compared with ZLI 1132.

Figure 5.11a shows that K_{11} varies from ~ 3 -10 pN in mixtures 9 and 12 compared to ~ 3 -10 pN in ZLI 1132. Figure 5.11b shows that K_{22} varies from ~ 1 -6 pN in mixtures 9 and 12 compared to ~ 0.5 -10.5 pN in ZLI 1132. Figure 5.11c shows that K_{33} varies from ~ 4 -15 pN in mixtures 9 and 12 compared to ~ 4.5 -20 pN in ZLI 1132. In summary, the changes in the elastic constants with respect to ZLI 1132 are negligible for K_{11} , approximately 40% for K_{22} and $\sim 10\%$ for K_{33} . Again, the dramatic reduction in K_{22} is especially noteworthy.

5.3 Bent-Core and Calamitic Liquid Crystal Mixtures

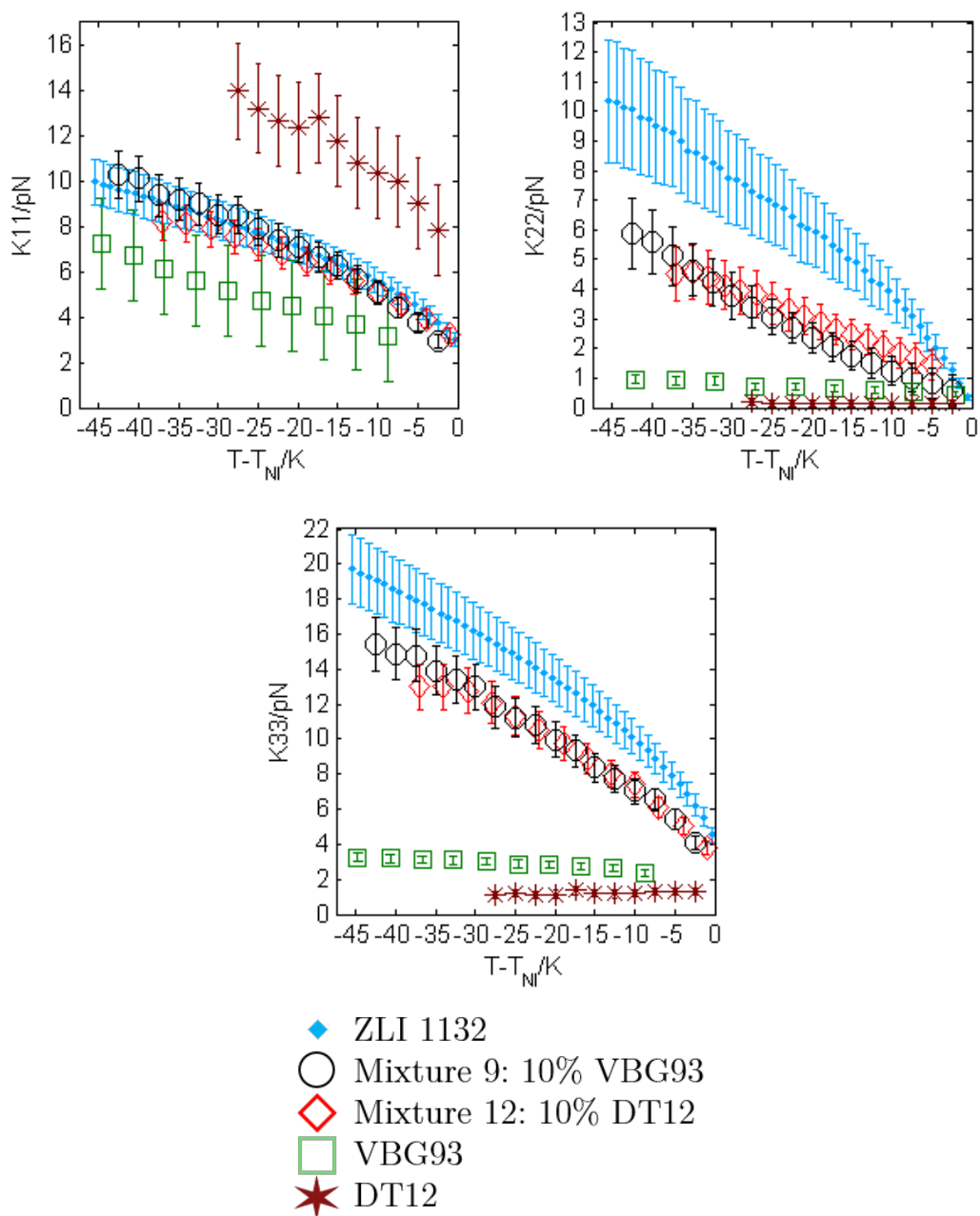


Figure 5.11: The splay, K_{11} (a), twist, K_{22} (b) and bend, K_{33} (c) elastic constants as a function of $T - T_{NI}$ for DT12, VBG93, ZLI 1132, and mixtures 9 and 12.[109]

5.3.3 Discussion of mixtures of calamitic and bent-core mesogens

There are marked similarities in the behaviour of all of the mixtures studied in this section. The first, perhaps surprising result is that the splay elastic constant, K_{11} is essentially unaffected by doping up to 10% of bent-core material into calamitic liquid crystals. Indeed, in the systems chosen here, one bent-core material exhibited relatively low (VBG93) and the other relatively high values (DT12) of K_{11} but no difference was observed in the splay elastic constants of any of the mixtures with respect to the host calamitic. On the other hand, both the twist and bend behaviour are significantly altered in the mixtures to some degree.

Reductions in K_{33} in bent-core/calamitic mixtures are well known and have already been reported by a number of other groups. Kundu et al.[118] doped 8OCB with a bent-core mesogen referred to as BC12[119] and reported that K_{33} reduced from $\sim 6-50$ pN in 8OCB to $\sim 2.5-4$ pN in a 11:89 BC12:8OCB mixture. Sathyanarayana et al.[120] doped 5CB with a bent-core mesogen[121] and measured K_{33} to decrease from $\sim 3.5-9$ pN in 5CB to $\sim 1.5-3.5$ pN when they added 12% of the bent-core mesogen to 5CB. Parthasarathi et al.[108] made a number of binary mixtures of CB7CB, which exhibits a twist bend (N_{TB}) phase, with 7OCB. When 7OCB was doped with 10% of CB7CB, K_{33} was found to reduce from $\sim 3-3.5$ pN in 7OCB to $\sim 0.5-2$ pN in the mixture. Whilst this section also discusses reductions in K_{33} in the mixtures, it provides detail on how K_{22} is reduced in the mixtures. K_{11} is shown to be unaffected by the inclusion of the bent-core mesogen, something also reported by the aforementioned groups.

An explanation for the reductions in the twist and bend elastic constants is given in the next section by considering the theory of the elastic constants. It also details an explanation for the interesting result of K_{11} being unaffected by the doping of the host liquid crystal with bent-core mesogens. This theoretical work was carried out by Mikhail Osipov.[109]

5.3.4 Theoretical Insight

It was explained in section 4.5 of chapter 4 how theoretically low K_{22} and K_{33} values can be exhibited by pure bent-core nematic liquid crystals, by considering the influence of spontaneous chirality and polarity. This section aims to build on that theory by considering the interesting elastic behaviour exhibited by the doped calamitic mixtures introduced in this chapter; namely the large reduction (up to $\sim 40\%$) in K_{22} when the calamitic liquid crystals are doped with 10% of bent-core mesogen.

The influence on the bend constant and the dramatic effect on the twist constant can be explained as follows. Note first that some time ago it was observed that the cholesteric pitch in a calamitic compound became shorter when doped with a relatively small amount of achiral bent-core molecules.[58] At first sight such behaviour is counter-intuitive and was explained by the twist deformation inducing some deracemisation in the system of bent-core conformers which then contributes to the total helical twisting power. However, it is now clear that the same chiral conformers also reduce the twist elastic constant.[57] Thus, the increase of the inverse pitch, $1/p = \lambda/K_{22}$ in ref. [58] is due to two factors; the increase of the helical twisting power (proportional to λ) due to the chiral conformers of the bent-core molecules, and an additional reduction of K_{22} also due to the conformers.

Next consider the influence of the dopants on the elastic constants of a nematic material. To a first order approximation, the elastic constant of a binary mixture of bent-core and calamitic nematic can be expressed as:[109]

$$K = x_c^2 K_c + 2x_c x_b K_{bc} + x_b^2 K_b, \quad (5.1)$$

where x_b and x_c are the molar fractions of bent-core and calamitic molecules, respectively. Here K_b and K_c are the elastic constants of pure bent-core and calamitic nematic materials, respectively, and K_{bc} is determined by interactions between calamitic and bent-core molecules and is generally different from either K_b or K_c .

5.3 Bent-Core and Calamitic Liquid Crystal Mixtures

Note that in the case where 10% of bent-core molecules are added, as in the experiments described in this section, x_b^2 is of the order of 10^{-2} and can be neglected unless K_b is very large, In fact, for these systems, all K_b are smaller than the corresponding K_c (except for the splay elastic constant of DT12). Thus the last term in equation 5.1 can be neglected for all twist and bend elastic constants. Taking into account that $x_b + x_c = 1$ the elastic constant of the mixture can be expressed in terms of x_b only. Neglecting again the quadratic terms (in x_b) one obtains approximately;

$$K = K_c + 2x_b(K_{bc} - K_c). \quad (5.2)$$

Thus, it is the second term in equation 5.2 which determines the deviation of the elastic constant of the mixtures from those of the pure calamitic host. Assuming that $K_{bc} - K_c$ is of the order of K_c and x_b is of the order of 0.1, one concludes that K_c can be reduced by the order of 10-20%, offering a crude estimate of the expected influence of the dopant in the bent-core/calamitic mixtures presented in this section.

In the above argument, everything depends on K_{bc} which should be sensitive to the structure of both calamitic and bent-core molecules. One may assume that for the splay constant, K_{bc} is close in value to K_c and then the reduction is small, as seen experimentally. In contrast, for bend the corresponding difference between K_{bc} and K_c may be significant and then one can explain the experimentally observed reduction in K_{33} of about 15% in all of the mixtures. However, it is hard to explain the 40% reduction of K_{22} using these arguments. Indeed, all elastic constants are positive and hence, according to 5.2, the maximum reduction is achieved when K_{bc} is much smaller than K_c . If we set K_{bc} to zero for simplicity, then one obtains $K = K_c - 2x_bK_c$, which results in a reduction of $\sim 20\%$.

Clearly, some contribution is missing and one can consider the fluctuations in polar and chiral conformers which also cause very low elastic constants of the pure bent-core materials. Unfortunately, the corresponding corrections from such contributions are very small as they are proportional to x_b^2 . Further, the bend

5.3 Bent-Core and Calamitic Liquid Crystal Mixtures

vector \mathbf{B} and the splay vector \mathbf{S} induce a local polarisation \mathbf{P} and hence there are additional terms in the free energy to be considered;[47, 57]

$$e_1\mathbf{P} \cdot \mathbf{S} + e_3\mathbf{P} \cdot \mathbf{B} + \frac{1}{2}AP^2, \quad (5.3)$$

where the last positive term is the dielectric energy (A is an arbitrary constant). Minimisation with respect to \mathbf{P} yields the standard flexoelectric polarisation $\mathbf{P} = Ae_1\mathbf{S} + Ae_3\mathbf{B}$. Substituting this back into the free energy, one obtains the negative corrections to the elastic constants considered in the paper by Srigengan et al.,[57] i.e. $-\frac{1}{2}Ae_1S^2 - \frac{1}{2}Ae_3B^2$.

However, that paper[57] referred to pure compounds and for this work one must consider how e_1 and e_3 depend on molar fractions. Consider for simplicity the case of perfect orientational order. In this case bent-core molecules, which possess only transverse electric and steric dipoles, contribute only to the bend polarisation, i.e. $e_3 = e_3^0 \times b$ (where b is the number of bent-core molecules). Polar calamitic molecules contribute only to the splay polarisation and hence $e_1 = e_1^0 \times c$ (where c is the number of calamitic molecules). Thus, one obtains the following corrections to the splay and bend elastic constants;

$$\begin{aligned} \text{Splay:} \quad & -\frac{1}{2}x_c^2Ae_1^0 = -\frac{1}{2}Ae_1^0 + 2x_b\frac{1}{2}Ae_1^0 - x_b^2Ae_1^2 \\ \text{Bend:} \quad & -x_b^2\frac{1}{2}Ae_3^0 \end{aligned} \quad (5.4)$$

We are interested in the corrections which depend on the presence of bent-core molecules i.e. on x_b . Other corrections are already included in the elastic constants of the pure calamitic material. Note that the negative corrections to both bend and play constants are quadratic in x_b and hence they cannot change anything dramatically. Interestingly, the correction to the splay constant, which is linear in x_b is positive, i.e. it leads to an increase in the elastic constant. Thus these corrections lead to weaker reduction of the bend constant compared to the second term in equation 5.2.

5.3 Bent-Core and Calamitic Liquid Crystal Mixtures

Calculations are similar in the case of the twist constant. A twist deformation induces a small enantiomeric excess (δx) in bent-core conformers which is coupled with the twist $= (\hat{\mathbf{n}} \cdot \nabla \times \hat{\mathbf{n}})$. Neglecting the interaction between bent-core molecules and the molecules of the host phase, the free energy of the mixture can be expressed as;^[57]

$$\begin{aligned} \Delta F = kT\rho_0 x_L \ln x_L + kT\rho_0 x_R \ln x_R + \frac{1}{2}\rho_0^2 U_{LL} x_L^2 + \frac{1}{2}\rho_0^2 U_{RR} x_R^2 + \\ \rho_0^2 U_{LR} x_R x_L + \mu(x_R - x_L)(\hat{\mathbf{n}} \cdot \nabla \times \hat{\mathbf{n}}) + \frac{1}{2}K_{22}(\hat{\mathbf{n}} \cdot \nabla \times \hat{\mathbf{n}})^2, \end{aligned} \quad (5.5)$$

where ρ_0 is the average number density, x_R and x_L are the molar fractions of the left and right conformers of the bent-core molecules respectively, $x_L + x_R = x_b$, and μ is the helical twisting power. Here $U_{LL} = U_{RR} = U$, U_{LR} is the effective interaction constant between conformers of equal and opposite handedness respectively, and $\Delta U = U_{LR} - U$ is the chiral discrimination energy.

In contrast to the previous paper by Srigengan et al.^[57] where a pure bent-core material has been considered, in the present mixture the molar fractions of bent-core conformers are of the order of x_b which is of the order or 0.1. Thus, one may neglect the terms quadratic in x_R and x_L in the first approximation, i.e. the terms which describe the interaction between the conformers. Expressing the molar fractions x_R and x_L in terms of the enantiomeric excess δx , i.e. $x_L = \frac{x_b}{2} - \delta x/2$, $x_R = \frac{x_b}{2} + \delta x/2$, and expanding in terms of δx one obtains the following approximate expression for the contribution to the free energy which depends on the enantiomeric excess;

$$\Delta F = \frac{\rho_0 kT}{x_b} (\delta x)^2 + \mu \delta x (\hat{\mathbf{n}} \cdot \nabla \times \hat{\mathbf{n}}). \quad (5.6)$$

Minimisation of this free energy with respect to δx yields;

$$\delta x \cong \frac{\mu x_b (\hat{\mathbf{n}} \cdot \nabla \times \hat{\mathbf{n}})}{2kT\rho_0}. \quad (5.7)$$

Substituting the expression for the enantiomeric excess back into the free energy,

5.3 Bent-Core and Calamitic Liquid Crystal Mixtures

one obtains the negative correction to the twist constant $-(1/4)x_bG$, where $G = \mu^2/kT\rho_0$. It should be noted that the correction to the twist elastic constant is linear in x_b and hence at small x_b it is expected to be much larger than the corresponding negative corrections to the splay and bend constants which are quadratic in x_b . This qualitatively explains why the maximum reduction is observed for the twist constant.

Taking into account only linear terms in x_b the twist constant of the mixture can now be estimated as;

$$K_{22} = K_{22}^c + 2x_b(K_{22}^{bc} - K_{22}^c) - \left(x_b \frac{1}{4}G\right), \quad (5.8)$$

and hence there are two negative corrections to the twist constant which are linear in x_b . Note that in the pure bent-core nematic, the twist elastic constant, $K_{22} = K_{22}^0 - (1/4)G$ and hence $G < 4K_{22}^0$. The correction $x_b(1/4)G$ is then less than $x_bK_{22}^0$. Thus the last term in equation 5.8 can account for at most a 10% reduction of the twist constant and the maximum value of the total negative correction is about 30%. This is already closer to experiment although is still a bit too low.

Perhaps the full explanation lies in an interesting influence of the system on chiral conformers of the host materials. Cyanobiphenyls are known to exist in chiral conformations (twisted about the direct bond between the aromatic rings). The enantiomeric excess of chiral bent-core conformations may in principle also induce some deracemisation in the biphenyl matrix which will lead to further reduction of the total twist constant.

First take into consideration interactions between chiral conformers of bent-core molecules x_R and x_L and chiral conformers of cyanobiphenyls x_{cL} and x_{cR} . Neglecting the quadratic terms in x_R and x_L the free energy of the mixture in the

5.3 Bent-Core and Calamitic Liquid Crystal Mixtures

presence of twist deformation can be written in the form;

$$\begin{aligned}
\Delta F = & kT\rho_0x_L\ln x_L + kT\rho_0x_R\ln x_R + kT\rho_0x_{cL}\ln x_{cL} + kT\rho_0x_{cR}\ln x_{cR} + \\
& \frac{1}{2}\rho_0^2U_{bLcL}x_Lx_{cL} + \frac{1}{2}\rho_0^2U_{bLcR}x_Lx_{cR} + \frac{1}{2}\rho_0^2U_{bRcL}x_Rx_{cL} + \frac{1}{2}\rho_0^2U_{bRcR}x_Rx_{cR} + \\
& \frac{1}{2}\rho_0^2V_{cRcR}x_{cR}^2 + \frac{1}{2}\rho_0^2V_{cLcR}x_{cR}x_{cL} + \frac{1}{2}\rho_0^2V_{cLcL}x_{cL}^2 + \mu(x_R - x_L)(\hat{\mathbf{n}} \cdot \nabla \times \hat{\mathbf{n}}) + \\
& \mu_c(x_{cR} - x_{cL})(\hat{\mathbf{n}} \cdot \nabla \times \hat{\mathbf{n}}) + \frac{1}{2}K_{22}(\hat{\mathbf{n}} \cdot \nabla \times \hat{\mathbf{n}})^2,
\end{aligned} \tag{5.9}$$

where U_{bLcL} , U_{bLcR} , U_{bRcL} , and U_{bRcR} are the interaction constants between bent-core and cyanobiphenyl conformers and V_{cRcR} , V_{cLcR} , and V_{cLcL} are the corresponding interaction constants between cyanobiphenyl conformers. Note that $U_{bLcL} = U_{bRcR} = U_{bc}$, $U_{bRcL} = U_{bLcR} = U_{bcLR}$, and $V_{cRcR} = V_{cLcL} = V_{cc}$. Here μ_c is the helical twisting power of a chiral cyanobiphenyl conformer.

Using the expressions $x_L = \frac{x_b}{2} - \delta x/2$, $x_R = \frac{x_b}{2} + \delta x/2$, and $x_{cL} = \frac{x_c}{2} + \delta x_c/2$, $x_{cR} = \frac{x_c}{2} - \delta x_c/2$, where δx_c is the enantiomeric excess of cyanobiphenyl conformers, and expanding the free energy in terms of δx_c and δx one obtains;

$$\begin{aligned}
\Delta F = & F_0 + \frac{\rho_0 kT}{x_b}(\delta x)^2 + \frac{\rho_0 kT}{x_c}(\delta x_c)^2 - \frac{1}{4}\rho_0^2\Delta U_{bc}\delta x\delta x_c - \frac{1}{4}\rho_0^2\Delta V(\delta x_c)^2 + \\
& \mu\delta x(\hat{\mathbf{n}} \cdot \nabla \times \hat{\mathbf{n}}) + \mu_c\delta x_c\hat{\mathbf{n}} \cdot \nabla \times \hat{\mathbf{n}} + \frac{1}{2}K_{22}(\hat{\mathbf{n}} \cdot \nabla \times \hat{\mathbf{n}})^2,
\end{aligned} \tag{5.10}$$

where F_0 is independent of δx , δx_c and the twist deformation $(\hat{\mathbf{n}} \cdot \nabla \times \hat{\mathbf{n}})$. Here $\Delta U_{bc} = U_{bcLR} - U_{bc}$ and $\Delta V = V_{cLcR} - V_{cc}$. Minimisation with respect to δx and δx_c yields the following system of simultaneous equations;

$$\begin{aligned}
\frac{2\rho_0 kT}{x_b}\delta x - \frac{1}{4}\rho_0^2\Delta U_{bc}\delta x_c + \mu(\hat{\mathbf{n}} \cdot \nabla \times \hat{\mathbf{n}}) &= 0, \\
\frac{2\rho_0 kT}{x_c}\delta x_c - \frac{1}{4}\rho_0^2\Delta U_{bc}\delta x_c - \frac{1}{4}\rho_0^2\Delta V\delta x_c + \mu_c(\hat{\mathbf{n}} \cdot \nabla \times \hat{\mathbf{n}}) &= 0.
\end{aligned} \tag{5.11}$$

Taking into account only terms linear in x_b the solution of equation 5.11 can be expressed as;

5.3 Bent-Core and Calamitic Liquid Crystal Mixtures

$$\delta x \cong -\frac{\mu x_b (\hat{\mathbf{n}} \cdot \nabla \times \hat{\mathbf{n}})}{2kT\rho_0} \quad (5.12)$$

$$\delta x_c \cong \frac{x_b U^* \mu^* (\hat{\mathbf{n}} \cdot \nabla \times \hat{\mathbf{n}})}{1 - x_c V^*} - \frac{\mu_c^* (\hat{\mathbf{n}} \cdot \nabla \times \hat{\mathbf{n}})}{1 - x_c V^*},$$

where $V^* = \rho_0 \Delta V / 8kT$, $U^* = \rho_0 \Delta U_{bc} / 8kT$ and $\mu^* = \mu / 2\rho_0 kT$, $\mu_c^* = \mu_c / 2\rho_0 kT$. One notes that the enantiomeric excess δx is given approximately by the same equation as equation 5.7 where the coupling with the cyanobiphenyl molecules has not been taken into account. In contrast, the enantiomeric excess δx_c is induced both by the twist deformation and by the interaction with chiral conformers of the bent-core molecules.

Substituting equation 5.12 back into the free energy in equation 5.10 and keeping only terms linear in x_b , one obtains the following correction to the twist elastic constant;

$$\delta K_{22} = -\frac{\mu^2}{4kT\rho_0} - \frac{\mu\mu_c^*}{1 + x_c V^*} - \frac{x_b}{4x_c \rho_0 kT} \frac{U^* \mu \mu_c}{1 + x_c V^*} (1 - x_c U^*), \quad (5.13)$$

where $1 > 2x_c U^*$ as generally $U^* \ll 1$.

The first negative correction in equation 5.13 is exactly the same as the one obtained earlier taking into account the partial deracemisation of the system of bent-core molecules in the presence of twist deformation. The second correction in equation 5.13 has already been included in the twist elastic constant of the cyanobiphenyl host phase. Finally, the third term describes the additional negative correction (taking into account that generally $U^* > 0$) which is determined by a partial deracemisation in the cyanobiphenyl host induced by chiral conformers of the bent-core molecules. Thus there are two additional negative corrections to the twist elastic constant of the mixture which are linear in x_b and which may account for a reduction of the order of 10% each. These corrections are absent in the expressions for the splay and bend elastic constants of the mixture which enables one at least qualitatively explain why the twist constant experiences the largest reduction among all elasticity coefficients.

5.4 Conclusions

In conclusion, the splay, twist and bend (K_{11} , K_{22} and K_{33}) elastic constants of a number of bent-core liquid crystal mixtures have been reported. The mixtures of two bent-core mesogens exhibit a similar temperature dependence to the pure bent-core compounds for the splay constant K_{11} as well as a similar temperature independence for the bend constant K_{33} . Interestingly for the twist constant K_{22} , the bent-core mixtures exhibited a more marked temperature dependence as increasing amounts of VBG93 were added to the mixture.

With regards to the doped calamitic mixtures, the results suggest that the underlying phase behaviour, SmA or filament, doesn't influence the way in which the mixed elastic constants combine. The formation and behaviour of the filaments will be discussed further in chapter 7. Reductions in the twist elastic constant were measured in all the calamitic and bent-core mixtures, not just those that exhibited the filament phase.

It has been shown that the influence of a bent-core mesogen on the three elastic constants, K_{11} , K_{22} , and K_{33} of a calamitic liquid crystal host is quite distinct. In the case of the splay constant, in all three mixture sets, the influence of the bent-core dopant is negligible. By considering the expected influence of a dopant on the elastic constants of the mixtures, one can draw two conclusions. Firstly, the splay interaction constant, K_{11}^{bc} , determined by interactions between calamitic and bent-core molecules, must be negligible. Further, there can be no additional contribution that might emerge from fluctuations in the conformers. Splay is more affected by a wedge-shaped structure; splay instabilities have recently been reported in the nematic phase of wedge-shaped molecules where there are issues with space-filling.^[111] There is apparently little scope for the bent-core molecules included in the mixtures here to show any wedge-shaped conformers that might have significant impact on the splay elastic constant.

The influence of the bent-core dopants on the bend elastic constant leads to a reduction of 10-20% in K_{33} , in line with the simple mixing rule described by equation 5.1 and with existing literature. However, the surprising result of this study was the remarkable reduction in the twist elastic constant, K_{22} (up to ~40%) observed in all of the bent-core/calamitic mixtures. This chapter provides an

explanation to this reduction that suggests that not only do the fluctuations results in chiral conformers of the bent-core system have a significant effect, but that they must also enhance the fluctuations in chiral conformers of the host calamitic liquid crystal. This surprising result indicates an amplification of fluctuations in chirality of the system which is important both from the technological point of view and from understanding how chirality can 'cascade' in a fluid system.

Both the measurements and explanation of the phenomena suggest how bent-core/calamitic mixtures could be employed to tune mixtures for devices. The effect on all three elastic constants, including the dramatic effect on the twist constant in particular has not previously been reported. As the elastic constants are related to the threshold voltages in devices, the measurements that are detailed in this chapter indicate the potential of these mixtures for use in lower threshold voltage devices. With this in mind the 8CB mixtures seem best suited for these applications; these mixtures exhibit the largest reductions in K_{22} , as well as the lowest absolute values of K_{22} over the whole nematic phase. However one would have to consider the effect of the underlying SmA phase in the mixtures. With regards to fundamental science, the dramatic reduction in the twist elastic constant offers a possible route for designing mixtures that exhibit nematic variant phases such as the twist-bend phase.

It is important to note that the simple mixing rules that determine the elastic constants in liquid crystals apply quite well to the bent-core mixtures of DT12 and VBG93; the elastic constant values for the bent-core mixtures all lie in between the respective values of the pure bent-core liquid crystals (see figure 5.4). Interestingly the simple mixing rules apply to the K_{11} values, which is what one would expect to happen. However, as shown in figures 5.8, 5.10 and 5.11, the K_{11} values for mixtures of calamitics and bent-cores don't adhere to the standard mixing rules; there is no change in the K_{11} values when the calamitic host is doped with 10% of bent-core mesogen. The reason behind this difference in behaviour of the K_{11} values in bent-core mixtures and mixtures of calamitics with bent-cores is still yet to be fully understood; perhaps full phase diagrams of the calamitics mixed with the bent-cores, relating to the elastic behaviour (similar to the plots shown in figure 5.4) need to be investigated? This will be discussed further in the future work in chapter 8.

The next chapter will look at the bent-core mixtures of DT12 and VBG93 further, detailing the phase behaviour observed in these mixtures using small angle X-ray scattering as a primary technique to characterise the underlying phases in the mixtures.

Chapter 6

Phase Behaviour in Bent-Core Liquid Crystal Mixtures

6.1 Introduction

This chapter will go into detail on the phase behaviour observed in mixtures of two bent-core nematic liquid crystals, DT12 and VBG93. The elastic behaviour in the nematic phase of these mixtures have already been discussed in the previous chapter; this chapter will discuss the phases below the nematic phase in these bent-core mixtures. The characterisation of these underlying phases was carried out using small angle X-ray scattering (SAXS) and POM.

SAXS is an important tool in characterising liquid crystal phases; the raw X-ray data are distinct for different phases, and the peak positions obtained from these images provide information about the structure that the phases exhibit. For example, nematic phases exhibit two crescents at small angles in the raw X-ray data,^[122] whilst the DC exhibits a diffuse ring.^[30, 123] By analysing the X-ray scattering data obtained for the mixtures, as well as the elastic behaviour measured in the nematic phase of the mixtures, insight can be gained into the driving factors of the formation of the underlying phases in bent-core systems. It has been predicted that the DC phase is driven by the saddle-splay constant K_{24} which is related to the other elastic constants by the inequalities $K_{24} \leq 2K_{11} + K_{22}$, and $K_{24} < K_{22}$.^[113–115] This chapter aims to use these inequalities to relate

the elastic behaviour in the mixtures to X-ray scattering data presented in the results section.

6.2 Experimental Methodology

6.2.1 Materials

The molecular structures and phase transition temperatures of the pure bent-core materials used in this chapter are shown in figure 6.1. Transition temperatures of the pure materials and the mixtures were determined by differential scanning calorimetry (DSC) and polarising optical microscopy (POM); the temperatures in table 6.1 were taken from the DSC measurements determined on cooling at a rate of 5 °C/min. The phase diagram of the mixtures is shown in figure 6.2 (copied from chapter 5). The phase diagram shows an approximately linear dependence of all of the phase transitions on concentration. An optically isotropic phase occurs at higher concentrations of VBG93, while a smectic phase is observed at lower concentrations.

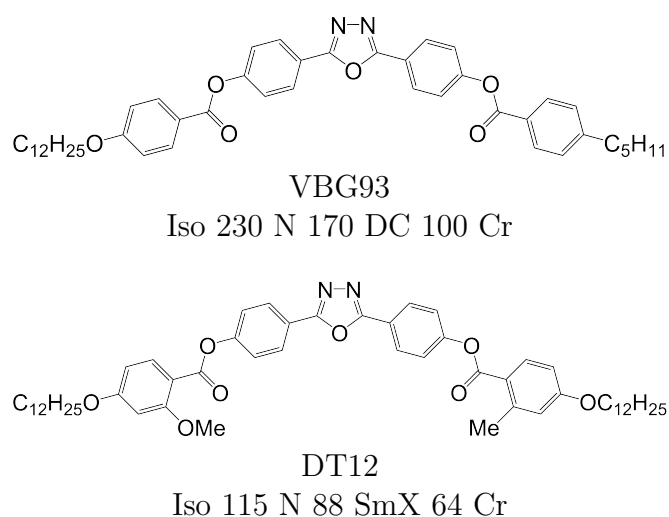


Figure 6.1: Molecular structures and phase transitions temperatures for the liquid crystals used in this chapter. Temperatures are recorded in °C.

6.2 Experimental Methodology

Mixture Number	Composition	Phase Transitions T/°C
Mixture 1	10:90 DT12:VBG93	Iso 224 N 164 OI 94 Cr
Mixture 2	25:75 DT12:VBG93	Iso 200 N 144 OI 95 Cr
Mixture 3	50:50 DT12:VBG93	Iso 190 N 140 SmX 90 Cr
Mixture 4	70:30 DT12:VBG93	Iso 170 N 117 SmX 80 Cr
Mixture 5	90:10 DT12:VBG93	Iso 140 N 100 SmX 70 Cr

Table 6.1: Compositions of the bent-core mixtures used in this chapter with the corresponding phase transitions and transition temperatures determined on cooling, where OI = optically isotropic phase.

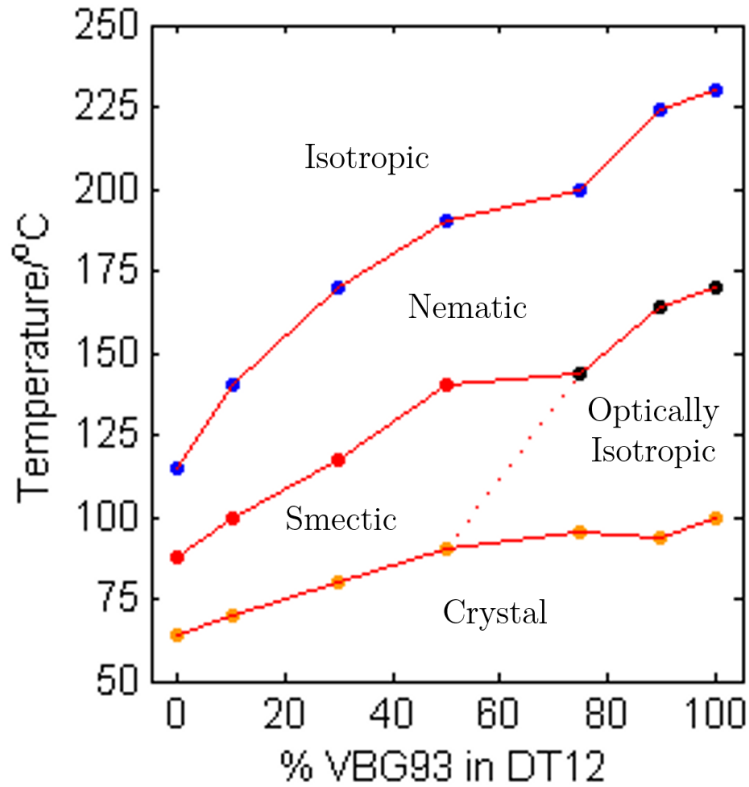


Figure 6.2: The phase diagram of mixtures of DT12 and VBG93. The blue points mark the isotropic to nematic transition, the red points represent the transition from the nematic to an unknown smectic phase, the black points represent the transition from a nematic to an optically isotropic phase, and the orange data points represent the transition from the mesophase to crystal phase. In the case of VBG93, the optically isotropic phase is the DC phase.

6.2.2 X-ray scattering

For the materials used in this chapter, SAXS was used to determine the lattice spacing in the various liquid crystal phases investigated, using the methodology described in section 3.7 in chapter 3. SAXS was carried out using a Bruker D8 Discover which was equipped with a temperature controlled, bored graphite rod furnace, custom built at the University of York which allowed the temperature to be controlled to an accuracy of 0.1 °C. The radiation used was a copper $K\alpha$ (wavelength of 0.154 nm) source. Samples were filled into 1 mm diameter capillary tubes and the system was used in transmission. The detector was placed 127 mm from the sample, which allowed spacings between 4-100 nm to be determined with an accuracy of 0.1 Å. The mixtures were heated to the isotropic phase and readings were taken as the sample was cooled. All the measurements were carried out under an applied magnetic field of ~ 0.7 T.

This methodology allowed the intensity of the X-ray scattering to be measured as a function of d_x , which allows one to understand how the periodicity and FWHM of the samples varied as a function of temperature. Here d_x refers to the lattice spacing of the sample. With the detector placed 127 mm away from the sample, the maximum lattice spacing that could be measured was 100 Å. An example of the plot of intensity against d_x for VBG93 is shown in figure 6.3.

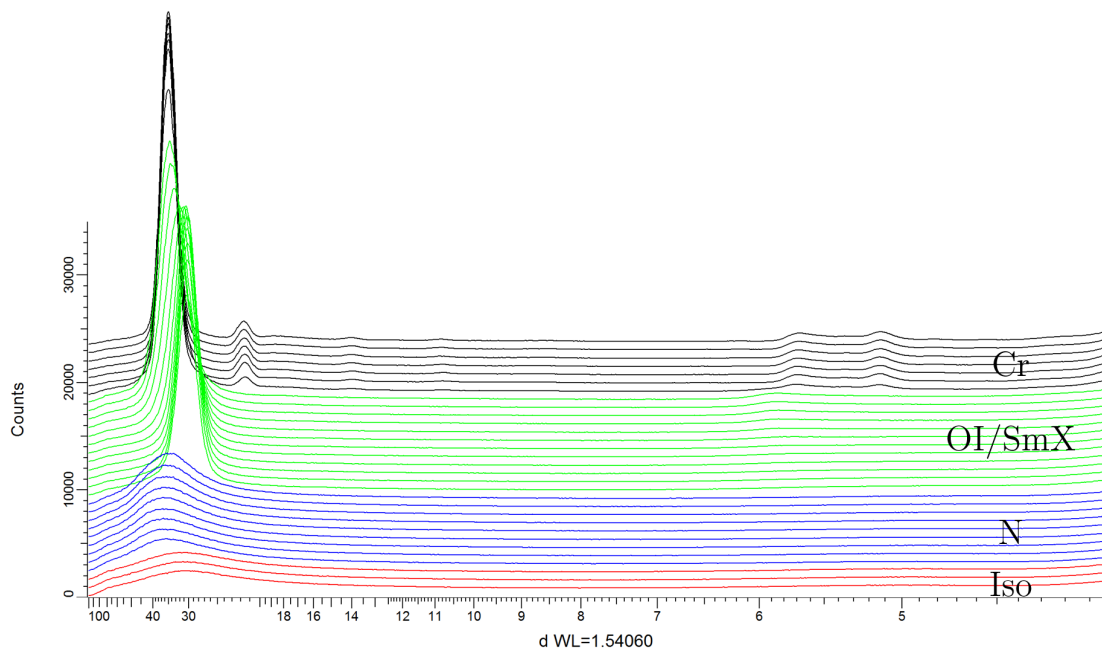


Figure 6.3: Example plots of intensity as a function of d_x for VBG93. For both bent-core liquid crystals and the mixtures, the red plots represent the isotropic phase, the blue plots represent the nematic phase, the green plots represent the underlying phase, and the black plots represent the crystal phase. In the case of DT12 and mixtures 3-5 the underlying phase is a SmX phase, and for VBG93 it is a DC phase. For mixtures 1 and 2 the underlying phase is an optically isotropic phase.

6.2 Experimental Methodology

The plots of intensity against d_x were obtained by integrating an average over the whole detector i.e. integrating in rings. Using the Bragg equation $2d_x \sin\theta = n\lambda$, the spacings that are of interest can be determined. For the measurements on the bent-core mixtures described in this chapter, the spacings that were of interest were ~ 30 Å. The chosen peaks around 30 Å were fitted using MATLAB in order to obtain the peak position and the full width at half maximum (FWHM) of the peak. The fit chosen was a Gaussian fit. Figure 6.4 shows an example of this fit applied to an X-ray spectrum taken for VBG93. The Gaussian fit allowed the spacing to be measured to an accuracy of 0.1 Å and the FWHM to 0.2 Å, however the instrument limited the resolution to 3 Å.

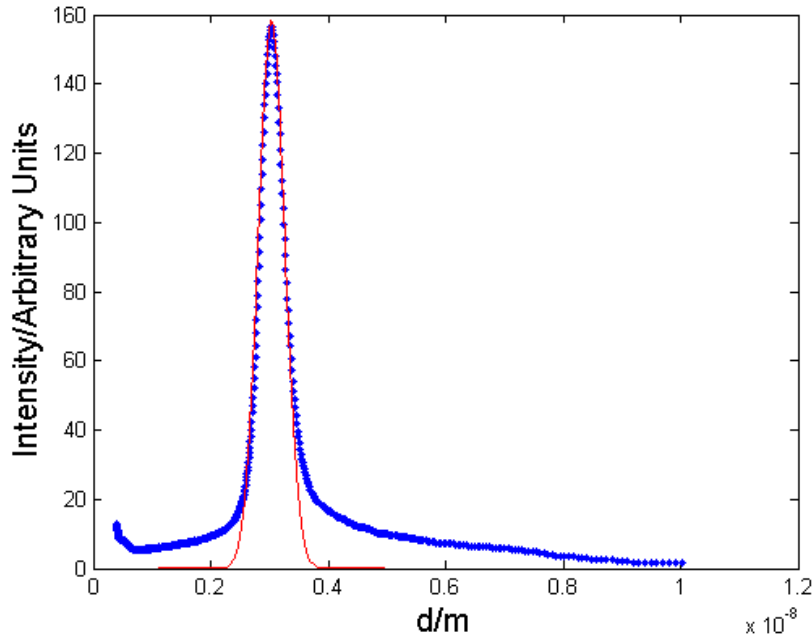


Figure 6.4: X-ray scattering intensity as a function of spacing d_x for VBG93 5 °C into the DC phase. The blue data points represent the experimental data and the red line represents the Gaussian fit applied to the data.

6.3 X-Ray Scattering in Bent-Core Mixtures

Using POM it was determined that mixture 1 and 2 exhibited optically isotropic phases below the nematic phase, whilst mixtures 3-5 exhibited smectic phases. Using the phase diagram (figure 6.2) as a reference, the following results section will be discussed in two parts; the first will compare the SAXS results obtained for mixtures 1 and 2 with VBG93, and the second part will compare the SAXS results obtained for mixture 3-5 with DT12.

6.3.1 Optically isotropic phases; mixtures 1 and 2

Figure 6.5 shows the peak position and FWHM as a function of $T-T_{N-OI}$ (where $N-OI$ is the transition from the nematic phase into the OI phase) in the optically isotropic phases observed in mixtures 1 and 2, along with the measurements taken for the DC phase in VBG93. The peak position for the mixtures as well as the temperature dependence is clearly maintained compared to VBG93, varying from ~ 30.3 Å to ~ 34.3 Å at $T-T_{N-OI} = -65$ K. The FWHM shows similar behaviour; the values and temperature dependence are mostly maintained in mixtures 1 and 2 with respect to VBG93, varying from ~ 5.2 - 4.8 Å before increasing to ~ 8.5 Å. Mixture 2 exhibits two data points outside of the general trend; ~ 7.5 Å just below the transition, and ~ 9.4 Å at $T-T_{N-OI} = -60$ K, however the rest of the data exhibited by mixture 2 is comparable to VBG93 and mixture 1.

From the results shown in the plots from figure 6.5, it is clear to see that the optically isotropic phases exhibited by mixture 1 and 2 can be defined as DC phases, similar to the DC phase in VBG93. One can also use the raw X-ray data to compare the underlying phases of the mixtures to that of VBG93. The raw data are shown in figure 6.6. The raw X-ray data show that the underlying phases in mixtures 1 and 2 exhibit a diffuse ring, also exhibited by the VBG93 sample. A diffuse ring is characteristic of a DC phase[30, 123] and again gives proof that the optically isotropic phases observed in mixtures 1 and 2 can be identified as DC phases. The brightness observed in the images shown in figure 6.6 determines the intensity of the signal detected; the yellow diffuse ring indicates the highest intensity peak measured. The closer the features to the centre of the image, the

6.3 X-Ray Scattering in Bent-Core Mixtures

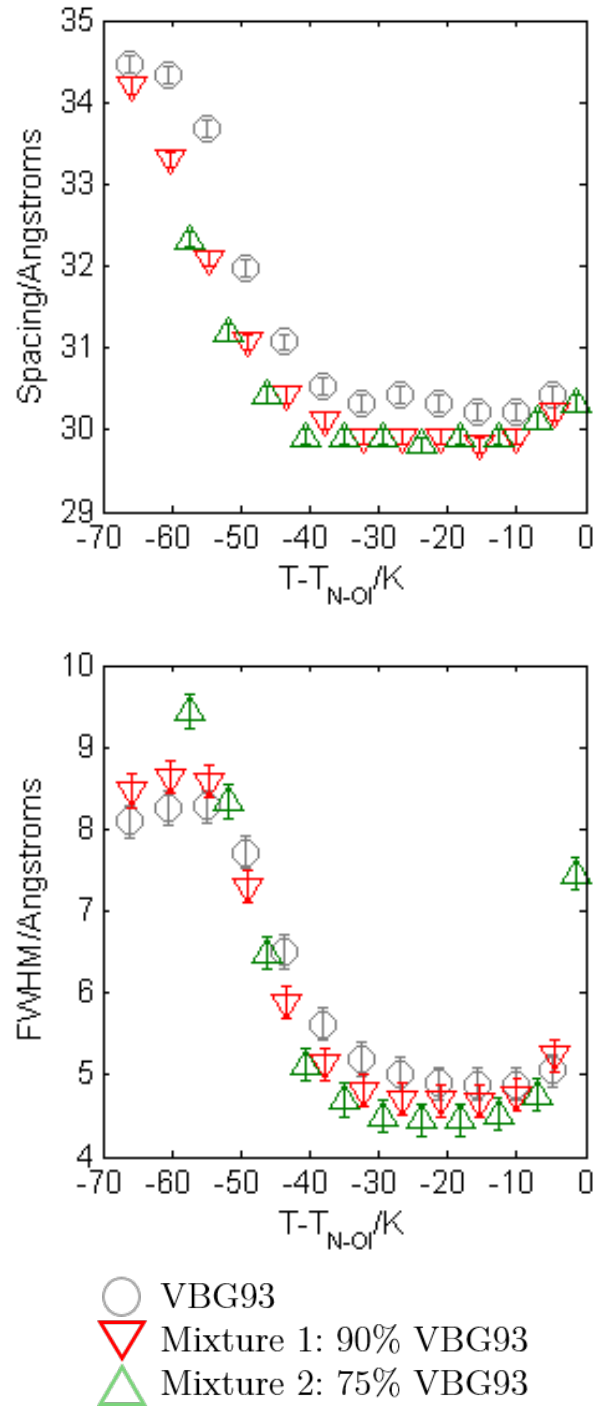


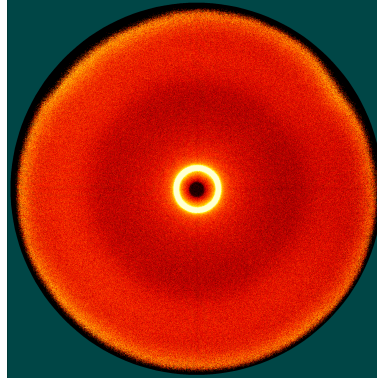
Figure 6.5: Spacing (a) and FWHM (b) as a function of $T-T_{N-OI}$ in the optically isotropic phases for VBG93, and mixtures 1 and 2.

6.3 X-Ray Scattering in Bent-Core Mixtures

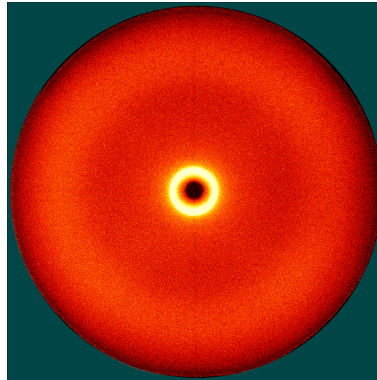
lower the scattering angle of the peak and thus the larger the spacing. In the data shown in figure 6.6 the diffuse rings correspond to peaks of ~ 30 Å.

The next section will look at the underlying phases observed in mixtures 3-5 and compares the respective spacings and FWHM of the mixtures to that measured in the SmX phase of DT12.

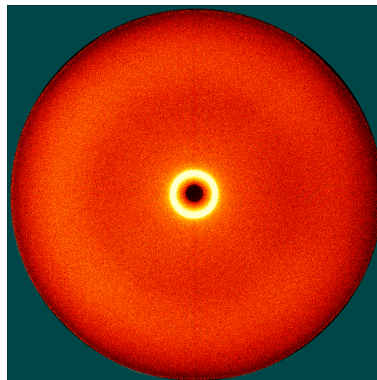
6.3 X-Ray Scattering in Bent-Core Mixtures



(a) VBG93



(b) Mixture 1: 90% VBG93



(c) Mixture 2: 75% VBG93

Figure 6.6: The raw X-ray data for the DC phases observed in VBG93 (a), mixture 1 (b) and 2 (c) respectively, just below the transition into the DC phases. The DC phase can be characterised by the bright yellow diffuse ring in the middle of the images.

6.3.2 Smectic phases; mixtures 3-5

Figure 6.7 shows the spacing and FWHM as a function of $T-T_{N-SmX}$ (where $N-SmX$ is the transition from the nematic phase into the SmX phase) in the smectic phases observed in mixtures 3-5, along with the measurements taken for the smectic phase in DT12. The temperature dependence of both the spacing and FWHM in the mixtures is maintained when DT12 is mixed with VBG93. The values of the spacing for each of the mixtures at the same reduced temperature increases as more DT12 is added to VBG93; the spacing varies from ~ 30 - 29 Å in mixture 3, from ~ 31.5 - 29.5 Å in mixture 4, from ~ 32 - 31 Å in mixture 5, and from ~ 32.5 - 32 Å in DT12. The FWHM behaves slightly differently from the spacing; mixtures 3-5 exhibit values that are similar to each other, varying between ~ 3.5 - 2.8 Å compared to DT12 which exhibits a FWHM of ~ 4.2 Å. It should be noted that the FWHM of the peaks measured in the crystal phases of DT12 and mixtures 3-5 are comparable to the FWHM values shown in figure 6.7. The FWHM of the crystal peaks should typically be much lower than those measured in the higher temperature phases. Thus, it cannot be simply stated that DT12 exhibits higher FWHM values in its smectic phase compared with the smectic phases of mixtures 3-5, as the resolution of the experiment is close to the values themselves.

The raw X-ray data for DT12 and mixtures 3-5 (shown in figure 6.8) provide more information on the underlying smectic phases. The raw X-ray data confirm that the underlying phases exhibited by DT12 and mixtures 4 and 5 are smectic phases;^[122] they all show the characteristic crescents with images (a), (b) and (c) being very similar to each other. Figure 6.8d suggests that mixture 3 exhibits an underlying SmC phase that includes a layer tilt.^[122] However another explanation could be that the director has been aligned by the magnetic field and that the smectic layers have formed at an angle on cooling from the nematic phase. From image (d) the angle of the layers can be measured to be approximately 45° . The angle of the layers is characteristic of the tilt angle of the director in the smectic layers, which can be obtained from the layer spacings using the equation $\cos\theta_t = d_x/L$ where θ_t is the tilt angle and L is the molecular length of the liquid crystal. L for mixture 3 can be assumed to be spacing measured in the

6.3 X-Ray Scattering in Bent-Core Mixtures

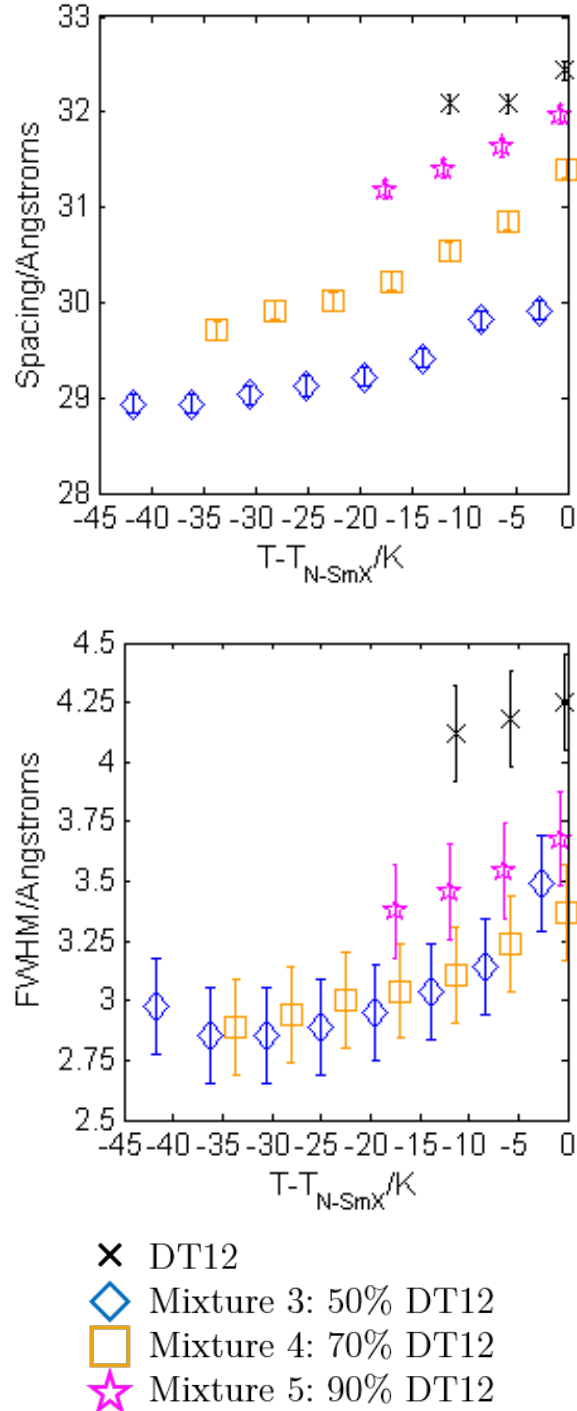


Figure 6.7: Spacing (a) and FWHM (b) as a function of $T - T_{N-SmX}$ in the smectic phases for DT12, and mixtures 3-5.

6.3 X-Ray Scattering in Bent-Core Mixtures

nematic phase, which was measured to be ~ 34 Å. Using the values of the spacing measured for mixture 3 from figure 6.7, it can be shown that the tilt angle in the smectic phase in mixture 3 varies from 29.0 - 32.2° as the temperature reduces to $T-T_{N-SmX}$. These values are far off from the 45° layer tilt measured from the raw X-ray data in figure 6.8.

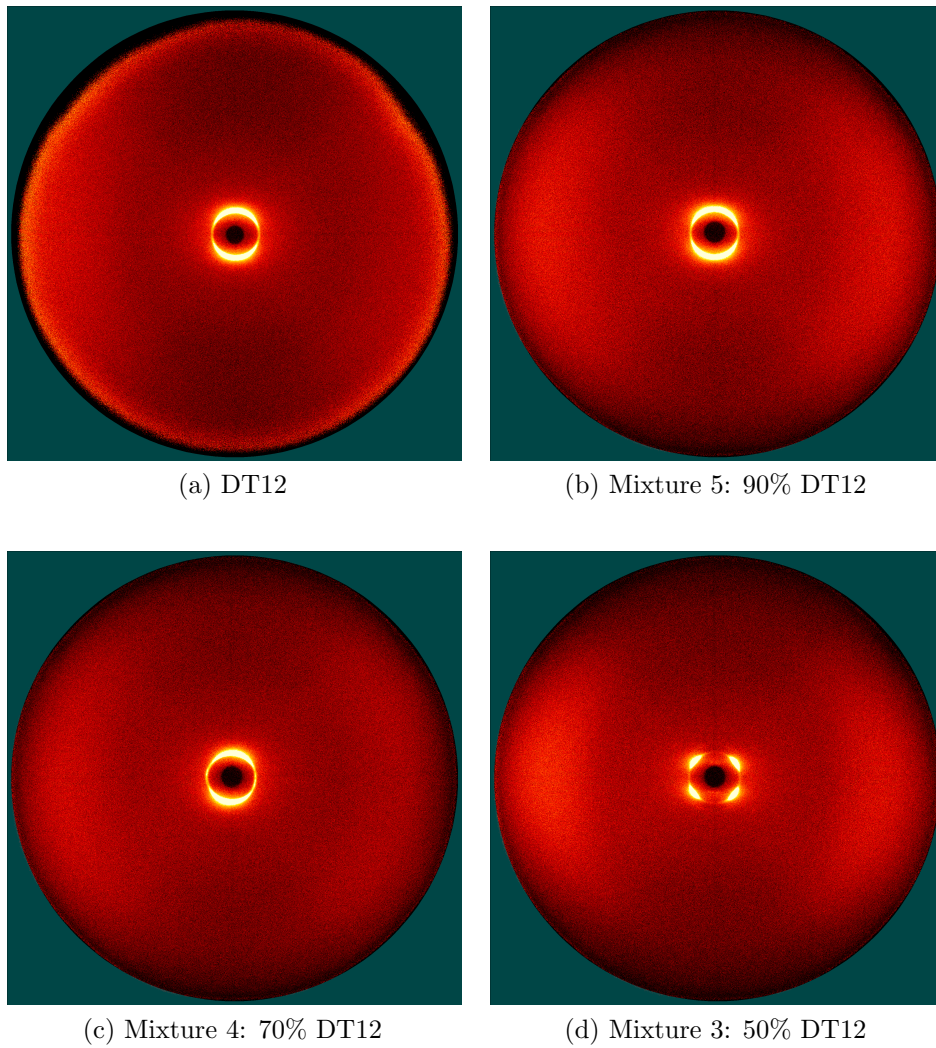


Figure 6.8: The raw X-ray data for the smectic phases observed in DT12 (a), mixture 5 (b), 4 (c) and 3 (d) respectively, just below the transition into the smectic phases.

Considering the tilt angle in the smectic phases in DT12 and mixtures 4 and

5 and comparing the values to that obtained for mixture 3 can provide more information. The plot of tilt angle in the smectic phases of DT12 and mixtures 3-5 are shown in figure 6.9, with the accuracy of the tilt angle to be $\pm 0.1^\circ$. The tilt angle was measured to vary from $19.9\text{-}21.5^\circ$ for DT12, $20.3\text{-}23.9^\circ$ for mixture 5, $21.7\text{-}28.5^\circ$ for mixture 4, and $29.0\text{-}32.2^\circ$ for mixture 3 (as mentioned earlier). It can be seen that the tilt angle increases as the temperature is reduced through the smectic phase in DT12 and mixture 3-5. Mixture 3 exhibits the highest tilt angle in its smectic phase with DT12 exhibiting the lowest out of the four samples. Whilst there appears to be a significant gap in the behaviour of the tilt angle between mixture 3 and 4 (which exhibits values closer to mixture 5 and DT12), there is no conclusive evidence to fully explain why the raw X-ray data for mixture 3 is so different to those obtained for DT12 and mixture 4 and 5.

The next section will discuss the implications of all the data, relating the emergence of the underlying phases to the elastic behaviour in the nematic phase of the respective mixtures. From the X-ray scattering data shown in this section it seems appropriate to compare results for VBG93 with mixtures 1 and 2 separately from the results for DT12 and mixtures 3-5.

6.4 Discussion

Analysing the X-ray scattering data has determined a number of results on the underlying phases in the bent-core mixtures investigated in this chapter. The optically isotropic phases in mixtures 1 and 2 can be characterised as DC phases, based on the spacing and FWHM measurements. The behaviour of the spacing measurements in DT12 and mixtures 3-5 can be explained by considering the spacing of VBG93 and amount of VBG93 in the corresponding mixtures. It is difficult to compare the FWHM values measured for the smectic phases in DT12 and mixture 3-5 due to the resolution of the apparatus set-up. The tilt angle measured for the smectic phases show that absolute values of the tilt angle increase as more VBG93 is added to DT12. Images taken using POM of the smectic phases show that the textures are different between the smectic phases observed in DT12 and mixture 5, and those observed in mixtures 3 and 4. These results will be discussed in the following subsections.

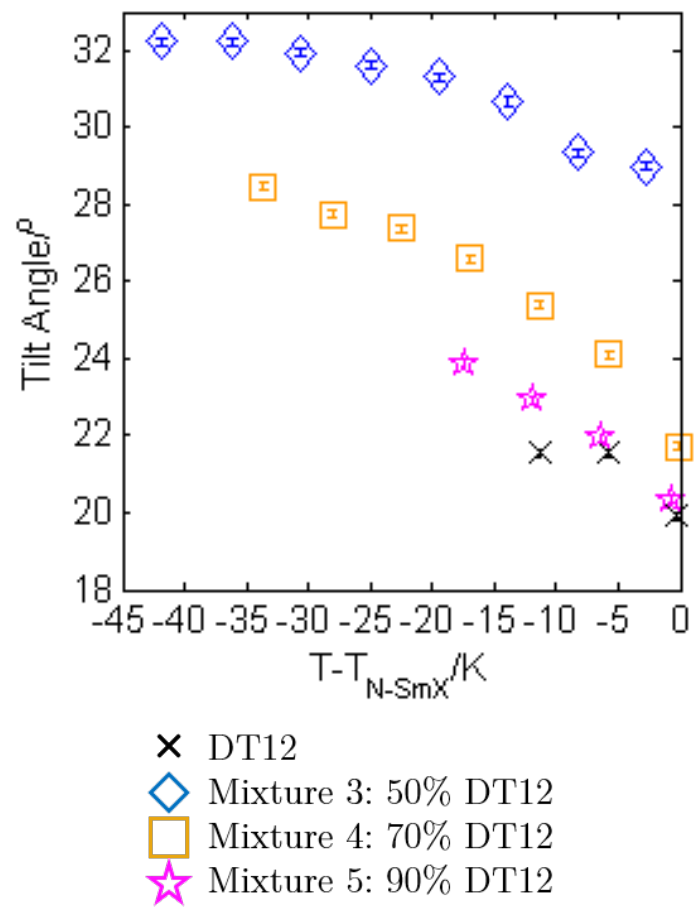


Figure 6.9: The tilt angle measured as a function of $T - T_{N-SmX}$ in the smectic phases for DT12, and mixtures 3-5

6.4.1 Characterisation of the optically isotropic phases

It is clear to see from figures 6.5 and 6.6 that mixtures 1 and 2 exhibit DC phases at temperatures beneath the nematic phases. The spacing and FWHM measured for the mixtures qualitatively and quantitatively match those values measured for the DC phase in pure VBG93. The raw X-ray data also show a diffuse ring which is characteristic and similar to the DC phase observed in VBG93.[30, 123]

6.4.2 Spacing in the smectic phases

The results measured for DT12 and mixtures 3-5 tell a different, more complicated story. The spacing at set reduced temperatures decrease as more VBG93 is added to DT12. From simple mixing rules this is to be expected; as the temperature is reduced to 45 °C below the transition into the underlying phase, VBG93 exhibits a lower spacing in comparison to DT12. Thus the relationship between the spacing and composition of the mixture can be explained. VBG93 exhibiting a lower spacing compared with DT12 can be easily explained by considering the molecular length of the molecules of the two individual bent-core mesogens. The molecular length of VBG93 was calculated to be ~ 34 Å.[30, 61] VBG93 contains asymmetrical terminal alkyl chains; a C₅ chain on one end and an OC₁₂ chain on the other (see figure 6.1). DT12 on the other hand contains an OC₁₂ chain for both terminal alkyl chains (see figure 6.1), which leads to a larger molecular structure. One can also use the measurements of spacings from the X-ray scattering in the nematic phase to obtain an estimate for the average molecular length for DT12; this was measured to be ~ 34.5 Å, which is still larger than the 34 Å measured for VBG93, if only slightly. Thus the behaviour of the spacings measured for DT12 and mixtures 3-5 with respect to each other can be explained.

6.4.3 FWHM in the smectic phases

The FWHM of mixtures 3-5 exhibit values that are within error of each other, varying from ~ 3.5 - 2.8 Å as the temperature is reduced through the smectic phase, compared to DT12 which exhibits a FWHM of ~ 4.25 Å. However it is difficult to make reliable comparisons of the FWHM measurements due to the resolution of

the apparatus set-up. The FWHM measured for the crystal phases were found to be comparable to those measured in the smectic phases at ~ 3 Å. One would expect the FWHM measured in the crystal phase to be much less than that measured for higher temperature phases, and as such the resolution does not allow reliable comparison of the FWHM data.

6.4.4 Tilt angle in the smectic phases

The tilt angle of the director in the smectic phases have been measured by considering the spacing in the nematic phase (shown in figure 6.9). The equation relating the tilt angle and the spacing is given by $\cos\theta_t = d_x/L$, where θ_t is the tilt angle, d_x is the spacing and L is the molecular length, taken from the spacing in the nematic phase. From the plot in figure 6.9) it can be seen that as more VBG93 is added to DT12, the absolute values of the tilt angle increases, with DT12 exhibiting the lowest tilt (19.9 - 21.5°) in the smectic phase and mixture 3 exhibiting the highest tilt (29.0 - 32.2°). Interestingly the tilt angle measured for the smectic phase in mixture 3 is much less than the layer tilt measured from the raw X-ray data (figure 6.8d), which was found to be $\sim 45^\circ$. The spacing and tilt angle measurements in the smectic phases of DT12 and mixtures 3-5 suggest that there is a tilt to the director within the smectic layers in the samples, and that the phases differ slightly depending on the concentration of the mixture itself.

6.4.5 POM images of the smectic phases

Investigations into the texture of the smectic phases can provide more information. The images taken for the smectic phases in DT12 and mixture 3-5 are shown in figure 6.10. The images were taken from 5 μm thick planar homogeneously aligned devices. At a first glance, the images in figure 6.10 suggest that DT12 and mixture 5 exhibit a very similar smectic phase to each other; both textures appear alike and exhibit a similar birefringence of $\Delta n \sim 0.18$. On the other hand the textures observed in the smectic phases of mixtures 3 and 4 exhibit a different birefringent behaviour, with two regions that exhibit two different birefringence values; one can be seen to be pink in colour with $\Delta n \sim 0.20$, and the other to be green in colour with $\Delta n \sim 0.15$. The textures of the smectic phases in mixtures 3

and 4 can be seen to very similar to each other with regards to the birefringence behaviour. There is a clear change in birefringence between the textures seen in figure 6.10a and b, and the textures in figure 6.10c and d. The spacing/FWHM measurements obtained from the X-ray scattering (figure 6.8) do not show any clear distinction between mixtures 3 and 4, and DT12 and mixture 5. Indeed from the raw X-ray data, only mixture 3 seems to be different, however even that does not explain the similarity in texture between the smectic phases in mixtures 3 and 4 shown in figure 6.10c and d.

The textures exhibited by DT12 and mixture 5 appear to be similar to the textures seen in the B_6 phase, which typically exhibits similar fan shaped textures.[124] However from X-ray scattering, the B_6 phase typically exhibits a layer spacing that is half of the molecular length due to the intercolation of the molecules.[125] The spacing measured for the smectic phases in DT12 and mixture 5 are comparable to the molecular length (taken from the spacing measured in the nematic phase), thus it is very hard to justify that the textures observed in figure 6.10a and b are due to the B_6 phase. From all the data on the smectic phases in DT12 and mixtures 3-5, it can be concluded that smectic phases are all similar to each other with slight differences in packing arising due to the concentrations of the two pure bent-cores. However, it is clear that the X-ray data and POM images alone cannot fully characterise the underlying smectic phases in DT12 and mixtures 3-5; more experimentation is required for a full characterisation to be obtained.

6.4.6 Elastic behaviour in DC phase mixtures

It is known that the DC phase is driven by the K_{24} elastic constant. It was discussed in section 5.2.3 in chapter 5 that the inequalities that relate K_{24} to the other elastic constants are $K_{24} \leq 2K_{11} + K_{22}$, and $K_{24} < K_{22}$. [113–115] The inequality that dominates is the one that provides the smaller value for K_{24} . For VBG93 and mixtures 1 and 2, K_{22} is always lower than K_{11} thus the second inequality is the one that applies to these systems; $K_{24} < K_{22}$. The elastic behaviour exhibited in the nematic phases of these samples are shown in figure 6.11. If we consider the inequality $K_{24} < K_{22}$ then the fact that mixtures 1 and 2

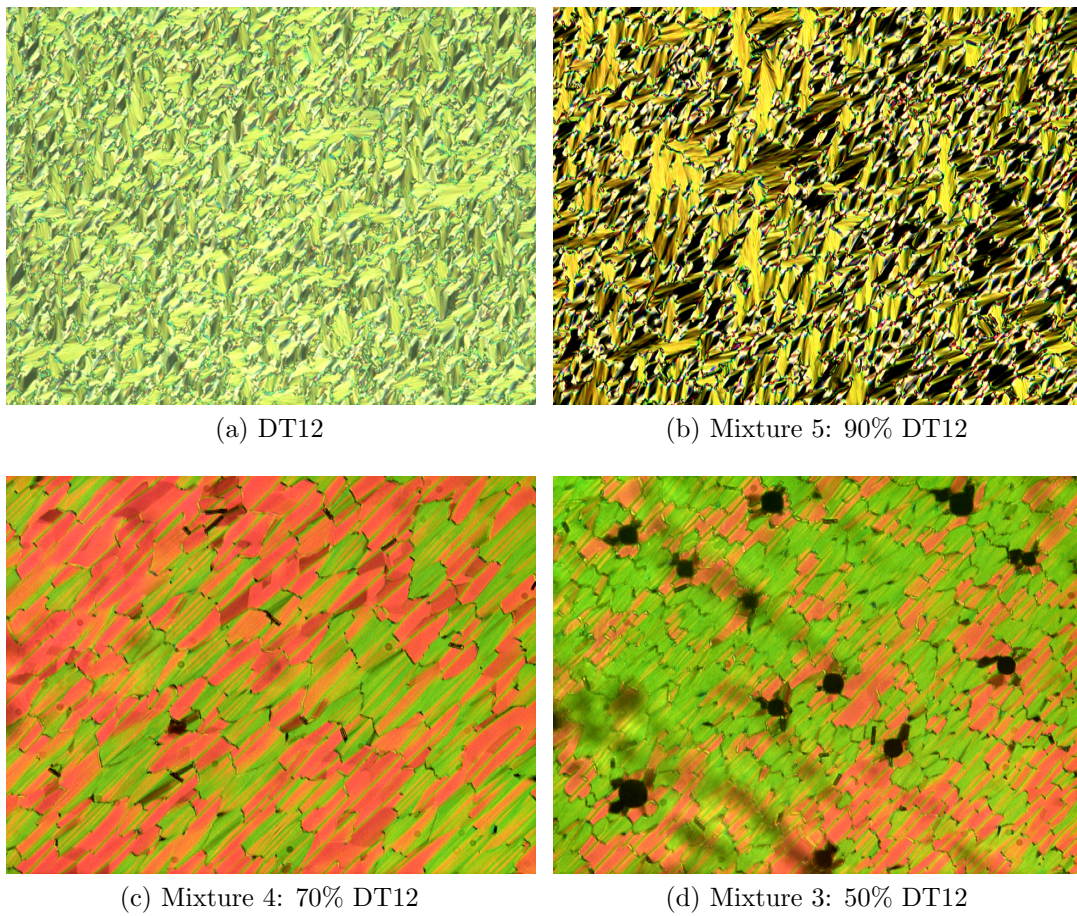


Figure 6.10: POM images taken for the underlying phases exhibited by (a) DT12, (b) mixture 5, (c) mixture 4, and (d) mixture 3 respectively. The width of the images are 0.6 mm.

exhibit DC phases can be justified; K_{22} measured for both mixtures 1 and 2 are lower across the whole nematic range when compared with VBG93.

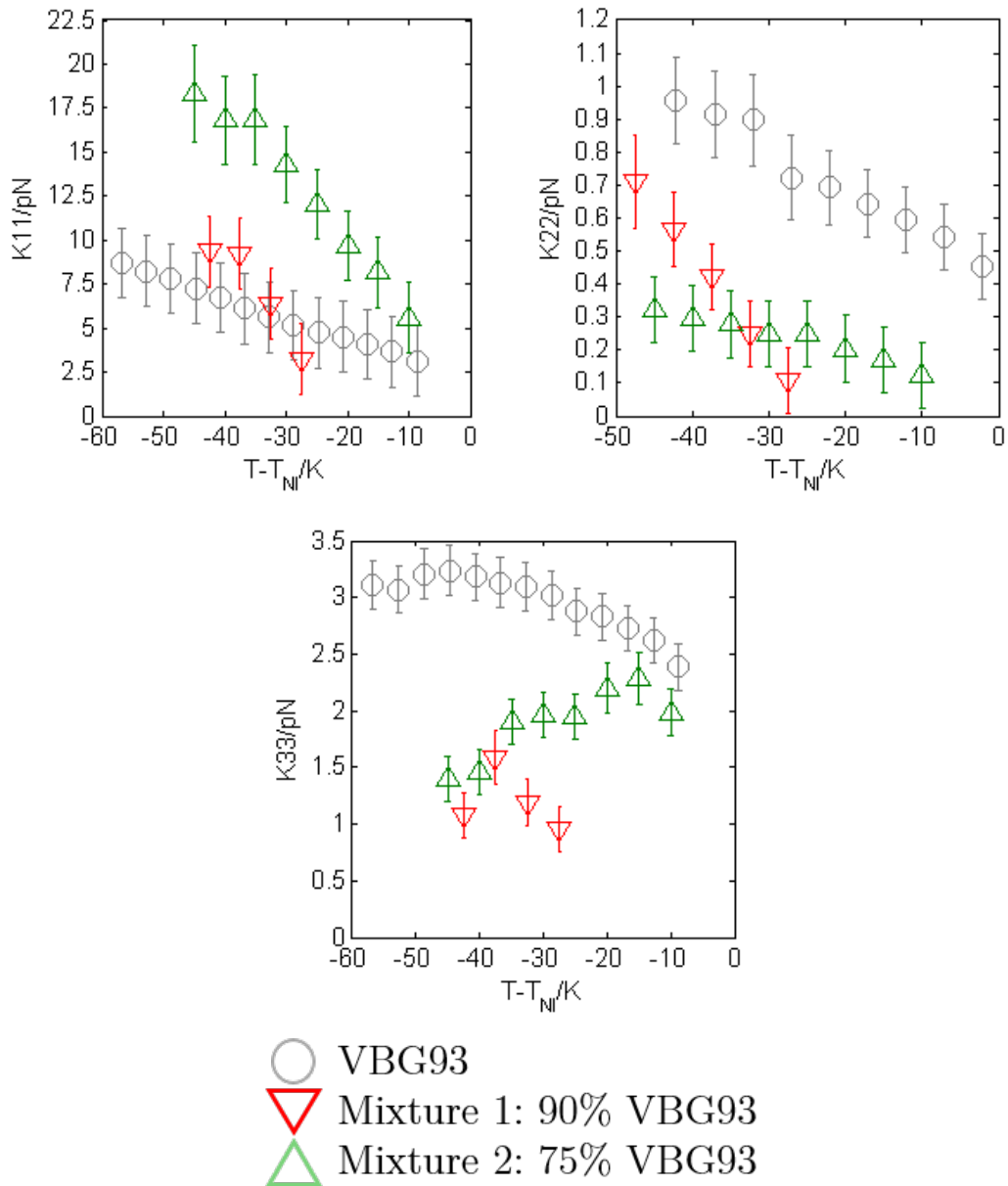


Figure 6.11: The splay, K_{11} (a), twist, K_{22} (b), and bend, K_{33} (c) elastic constants as a function of $T - T_{NI}$ for VBG93 and mixtures 1 and 2.

6.4.7 Elastic behaviour in smectic phase mixtures

Considering the elastic behaviour in the nematic phases of DT12 and mixtures 3-5 (shown in figure 6.12) we find that these samples all exhibit K_{22} values smaller than VBG93 across the whole nematic range, yet they do not exhibit a DC phase. Interestingly mixtures 3-5 exhibit K_{22} values larger than those exhibited by mixtures 1 and 2, yet mixtures 3-5 exhibit an underlying smectic phase whilst mixtures 1 and 2 exhibit underlying DC phases. The elastic behaviour of the bent-core mixtures suggest that DC phase in mixtures 1 and 2 is not solely driven by the elastic behaviour in the nematic phase.

Considering the elastic behaviour of just DT12 and mixtures 3-5, we find that as more VBG93 is added to DT12 that K_{11} reduces with respect to DT12, whilst K_{22} and K_{33} both increase with respect to DT12. The behaviour of the elastic constants as a function of concentration is expected and has already been discussed in section 5.2.3 in chapter 5. In the context of the underlying smectic phases, we find some interesting results; mixtures 3 and 4 exhibit similar K_{11} and K_{33} values across the nematic range, along with similar K_{11} and K_{33} values between DT12 and mixture 5. This behaviour is similar to the POM images of the smectic phases in the mixtures (figure 6.10); the textures observed for DT12 and mixture 5 are similar to each other, whilst the textures observed for mixtures 3 and 4 are similar, especially considering the birefringence colours. The plots in figure 6.12 suggest that the textures of the smectic phases exhibited by DT12 and mixtures 3-5 are somehow driven by the splay and bend elastic constants. However, given the behaviour of the spacing and tilt angle in the smectic phases of the mixtures, there is very little conclusive evidence that the elastic behaviour in the nematic phase of the mixtures are a driving factor.

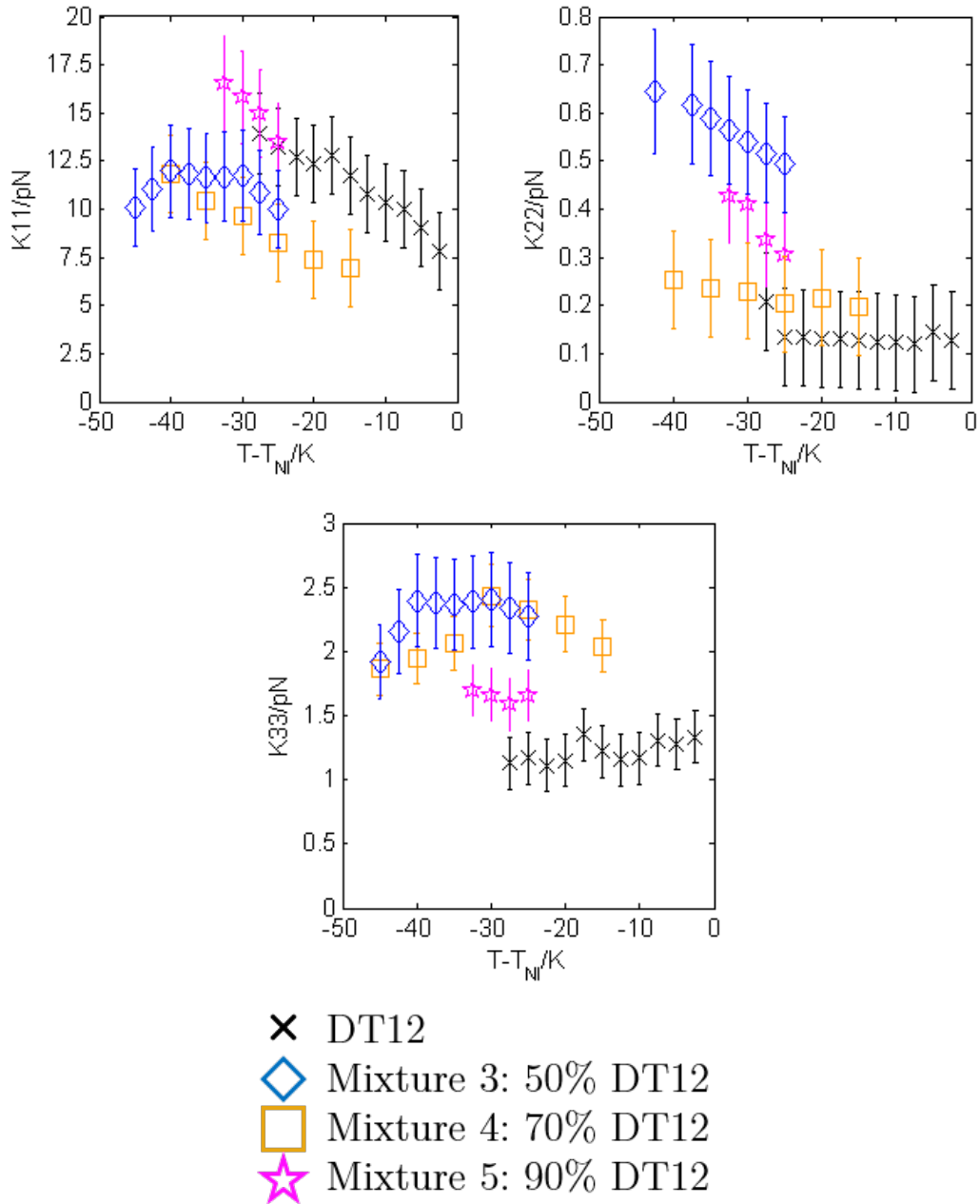


Figure 6.12: The splay, K_{11} (a), twist, K_{22} (b), and bend, K_{33} (c) elastic constants as a function of $T - T_{NI}$ for DT12 and mixtures 3-5.

6.5 Summary

To summarise, the X-ray scattering measurements for a number of bent-core liquid crystal mixtures have been reported. The spacing and FWHM for the mixtures have been compared with those measured for the two pure materials, and it was found that the mixtures exhibited two different underlying phases below the nematic phases, dependent on the concentrations of the bent-core liquid crystals in the respective mixture.

Mixtures 1 and 2 (90% and 75% VBG93 in the mixtures respectively) both exhibited a DC phase below the nematic phase, similar to VBG93. This was backed up the POM images which showed the phase being optically isotropic, as well as the spacing and FWHM values (figure 6.5) which behaved very similar to the DC phase observed in pure VBG93. Mixtures 3-5 (50%, 70% and 90% DT12 in the mixtures respectively) all exhibited a smectic phase below the nematic phase. The raw X-ray data taken for the mixtures 4 and 5 were very similar to that taken for DT12 suggesting the smectic phases in these mixtures were similar in structure to that observed in DT12. The raw X-ray data taken for mixture 3 suggested that the smectic phase had been aligned by the magnetic field in the X-ray scattering apparatus. Analysis of the X-ray scattering data was carried out to confirm these initial observations.

The spacing and FWHM values showed a very similar temperature dependence between mixtures 3-5 and DT12 (figure 6.7), although the absolute values differed slightly; the spacing decreased as more VBG93 was added to DT12, whilst the FWHM values measured for mixtures 3-5 were practically identical to each other, with the values measured for DT12 being found to be higher. The FWHM of the scattering peaks in the crystal phases were found to be comparable to those measured in the mixtures and as such reliable comparison of the FWHM between DT12 and mixtures 3-5 cannot be carried out due to the relatively low resolution of the apparatus set-up. The tilt angle of the director in the smectic phases was measured for these mixtures and it was found that the tilt angle increase as more VBG93 was added to DT12; DT12 exhibited the lowest tilt angle (19.9-21.5°) and mixture 3 exhibited the tilt angle (29.0-32.2°) in the smectic phases. The

behaviour of the tilt angle as a function of concentration was found to be similar to the behaviour of the spacing which was to be expected.

POM images were taken for the smectic phases in mixtures 3-5 to compare with the smectic phase observed in pure DT12. Based on the X-ray scattering data, it was initially believed that mixtures 4 and 5 would exhibit smectic phases that looked similar to the smectic phase observed in DT12, with mixture 3 exhibiting a different texture. Instead what was found was that, based on the texture observed using POM, DT12 and mixture 5 exhibited similar smectic phases to each other, whilst mixtures 3 and 4 exhibited similar smectic phases. The X-ray data and POM images suggest that the smectic phases exhibited by DT12 and mixtures 3-5 are similar to each other and that any differences are due to the concentration of the particular mixture.

It was believed that the elastic behaviour in the nematic phases of the mixtures would provide more information on the underlying phases in the mixtures. Considering VBG93 and mixtures 1 and 2, the results shown in figure 6.11 showed that the elastic behaviour of the mixtures agreed with the inequality $K_{24} < K_{22}$, with mixtures 1 and 2 exhibiting lower K_{22} values compared to VBG93 and with both mixtures exhibiting DC phases. However the results shown in figure 6.12 show that DT12 and mixtures 3-5 also exhibit lower K_{22} values than VBG93 yet these samples exhibited underlying smectic phases, suggesting that the formation of the DC phases in mixtures 1 and 2 are not solely due to the elastic behaviour in the nematic phase. Figure 6.12 also showed that DT12 and mixture 5 exhibited similar K_{11} and K_{33} values to each other, whilst mixtures 3 and 4 exhibit similar K_{11} and K_{33} values across a similar temperature range. The elastic behaviour, whilst providing some information on why mixtures 3 and 4 exhibit smectic phases that look similar optically does not provide enough information to explain why mixtures 3-5 exhibit the smectic phases, whilst mixtures 1 and 2 exhibit DC phases.

Clearly, more is needed to fully understand the mechanisms to forming the DC phase and other exotic phases in bent-core systems. One consideration that would provide extra information would be to look at a mixture that contains $\sim 60/65\%$ DT12 in the mixture. This will be discussed further in the future work section of chapter 8. The next chapter will look at the self-assembly of filaments in mixtures

6.5 Summary

of calamitic liquid crystals doped with bent-core liquid crystals; more specifically the phase behaviour that the mixtures exhibit, using techniques such as POM, AFM and SEM to illustrate the formation of the filaments.

Chapter 7

Phase Behaviour in Calamitic and Bent-Core Liquid Crystal Mixtures

7.1 Introduction

This chapter will go into detail on the phase behaviour exhibited by liquid crystal mixtures that exhibit filaments that form through self-assembly. These filaments were introduced in chapter 5 and are detailed in the paper by Gleeson et al.[112] The liquid crystal mixtures were made by doping calamitic liquid crystals with $\sim 10\%$ VBG93. A number of experimental techniques were used to gain a better insight into the formation of the filaments. The majority of the experiments were carried out by myself. The high resolution microscopy was carried out at the Merck Chemicals Ltd. Chilworth site with help from James Allen (AFM) and Vicki Poole (SEM). The investigations on the director field behaviour were carried out with help from another student in the group, Ethan Jull.

Filament structures have been a topic of research for a number of years since the 1990s, most notably in the form of polymer stabilised liquid crystals (PSLCs).[126–128] These systems were initially investigated for improving the liquid crystalline properties in devices, such as director field stability and the electro-optic properties. Filament structures have also been found to be exhibited in bent-core molecules, more specifically in systems that exhibit the B4 phase which is known to exhibit

helical nanofilaments.[129] This is an important distinction as the systems that are described in this chapter contain filaments that have no obvious helicity. More recently, mixtures of bent-core molecules with calamitic molecules have shown viscoelastic phase separation analogous to those seen in cellular structures.[130] These are especially interesting to those investigating morphology and stability in biological systems and this is noted by Anjali et al.[130] in their paper. Gleeson et al. have already investigated a novel binary system that includes a small amount of a bent-core liquid crystal in 5CB.[112] It was discussed in that paper how the filaments interacted with the bulk nematic, studied using a number techniques such as X-ray scattering and rheology. Whilst the results shown in this paper provide a lot of information on the filament structures exhibited by mixture 6 (introduced in chapter 5), there still remain a number of questions that have yet to be answered;

- (i) Do the filaments exhibit any helical structure? It should be noted that helical structures are observed in almost all other nanofilaments.
- (ii) Does the phase in which the filaments grow influence the self-assembly?
- (iii) How does the nematic director influence the formation of the filaments?
- (iv) What is the influence of the time dependency on the self-assembly of the filaments?

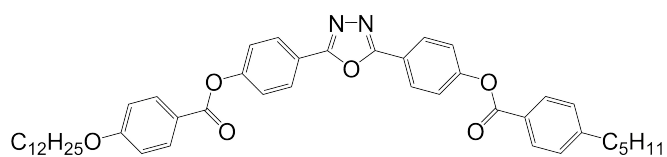
In this chapter I introduce a number of binary and tertiary mixtures of bent-core liquid crystals in calamitic liquid crystals, with the purpose of answering the questions provided above.

7.2 Experimental Methodology

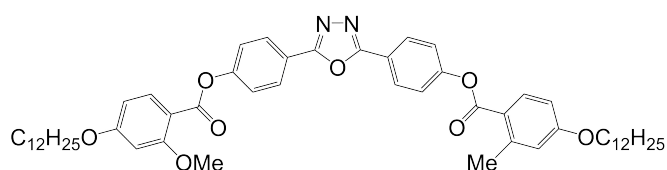
7.2.1 Materials

The bent-core liquid crystals used to dope calamitic liquid crystals were DT12 and VBG93; their molecular structures and phase transition temperatures are shown in figure 7.1. The molecular structures and phase transition temperatures of the pure calamitic liquid crystals are shown in figure 7.2. In addition to the pure materials 5CB (nematic) and 8CB (nematic and SmA), a chiral nematic/blue phase mixture, TM 1001 was also used as well as a photo-chromic calamitic liquid crystal, BAAB2 which is an azo-benzene derivative.[66, 67] The transition temperatures of the pure materials and the mixtures were determined by differential scanning calorimetry (DSC) and confirmed using polarising optical microscopy (POM); the temperatures of the mixtures in table 7.1 were taken from the DSC measurements. Mixtures were made by dissolving the pure compounds in a vial using dichloromethane (DCM) before allowing the DCM to evaporate completely at a temperature of 50 °C. Figure 7.3 shows a graphical representation of the transition temperatures for all mixtures from table 7.1. Mixtures 13 and 14 both include small amounts of the bent-core material DT12 in the mixtures. Mixtures of 10% DT12 in calamitic liquid crystals showed no evidence of filament growth. However mixtures 13 and 14 do exhibit filament growth. These mixtures were investigated to gain an insight into the inclusion of DT12 into the filament mixtures. The birefringence measurements were carried out on mixtures 13 and 14 and the results are discussed in section 7.5

7.2 Experimental Methodology

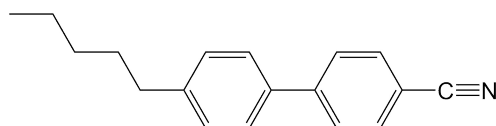


VBG93
Iso 230 N 170 DC 100 Cr

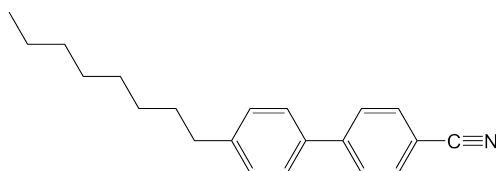


DT12
Iso 115 N 88 SmX 64 Cr

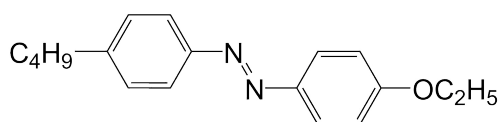
Figure 7.1: Molecular structures and phase transitions temperatures for the liquid crystals used in this chapter. Temperatures are recorded in °C.



5CB
Iso 35 N 18 Cr



8CB
Iso 40 N 33.5 SmA 21.5 Cr



BAAB2
Iso 83 N 33 Cr

Figure 7.2: Molecular structures and phase transitions temperatures for the liquid crystals used in this chapter. Temperatures are recorded in °C.

7.2 Experimental Methodology

Mixture Number	Composition	Phase Transitions T/°C
Mixture 6	10:90 VBG93:5CB	N+F 40.5 I+F 51.8 Iso
		Iso 49.0 N 26.1 N+F
Mixture 7	10:90 VBG93:8CB	SmA+F 36.0 N+F 45.6 I+F 60.1 Iso
		Iso 52.0 N 40.0 N+F 38.4 SmA+F
Mixture 8	5:95 VBG93:5CB	N+F 39.7 I+F 49.1 Iso
		Iso 41.9 N 28.0 N+F
Mixture 13	10.4:1.2:88.4 VBG93:DT12:5CB	N+F 42.7 I+F 53.7 Iso
		Iso 51.6 N 28.4 N+F
Mixture 14	9.9:3.3:86.8 VBG93:DT12:5CB	N+F 44.5 I+F 55.1 Iso
		Iso 54.3 N 30.6 N+F
Mixture 15	10:10:80 VBG93:BAAB2:5CB	N+F 48.8 I+F 58.4 Iso
		Iso 56.2 N 30.6 N+F
Mixture 16	8:92 VBG93:TM 1001	SmA+F 24.6 N*+F 32.0 BPII+F 42.6 BPI+F 45.5 Iso+F 68.1 Iso
		Iso 52.6 BPI 49.3 BPII 45.5 N* 35.4 N*+F 26.4 SmA+F

Table 7.1: Compositions of mixtures used in this chapter with the corresponding phase transitions and transition temperatures determined on cooling, where N* = chiral nematic phase, N*+F = chiral nematic phase with filaments, BPI = blue phase 1, BPI+F = blue phase 1 with filaments, BPII = blue phase 2, and BPII+F = blue phase 2 with filaments.

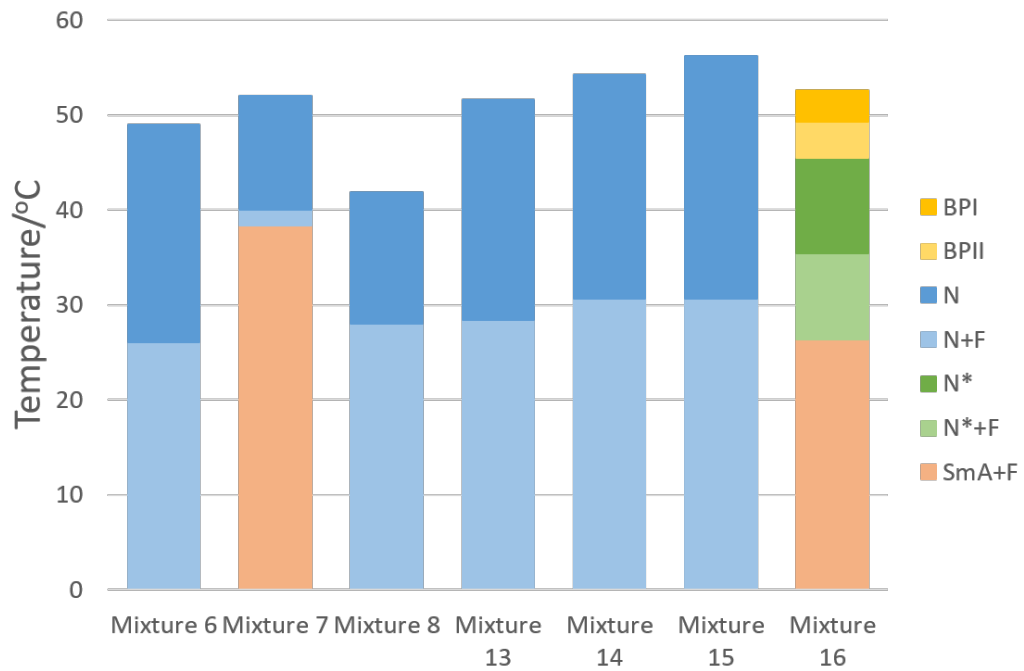


Figure 7.3: Histogram showing the phase transitions with the transition temperatures on cooling for the mixtures discussed in this chapter. Everything above the bars indicates the isotropic phase, with the dark blue bars representing the nematic phase, the light blue bars representing the nematic phase with filaments, the light orange bars representing the smectic A phase with filaments, the dark green bar representing the chiral nematic phase, the light green bar representing the chiral nematic phase with filaments, the gold bar representing the blue phase 1 phase, and the light gold bar representing the blue phase 2 phase.

7.2.2 High Resolution Microscopy

Atomic force microscopy (AFM) and scanning electron microscopy (SEM) were used to obtain high resolution images of the filament structures. The methodology for these experiments can be found in section 3.9 of chapter 3.

7.2.3 Measurements of birefringence

The birefringence Δn of the nematic phase (with filaments growing) was measured using a Berek compensator, as described in section 3.8 in chapter 3. The compensator was inserted into the polarising optical microscope at 45° to the crossed polarisers. The liquid crystal device was then orientated such that the director of the liquid crystal was perpendicular to the fast axis of the compensator. The tilt α of the compensator was adjusted such that its retardance $\Delta\Gamma$ matched the retardance due to the liquid crystal device, thus cancelling each other out. The equations used to measure the tilt and thus calculate the birefringence of the liquid crystal in the device (equations 3.13, 3.14, and 3.15) can be found in section 3.8 in chapter 3. These equations allowed the birefringence to be determined with an accuracy of $\sim 5\%$ or 0.01 (whichever is larger). All values of the birefringence are quoted for monochromatic light of wavelength 589 nm. Birefringence measurements were carried out on 5CB, and mixtures 6, 8, 13, and 14.

7.3 High Resolution Microscopy Measurements

High resolution microscopy (AFM and SEM) was carried out in order to find if there was any helical nano structure exhibited by the filaments. There have been a number of groups who have extensively investigated the helical nano-filament (HNF) phase in bent-core mesogens.[129, 131–134] It is thus important to check helicity within the filaments, to confirm whether or not the filaments are indeed the HNF phase observed in other bent-core systems. It has been shown that the filaments observed in the HNF phase exhibit SmA type ordering.[129] Initial X-ray scattering results of the filaments exhibited by mixture 6 (10% VBG93 in 5CB) suggest that the filaments investigated here grow in a columnar fashion.

7.3 High Resolution Microscopy Measurements

The X-ray scattering data provide initial proof that the filaments in our mixtures are not similar to those observed in the HNF phase.

The measurements were carried out on three different filament mixtures, these being mixtures 6, 7, and 16. The two high resolution techniques used were AFM and SEM. The mixtures used were chosen as they each exhibit filament growth in different phases; mixture 6 exhibits filament growth in the nematic phase, whilst filament growth can be observed in the SmA phase in mixture 7, and in the N* phase in mixture 16. These measurements also provided information on the filament formation in phases besides the nematic phase. Standard POM was unable to determine whether the filament structure is the same irrespective of the phase it grows in. It was believed that AFM and SEM would provide more answers.

Due to the three different mixtures investigated using the high resolution microscopy techniques, it is appropriate to present the results for each mixture individually, comparing the results from AFM and SEM for each mixture with each other. Thus this results section will be discussed in three parts; the first will detail the results obtained for mixture 6 (filaments grown in the nematic phase), whilst the second and third parts will detail the results obtained for mixtures 7 (filaments grown in the SmA phase) and 16 (filaments grown in the N* phase) respectively.

The high resolution microscopy (AFM and SEM) measurements were carried out at the Merck Chemicals Ltd. Chilworth site.

7.3.1 5CB mixture; mixture 6

SEM images have been taken before on this mixture, shown in the paper by Gleeson et al.[112] However AFM had not been carried out so it is appropriate to compare the AFM and SEM images with each other. Not only was this mixture used to check for any helicity in the filaments, but also as a reference to investigate if the filaments grow differently if they are formed in a different phase from the nematic phase. The SEM images taken for mixture 6 are shown in figure 7.4.

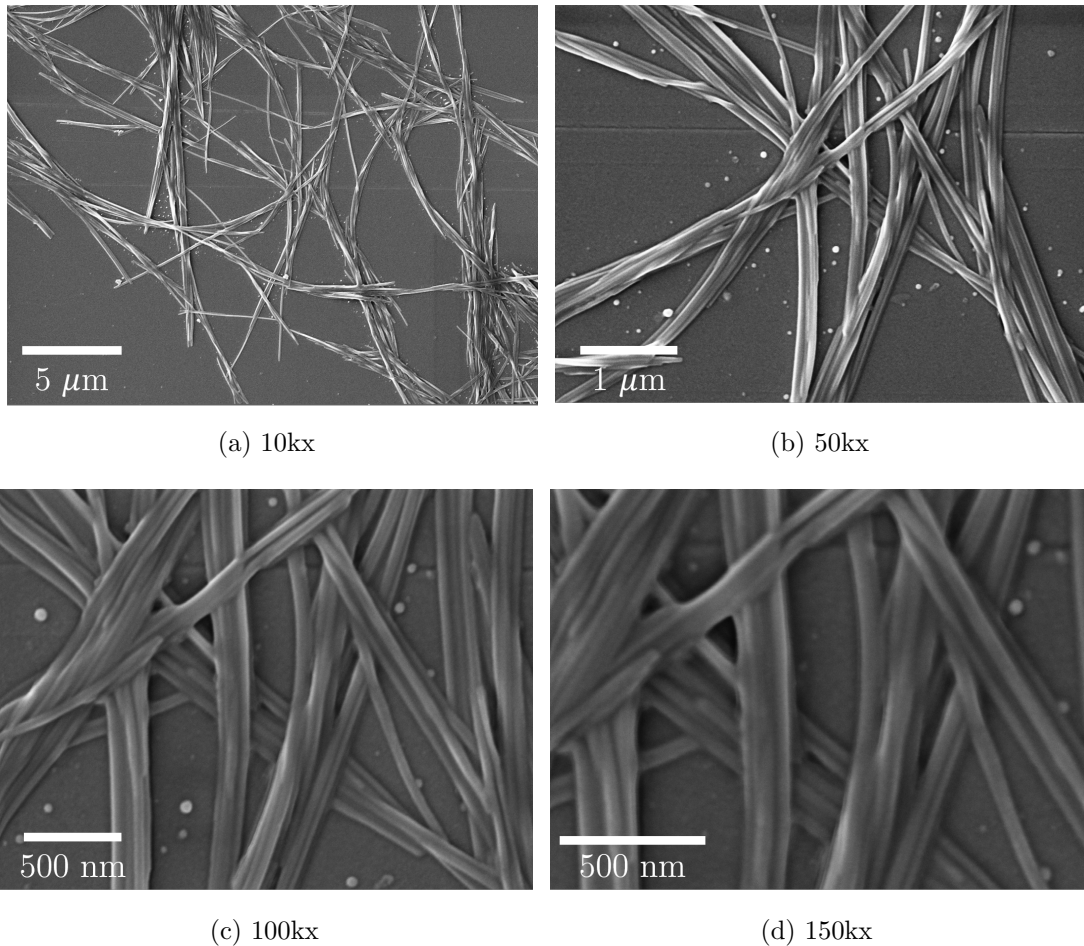


Figure 7.4: SEM images of mixture 6 (10% VBG93 in 5CB) taken at 10kx (a), 50kx (b), 100kx (c), and 150kx (d) magnifications.

7.3 High Resolution Microscopy Measurements

It can be seen from the images shown in figure 7.4 that even filaments of thickness ~ 50 nm show no evidence of a helical structure. Comparatively, the helical fibres observed in HNF phases exhibit clear helicity at these length scales.[129] The images give clear proof that the filament structures formed in mixture 6 are not part of the HNF phase, and suggest that the columnar structure proposed by Gleeson et al.[112] is more correct. The images taken of the filaments using AFM (shown in figure 7.5) also show no obvious helicity in the filaments. However, it is interesting to note the "weaving" structure that the filaments exhibit as well as the apparent bifurcations in the structure.

7.3 High Resolution Microscopy Measurements

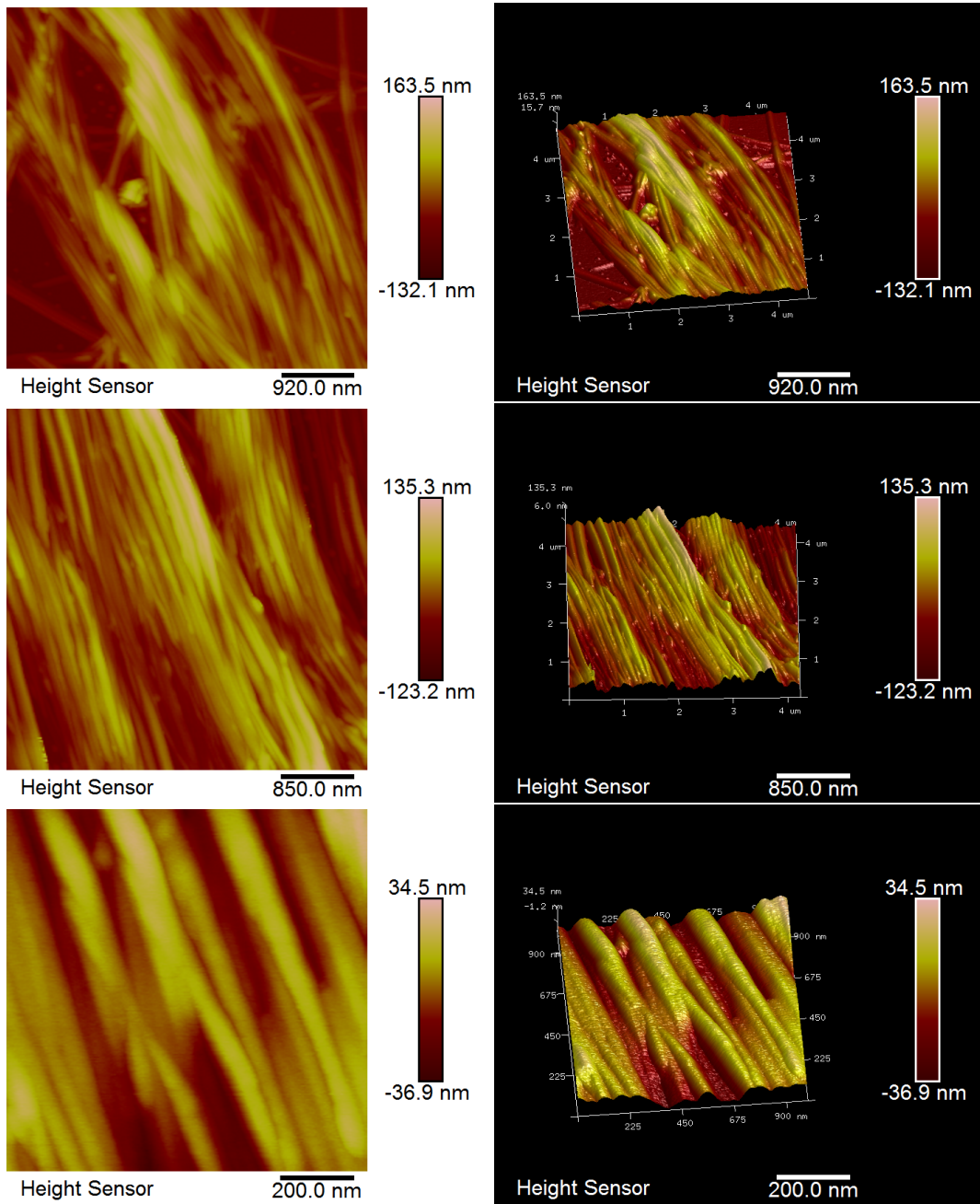


Figure 7.5: AFM images of mixture 6 (10% VBG93 in 5CB). The left hand images show the 2D images and the right hand images show the corresponding 3D images taken. The magnification increases from top to bottom.

7.3.2 8CB mixture; mixture 7

This section will show the AFM and SEM measurements taken for mixture 7 which is a mixture of 10% VBG93 in 8CB. The filaments were formed in the SmA phase of the mixture. The SEM and AFM images taken for mixture 7 are shown in figures 7.6 and 7.7 respectively. Similar to mixture 6, there is no evidence of helicity observed by the filaments grown in the SmA phase. Interestingly there is no discernible difference in the way the filaments have formed in the SmA phase of mixture 7, compared with the way the filaments formed in the nematic phase of mixture 6.

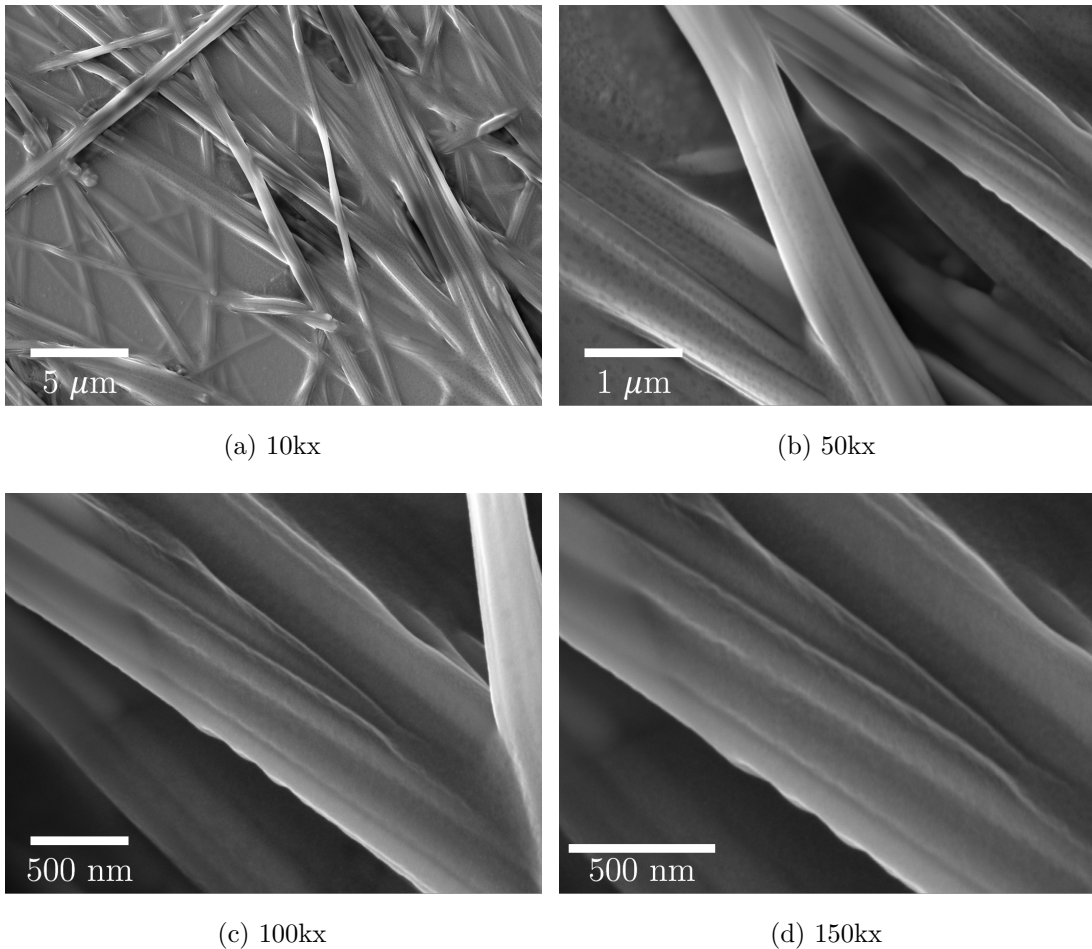


Figure 7.6: SEM images of mixture 7 (10% VBG93 in 8CB) taken at 10kx (a), 50kx (b), 100kx (c), and 150kx (d) magnifications.

7.3 High Resolution Microscopy Measurements

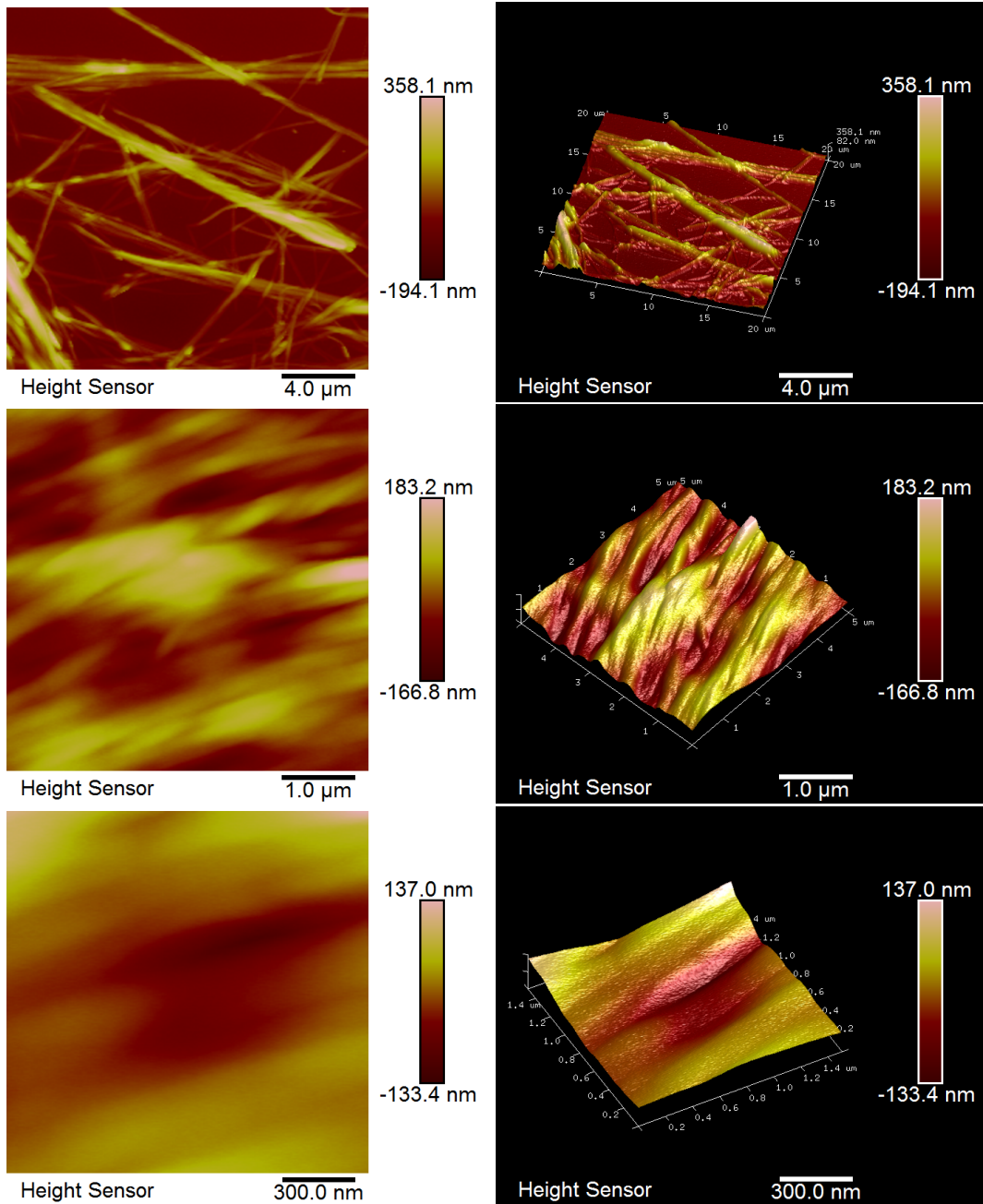
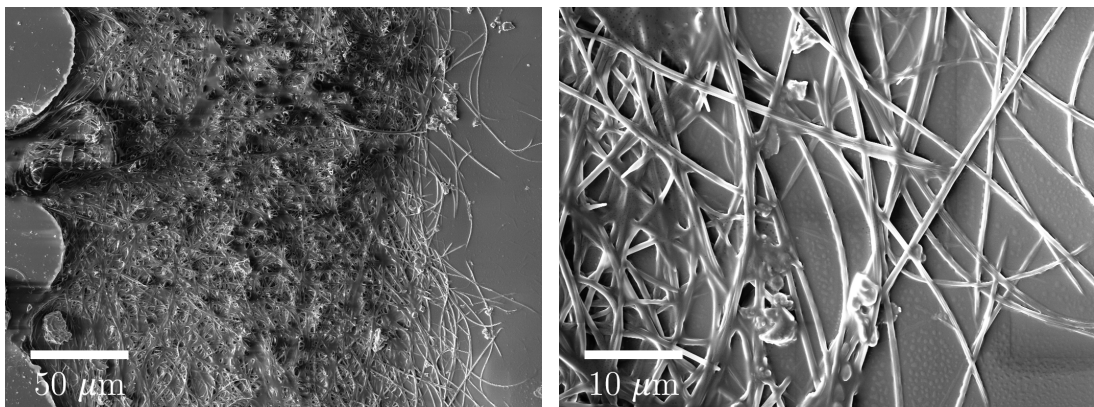


Figure 7.7: AFM images of mixture 7 (10% VBG93 in 8CB). The left hand images show the 2D images and the right hand images show the corresponding 3D images taken. The magnification increases from top to bottom.

7.3.3 TM 1001 mixture; mixture 16

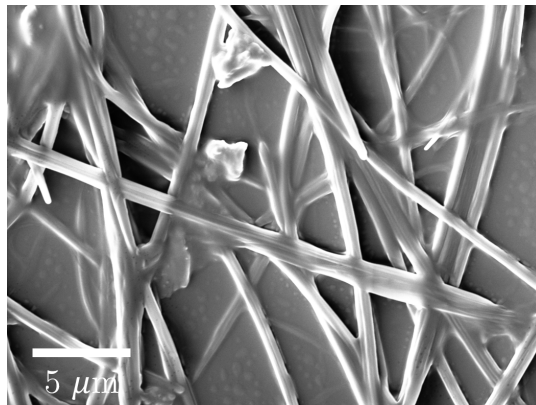
The final mixture that was investigated using AFM and SEM was mixture 16 which is a mixture of 8% VBG93 in TM 1001. The filaments were formed in the N^* phase of the mixture. The SEM and AFM images taken for mixture 16 are shown in figures 7.8 and 7.9 respectively. As with mixture 6 and 7, the images show no evidence of helical structure within the filaments grown in mixture 16. There is also no evidence that the filaments have grown in a specific manner due to the N^* phase; the filaments seem to grow in an undefined manner in the nematic, SmA and N^* phases, with no correlation on what phase the filaments have been grown in.

7.3 High Resolution Microscopy Measurements



(a) 1kx

(b) 5kx



(c) 10kx

Figure 7.8: SEM images of mixture 16 (8% VBG93 in TM 1001) taken at 10kx (a), 50kx (b), 100kx (c), and 150kx (d) magnifications.

7.3 High Resolution Microscopy Measurements

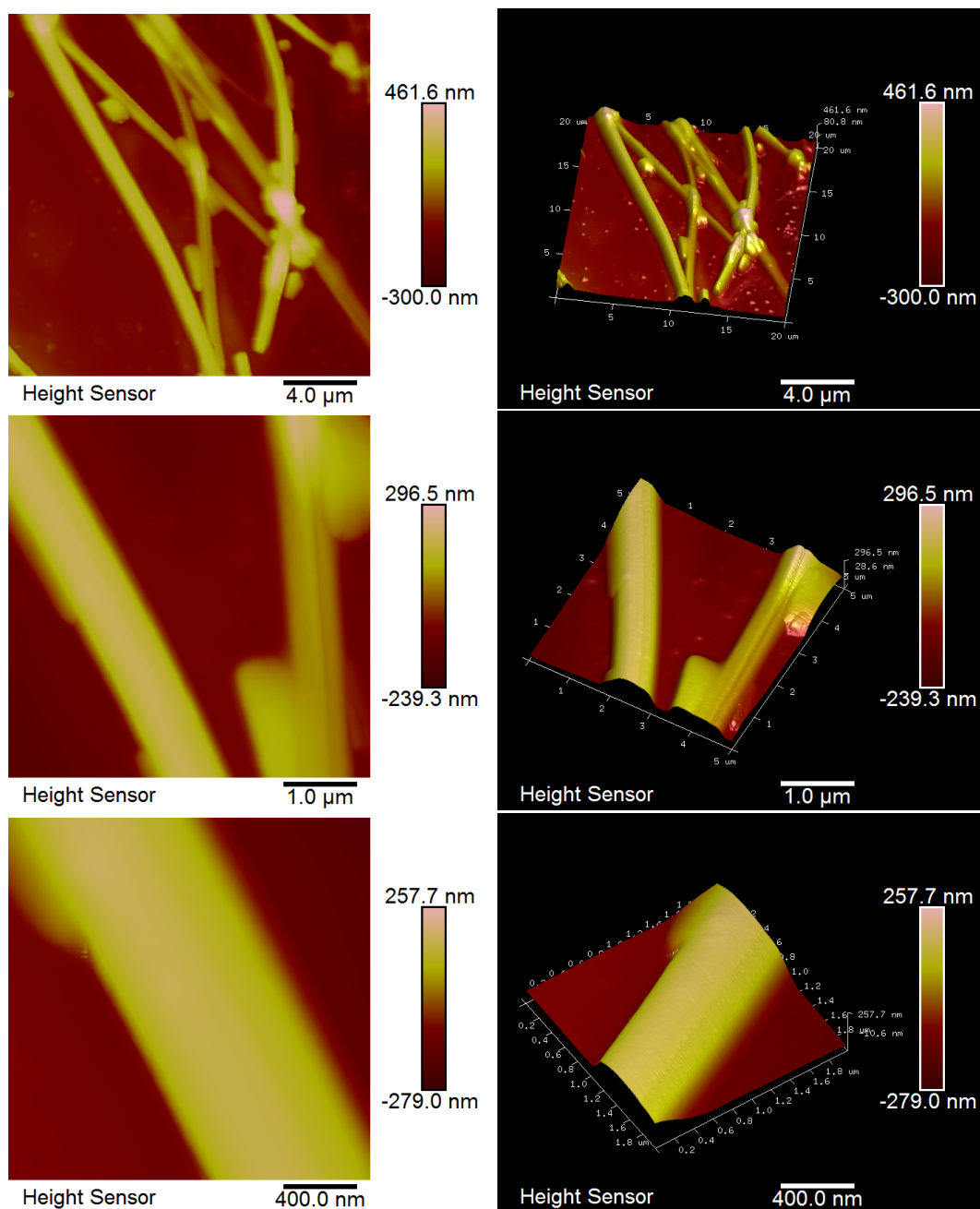


Figure 7.9: AFM images of mixture 16 (8% VBG93 in TM 1001). The left hand images show the 2D images and the right hand images show the corresponding 3D images taken. The magnification increases from top to bottom.

7.3.4 Discussion

This section has answered one of the questions that Gleeson et al.[112] had yet to answer; the filaments do not exhibit any helical structure, even down to a length scale of ~ 50 nm. The AFM and SEM also seem to have answered the question on whether the phase in which the filaments grow in affects the manner of the filament growth. However these results have been obtained by observing the behaviour of the filaments on the nanoscale; observations of the filaments on the macro-scale have shown different behaviour, and this will be discussed in the next section.

7.4 Director Field Behaviour in Filament Mixtures

This section details the results on the director field behaviour in the filament mixtures. This work aims to answer the question of whether the nematic director has any influence on the self-assembly of the filaments.

7.4.1 Initial observations in the photo-chromic mixture

Mixture 15 was used for the measurements of understanding the director field behaviour. This mixture included 10% of BAAB2 which is an azo-benzene derivative photo-chromic. This material was included to allow more control over the nematic phase as the photo-chromic can induce iso-thermal phase transitions of the background nematic to an isotropic phase. It was believed that if the azo-benzene also forms part of the filaments, then the filaments might also undergo a phase change when illuminated. However no change in the filaments was observed when the system was illuminated and the iso-thermal phase transition was induced. Instead this nematic system allowed a clear observation of the direction of growth of the filament structures, which was found to be at $\sim 60^\circ$ either side of the director. This is shown in figure 7.10.

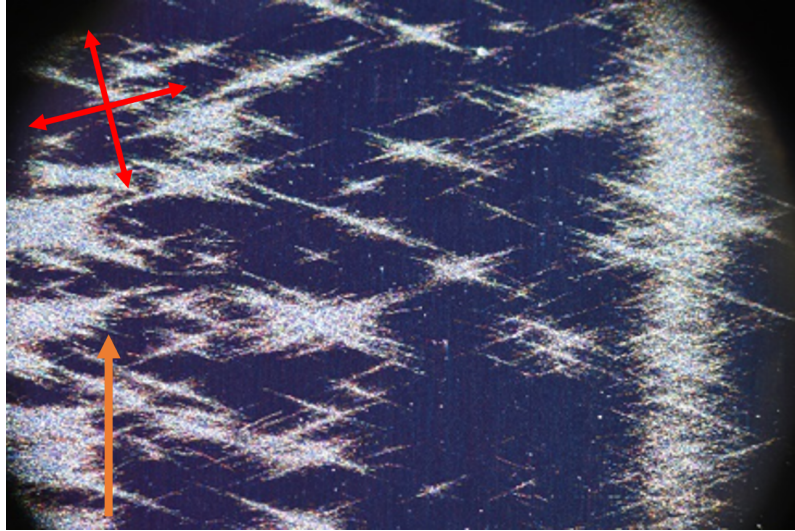


Figure 7.10: Growth of the filaments as the system is cooled through the nematic phase. The orange arrow shows the direction of the nematic director, with the red arrows showing the orientations of the polariser and analyser.

It is important to note that the filaments do deviate from this average angle, generally curving slightly as they grow larger. The image in figure 7.10 is a surprising result given that one would expect the filaments to grow along the director.

7.4.2 Observations in the SmA mixture

Investigations were also taken using mixture 7 (10% VBG93 in 8CB) to gain an insight into how the the filaments grew in the SmA phase. Figure 7.11 shows an image of how the filaments appeared in the I+F phase. It is clear from the image that the filaments grown in the SmA phase of 8CB have grown in very straight lines perpendicular to the director. The image suggests that filaments have grown along the smectic layers, in contrast to the SEM images taken for mixture 7 (figure 7.6) which showed very little orientation of the filament growth. Figures 7.10 and 7.11 suggest that the self-assembly of the filaments is affected by the bulk liquid crystal phase; in the nematic phase of 5CB the filaments grow at $\sim 60^\circ$ either side of the director, whilst in the SmA phase the filaments grow along the smectic layers.



Figure 7.11: Mixture 7 heated to the isotropic phase with filaments. Filaments were grown in the SmA phase. The red arrows represent the polariser orientations and the orange arrow represents the director orientation.

7.4.3 Investigations using a waveplate

Further investigations into the optical properties of the filaments in mixture 15 have yielded interesting results. From standard POM it can be seen that the filaments growing to the left of the director appear blue in colour, whilst those growing to the right appear more yellow (see figure 7.12a).

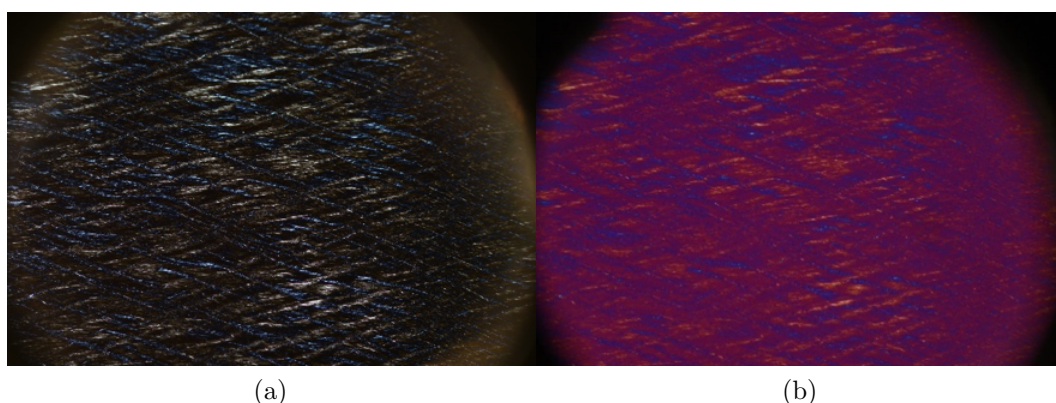


Figure 7.12: Sample in the isotropic phase with filaments, (a) without the waveplate, and (b) with the waveplate.

7.4 Director Field Behaviour in Filament Mixtures

By using a waveplate orientated at 45° to the left of the director this discrepancy can be observed more clearly. The sample shown in figure 7.12 is planar homogeneously aligned, thus the change in colour under a waveplate is not due to the calamitic mesogens, but rather the bent-core liquid crystal. When using a waveplate on an aligned sample the change in colour would be uniform across the sample, as the long axis of the molecules are aligned. However, as can be seen from figure 7.12b the filaments are exhibiting two different colours. This indicates that the long axes of the bent-core molecules are orientated along the fibres at different angles to each other. This suggests that the filaments are comprised of the bent-core molecules aligning in two different orientations, depending on which side of the director the filament has grown.

To investigate the properties of the filaments further, an un-rubbed planar device filled with mixture 15 (BAAB2 mixture) was also used. The alignment being un-rubbed in a preferential direction results in a schlieren nematic liquid crystal texture. As with figure 7.12, a waveplate was inserted into the POM setup. An image was taken when the sample was cooled to 42°C (nematic phase) from the isotropic phase and another when the sample was heated to 50°C from room temperature (isotropic phase with filaments). These are shown in figure 7.13.

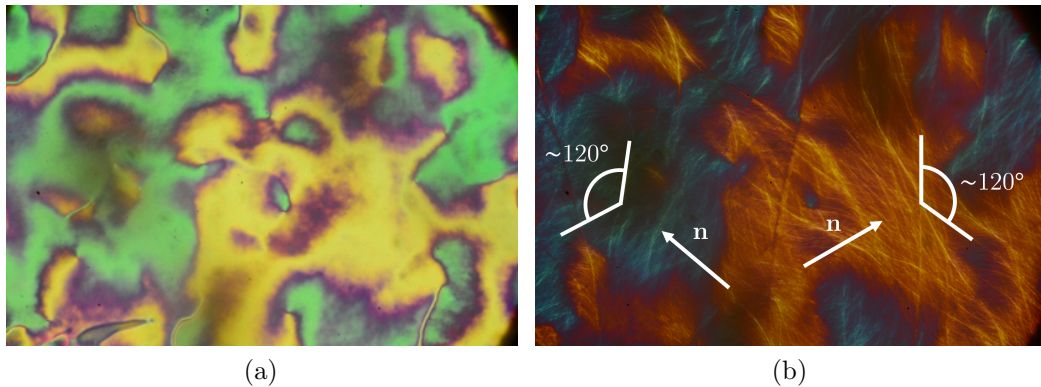


Figure 7.13: Mixture 15 in an un-rubbed planar aligned device with a waveplate in the optical set-up, (a) when the sample was cooled into the nematic phase at 42°C from the isotropic phase, and (b) when the sample was heated to isotropic phase with filaments still present at 50°C . The white arrows in (b) denote the direction of the nematic director in the two different regions, one blue in colour with the other orange in colour.

7.4 Director Field Behaviour in Filament Mixtures

It can be seen in figure 7.13a that the director is tilted in opposite directions between the domains with respect to the polariser orientation. This is inferred by one region being green in colour and the other region being yellow in colour. When the system is heated to the isotropic phase with filaments these two different regions remain separate, shown in figure 7.13b by the blue and orange regions respectively. It can be seen in figure 7.13b that the filaments in all regions grow at approximately 120° to each other (60° either side of the director), as seen by the filaments crossing one another. This suggests that the nematic director in the green regions (from figure 7.13a) were aligned at $\sim 45^\circ$ to the left of the vertical direction, whilst the yellow regions were at $\sim 45^\circ$ to the right of the vertical direction. This result is inferred using the knowledge that the filaments grow at 60° either side of the director. The approximate director of the background nematic is thus labelled, whilst the filament angle to each other is shown. It should be noted that the filaments seem to have templated the nematic structure in some way. This indicates that the filaments retain some of the calamitic mesogens which resulted in the domains observed in figure 7.13b being similar to those observed in figure 7.13a.

7.4.4 Proposed structure within the filaments

The results presented in this section provide more proof that the filaments are comprised mostly of the bent-core mesogen with a small amount of the calamitic host. A representation of the proposed structure in the nematic phase is shown in figure 7.14. The structure includes the fact that the filaments grow at $\sim 60^\circ$ either side of the nematic director. The diagram also indicates how the molecules in the filaments stay locked within the filaments even when the bulk nematic has undergone the transition into the isotropic phase.

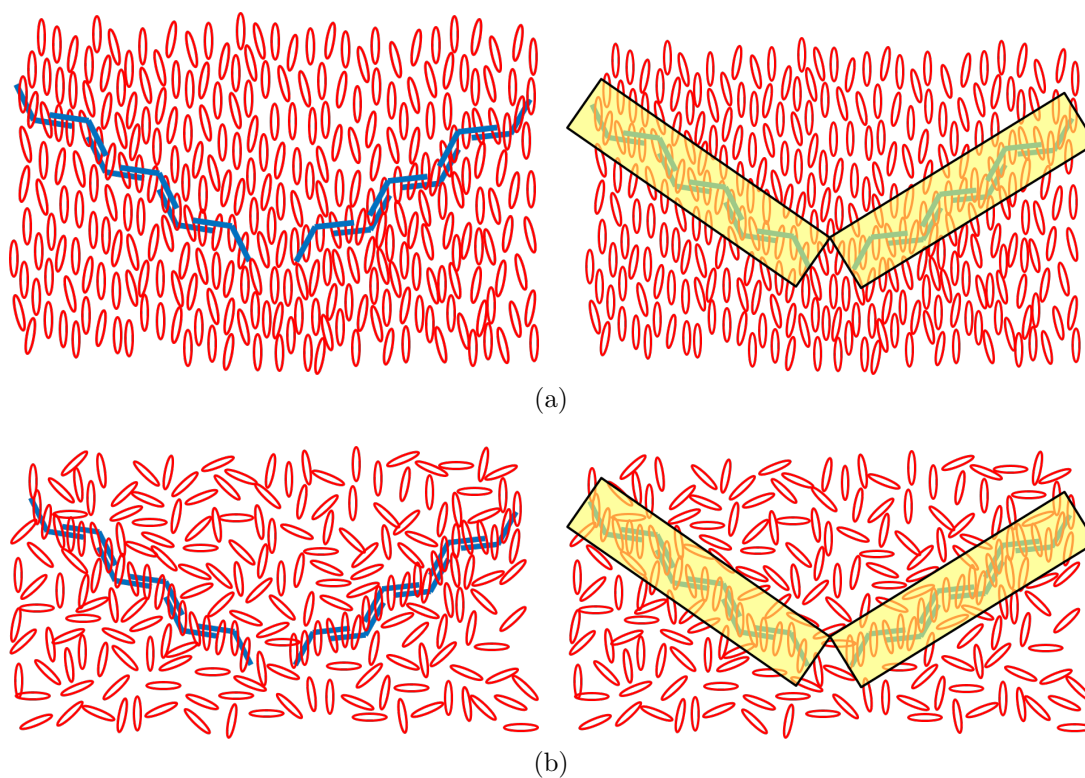


Figure 7.14: Proposed structure of the filaments in a bulk calamitic host, (a) in the nematic phase with filaments, and (b) in the isotropic phase with filaments. The right hand images show how the filaments are usually viewed using POM, with the left hand images showing the formation of the bent-core and calamitic liquid crystal molecules within the filaments.

7.4.5 Investigations under illumination of 405 nm light

As mentioned earlier in this chapter, the addition of BAAB2 in the mixture allowed direct control over the nematic phase without needing to change the temperature. By illuminating the sample using a blue laser of wavelength 405 nm, a trans-cis reversible isomerisation occurred for the BAAB2 molecules. This disrupted the packing of the 5CB molecules preventing the formation of the nematic phase. It is known that that the filaments grow in phases below the isotropic phase, with the liquid crystal director having a major effect of the self-assembly of the filaments. Thus by having the system in the isotropic phase at a lower temperature, one can gain insight into how the filament growth is affected by the lack of the director. The images presented in figure 7.15 were taken when the sample was cooled from the isotropic phase to 30 °C whilst under the illumination of the blue light. During illumination the BAAB2 undergoes the trans-cis isomerisation, meaning that the system investigated was in an induced isotropic phase from the start of the experiment.

It can be seen from figure 7.15 that the filaments nucleate in a much more random process to that observed when they grow in the nematic phase. There are multiple nucleation zones, instead of the filaments growing through the system in a more uniform manner. It is also important to note that the filaments are much smaller and fainter, resulting in a high camera exposure time being required to capture the images in figure 7.15. The images provide further proof that the director is an influential component of the self-assembly of the filaments; without the director (be it in the nematic phase or smectic phase), the filaments grow randomly throughout the system. When the director is present, the filaments grow in a much more orderly fashion with the direction determined by the liquid crystal phase itself.

The next section will detail the work on understanding the time-dependency of the self-assembly of the filaments. This work was carried out by investigating the birefringence of the filament systems in order to gain an insight into how the order of the system is affected by the filaments.

7.4 Director Field Behaviour in Filament Mixtures

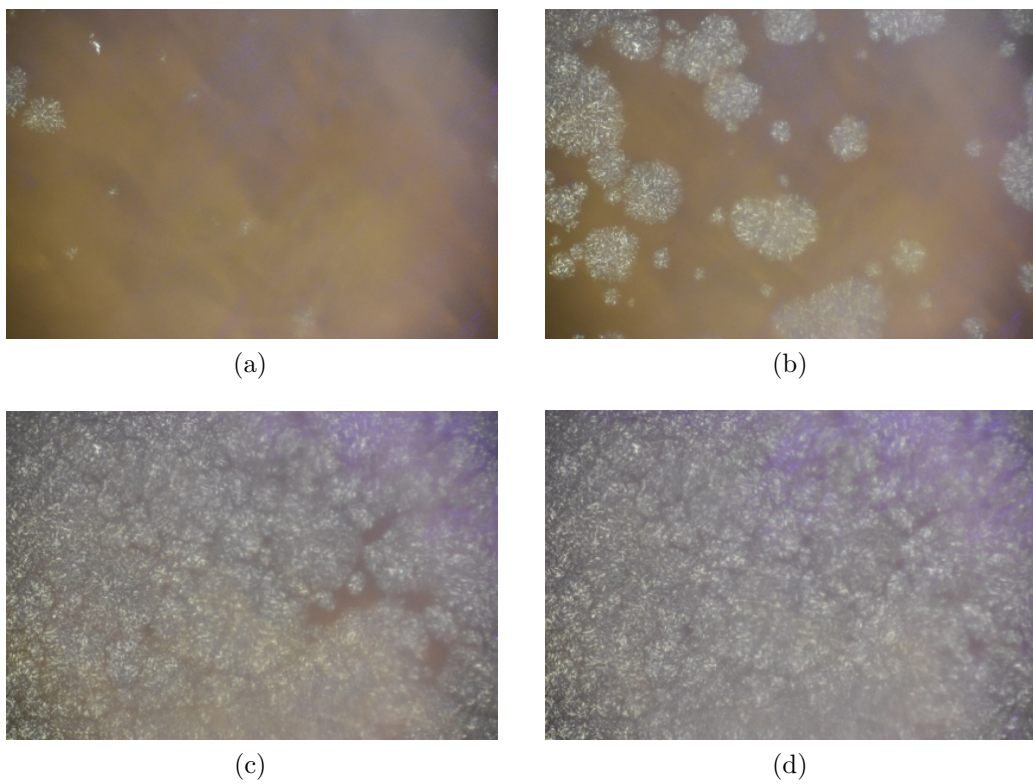


Figure 7.15: Growth of the filaments through mixture 15 whilst under the illumination of a 405 nm blue laser, whilst the sample was held at 30 °C.

7.5 Birefringence Behaviour in Filament Mixtures

Two sets of experiments were carried out by measuring the birefringence of the mixtures that exhibit filament formation. Measuring the birefringence as a function of temperature provides information on how the system changes as the temperature changes. In the filament mixtures it can give an insight into how the system changes as the filaments grow through the system. With regards to time dependent studies, Gleeson et al.[112] found that particular peaks measured via X-ray scattering merged over a time period of ~ 30 mins as the filaments formed. The results presented in that paper suggested a degree of time-dependent self-assembly of the filaments. Thus it seemed appropriate to measure Δn as a function of time as the filaments formed to gain an insight into how the system is affected by the filament growth. In this results section the temperature dependent measurements will be detailed first, with the time dependent measurements being shown after.

7.5.1 Temperature dependent studies

The birefringence was measured as a function of reduced temperature $T-T_{NI}$ throughout the whole nematic range until room temperature. The results are shown in figure 7.16a for mixtures 6 (10% VBG93), 8 (5% VBG93), 11 (10.4% VBG93 and 1.2% DT12), and 12 (9.9% VBG93 and 3.3% DT12), with 5CB being the calamitic host. The data for the pure compounds are also included in figure 7.16 for reference. It was shown by Kaur et al.[63] that oxadiazole based bent-core liquid crystals, such as VBG93 and DT12, have indistinguishable birefringence behaviour at the same reduced temperature. Hence in figure 7.16 I only include the birefringence measured for VBG93.

It can be seen, as expected, that the birefringence measured for the mixtures lie between that measured for the pure compounds, with the results being closer to those measured for 5CB. What is also clear to see is that the birefringence increases as the temperature of the systems decreased. All mixtures exhibited $\Delta n \sim 0.14$ near $T-T_{NI}$ increasing to ~ 0.20 for mixture 6, ~ 0.21 for mixture 8, ~ 0.20 for

7.5 Birefringence Behaviour in Filament Mixtures

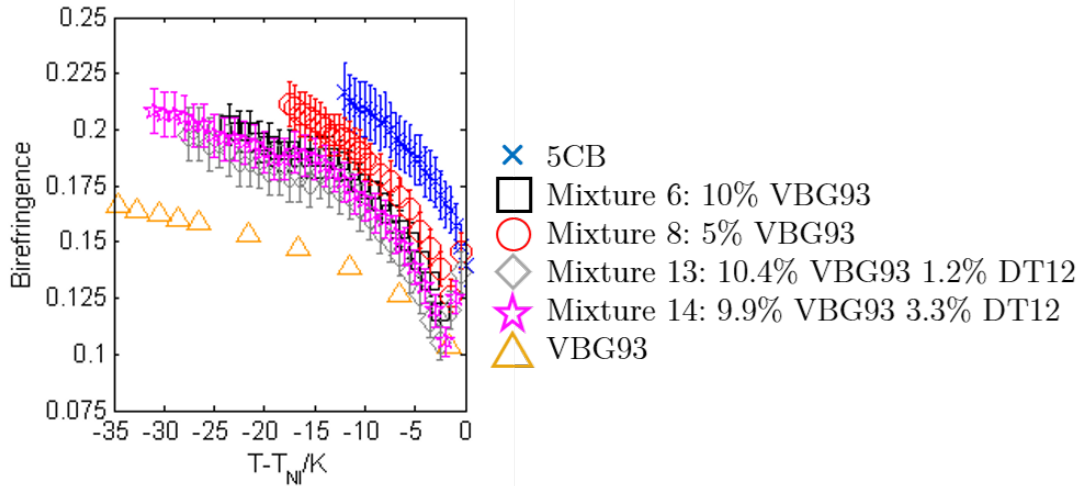


Figure 7.16: The birefringence Δn as a function of $T-T_{NI}$ for VBG93,^[63] 5CB, and mixtures 6, 8, 13 and 14. It should be noted that the lower temperature results for VBG93 have not been included for better clarity of the data taken for the mixtures.

mixture 11, and ~ 0.21 for mixture 12 as room temperature is approached. These results are consistent with what is observed in other nematic materials. However on closer inspection of the relationship between the birefringence and $T-T_{NI}$ there appears to be a "plateau" at $T-T_{NI} \sim -15$ K, which continues for a few degrees before the birefringence begins to increase again. Figure 7.17 shows this "plateau" better, using the data for mixture 6 as an example.

For normal nematic systems (e.g. 5CB and VBG93) one would expect a smooth curve with the birefringence increasing as the temperature decreases, so the "plateau" seen in figure 7.16 is unexpected. However it is important to note that the "plateau" occurs around the temperature that the filaments begin to grow within the systems for this rate of cooling. Through observations using POM it can be seen that there is a distinct colour change when the filaments grow (see figure 7.18) which indicates a change in the birefringence. The images in figure 7.18 were taken at a set temperature ($T-T_{NI} = -15$ K) and will be discussed in the next section on the time dependent measurements of Δn .

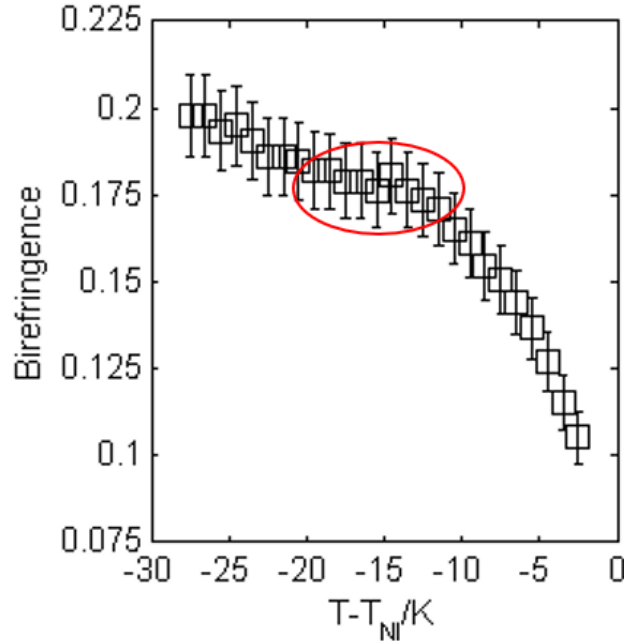


Figure 7.17: The birefringence Δn as a function of $T-T_{NI}$ for mixture 6 (black squares). The red circle highlights the "plateau" in the trend.

7.5.2 Time dependent studies

Gleeson et al.[112] showed that the filament growth was both temperature and time dependent. If the filament growth is indeed time dependent then it would be possible to measure the change in birefringence as a function of time when held at a specific temperature. Based on the data shown in figures 7.16 and 7.18, the time dependent measurements were carried out at a reduced temperature $T-T_{NI} = -15$ K with the birefringence being measured every minute for a period of 1 hour. Figure 7.19 shows the data taken for mixtures 6, 13 and 14, which are shown separately to provide a clear view of the relationship with time.

It can be seen that for all three sets of data shown in figure 7.19 that the birefringence decreases as a function of time. The decrease was measured to be 0.017 for mixture 6, 0.015 for mixture 11, and 0.014 for mixture 12. The magnitude of this change in Δn is an order of magnitude smaller than that measured across the whole nematic range of the mixtures. However considering that the change in birefringence occurs with the sample is held at one temperature,

7.5 Birefringence Behaviour in Filament Mixtures

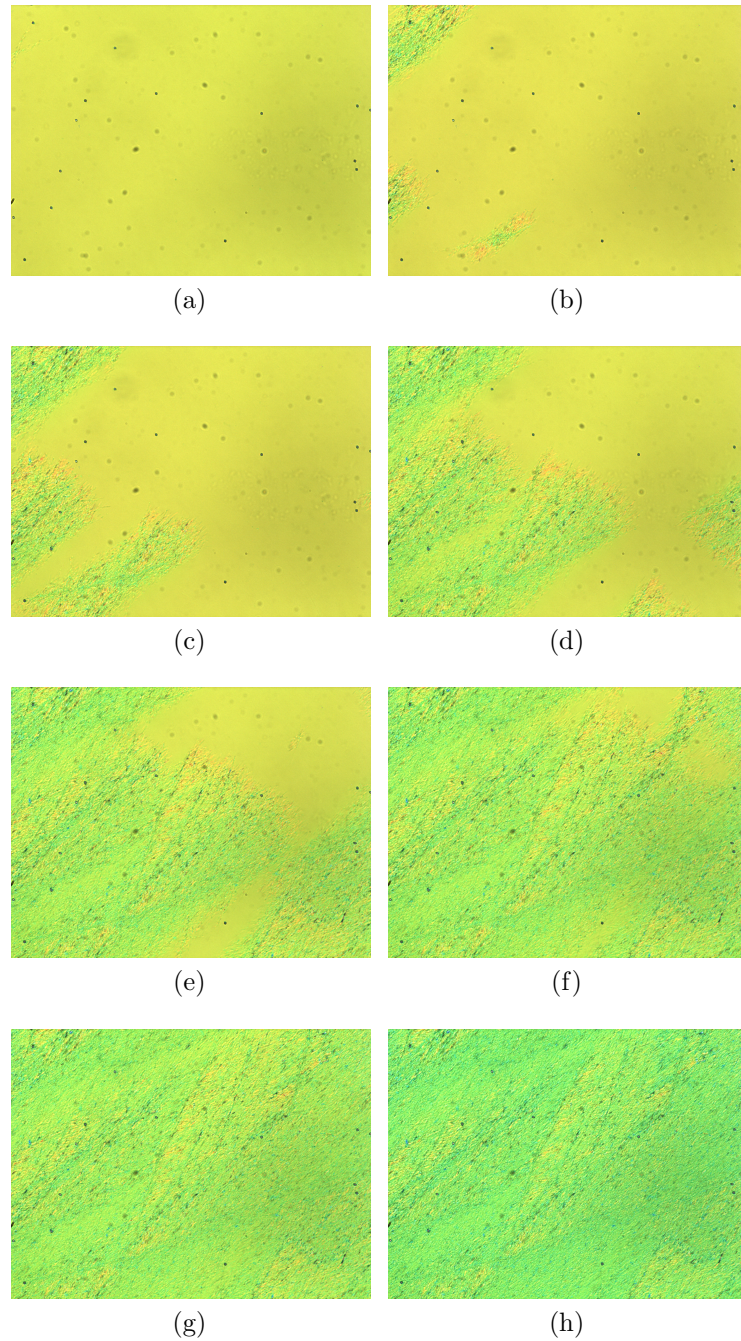


Figure 7.18: POM images of mixture 6 held at $T - T_{NI} = -15$ K whilst filaments grow through the sample. The times at which the images were taken were (a) 0 mins, (b) 1 min, (c) 2 mins, (d) 3 mins, (e) 4 mins, (f) 5 mins, (g) 6 mins, and (h) 60 mins.

7.5 Birefringence Behaviour in Filament Mixtures

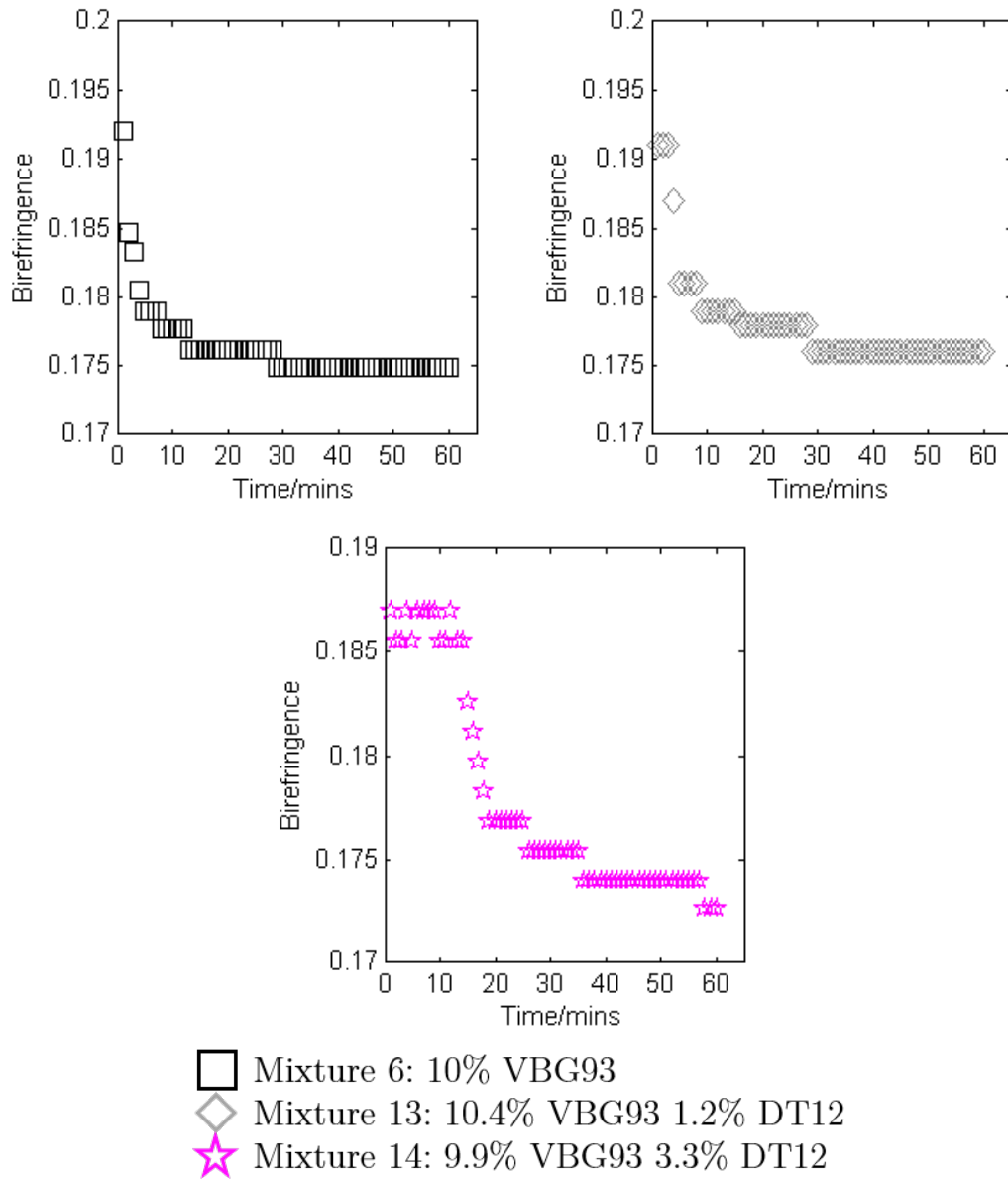


Figure 7.19: The birefringence Δn as a function of time for mixtures 6, 13 and 14.

7.5 Birefringence Behaviour in Filament Mixtures

this is a considerable difference to measure. The observations shown in figure 7.18 indicate that a decrease in birefringence is to be expected, as the colour change corresponds to a lower birefringence on the Michel-Lévy chart. It is known that the bent-core liquid crystals exhibit a lower birefringence compared to that measured for 5CB.[63] The decrease in Δn shown in figure 7.19 can be explained in two ways; first we can consider the filaments to be comprised of mainly the bent-core liquid crystal that is coming out of solution from the bulk 5CB. Thus when using POM, an increase in the amount of bent-core in the field of view is observed and hence a drop in the birefringence is measured when using the Berek compensator. The second explanation is based on the direction of the filament growth in the bulk nematic; the filaments grow at $\sim 60^\circ$ either side of the director, thus when they grow the effective birefringence that the system exhibits is lowered as the Δn values of the filaments acts against the birefringence of the bulk nematic. Considering the reduction in Δn overall, if the system is undergoing cooling then the drop in Δn due to growth of the filaments would counter-act the increase in Δn that naturally occurs in the bulk nematic. This helps explain the "plateau" seen in figure 7.16. Once the filaments have fully grown throughout the system the increase in birefringence, due to cooling, dominates over the decrease in birefringence due filament growth thus exhibiting an overall effective increase in Δn as the system cools further.

Time dependent behaviour has been reported before in liquid crystals by Collings et al.[135] and Bertrand et al.[136] The time dependent measurements carried out by these two groups were on chromonic liquid crystals that exhibited aggregation in the form of fibres and bundles (much like the systems shown in this paper). Using dynamic light scattering they found that the correlation function followed a $e^{-t^{1/2}}$ function. The birefringence data shown in figure 7.19 follows a similar relationship so it is interesting to note an analogy between the chromonic systems investigated by Collings et al.[135] and Bertrand et al.[136] and the thermotropic systems presented in this chapter with regards to self-assembly of soft matter structures. Figure 7.20 shows a fit using the $e^{-t^{1/2}}$ function applied to the data for mixture 6 (10% VBG93 in 5CB), showing good qualitative agreement between the experimental data and the fit.

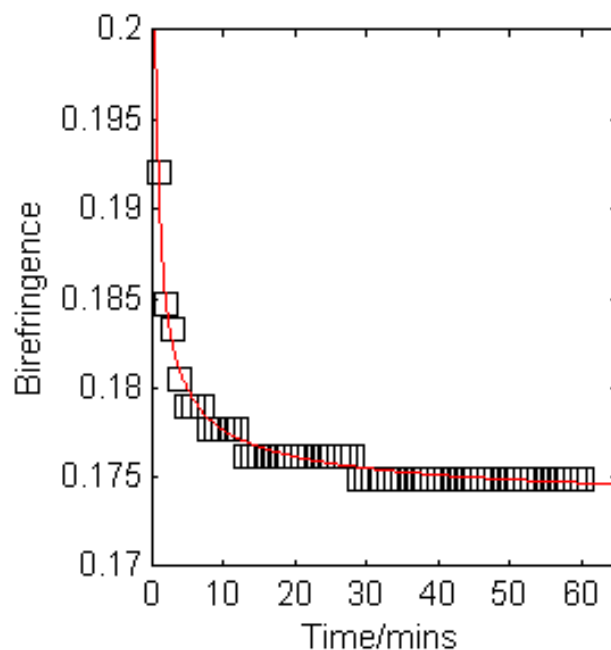


Figure 7.20: The birefringence Δn as a function of time for mixture 6 (black squares) fitted with the $e^{-t^{1/2}}$ function (red line).

7.6 Summary

To summarise, the phase behaviour of mixtures of calamitic liquid crystals doped with bent-core mesogens have been investigated. These mixtures exhibited self-assembly of filaments and a number of experiments were carried out to understand the behaviour of the filaments in relation to the bulk liquid crystal. The aim of this chapter was to answer a number questions that arose from initial investigations carried out by Gleeson et al.;[112]

- (i) Do the filaments exhibit any helical structure? It should be noted that helical structures are observed in almost all other nanofilaments.
- (ii) Does the phase in which the filaments grow influence the self-assembly?
- (iii) How does the nematic director influence the formation of the filaments?
- (iv) What is the influence of the time dependency on the self-assembly of the filaments?

Initial investigations presented by Gleeson et al.[112] showed that the filaments grew only in the nematic phase of a mixture of 10% VBG93 in 5CB. These filaments showed no sign of helical structure so high resolution AFM and SEM was carried out to confirm whether the filaments exhibited any helicity. Three mixtures were investigated; the original 5CB host mixture along with an 8CB mixture in which the filaments grew in the SmA phase, and a TM 1001 mixture in which the filaments grew in the N* phase. No helical structure was observed in any of the mixtures using AFM or SEM, providing proof that these filaments are not those observed in HNF phases in other bent-core systems. The images also suggested that the phase in which the filaments grew in had no effect on the self-assembly at the nanoscale.

In order to understand the effect of the nematic director on the filament growth, a mixture containing 10% photo-chromic BAAB2 was used. The photo-chromic allowed better control over the nematic phase. Initial observations in a planar aligned homogeneous device showed that in the nematic phase, the filaments grew at an angle of $\sim 60^\circ$ either side of the director (figure 7.10). Observations of the 8CB mixture showed that filaments grown in the SmA phase grew along the smectic layers and were found to be practically parallel to each other (figure 7.11). These measurements showed that the director was a major component in the self-assembly of the filaments in the bulk liquid crystal, in contrast to the how the filaments grow on the nanometre scale which was found to be in a more random fashion (section 7.3).

The time-dependency of the filament self-assembly was investigated by measuring the birefringence of a number of mixtures that exhibited the filaments. The temperature dependent results showed that the systems behaved as they should; Δn increased as the temperature reduced through the nematic phase with values being closer to that measured for calamitic host 5CB compared with the bent-core dopants VBG93 and DT12. However a "plateau" in the trend was observed at the temperature when the filaments began to grow. Further investigations of the birefringence showed that as the filaments grew Δn decreased over a time period of about 1 hour, when the mixtures were held at a set temperature of $T - T_{NI} = -15$ K. The reduction in Δn followed an exponential trend similar to that measured in chromic liquid crystals that also exhibited nanoscale self-assembly

that aggregated.[135, 136] It is interesting to find thermotropic systems exhibit self-assembling time dependent structures similar to those exhibited by lyotropic systems. Chromic liquid crystals in particular tend to form columnar phases, and so an analogy can be drawn between those systems and the filaments discussed in this chapter, based on the X-ray scattering results obtained by Gleeson et al.[112] which suggested the filaments grew in a columnar fashion.

The next chapter summarises and concludes all of the results presented in this thesis, and will provide context to how this project impacts the field of liquid crystals and soft matter, along with introducing potential future work that could be carried out following these experiments.

Chapter 8

Conclusion and Future Work

8.1 Conclusion

In this thesis, investigations of the phase behaviour of bent-core nematic liquid crystals and their mixtures have been presented. The elastic behaviour of the pure bent-core materials and their mixtures were introduced first in chapters 4 and 5 respectively. The underlying phases in the bent-core mixtures were discussed in chapter 6 using results obtained from X-ray scattering. Phase behaviour in the calamitic and bent-core mixtures were discussed in chapter 7, more specifically the filament structures that formed in a number of mixtures. This section aims to provide a summary on the results presented in each of these chapters.

Chapter 4 presented the elastic behaviour measured in the nematic phase of the bent-core liquid crystal DT12. K_{11} was found to be rather high and to exhibit an expected temperature dependence, whilst K_{22} and K_{33} were both measured to be anomalously small and almost temperature independent throughout the whole nematic phase regime. Such unusual behaviour of both the twist and bend elastic constants has not been observed in other bent-core liquid crystals. The elastic behaviour of DT12 was further investigated using two theoretical approaches; a molecular theory based on atomistic simulations of the real molecular structure of DT12 including its conformations (carried out by Alberta Ferrarini), and an analytical mean-field theory which explicitly takes into account polar intermolecular interactions and chiral fluctuations between the bent molecules (carried out by Mikhail Osipov and Grzegorz Pająk).

The atomistic modelling of DT12 showed excellent agreement both qualitatively and quantitatively with the experimental data for both K_{22} and K_{33} . For K_{11} the absolute values of the calculated and experimental results differed, however both sets of data exhibited similar temperature dependence. In the context of the mean-field theory, the reduction in K_{33} is related to the existence of local polar order in the bent-core molecules which is linearly coupled to the bend deformation vector. The coupling reduces the free energy and results in a negative correction to the bend constant which was found to be large in DT12. In a similar way the free energy is reduced due to fluctuations in chirality due to chiral conformers of the molecules, which is linearly coupled to the fluctuating twist. This yields a negative correction to K_{22} in DT12, but can also apply to other bent-core nematic liquid crystals that possess strongly chiral local states (or conformers). The theory was then used to calculate values for the three elastic constants which agreed qualitatively with the experimental data. The theory also provides an insight into the low values of K_{22} measured for other oxadiazole based bent-core materials. Although the magnitude of the negative correction to K_{22} will depend on the material, the correction always leads to a weaker temperature variation of K_{22} than that of K_{11} in relative terms.

Chapter 5 presented results obtained for the elastic behaviour in the nematic phases of bent-core mixtures of DT12 and another bent-core material VBG93, as well as for mixtures of the bent-core mesogens with three calamitic materials 5CB, 8CB, and ZLI 1132.

For the mixtures of two bent-core liquid crystals, K_{11} in all of the mixtures was found to exhibit a similar temperature dependence with respect to the pure materials. Similarly, K_{33} was found to exhibit a similar temperature independence in all mixtures. Interestingly for K_{22} the bent-core mixtures exhibited a more marked temperature dependence as increasing amounts of VBG93 were added to the mixtures. The results suggest that simple mixing rules that determine the elastic constants in liquid crystal mixtures apply quite well in the bent-core mixtures; the elastic constant values for the bent-core mixtures all lie in between the respective values of the pure bent-core liquid crystals.

For the mixtures of calamitic and bent-core liquid crystals, it was shown that the influence of a bent-core mesogen on the three elastic constants K_{11} ,

K_{22} , and K_{33} of a calamitic liquid crystals host is quite distinct. For K_{11} , in all three mixture sets, the influence of the bent-core mesogen is negligible. This suggests that the splay interaction constant K_{11}^{bc} (determined by interactions between the calamitic and bent-core molecules) must be negligible. There can also be no additional contribution from fluctuations in the conformers; splay is affected by a wedge-shaped structure and so there is apparently little scope for the bent-core mesogens included in the mixtures here to show any wedge-shaped conformers that might have significant impact on the splay elastic constant. For the K_{33} results, a reduction of 10-20% was measured due to the influence of the bent-core dopants, which is in line with simple mixing rules and existing literature. The surprising result from this work was the remarkable reduction in K_{22} (up to $\sim 40\%$) observed in all of the calamitic and bent-core mixtures. The results suggest that the fluctuations in the chiral conformers in the bent-core mesogens have a significant effect on the values of K_{22} in the mixtures, but that they also enhance the fluctuations in the chiral conformers of the host calamitic liquid crystal. This is an important result as it suggests an amplification of fluctuations in chirality of a system and provides an insight into how chirality can "cascade" in a fluid system.

Chapter 6 investigated the underlying phase behaviour in the bent-core mixtures of DT12 and VBG93. It was found that the mixtures exhibited two different underlying phases below the nematic phase, dependent on the concentration of the bent-core liquid crystals in the mixture.

Mixtures 1 and 2 (90% and 75% VBG93 in the mixtures respectively) both exhibited a DC phase below the nematic phase, similar to VBG93. POM images showed the underlying phases being optically isotropic, and the spacing and FWHM measurements behaved very similar to the DC observed in pure VBG93. Mixtures 3-5 (50%, 70% and 90% DT12 in the mixtures respectively) all exhibited a smectic phase below the nematic phase. The raw X-ray data taken for the mixtures 4 and 5 were very similar to that taken for DT12 suggesting the smectic phases in these mixtures were similar in structure to that observed in DT12. The raw X-ray data taken for mixture 3 suggested that the smectic phase show some tilted layer structures.

The spacing and FWHM values showed a very similar temperature dependence between mixtures 3-5 and DT12 (figure 6.7), although the absolute values differed slightly; the spacing decreased as more VBG93 was added to DT12, whilst the FWHM values measured for mixtures 3-5 were practically identical to each other, with the values measured for DT12 being found to be higher. The FWHM of the scattering peaks in the crystal phases were found to be comparable to those measured in the mixtures and as such reliable comparison of the FWHM between DT12 and mixtures 3-5 cannot be carried out due to the relatively low resolution of the apparatus set-up. The tilt angle of the director in the smectic phases was measured for these mixtures and it was found that the tilt angle increases as more VBG93 was added to DT12; DT12 exhibited the lowest tilt angle ($19.9\text{-}21.5^\circ$) and mixture 3 exhibited the tilt angle ($29.0\text{-}32.2^\circ$) in the smectic phases. The behaviour of the tilt angle as a function of concentration was found to be similar to the behaviour of the spacing which was to be expected. It should be noted that from the raw X-ray data, an estimate of the tilt angle for mixture 3 was found to be $\sim 45^\circ$.

It was believed that the elastic behaviour in the nematic phases of the mixtures might provide more information on the underlying phases in the mixtures. Considering VBG93 and mixtures 1 and 2, the results showed that the elastic behaviour of the mixtures agreed with the inequality $K_{24} < K_{22}$, with mixtures 1 and 2 exhibiting lower K_{22} values compared to VBG93 and with both mixtures exhibiting DC phases. However the results also show that DT12 and mixtures 3-5 exhibit lower K_{22} values than VBG93 yet these samples exhibited underlying smectic phases, suggesting that the formation of the DC phases in mixtures 1 and 2 is not solely due to the elastic behaviour in the nematic phase. DT12 and mixture 5 were found to exhibit similar K_{11} and K_{33} values to each other, whilst mixtures 3 and 4 exhibited similar K_{11} and K_{33} values across a similar temperature range. The elastic behaviour, whilst providing some information does not provide enough information to explain why mixtures 3-5 exhibit the smectic phases whilst mixtures 1 and 2 exhibit DC phases. Clearly there is more needed to fully understand the mechanisms to forming the DC phase and other exotic phases in bent-core systems.

Chapter 7 investigated the filament structures exhibited by mixtures of calamitic liquid crystals doped with bent-core mesogens. The aim of this chapter was to answer a number of questions that arose from initial investigations carried out by Gleeson et al.;[112]

- (i) Do the filaments exhibit any helical structure? It should be noted that helical structures are observed in almost all other nanofilaments.
- (ii) Does the phase in which the filaments grow influence the self-assembly?
- (iii) How does the nematic director influence the formation of the filaments?
- (iv) What is the influence of the time dependency on the self-assembly of the filaments?

To investigate if the filaments exhibited any helical structure high resolution microscopy was carried out using AFM and SEM. Three mixtures were investigated; the original 5CB host mixture along with an 8CB mixture in which the filaments grew in the SmA phase, and a TM 1001 mixture in which the filaments grew in the N* phase. No helical structure was observed in any of the mixtures using AFM or SEM, providing proof that these filaments are not those observed in HNF phases in other bent-core systems. The images also suggested that the phase in which the filaments grew in had no effect on the self-assembly of the filaments at the nanoscale.

In order to understand the effect of the nematic director on the filament growth, a mixture containing 10% photo-chromic BAAB2 was used. The photo-chromic allowed better control over the nematic phase. Initial observations in a planar aligned homogeneous device showed that in the nematic phase, the filaments grew at an angle of $\sim 60^\circ$ either side of the director. Observations of the 8CB mixture showed that filaments grown in the SmA phase grew along the smectic layers and were found to be practically parallel to each other. These measurements showed that the director was a major component in the self-assembly of the filaments in the bulk liquid crystal, in contrast to the way the filaments grow on the nanometre scale which was found to be in a more random fashion. These

results also suggested that the phase in which the filaments grew in did indeed affect the self-assembly.

The time-dependency of the filament self-assembly was investigated by measuring the birefringence of a number of mixtures that exhibited the filaments. The temperature dependent results showed that the systems behaved as they should; Δn increased as the temperature reduced through the nematic phase with values being closer to that measured for calamitic host 5CB compared with the bent-core dopants VBG93 and DT12. However a "plateau" in the trend was observed at the temperature when the filaments began to grow. Further investigations of the birefringence showed that as the filaments grew Δn decreased over a time period of about 1 hour, when the mixtures were held at a set temperature of $T - T_{NI} = -15$ K. The reduction in Δn followed an exponential trend similar to that measured in cholic liquid crystals that also exhibited nanoscale self-assembly that aggregated.[135, 136] It is interesting to find thermotropic systems exhibit self-assembling time dependent structures similar to those exhibited by lyotropic systems. Cholic liquid crystals in particular tend to form columnar phases, and so an analogy can be drawn between those systems and the filaments discussed in this chapter, based on the X-ray scattering results obtained by Gleeson et al.[112] which suggested the filaments grew in a columnar fashion.

8.2 Future Work

The work presented in this thesis has provided a detailed study on the the phase behaviour in bent-core liquid crystals and their mixtures. There are a number of directions that can come out of this work for further research.

Firstly we have found that lower temperature DC phases can be achieved through bent-core liquid crystal mixtures. Investigations of the DC phase in pure VBG93 have brought forward interesting results; in particular there is a decrease in the refractive index in the DC phase (~ 0.05) under the effect of an electric field.[31, 32] Measurements of the refractive index in the DC phases of the bent-core mixtures were not carried out as part of this thesis, and so it would be interesting to find out if the DC phases in the mixtures also exhibit a similar change in refractive index of ~ 0.05 . An electrically tuneable refractive index in

an optically isotropic liquid crystal phase is useful for applications such as for optical waveguides and in liquid crystal lenses. Finding a lower temperature DC phase with similar tuneable refractive indices is thus desirable for these potential applications.

The investigations of the elastic behaviour in calamitic and bent-core mixtures have shown that there is the possibility of tuning mixtures. More specifically the results suggest that the elastic constants can be tuned using small amounts of bent-core dopant. In this thesis only two bent-core dopants were considered and thus considering other bent-core mesogens for mixtures would provide a library for tuning the elastic constants. This is also relevant to other liquid crystal phases beyond the nematic phase that might be of use in device, such as blue phases where the stability is known to depend on the elastic constants.[58]

With regards to the filaments structures in the calamitic and bent-core liquid crystal mixtures, there is a lot of potential for future work. Gleeson et al.[112] found that the filaments exhibits polymer-like structure by considering very small angle X-ray scattering. Detailed studies at the time could not be carried out at these small angles, and as such investigating the nature of the scattering is of great interest. One method in investigating the potential polymer structure of the filaments is to carry out resonant X-ray scattering on the filaments. Whilst it is believed that the filaments self-assemble in a columnar fashion, Resonant X-ray scattering will probe the order of the filaments in much more details. Resonant X-ray scattering measurements have already been carried out to investigate polymer structures[137–140] and indeed on helical nanofilaments to great effect.[141] Measuring the behaviour of the filaments using resonant X-ray scattering can provide an insight into the structure of the filaments.

In summary, this thesis has presented new results on bent-core liquid crystals and their mixtures, providing corrections to the elastic theory that applies to bent-core liquid crystals, as well as more information on the nature of self-assembling filaments in mixtures of calamitic liquid crystals doped with bent-core mesogens. This thesis has also highlighted directions for future work which can allow insight to be gained on the potential of bent-core materials in applications, as well as fundamental knowledge on self-assembling structures in soft matter systems.

Appendix A

Error Analysis

In chapter 3, errors were assigned to values measured for the splay (K_{11}), twist (K_{22}), and bend (K_{33}) elastic constants. The errors were based on the methodology of obtaining the elastic constants optically, by measuring the transmitted light intensity through the liquid crystal device. How the errors were calculated is discussed in this appendix. First consider the plot of retardance against RMS voltage V_{RMS} . An example of the plot is shown in figure A.1.

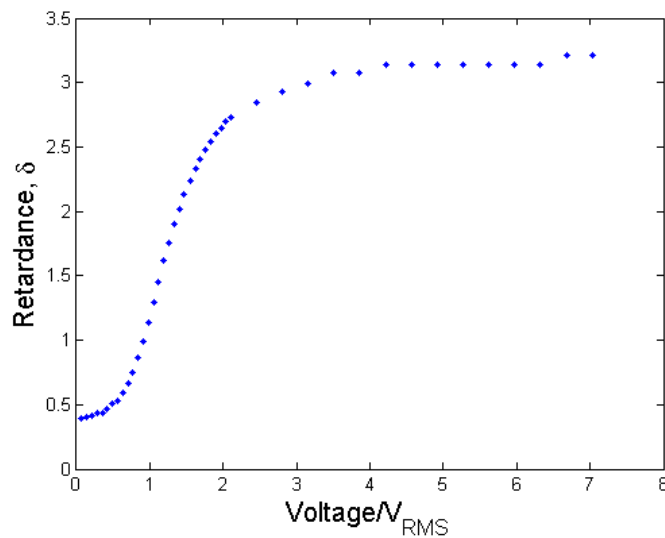


Figure A.1: δ as a function of V_{RMS} for DT12 at $T-T_{NI} = -2.5$ K.

K_{33} is measured by considering the threshold voltage, V_{th} . V_{th} is the point

when the retardance starts to rise and can be obtained from the intersection of two straight lines as shown in figure A.2.

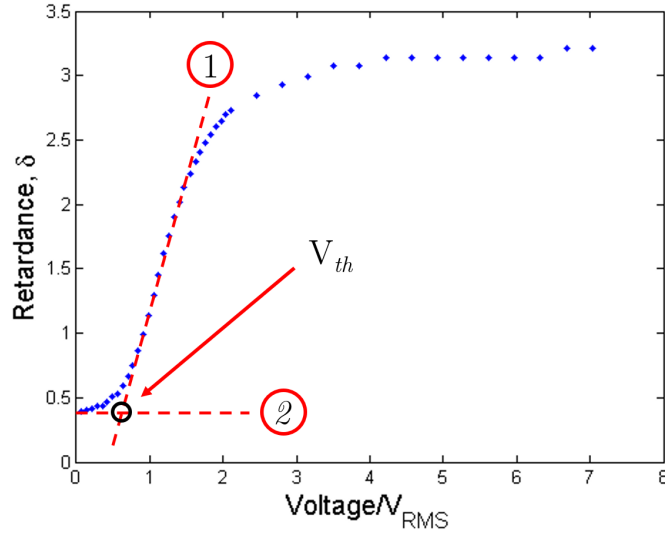


Figure A.2: δ as a function of V_{RMS} for DT12 at $T - T_{NI} = -2.5$ K, denoting where V_{th} is obtained.

It can be seen from figure A.2 that the gradient of line 1 can vary based on the interpretation of the person analysing the data. Figure A.3 shows how the gradient can vary, resulting in a different V_{th} being calculated.

The fact that V_{th} can vary based on how the gradient of line 1 can be assigned means that the measurement of K_{33} can vary as well; K_{33} is directly related to the threshold voltage (see equation 3.5 in chapter 3). This variation in K_{33} is incorporated into the error assigned to K_{33} which was determined to be $\sim 10\%$ or 0.2 pN (whichever was larger). Similarly, the measurement of K_{11} is related to the gradient of the straight line part just above the threshold; taken from line 1, and as such the variation in how line 1 can be assigned varies the value of K_{11} that is measured. K_{11} is also dependent on the value measured for K_{33} obtained from the threshold voltage (see equation 3.10 from chapter 3). Thus the error assigned to K_{33} is also incorporated into the error assigned to K_{11} which was determined to be $\sim 15\%$ or 2 pN (whichever was larger).

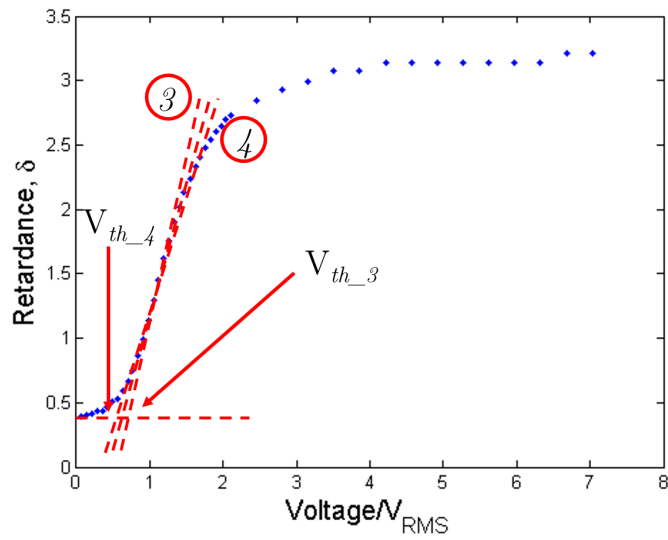


Figure A.3: δ as a function of V_{RMS} for DT12 at $T-T_{NI} = -2.5$ K, denoting where V_{th-3} and V_{th-4} are obtained.

References

- [1] F. Reinitzer, "Contributions to the knowledge of cholesterol," *Liq. Cryst.*, vol. 5, p. 7, 1989. (Translation from original paper by Reinitzer published in *Monatshefte für Chemie*, 9:421-441, 1888). [1](#)
- [2] I. Dierking, *Textures of Liquid Crystals*. Wiley-VCH GmbH and Co., 2003. [1](#), [2](#), [36](#), [37](#)
- [3] I.-C. Khoo, *Liquid Crystals*. Wiley, 2nd ed., 2007. [1](#)
- [4] P. G. de Gennes and J. Prost, *The Physics of Liquid Crystals*. Clarendon Press, Oxford, 2nd ed., 1993. [1](#), [4](#)
- [5] T. C. Lubensky, "Molecular description of nematic liquid crystals," *Phys. Rev. A*, vol. 2, p. 2497, 1970. [2](#)
- [6] C. W. Oseen, "The theory of liquid crystals," *Trans. Faraday Soc.*, vol. 29, p. 883, 1933. [4](#)
- [7] F. C. Frank, "1. liquid crystals. on the theory of liquid crystals," *Discuss. Faraday Soc.*, vol. 25, p. 19, 1958. [4](#), [20](#)
- [8] P. Boltenhagen, O. D. Lavrentovich, and M. Kleman, "Oily streaks and focal conic domains in L_a lyotropic liquid crystals," *J. Phys. II*, vol. 1, p. 1233, 1991. [4](#)
- [9] P. Boltenhagen, M. Kleman, and O. D. Lavrentovich, "Freeze-fracture observations in the L_a phase of a swollen surfactant in the vicinity of the L_3 and the L_1 phase transitions," *J. Phys. II*, vol. 4, p. 1439, 1994.

REFERENCES

- [10] P. Boltenhagen, O. D. Lavrentovich, and M. Kleman, “Focal conic domains with positive Gaussian curvature and saddle-splay rigidity of smectic L_a phases,” *Phys. Rev. A*, vol. 46, p. R1743, 1992. 4
- [11] A. Sparavigna, O. D. Lavrentovich, and A. Strigazzi, “Periodic stripe domains and hybrid-alignment regime in nematic liquid crystals: threshold analysis,” *Phys. Rev. E*, vol. 49, p. 1344, 1994. 4
- [12] E. Páram, J. Vallamkondu, V. Koning, B. C. van Zuiden, P. W. Ellis, M. A. Bates, V. Vitelli, and A. Fernandez-Nieves, “Stable nematic droplets with handles,” *Proc. Natl. Acad. Sci. U.S.A.*, vol. 110, p. 9295, 2013. 4
- [13] A. Jákli, O. D. Lavrentovich, and J. V. Selinger, “Physics of liquid crystals of bent-shaped molecules,” *Rev. Mod. Phys.*, vol. 90, p. 045004, 2018. 5
- [14] H. Takezoe and Y. Takanishi, “Bent-core liquid crystals: Their mysterious and attractive world,” *Jpn. J. Appl. Phys.*, vol. 45, p. 597, 2006. 5
- [15] G. Dantlgraber, A. Eremin, S. Diele, A. Hauser, H. Kresse, G. Pelzl, and C. Tschierske, “Chirality and macroscopic polar order in a ferroelectric smectic liquid crystalline phase formed by achiral polyphilic bent core molecules,” *Angew. Chem. Int. Ed.*, vol. 41, p. 2408, 2002. 5
- [16] J. Thisayukta, Y. Nakayama, S. Kawauchi, H. Takezoe, and J. Watanabe, “Distinct formation of a chiral smectic phase in achiral banana-shaped molecules with a central core based on a 2,7-dihydroxynaphthalene unit,” *J. Am. Chem. Soc.*, vol. 122, p. 7441, 2000.
- [17] J. Ortega, C. L. Folcia, J. Etxebarria, N. Gimeno, and M. B. Ros, “Interpretation of unusual textures in the B_2 phase of a liquid crystal composed of bent-core molecules,” *Phys. Rev. E*, vol. 68, p. 011707, 2003. 6
- [18] Y. Zhang, U. Baumeister, C. Tschierske, M. J. O’Callaghan, and C. Walker, “Achiral bent-core molecules with a series of linear or branched carbosilane termini: Dark conglomerate phases, supramolecular chirality and macroscopic polar order,” *Chem. Mater.*, vol. 22, p. 2869, 2010. 5

REFERENCES

- [19] W. Weissflog and M. W. Schr
- [20] S. K. Lee, L. Shi, M. Tokita, H. Takezoe, and J. Watanabe, “Chirality transfer between weakly birefringent and electric-field induced highly birefringent b2 phases in a bent-core mesogen,” *J. Phys. Chem. B*, vol. 111, p. 8698, 2007. [5](#)
- [21] L. E. Hough, M. Spannuth, M. Nakata, D. A. Coleman, C. D. Jones, G. Dantlgraber, C. Tschierske, J. Watanabe, E. Körblova, D. M. Walba, J. E. MacLennan, M. A. Glaser, and N. A. Clark, “Chiral isotropic liquids from achiral molecules,” *Science*, vol. 325, p. 452, 2009. [5](#), [6](#), [59](#)
- [22] A. Eremin, S. Diele, G. Pelzl, and W. Weissflog, “Field-induced switching between states of opposite chirality in a liquid crystalline phase,” *Phys. Rev. E*, vol. 67, p. 020702, 2003. [5](#)
- [23] J. Martinez-Perdiguero, I. Alonso, C. L. Folcia, J. Etxebarria, and J. Ortega, “Some aspects about the structure of the optically isotropic phase in a bent-core liquid crystal: Chiral, polar or steric origin,” *Phys. Rev. E*, vol. 74, p. 031701, 2006.
- [24] J. Ortega, C. L. Folcia, J. Etxebarria, J. Martinez-Perdiguero, J. A. Gallastegui, P. Ferrer, N. Gimeno, and M. B. Ros, “Electric-field-induced phase transitions in bent-core mesogens determined by x-ray diffraction,” *Phys. Rev. E*, vol. 84, p. 021707, 2011. [5](#), [6](#)
- [25] W. Weissflog, S. Sokolowski, H. Dehne, B. Das, S. Grande, M. W. Schröder, A. Eremin, S. Diele, G. Pelzl, and H. Kresse, “Chiral ordering in the nematic and an optically isotropic mesophase of bent-core mesogens with a halogen substituent at the central core,” *Liq. Cryst.*, vol. 31, p. 923, 2003.
- [26] G. Liao, S. Stojadinovic, G. Pelzl, W. Weissflog, S. Sprunt, and A. Jákli, “Optically isotropic liquid crystal phase of bent-core molecules with polar nanostructure,” *Phys. Rev. E*, vol. 72, p. 021710, 2005.

REFERENCES

- [27] C. Keith, R. A. Reddy, M. Prehm, U. Baumeister, H. Kresse, J. L. Chao, H. Hahn, H. Lang, and C. Tschierske, “Layer frustration, polar order and chirality in liquid crystalline phases of silyl-terminated achiral bent-core molecules,” *Chem. Eur. J.*, vol. 13, p. 2556, 2007.
- [28] D. Chen, Y. Shen, C. Zhu, L. E. Hough, N. Gimeno, M. A. Glaser, J. E. MacLennan, M. B. Ros, and N. A. Clark, “Interface structure of the dark conglomerate liquid crystal phase,” *Soft Matter*, vol. 7, p. 1879, 2011. [6](#), [59](#)
- [29] G. Porte, J. Appell, P. Bassereau, J. Marignan, M. Skouri, I. Billard, and M. Delsanti, “Lamellar versus isotropic structures in dilute phases of fluid membranes,” *Physica A*, vol. 176, p. 168, 1991. [6](#)
- [30] M. Nagaraj, J. C. Jones, V. P. Panov, H. Liu, G. Portale, W. Bras, and H. F. Gleeson, “Understanding the unusual reorganization of the nanostructure of a dark conglomerate phase,” *Phys. Rev. E: Stat., Nonlinear, Soft Matter Phys.*, vol. 91, p. 042504, 2015. [6](#), [29](#), [59](#), [109](#), [115](#), [124](#)
- [31] M. Nagaraj, K. Usami, Z. Zhang, V. Görtz, J. W. Goodby, and H. F. Gleeson, “Unusual electric-field-induced transformations in the dark conglomerate phase of a bent-core liquid crystal,” *Liq. Cryst.*, vol. 41, p. 800, 2014. [6](#), [76](#), [172](#)
- [32] M. Nagaraj, V. Görtz, J. W. Goodby, and H. F. Gleeson, “Electrically tunable refractive index in the dark conglomerate phase of a bent-core liquid crystal,” *Appl. Phys. Lett.*, vol. 104, p. 021903, 2014. [6](#), [8](#), [29](#), [59](#), [172](#)
- [33] H. Gruler and G. Meier, “Electric field-induced deformations in oriented liquid crystals of the nematic type,” *Molec. Cryst. and Liq. Cryst.*, vol. 16, p. 299, 1972. [10](#)
- [34] H. J. Deuling, “Deformation of nematic liquid crystals in an electric field,” *Molec. Cryst. and Liq. Cryst.*, vol. 19, p. 123, 1972. [12](#)
- [35] L. M. Blinov and V. G. Cigrinov, *Electrooptic Effects in Liquid Crystal Materials*. Springer-Verlag, New York, 1994. [12](#), [48](#), [90](#)

REFERENCES

- [36] A. Saupe, “Temperaturabhängigkeit und grÖÙe der deformationskonstanten nematischer flüssigkeiten (Temperature dependence and magnitude of elastic constants of nematic liquid crystals),” *Z. Naturforsch.*, vol. 15A, p. 810, 1960. [13](#), [69](#)
- [37] P. G. de Gennes, *The Physics of Liquid Crystals*. Oxford University Press, London, 1974. [15](#)
- [38] M. Oh-e and K. Kondo, “Electro-optical characteristics and switching behaviour of the in-plane switching mode,” *Appl. Phys. Lett.*, vol. 67, p. 3895, 1995. [15](#), [49](#)
- [39] R. B. Meyer, “Piezoelectric effects in liquid crystals,” *Phys. Rev. Lett.*, vol. 22, p. 918, 1969. [16](#), [18](#), [20](#)
- [40] S. Kaur, V. P. Panov, C. Greco, A. Ferrarini, V. Görtz, J. W. Goodby, and H. F. Gleeson, “Flexoelectricity in an oxadiazole bent-core nematic liquid crystal,” *Appl. Phys. Lett.*, vol. 105, p. 223505, 2014. [18](#), [19](#), [47](#), [49](#), [58](#)
- [41] A. Buka and N. Éber, *Flexoelectricity in Liquid Crystals: Theory, Experiments and Applications*. Imperial College Press, London, 2012. [18](#)
- [42] W. Helfrich, “A simple method to observe the piezoelectricity of liquid crystals,” *Phys. Lett. A*, vol. 35, p. 393, 1971. [18](#)
- [43] A. Derzhanski and A. G. Petrov, “A molecular-statistical approach to the piezoelectric properties of nematic liquid crystals,” *Phys. Lett. A*, vol. 36, p. 483, 1971. [18](#)
- [44] T. C. Lubensky and L. Radzihovsky, “Theory of bent-core liquid crystal phases and phase transitions,” *Phys. Rev. E*, vol. 66, p. 031704, 2002. [19](#)
- [45] L. Longa, G. Pająk, and T. Wydro, “Chiral symmetry breaking in bent-core liquid crystals,” *Phys. Rev. E*, vol. 79, p. 040701, 2009. [xvi](#), [19](#)
- [46] S. Dhakal and J. V. Selinger, “Statistical mechanics of splay flexoelectricity in nematic liquid crystals,” *Phys. Rev. E*, vol. 81, p. 031704, 2010. [21](#)

-
- [47] S. M. Shamid, S. Dhakal, and J. V. Selinger, “Statistical mechanics of bend flexoelectricity and the twist-bend phase in bent-core liquid crystals,” *Phys. Rev. E: Stat., Nonlinear, Soft Matter Phys.*, vol. 87, p. 052503, 2013. [21](#), [71](#), [101](#)
- [48] R. Basu, J. S. Pendery, R. G. Petschek, R. P. Lemieux, and C. Rosenblatt, “Macroscopic torsional strain and induced molecular conformational deracemisation,” *Phys. Rev. Lett.*, vol. 107, p. 237804, 2011. [22](#)
- [49] I. Dozov, “On the spontaneous symmetry breaking in the mesophases of achiral banana-shaped molecules,” *EPL (Europhysics Letters)*, vol. 56, p. 247, 2001. [xvi](#), [23](#), [24](#), [59](#), [79](#)
- [50] M. Cestari, S. Diez-Berart, D. A. Dunmur, A. Ferrarini, M. R. de la Fuente, D. J. B. Jackson, D. O. Lopez, G. R. Luckhurst, M. A. Perez-Jubindo, R. M. Richardson, J. Salud, B. A. Timimi, and H. Zimmermann, “Phase behaviour and properties of the liquid crystal dimer 1”,7”-bis(4-cyanobiphenyl-4’-yl) heptane: A twist-bend nematic liquid crystal,” *Phys. Rev. E*, vol. 84, p. 031704, 2011. [25](#)
- [51] V. Borshch, Y.-K. Kim, J. Xiang, M. Gao, A. Jákli, V. P. Panov, J. K. Vij, C. T. Imrie, M. G. Tamba, G. H. Mehl, and O. D. Lavrentovich, “Nematic twist-bend phase with nanoscale modulation of molecular orientation,” *Nat. Commun.*, vol. 4, p. 2635, 2013. [59](#), [69](#), [79](#)
- [52] D. Chen, J. H. Porada, J. B. Hooper, A. Klittnick, Y. Shen, M. R. Tuchband, E. Korblova, D. Bedrov, D. M. Walba, M. A. Glaser, J. E. Maclennan, and N. A. Clark, “Chiral heliconical ground state of nanoscale pitch in a nematic liquid crystal of achiral molecular dimers,” *Proc. Natl. Acad. Sci. U.S.A.*, vol. 110, p. 15931, 2013. [79](#)
- [53] C. Zhu, M. R. Tuchband, A. Young, M. Shuai, A. Scarborough, D. M. Walba, J. E. Maclennan, C. Wang, A. Hexemer, and N. A. Clark, “Resonant carbon k-edge soft x-ray scattering from lattice-free heliconical molecular ordering: Soft dilative elasticity of the twist-bend liquid crystal phase,” *Phys. Rev. Lett.*, vol. 116, p. 147803, 2016. [25](#)

REFERENCES

- [54] L. Beguin, J. W. Emsley, M. Lelli, A. Lesage, G. R. Luckhurst, B. A. Timimi, and H. Zimmermann, “The chirality of a twist-bend nematic phase identified by nmr spectroscopy,” *J. Phys. Chem. B*, vol. 116, p. 7940, 2012. [26](#)
- [55] D. Chen, M. Nakata, R. Shao, M. R. Tuchband, M. Shuai, U. Baumeister, W. Weissflog, D. M. Walba, M. A. Glaser, J. E. Maclennan, and N. A. Clark, “Twist-bend heliconical chiral nematic liquid crystal phase of an achiral rigid bent-core mesogen,” *Phys. Rev. E*, vol. 89, p. 022506, 2014.
- [56] M. A. Osipov and G. Pająk, “Effect of polar intermolecular interactions on the elastic constants of bent-core nematics and the origin of the twist-bend phase,” *Eur. Phys. J. E: Soft Matter Biol. Phys.*, vol. 39, p. 45, 2016. [26](#), [59](#), [71](#), [74](#)
- [57] S. Srigengan, M. Nagaraj, A. Ferrarini, R. Mandle, S. J. Cowling, M. A. Osipov, G. Pająk, J. W. Goodby, and H. F. Gleeson, “Anomalously low twist and bend elastic constants in an oxadiazole-based bent-core nematic liquid crystal and its mixture; contributions of spontaneous chirality and polarity,” *J. Mater. Chem. C*, vol. 6, p. 980, 2018. [xviii](#), [xix](#), [26](#), [58](#), [60](#), [62](#), [63](#), [64](#), [68](#), [69](#), [70](#), [72](#), [74](#), [77](#), [90](#), [99](#), [101](#), [102](#)
- [58] D. J. Earl, M. A. Osipov, H. Takezoe, Y. Takanishi, and M. R. Wilson, “Induced and spontaneous deracemization in bent-core liquid crystal phases and in other phases doped with bent-core molecules,” *Phys. Rev. E: Stat., Nonlinear, Soft Matter Phys.*, vol. 71, p. 021706, 2005. [26](#), [72](#), [73](#), [99](#), [173](#)
- [59] H. F. Gleeson, S. Kaur, V. Görtz, A. Belaïssaoui, S. J. Cowling, and J. W. Goodby, “The nematic phases of bent-core liquid crystals,” *ChemPhysChem*, vol. 15, p. 1251, 2014. [29](#), [78](#)
- [60] V. Görtz and J. W. Goodby, “Enantioselective segregation in achiral nematic liquid crystals,” *Chem. Comm.*, vol. 26, p. 3262, 2005. [59](#), [74](#)
- [61] V. Görtz, C. Southern, N. W. Roberts, H. F. Gleeson, and J. W. Goodby, “Unusual properties of a bent-core liquid-crystalline fluid,” *Soft Matter*, vol. 5, p. 463, 2009. [29](#), [59](#), [74](#), [76](#), [124](#)

REFERENCES

- [62] S. Kaur, J. Addis, C. Greco, A. Ferrarini, V. Görtz, J. W. Goodby, and H. F. Gleeson, “Understanding the distinctive elastic constants in an oxadiazole bent-core nematic liquid crystal,” *Phys. Rev. E: Stat., Nonlinear, Soft Matter Phys.*, vol. 86, p. 041703, 2012. [29](#), [59](#), [90](#)
- [63] S. Kaur, H. Liu, J. Addis, C. Greco, A. Ferrarini, V. Görtz, J. W. Goodby, and H. F. Gleeson, “The influence of structure on the elastic, optical and dielectric properties of nematic phases formed from bent-core molecules,” *J. Mater. Chem. C*, vol. 1, p. 6667, 2013. [xix](#), [xxiii](#), [29](#), [49](#), [59](#), [63](#), [65](#), [67](#), [68](#), [70](#), [74](#), [75](#), [90](#), [158](#), [159](#), [163](#)
- [64] G. W. Gray, K. J. Harrison, and J. A. Nash, “New family of nematic liquid crystals for displays,” *Electron. Lett.*, vol. 9, p. 130, 1973. [29](#)
- [65] G. W. Gray and A. Mosley, “Trends in the nematic-isotropic liquid transition temperatures for homologous series of 4-n-alkoxy- and 4-n-alkyl-4'-cyanobiphenyls,” *J. Chem. Soc., Perkin Trans. 2*, vol. 0, p. 97, 1976. [29](#)
- [66] E. I. L. Jull and H. F. Gleeson, “All-optical responsive azo-doped liquid crystal laser protection filter,” *Optics Express*, vol. 26, p. 34179, 2018. [29](#), [136](#)
- [67] S. V. Serak, E. O. Arikainen, H. F. Gleeson, V. A. Grozhik, J. P. Guillou, and N. A. Usova, “Laser-induced concentric colour domains in a cholesteric liquid crystal mixture containing a nematic azo-benzene dopant,” *Liq. Cryst.*, vol. 29, p. 19, 2002. [29](#), [136](#)
- [68] N. H. Hartshorne and A. Stuart, *Crystals and The Polarising Microscope*. Edward Arnold, London, 4th ed., 1970. [36](#)
- [69] D. Demus and L. Richter, *Textures of Liquid Crystals*. VEB Deutscher Verlag, Leipzig, 1978.
- [70] G. W. Gray and J. W. Goodby, *Smectic Liquid Crystals: Textures and Structures*. Leonard Hill, Philadelphia, PA, 1984. [36](#)

REFERENCES

- [71] H. Allinson, *A Study of Photochromic Fulgide Doped Liquid Crystals*. PhD thesis, University of Manchester, 1994. [43](#)
- [72] H. Gruler, T. J. Scheffer, and G. Meier, “Elastic constants of nematic liquid crystals,” *Z. Naturforsch.*, vol. 27a, p. 966, 1972. [43](#)
- [73] S. Kaur, L. Tian, H. Liu, C. Greco, A. Ferrarini, J. Seltmann, M. Lehmann, and H. F. Gleeson, “The elastic and optical properties of a bent-core thiadiazole nematic liquid crystal: the role of the bend angle,” *J. Mater. Chem. C*, vol. 1, p. 2416, 2013. [49](#), [59](#)
- [74] M. Berek, *Berek Compensator Manual*. Leica. [53](#)
- [75] J. R. DeVore, “Refractive indices of rutile and sphalerite,” *J. Opt. Soc. Am.*, vol. 41, p. 416, 1951. [53](#)
- [76] J. Addis, S. Kaur, D. J. Binks, M. R. Dickenson, C. Greco, A. Ferrarini, V. Görtz, J. W. Goodby, and H. F. Gleeson, “Second-harmonic generation and the influence of flexoelectricity in the nematic phases of bent-core oxadiazoles,” *Liq. Cryst.*, vol. 43, p. 1315, 2016. [58](#), [63](#)
- [77] C.-J. Yun, M. R. Vengatesan, J. K. Vij, and J.-K. Song, “Hierarchical elasticity of bimesogenic liquid crystals with twist-bend nematic phase,” *Appl. Phys. Lett.*, vol. 106, p. 173102, 2015. [59](#), [69](#), [79](#)
- [78] K. Adlem, M. Čopič, G. R. Luckhurst, A. Mertelj, O. Parri, R. M. Richardson, B. D. Snow, B. A. Timimi, R. P. Tuffin, and D. Wilkes, “Chemically induced twist-bend nematic liquid crystals, liquid crystal dimers, and negative elastic constants,” *Phys. Rev. E: Stat., Nonlinear, Soft Matter Phys.*, vol. 88, p. 022503, 2013. [59](#), [69](#), [79](#)
- [79] H. Ocak, B. Bilgin-Eran, M. Prehm, and C. Tschierske, “Effects of molecular chirality on superstructural chirality in liquid crystalline dark conglomerate phases,” *Soft Matter*, vol. 8, p. 7773, 2012. [59](#)

REFERENCES

- [80] P. Sathyanarayana, M. Mathew, Q. Li, V. S. S. Sastry, B. Kundu, K. V. Le, H. Takezoe, and S. Dhara, “Splay bend elasticity of a bent-core nematic liquid crystal,” *Phys. Rev. E: Stat., Nonlinear, Soft Matter Phys.*, vol. 81, p. 010702, 2010. [59](#)
- [81] M. Majumdar, P. Salamon, A. Jákli, J. T. Gleeson, and S. Sprunt, “Elastic constants and orientational viscosities of a bent-core nematic liquid crystal,” *Phys. Rev. E: Stat., Nonlinear, Soft Matter Phys.*, vol. 83, p. 031701, 2011. [67](#)
- [82] P. Tadapatri, U. S. Hiremath, C. V. Yelamaggad, and K. S. Krishnamurthy, “Permittivity, conductivity, elasticity, and viscosity measurements in the nematic phase of a bent-core liquid crystal,” *J. Phys. Chem. B*, vol. 114, p. 1745, 2010. [67](#)
- [83] P. S. Salter, C. Tschierske, S. J. Elston, and E. P. Raynes, “Flexoelectric measurements of a bent-core nematic liquid crystal,” *Phys. Rev. E: Stat., Nonlinear, Soft Matter Phys.*, vol. 84, p. 031708, 2011.
- [84] R. Balachandran, V. P. Panov, J. K. Vij, A. Lehmann, and C. Tschierske, “Effect of cybotactic clusters on the elastic and flexoelectric properties of bent-core liquid crystals belonging to the same homologous series,” *Phys. Rev. E: Stat., Nonlinear, Soft Matter Phys.*, vol. 88, p. 032503, 2013.
- [85] A. Chakraborty, M. K. Das, B. Das, A. Lehmann, and C. Tschierske, “Rotational viscosity measurements of bent-core nematogens,” *Soft Matter*, vol. 9, p. 4273, 2013.
- [86] N. Avci, V. Borshch, D. D. Sarkar, R. Deb, G. Venkatesh, T. Turiv, S. V. Shiyankovskii, N. V. S. Rao, and O. D. Lavrentovich, “Viscoelasticity, dielectric anisotropy, and birefringence in the nematic phase of three four-ring bent-core liquid crystals with an l-shaped molecular frame,” *Soft Matter*, vol. 9, p. 1066, 2013. [59](#)
- [87] S. Kaur, “Elastic properties of bent-core nematic liquid crystals: The role of the bend angle,” *Liq. Cryst.*, vol. 43, p. 2277, 2016. [59](#)

REFERENCES

- [88] D. Chen, Y. Shen, J. Agüero, E. Korblova, D. M. Walba, N. Kapernaum, F. Giesselmann, J. Watanabe, J. E. MacLennan, M. A. Glaser, and N. A. Clark, “Chiral isotropic sponge phase of hexatic smectic layers of achiral molecules,” *ChemPhysChem*, vol. 15, p. 1502, 2014. [59](#), [79](#)
- [89] J. L. Ericksen, “Inequalities in liquid crystal theory,” *Phys. Fluids*, vol. 9, p. 1205, 1966. [59](#), [79](#)
- [90] N. Metropolis, A. W. Rosenbluth, M. N. Rosenbluth, A. H. Teller, and E. Teller, “Equation of state calculations by fast computing machines,” *J. Chem. Phys.*, vol. 21, p. 1087, 1953. [62](#), [68](#)
- [91] M. Cestari, A. Bosco, and A. Ferrarini, “Molecular field theory with atomistic modeling for the curvature elasticity of nematic liquid crystals,” *J. Chem. Phys.*, vol. 131, p. 054104, 2009. [62](#), [67](#)
- [92] C. Greco, A. Marini, E. Frezza, and A. Ferrarini, “From the molecular structure to spectroscopic and material properties: computational investigation of a bent-core nematic liquid crystal,” *ChemPhysChem*, vol. 15, p. 1336, 2014. [62](#)
- [93] P. W. Flory, *Statistical Mechanics of Chain Molecules*. Wiley-Interscience, 1969. [62](#)
- [94] M. J. Frisch *et al.*, *Gaussian 09 (Revision B.01)*. Gaussian, Inc., Wallingford CT, 2010. [63](#)
- [95] R. Balachandran, V. P. Panov, V. J. K, A. Kocot, M. G. Tamba, A. Kohlmeier, and G. H. Mehl, “Elastic properties of bimesogenic liquid crystals,” *Liq. Cryst.*, vol. 40, p. 681, 2013. [69](#)
- [96] V. P. Panov, J. K. Vij, and G. H. Mehl, “Twist-bend nematic phase in cyanobiphenyls and difluoroterphenyls bimesogens,” *Liq. Cryst.*, vol. 44, p. 147, 2017. [69](#)
- [97] R. G. Priest, “Theory of the Frank elastic constants of nematic liquid crystals,” *Phys. Rev. A*, vol. 7, p. 720, 1973. [69](#)

REFERENCES

- [98] J. P. Straley, “Frank elastic constants of the hard-rod liquid crystal,” *Phys. Rev. A*, vol. 8, p. 2181, 1973.
- [99] A. Poniewierski and J. Stecki, “Statistical theory of the elastic constants of nematic liquid crystals,” *Mol. Phys.*, vol. 38, p. 1931, 1979.
- [100] J. Stecki and A. Poniewierski, “Application of the statistical theory of elastic constants of nematics to spherocylindrical molecules with attractive forces,” *Mol. Phys.*, vol. 41, p. 1451, 1980. [69](#)
- [101] M. A. Osipov and G. Pająk, “Polar interactions between bent-core molecules as a stabilising factor for inhomogeneous nematic phases with spontaneous bend deformations,” *Liq. Cryst.*, vol. 44, p. 58, 2017. [71](#), [72](#)
- [102] M. A. Osipov and S. Hess, “The elastic constants of nematic and nematic discotic liquid crystals with perfect local orientational order,” *Mol. Phys.*, vol. 78, p. 1191, 1993. [71](#)
- [103] C. Greco, G. R. Luckhurst, and A. Ferrarini, “Molecular geometry, twist-bend nematic phase and unconventional elasticity: a generalised maier-saupe theory,” *Soft Matter*, vol. 10, p. 9318, 2014. [72](#)
- [104] P. Salamon, N. Éber, A. Buka, J. T. Gleeson, S. Sprunt, and A. Jákli, “Dielectric properties of mixtures of a bent-core and a calamitic liquid crystal,” *Phys. Rev. E*, vol. 81, p. 031711, 2010. [76](#)
- [105] M. Cvetinov, D. Obadović, M. Stojanović, D. Lazar, A. Vajda, N. Éber, K. Fodor-Csorba, and I. Ristić, “Mesophase behaviour of binary mixtures of bent-core and calamitic compounds,” *Liq. Cryst.*, vol. 40, p. 1512, 2013.
- [106] P. Sathyanarayana, B. K. Sadashiva, and S. Dhara, “Splay-bend elasticity and rotational viscosity of liquid crystal mixtures of rod-like and bent-core molecules,” *Soft Matter*, vol. 7, p. 8556, 2011.
- [107] M. R. Dodge, C. Rosenblatt, R. G. Petschek, M. E. Neubert, and M. E. Walsh, “Bend elasticity of mixtures of v-shaped molecules in ordinary nematogens,” *Phys. Rev. E*, vol. 62, p. 5056, 2000.

-
- [108] S. Parthasarathi, D. S. S. Rao, N. B. Palakurthy, C. V. Yelamaggad, and S. K. Prasad, “Binary system exhibiting the nematic to twist-bend nematic transition: behavior of permittivity and elastic constants,” *J. Phys. Chem. B*, vol. 120, p. 5056, 2016. [76](#), [98](#)
- [109] S. Srigengan, H. Liu, M. A. Osipov, R. Mandle, S. J. Cowling, J. W. Goodby, and H. F. Gleeson, “The elastic behaviour of mixtures of calamitic and bent-core liquid crystals and anomalies in the twist deformation,” *J. Mater. Chem. C, Manuscript in Review*, 2019. [xx](#), [77](#), [86](#), [96](#), [97](#), [98](#), [99](#)
- [110] H. Liu, *Elastic Properties and Phases of Bent-Core Liquid Crystals*. PhD thesis, University of Manchester, 2016. [77](#), [96](#)
- [111] A. Mertelj, L. Cmok, N. Sebastián, R. J. Mandle, R. R. Parker, A. C. Whitwood, J. w. Goodby, and M. Čopič, “Splay nematic phase,” *Phys. Rev. X*, vol. 8, p. 041025, 2018. [79](#), [106](#)
- [112] H. F. Gleeson, H. Liu, S. Kaur, S. Srigengan, V. Görtz, R. Mandle, and J. Lydon, “Self-assembling, macroscopically oriented, polymer filaments; a doubly nematic organogel,” *Soft Matter*, vol. 14, p. 9159, 2018. [79](#), [89](#), [134](#), [135](#), [142](#), [143](#), [150](#), [158](#), [160](#), [164](#), [165](#), [166](#), [171](#), [172](#), [173](#)
- [113] R. D. Polak, G. P. Crawford, B. C. Kostival, J. W. Doane, and S. Žumer, “Optical determination of the saddle-splay elastic constant K_{24} in nematic liquid crystals,” *Phys. Rev. E*, vol. 49, p. 978, 1994. [85](#), [109](#), [126](#)
- [114] V. M. Pergamenschchik and S. Žumer, “Surface variations of the density and scalar order parameter and the elastic constants of a uniaxial nematic phase,” *Phys. Rev. E*, vol. 59, p. 2531, 1995.
- [115] G. Barbero and V. M. Pergamenschchik, “Intermediate periodic saddle-splay nematic phase in the vicinity of a nematic-smectic a transition,” *Phys. Rev. E*, vol. 66, p. 051706, 2002. [85](#), [109](#), [126](#)
- [116] A. Bogi and S. Faetti, “Elastic, dielectric and optical constants of 4'-pentyl-4-cyanobiphenyl,” *Liq. Cryst.*, vol. 28, p. 729, 2001. [90](#)

REFERENCES

- [117] M. J. Bradshaw, E. P. Raynes, J. D. Bunning, and T. E. Faber, "The Frank constants of some nematic liquid crystals," *J. Phys. (Fr.)*, vol. 46, p. 1513, 1985. [90](#)
- [118] B. Kundu, R. Pratibha, and N. V. Madhusudana, "Anomalous temperature dependence of elastic constants in the nematic phase of binary mixtures made of rodlike and bent-core molecules," *Phys. Rev. Lett.*, vol. 99, p. 247802, 2007. [98](#)
- [119] R. Pratibha, N. V. Madhusudana, and B. K. Sadashiva, "An orientational transition of bent-core molecules in an anisotropic matrix," *Science*, vol. 288, p. 2184, 2000. [98](#)
- [120] P. Sathyanarayana, V. S. R. Jampani, M. Skarabot, I. Musevic, K. V. Le, H. Takezoe, and S. Dhara, "Viscoelasticity of ambient-temperature nematic binary mixtures of bent-core and rodlike molecules," *Phys. Rev. E*, vol. 85, p. 011702, 2012. [98](#)
- [121] J. Matraszek, J. Mieczkowski, J. Szydowska, and E. Gorecka, "Nematic phase formed by banana-shaped molecules," *Liq. Cryst.*, vol. 27, p. 429, 2000. [98](#)
- [122] J. W. Goodby, P. J. Collings, T. Kato, C. Tschierske, H. F. Gleeson, and P. Raynes, *Handbook of Liquid Crystals*. Wiley-VCH GmbH and Co., 2nd ed., 2014. [37](#), [109](#), [119](#)
- [123] C. D. Southern, *Order Parameter Measurements and Phase Behaviour in Bent-Core Liquid Crystal Systems*. PhD thesis, University of Manchester, 2008. [109](#), [115](#), [124](#)
- [124] D. Shen, S. Diele, G. Pelzl, I. Wirth, and C. Tschierske, "Designing banana-shaped liquid crystals without schiff's base units: m-terphenyls, 2,6-dihelypyridines and v-shaped tolane derivatives," *J. Mater. Chem.*, vol. 9, p. 661, 1999. [126](#)
- [125] G. Pelzl, S. Diele, and W. Weissflog, "Banana-shaped compounds - a new field of liquid crystals," *Adv. Mater.*, vol. 11, p. 707, 1999. [126](#)

REFERENCES

- [126] D. K. Yang, L. C. Chien, and J. W. Doane, "Cholesteric liquid crystal/polymer dispersion for haze-free light shutters," *Appl. Phys. Lett.*, vol. 60, p. 3102, 1992. [134](#)
- [127] I. Dierking, "Polymer network-stabilized liquid crystals," *Adv. Mater.*, vol. 12, p. 167, 2000.
- [128] R. A. M. Hikmet, "Anisotropic gels and plasticized networks formed by liquid crystal molecules," *Liq. Cryst.*, vol. 9, p. 405, 1991. [134](#)
- [129] L. E. Hough, H. T. Jung, D. Krüerke, M. S. Heberling, M. Nakata, C. D. Jones, D. Chen, D. R. Link, J. Zasadzinski, G. Heppke, J. P. Rabe, W. Stocker, E. Korblova, D. M. Walba, M. A. Glaser, and N. A. Clark, "Helical nanofilament phases," *Science*, vol. 325, p. 456, 2009. [135](#), [140](#), [143](#)
- [130] S. Anjali and R. Pratibha, "Cellular structures arising from viscoelastic phase separation in binary mixtures of thermotropic liquid crystals," *Soft Matter*, vol. 13, p. 2330, 2017. [135](#)
- [131] S. H. Ryo, H. Kim, S. Lee, Y. J. Cha, T. J. Shin, H. Ahn, E. Korblova, D. M. Walba, N. A. Clark, S. B. Lee, and D. K. Yoon, "Nucleation and growth of a helical nanofilament (B_4) liquid crystal phase confined in nanobowls," *Soft Matter*, vol. 11, p. 7778, 2015. [140](#)
- [132] H. Niwano, M. Nakata, J. Thisayukta, D. R. Link, H. Takezoe, and J. Watanabe, "Chiral memory on transition between the B_2 and B_4 phases in an achiral banana-shaped molecular system," *J. Phys. Chem. B*, vol. 108, p. 14889, 2004.
- [133] T. Niori, T. Sekine, J. Watanabe, T. Furukawa, and H. Takezoe, "Distinct ferroelectric smectic liquid crystals consisting of banana shaped achiral molecules," *J. Mater. Chem.*, vol. 6, p. 1231, 1996.
- [134] C. Zhang, N. Diorio, O. D. Lavrentovich, and A. Jákli, "Helical nanofilaments of bent-core liquid crystals with a second twist," *Nat. Commun.*, vol. 5, p. 1, 2014. [140](#)

REFERENCES

- [135] P. J. Collings, A. J. Dickinson, and E. C. Smith, “Molecular aggregation and chromonic liquid crystals,” *Liq. Cryst.*, vol. 37, p. 701, 2010. [163](#), [166](#), [172](#)
- [136] C. E. Bertrand, K. L. Linegar, A. F. Kostko, and M. A. Anisimov, “Multiscale dynamics of pretransitional fluctuations in the isotropic phase of a lyotropic liquid crystal,” *Phys. Rev. E*, vol. 79, p. 041704, 2009. [163](#), [166](#), [172](#)
- [137] F. Liu, C. Wang, J. K. Baral, L. Zhang, J. J. Watkins, A. L. Briseno, and T. P. Russell, “Relating chemical structure to device performance via morphology control in diketopyrrolopyrrole-based low band gap polymers,” *J. Am. Chem. Soc.*, vol. 135, p. 19248, 2013. [173](#)
- [138] J. M. Virgili, Y. Tao, J. B. Kortright, N. P. Balsara, and R. A. Segalman, “Analysis of order formation in block copolymer thin films using resonant soft x-ray scattering,” *Macromolecules*, vol. 40, p. 2092, 2007.
- [139] J. R. Tumbleson, B. A. Collins, L. Yang, A. C. Stuart, E. Gann, W. Ma, W. You, and H. Ade, “The influence of molecular orientation on organic bulk heterojunction solar cells,” *Nat. Photonics*, vol. 8, p. 385, 2014.
- [140] B. A. Collins, J. E. Cochran, H. Yan, E. Gann, C. Hub, R. Fink, C. Wang, T. Schuettfort, C. R. McNeill, M. L. Chabinyk, and H. Ade, “Polarised x-ray scattering reveals non-crystalline orientational ordering in organic films,” *Nat. Mater.*, vol. 11, p. 536, 2012. [173](#)
- [141] C. Zhu, C. Wang, A. Young, F. Liu, I. Gunkel, D. Chen, D. Walba, J. Maclennan, N. Clark, and A. Hexemer, “Probing and controlling liquid crystal helical nanofilaments,” *Nano Lett.*, vol. 15, p. 3420, 2015. [173](#)